UNIVERSITY OF SOUTHAMPTON
FACULTY OF ENGINEERING, SCIENCE AND MATHEMATICS
INSTITUTE OF SOUND AND VIBRATION RESEARCH

A statistical jet-noise model based on the acoustic analogy and a RANS solution

by

Alessandro Bassetti

A thesis submitted in partial fulfilment of the degree of
Doctor of Philosophy

Jan 2009

Abstract

We introduce a hybrid model for the evaluation of jet noise. The model uses the information from a solution of the Reynolds-averaged Navier–Stokes equations (RANS). It evaluates the jet-noise power spectral density (PSD) in the quiescent region outside the turbulent jet. It includes the following components:

1. A propagation model based on the high- and low-frequency approximations of the Lilley-analogy Green's function. The high-frequency approximation is determined by combining a moving-medium Lighthill analogy and ray acoustics. The low-frequency model is made by using a flow-factor approach on each component of the source two-point CPSD. We use available analytical expressions of flow factors evaluated in the low-frequency limit.

2. A fixed-frame source model based on the source terms of the Goldstein (2001) expression for the Lilley analogy. Both the applied-stress and applied-force equivalent acoustic sources are retained. The used acoustic analogy allows for expressing the 2-point covariance of the applied-stress source by using 2-point velocimetry measurements in a turbulent jet. Specifically the applied-stress source can be put in correspondence to the unit-density Reynolds-stress statistics. Available measurements of the unit-density Reynolds-stress 2-point statistics are here used to derive an analytical model for the applied-stress 2-point correlation coefficient. Also the applied-force 2-point statistics, required for modelling noise source mechanisms at the presence of density inhomogeneities in the flow, is expressed on the basis of the unit-density Reynolds-stress 2-point statistics. Numerical methods are used to derive the frequency–wavenumber expression for a volumetric source-strength tensor.

3. A jet-flow prediction by using a commercial RANS solver and a set of connection relations expressing source-model parameters starting from the RANS solution. The RANS system includes Reynolds Stress modelling (RSM) closure equations. Turbulence anisotropy is then incorporated in the flow-statistics estimation. The proposed connection relations introduce a set of empirical parameters which are evaluated by matching model components to both velocimetry and acoustics measurements.

Modelled far-field jet-noise 1/3-octave spectra are compared to corresponding measurements for isothermal, unheated and hot jets.

Acknowledgements

This work has been carried out under the supervision of Prof. Christopher L. Morfey. Chris greatly contributed to the value of the present work. I wish to thank Chris for the many things I learnt through his guidance, for the mistakes he underlined, the omissions he noted and the problems he posed. Chris also gave moral support. To have him on my side during the whole duration of the PhD work has been fundamental. I am especially grateful to him for having followed this work after retirement from his academic position at the ISVR. Chris developed the solution of the flow-factor low-frequency asymptote associated with the Lilley–Goldstein analogy. He patiently read the present thesis and his feedback helped improving both the contents and the English.

Dr. Michael J. Fisher has been my first line manager at the ISVR; he suggested to start this research and formed the PhD team by inviting Chris to supervise the work. The present work is the continuation of a jet-noise research programme to which I contributed and where Mike acted as principal investigator. Mike also helped with many answers to my technical questions and with great encouragement.

This work has been done on a part-time basis. I want to thank all my research-job line managers at the ISVR for inviting me to spend time on the PhD research. Prof. R. J. Astley, one of them, took on the administrative duties as supervisor, after the retirement of Chris from his academic position; I wish to thank him also for this. Prof. John A. Fitzpatrick offered the hospitality of Trinity College Dublin, where I wrote the largest part of the present thesis. Working under John's guidance on LDA-data analysis contributed to the present work by clarifying technical aspects related to the Reynolds-stress statistics. Marcus Harper-Bourne contributed by providing data and diagrams regarding two-point flow measurements on a turbulent jet. The source-modelling part of the present work has been greatly inspired by his previous work on the subject. Technical input on both the low-frequency flow-factor asymptote and scaling aspects of the high-frequency solution has been provided by Dr. Brian J. Tester.

Sara helped immensely, especially when things have not gone as smoothly as I hoped; her patience and continuous support have been and are fundamental. A great support also came from my sister Erica who took care of my other life, in Italy. I would like to smile with the many friends who have been around during my stay in Southampton and the colleagues who made pleasant my work experience at the ISVR.

Contents

Chapter 1

Introduction

This work introduces a statistical model for the estimation of jet noise, based on the acoustic analogy applied to a statistically-described region of unsteady flow. The flow statistics are assumed time-stationary, but spatially inhomogeneous. The term "jet noise" refers here to the aerodynamic sound produced by the turbulent mixing of unbounded shear flows. Jet noise has been studied since the advent of turbojet propulsion in aeronautics, when it became part of our life as one of the dominant components of aircraft noise. Following over half a century of aeroacoustic research and development of propulsion systems, jet noise lost part of its impact as an aircraft-noise source.[a] It still represents the main source of noise during take-off. Its importance as a component of environmental noise pollution in areas near airports means that research on jet noise estimation, control and reduction is still a very active subject in the aeroacoustic community.

The sound-production mechanism associated with turbulent jet flows was first put on a theoretical basis by Lighthill.[1] In his ground-breaking work Lighthill rearranged the fluid-mechanics conservation equations in order to obtain a wave equation forced by non-linear terms in the flow variables. The assumption that the forcing terms are not affected by the acoustic field leads to an acoustic analogy in which flow non-linearities become the equivalent forcing terms of the linear differential equation that represents the acoustic radiation. In this way the sound generated by the flow can be scaled on the basis of the flow statistics.

Similarly, the model introduced here establishes a relation between the statistics of a given unbounded subsonic turbulent flow and the corresponding sound production. The model contains two main components

- An acoustic analogy that includes the mean-flow effect in the radiation operator and allows for analytical derivation of the Green function

[a]The advent of turbofan engines as aircraft propulsion system in the 1970s meant a reduction of jet-noise emissions and a relative amplification of other noise sources such as fan-generated noise, which had begun to be reduced by design changes (e. g. blade–vane numbers and axial spacing) as well as by the introduction of inlet liners.

- A model for the acoustic-source statistics that is compatible with available measurements of the relevant two-point flow statistics

The model uses two complementary acoustic analogies in order to define a field of equivalent acoustic sources associated with the prescribed stationary turbulence-statistics field. These acoustic analogies can be identified as the high-frequency and the low-frequency limits of the Lilley[2] analogy as formulated by Goldstein[3] (Lilley–Goldstein analogy). Both the applied-stress and the applied-force equivalent acoustic sources identified by Goldstein[3] are considered. The acoustic-pressure power spectral density (PSD) in the quiescent region surrounding the jet is derived by defining a volumetric source strength, by combining it with the appropriate Green function[b] and by performing spatial integration across the turbulent region. The source modelling that defines the volumetric source strength is based on published two-point-anemometry measurements; the source strength is derived as follows.

1. The two-point correlation associated with both the applied-stress and the applied-force equivalent sources is defined on the basis of the Reynolds-stress two-point statistics. A closure scaling hypothesis is applied in order to represent the applied-force term on the basis of the Reynolds-stress two-point correlation.

2. A suitable model for the Reynolds-stress two-point correlation coefficient is defined. The model assumes an exponential decay in terms of a space–time distance. The frequency-independent parameters associated with the model are assumed to be scalable from the local value of the time-averaged flow statistics; the decay shape is assumed to be universal for jet-type flows. The model shows agreement with the Harper-Bourne[4,5] two-point anemometry measurements for the Reynolds-stress component in the axial direction.

3. A model for the Reynolds-stress two-point cross power spectral density (CPSD) is obtained by applying a numerical Fourier transform to the two-point correlation function. The resulting two-point CPSD is phase shifted, according to source–observer radiation parameters, and integrated across the local region of coherence to give the contribution per unit source volume to the far-field pressure PSD.

The spatial distribution of time-stationary statistics associated with the jet flow is estimated by performing a solution of the Reynolds-averaged Navier–Stokes equations (RANS).[c] The

[b] This is different between the high- and low-frequency analogies.

[c] This approach is not new; it has been widely adopted since the early nineties, when the aeroacoustic research community found in the RANS numerical solvers a way to consistently estimate the statistics associated with turbulent jets. The work by Khavaran, Krejsa and Kim[6] used the solution of steady RANS with the two-equation k-ϵ closure. Following the work in Ref. [6], many other research programmes used this two-step hybrid approach for noise computation, combining RANS flow-statistics prediction and the acoustic analogy. Bailly Lafon and Candel[7] compare various acoustic-analogy approaches in combination with a RANS–k-ϵ solution for the flow. The two-equation closures used in the early works allow for describing the energetic content of the turbulent field; more complex closures enable a more detailed description. In the present work, the Reynolds-stress transport equation closure allows for anisotropy in the description of the turbulent-field statistics. This is a note of originality, compared to RANS-based jet noise models that are known to the author; see the review proposed in Chapter 2.

RANS solution outputs an incomplete description of the jet-flow statistics required by the acoustic-source model. This implies the definition of closure relations connecting the RANS solution to the acoustic-source two-point statistics. These closure relations introduce a set of universal[d] empirical parameters which needs to be estimated in order to perform noise predictions.

The present thesis is divided into 6 chapters and 9 appendices. A brief review of jet-noise models based on a RANS solution is presented in Chapter 2. The theory for aerodynamic-sound generation and radiation, according to the low- and high-frequency asymptotes of the Lilley–Goldstein analogy, is introduced in Chapter 3. A review of the derivation of the perfect-gas Lilley–Goldstein equation is presented in Appendix B. The high-frequency model uses a solution for the convective wave equation; this solution is derived in Appendix C by using a moving-source solution of the stationary-medium wave equation.[e] The source modelling procedure, as described in points 1 to 3 above, is detailed in Chapter 4. The application of the model to jet-noise prediction is described in Chapter 5, where a description of the RANS solution is given and the volumetric acoustic-source strength is defined on the basis of the RANS output. The 90-degree 1/3-octave spectral predictions associated with the model low-frequency and high-frequency solutions are broken down into their corresponding applied-stress (quadrupole) and applied-force (dipole) contributions. The modelled spectral contributions are compared to corresponding noise measurements.[f] A preliminary comparison between modelled far-field jet-noise spectral contributions and corresponding measurements at rear-arc polar angles has been performed. The comparison is limited to one isothermal single-stream jet and is presented in Appendix I.

[d]These parameters are universal in the sense that they do not change by changing nozzle geometry, nozzle-exit velocity and temperature, presence of co-flowing stream etc. The set of parameters is fixed once a given turbulence closure is defined (closure model and corresponding empirical parameters) for the RANS solution; it does not depend on the RANS-solution boundary conditions.

[e]The derivation makes use of the invariance of the wave equation to Lorentz-type transformations. A Lorentz transformation is applied in order to reduce the moving-source free-field Green problem to a stationary-source standard free-field Green problem. The solution is given for the free acoustic field of monopole, dipole and quadrupole sources moving at uniform speed. For multipole sources, it includes the near-field terms. The approach is alternative to the Garrick-triangle method introduced in Ref. [8] and normally used in aeroacoustics when dealing with moving sources.

[f]The noise measurements are far-field jet noise measurements acquired in dedicated anechoic facilities. The subsonic-jet data acquired by Tanna Dean and Burrin[9] are used in conjunction with data measured at the QinetiQ Noise Test Facility (NTF) in Pyestock. The NTF measurements include single-stream data acquired in 1983 on a 86 mm convergent nozzle, as described in Ref. [10]; these data were delivered by QinetiQ to the EU jet-noise programme JEAN and made available to the ISVR as JEAN partner. The NTF data also include coaxial-jet measurements acquired in 2000 for the ISVR as part of a jet-noise programme funded by the United Kingdom Engineering and Physical Sciences Research Council (EPSRC); Airbus UK partly funded the programme by sponsoring the experimental-data acquisition.

Chapter 2

A review of RANS-based jet-noise models

The principal subject of the present chapter is a literature review regarding published research on hybrid[a] jet-noise models which base the turbulent-flow prediction on a RANS solution. The reviewed jet-noise models include the following components:

i Estimation of the flow time-stationary statistics. This is done by solving the Reynolds averaged Navier–Stokes (RANS) equations. The system of RANS equations will depend on the particular turbulence-model hypotheses and the associated closure strategy.[b]

ii Estimation of the two-point cross power spectral density (CPSD) associated with the equivalent acoustic sources. This is done by defining the equivalent acoustic sources model and assuming a shape function for the corresponding two-point statistics. The equivalent-source mean-product values and the parameters associated with the two-point statistics shape function are then to be expressed on the basis of the RANS-solution flow. The incomplete flow-statistics description offered by the RANS solution requires defining a further set of empirical closure relations connecting the source-statistics to the RANS solution. These closure relations, referred to as connection relations, introduce a set of empirical parameters. The value of these empirical parameters is defined on the basis of a calibration procedure that matches model components to experimental data.

iii Acoustic radiation from source region to an observer outside the turbulent region. Here

[a]By using the same terminology as in Colonius and Lele,[11] with hybrid jet-noise models we indicate those models that estimate turbulent-mixing noise by integrating across a relevant spatial region of unsteady flow the noise contributions associated with appropriately modelled equivalent acoustic sources. Hybrid models combine a flow-prediction model to an acoustic model to generate an estimate of the noise contribution associated with a given flow volume. Models that directly address the compressible fluid dynamics and simulate the pressure-field signal at a given location are referred to as direct models, Ref. [11].

[b]Although the reviewed works assume isotropic turbulence and adopt a k-ϵ two-equation closure RANS system, subtle differences occur in the choice of the turbulence-closure parameters and, in one case, an extra turbulent scalar is introduced and modelled.

the solution of the Green problem is used to derive a propagation factor that, if applied to the source two-point CPSD, outputs the unit-volume contribution to the observer-region acoustic-pressure PSD. The Green problem is solved by assuming a stationary base flow between the source and the observer; the solution is found either numerically or by using asymptotic approximations yielding to analytical solutions.

The reviewed models are analysed in a systematic way; the above 3 points are put in evidence for each model. The model derived in the present thesis is then compared to the reviewed models in order to underline possible analogies and points of originality. The original components of the model are then briefly stated.

2.1 Review

Hybrid models for jet-noise estimation process the information associated with a turbulent-jet flow field. The use of a RANS solution to determine the flow-statistics field has been widely adopted since the 1990s. Khavaran, Krejsa and Kim[6] used the solution of steady RANS with the two-equation k-ϵ closure; their work, based on the work of Mani, Balsa and Gliebe,[12] describes the first version of the prediction scheme referred to as the MGBK model.[a] The MGBK model is based on the Lilley[2] acoustic analogy, with the forcing terms is the form given by Goldstein.[13] The applied-force equivalent source is not considered in the model which is based on the Goldstein[13] applied-stress source $\mathbf{u}' \otimes \mathbf{u}'$ ($\mathbf{u}'$ is the fluctuating part of the velocity). We refer to this source as the unit-density Reynolds stress. The Lilley-analogy Green function is solved for point sources moving at a given convection velocity $\mathbf{u}_C$, directed as the jet axis. This implies that the acoustic-radiation operator of the model incorporates the source-convection effect and operates on a modified two-point CPSD of the equivalent source. In the MGBK model, the source modified two-point CPSD does not explicitly contain the convection effect. It is derived from a model of the equivalent-source two-point correlation, which is expressed in the moving frame.[b] The two-point correlation of the unit-density Reynolds stress is modelled as a combination of opportune components of the turbulent-velocity correlations. For the generic ij, kl component, it is given as follows:

$$\begin{aligned} \overline{[u_i' u_j']_A \, [u_k' u_l']_B} \;=\; & \overline{[u_i']_A \, [u_k']_B} \;\; \overline{[u_j']_A \, [u_l']_B} \\ & + \overline{[u_i']_A \, [u_l']_B} \;\; \overline{[u_j']_A \, [u_k']_B} \\ & + \overline{[u_i']_A \, [u_j']_B} \;\; \overline{[u_k']_A \, [u_l']_B} \end{aligned} \tag{2.1}$$

[a] This prediction scheme introduced a RANS-solution flow- and turbulence-field prediction in the jet noise model by Mani, Balsa and Gliebe[12] (MGB). The MGB model used an extension of Reichardt's theory in order to predict spatial distributions for the mean velocity, temperature and axial turbulence intensity in both single-stream and coaxial round jets.

[b] This is an inertial reference frame moving at the convection velocity of a given source region.

Here we used the notation $[\mathrm{x}]_A = \mathrm{x}(\mathbf{y}_A, t_A)$ and $[\mathrm{x}]_B = \mathrm{x}(\mathbf{y}_B, t_B)$, where $\mathbf{y}$ indicates a space location in the fixed[c] reference frame, t denotes times and subscripts A and B are used to distinguish quantities measured at different points. Khavaran, Krejsa and Kim[14] justify expression (2.1) as a consequence of the isotropic turbulence model of Batchelor.[15] Through the hypothesis (2.1), referred to below as quasi-normality hypothesis, the modelling effort is transferred from the unit-density-Reynolds-stress to the velocity two-point covariance function. The velocity moving-frame two-point covariance is assumed to be a separable function of time and space separations. It is factorised as the product of mean-square value and correlation coefficient. The mean-square value is assumed to be proportional to the local value of the turbulent kinetic energy and the two-point correlation coefficient is given as follows:

$$\hat{c}_{i,j} = \left(\left(\mathrm{f}(\xi) + \frac{\xi}{2} \mathrm{f}'(\xi) \right) \delta_{ij} - \frac{\xi_i \xi_j}{2\xi} \mathrm{f}'(\xi) \right) \mathrm{g}(\tau) \tag{2.2}$$

Here τ denotes the time separation $t_B - t_A$ and ξ is the space-separation modulus in the moving frame ($\boldsymbol{\xi} = \boldsymbol{\eta} - \tau \mathbf{u}_C$, with $\boldsymbol{\eta} = \mathbf{y}_B - \mathbf{y}_A$) and f' is the derivative of f with respect to ξ. The decay trend of the functions f and g is assumed Gaussian and controlled by moving-frame length and time scales l_m and τ_m:

$$\mathrm{f}(\xi) = \exp\left(- \left(\frac{\xi}{l_m(\mathbf{y})} \right)^2 \right) \qquad \mathrm{g}(\tau) = \exp\left(- \left(\frac{\tau}{\tau_m(\mathbf{y})} \right)^2 \right) \tag{2.3}$$

As previously stated, the moving-frame equivalent-source two-point correlation coefficient model (2.2) does not explicitly contain a convection effect. The connection relations express the local value of the moving-axis length and time scales as follows:

$$\tau_m(\mathbf{y}) = C_\tau \frac{k}{\epsilon} \qquad l_m(\mathbf{y}) = C_l \frac{\sqrt{k^3}}{\epsilon} \tag{2.4}$$

where k and ϵ respectively denote the turbulent kinetic energy and the turbulent dissipation rate. We refer to expressions (2.4) as the traditional connection relations for time and length scales. The mean-square value of the acoustic source is assumed proportional to the squared turbulent kinetic energy. The acoustic-pressure PSD is modelled for observers in the fixed frame, this implies a source–observer Doppler shift. The radiation from a given source region is modelled by using an high-frequency approximation of the Lilley analogy. The high-frequency approximation was developed by Balsa[16] for axisymmetric base flows. For supersonic acoustic Mach numbers, singularities occur both in the sound-transmission factor and in the Doppler factor relating the source and observer frequencies. The singularities occur at the zeroes of $D = 1 - M\cos(\vartheta)$ and $D_c = 1 - M_c \cos(\vartheta)$, where $M(\mathbf{y}) = u(\mathbf{y})/c_\infty$ is the acoustic Mach number, $M_c(\mathbf{y}) = u_c(\mathbf{y})/c_\infty$ is the convection Mach number and ϑ is the downstream

[c]This is the reference frame where the flow statistics can be assumed as time-stationary. In general we can assume that this frame is fixed to the time-invariant boundary conditions associated with the experiment. In jet-flow experiments this reference frame is the reference frame fixed to the nozzle.

source–observer polar angle. We refer to this singularity as the critical-layer singularity. The critical-layer singularity is removed by using modified factors

$$D = \sqrt{(1 - M\cos(\vartheta))^2 + (\mathrm{h}(\mathbf{y}))^2} \qquad D_c = \sqrt{(1 - M_c\cos(\vartheta))^2 + (\mathrm{h}(\mathbf{y}))^2} \tag{2.5}$$

Where the real function $\mathrm{h}(\mathbf{y})$ and the convection Mach number are assumed to depend on the local value of flow-field statistics through the following connection relations.

$$\mathrm{h}(\mathbf{y}) = C_h \frac{\sqrt{k}}{c_\infty} \qquad M_c = 0.5 M_J + C_M M(\mathbf{y}) \tag{2.6}$$

Here M_J is the nozzle-exit Mach number and M is the local mean-flow Mach number. The calibration procedure used to define the connection-relation parameters is not specified in Ref. [14]; presumably the parameters are set by using a best-match criterion between noise prediction and available jet-noise spectral measurements.
The components associated with the MGBK model are summarised as follows:

i RANS equations with k-ϵ closure

ii Lilley-analogy applied-stress sources, as in Goldstein[13] (unit-density Reynolds stress)
Moving-frame modelling for the equivalent-source statistics
Unit-density Reynolds-stress two-point correlation function derived as a combination of turbulent-velocity covariance functions (quasi-normality hypothesis)
Turbulent velocity two-point covariance with separable-variable function (Gaussian for both space and time separations)
Traditional connection relations for time and length scales, see expressions (2.4)
Modified source-convection factor to remove the critical-layer singularity
Connection-relation empirical parameters chosen by best matching model predictions and jet-noise measurements

iii High-frequency asymptotic solution of the Lilley-operator Green function with axisymmetric base flow, as derived by Balsa[16]

Tam and Auriault[17] proposed a hybrid model for "fine-scale turbulence" jet noise.[d] The principal originality included in the work by Tam and Auriault[17] is an equivalent-source definition that deviates from the traditional acoustic-analogy procedure introduced by Lighthill.[1] Tam and Auriault[17] linearised the Euler equations around the mean-flow solution and neglected the second-order terms in the fluctuation variable. The linearised Euler equations were used to derive the sound propagation from a given source region. A source term was then added,

[d]The concept of fine-scale turbulence noise has been introduced by Tam, Golebiowski and Seiner[18] after a study of far-field noise spectra measured on round single-stream jets. The jet-noise spectra were interpreted as a sum of two components. These components were associated with two distinct source mechanisms: one with large-scale coherent flow structures and the other with small-scale flow structures. The large-scale structure noise was assumed to dominate the jet-noise spectra recorded at low polar angles, while the fine-scale structures were assumed the dominant noise component in the sideline and upstream directions.

forcing the momentum-conservation equation. Obtained following similar reasoning as in the gas kinetic theory, the source was an equivalent pressure which was assumed as a result of fine-scale velocity fluctuations; it was taken to scale with the mean turbulent kinetic energy k. We indicate this source with the symbol q_T and we refer to it as the Tam–Auriault source. The radiation solution was obtained by solving the adjoint Green-function problem on the LEE. The mean flow was taken axisymmetric, transversely sheared, and 1-D; this reduced the problem to the axisymmetric Lilley-analogy Green problem. The propagation factor derived by Tam and Auriault[17] acts on the two-point CPSD of the material derivative of the Tam–Auriault source; the centre of the source-statistics modelling in Ref [17] is thus the derivation of a model for

$$\overline{\left[\frac{Dq_T}{Dt}\right]_A \left[\frac{Dq_T}{Dt}\right]_B}$$

Such model was derived by fitting a suitable analytical function for the two-point correlation coefficient and assuming that the mean-square value associated with the Lagrangian derivative of q_T is proportional to the mean-square value of q_T divided by a squared time scale. It is given as

$$\overline{\left[\frac{Dq_T}{Dt}\right]_A \left[\frac{Dq_T}{Dt}\right]_B} = C_{q_T} \frac{\overline{q_T^2(\mathbf{y})}}{\tau_T^2} \exp\left(-\frac{|\eta_1|}{\bar{u}\tau_T} - \frac{\ln(2)}{l_T^2}\left((\eta_1 - \bar{u}\tau)^2 + \eta_2^2 + \eta_3^2\right)\right) \tag{2.7}$$

Here τ_T denotes the correlation-coefficient $1/e$-decay time for zero space separation in the moving frame;[e] l_T is the transverse-space-separation length scale. The 2-point correlation coefficient in expression (2.7) was compared to the two-point correlation coefficient of the velocity covariance in a low-Mach-number jet, as published by Davies, Fisher and Barratt.[19] We note that in general the velocity two-point covariance and the two-point correlation of q_T (or its Lagrangian derivative) are different functions; the "reasonably good agreement" (in the time-separation domain) between the correlation coefficient in (2.7) and the velocity measurements by Davies, Fisher and Barratt[19] was anyway considered sufficient by Tam and Auriault[17] to ensure "the right" functional characteristics for model (2.7). The time and length scales (τ_T and l_T) in expression (2.7) were related to the RANS solution by the traditional connection relations, analogous to (2.4). Note that the model only uses 3 empirical parameters: 2 for the time and length scales and a further one represents the fraction of turbulent kinetic energy associated with the acoustic source. The RANS solution was in this case determined by using a two-equation k-ϵ closure, with non-standard closure empirical parameters. These non-standard turbulence-closure parameters were identified by Thies and Tam[20] and allow to generate a mean-flow solution for the jet in closer agreement with jet-flow measurements. The model described in Ref. [17] can be summarised as follow:

i RANS equations with k-ϵ closure, with closure empirical parameters as described by

[e]Here the convection velocity is assumed equal to the mean velocity and directed in axial direction. Transforming equation (2.7) into moving-frame coordinates ($\eta_1 = \xi_1 + \bar{u}\tau$, $\eta_2 = \xi_2$, $\eta_3 = \xi_3$) shows that τ_T is the $1/e$-decay time of the correlation coefficient at space-separation modulus $\xi = 0$.

Thies and Tam[20]

ii Tam–Auriault source model for fine-scale turbulent mixing
Source two-point correlation model in the fixed frame with non-separable function of time and space separations, see (2.7)
Source two-point correlation coefficient in agreement with velocity two-point correlation coefficient measured by Davies, Fisher and Barratt[19]
Traditional connection relations
Connection-relation parameters determined by best match to suitable[f] acoustic measurements

iii Adjoint Green function of the Euler equations linearised around an axisymmetric, transversely sheared, 1-D mean flow (equivalent to axisymmetric-flow Lilley-analogy Green function)

Morris and Farassat[21] introduced an acoustic analogy based on the Linearised Euler equations (LEE). A pressure-related variable $\pi_M = \gamma^{-1}\ln(p/p_\infty)$, the flow velocity and the speed of sound were used as independent variables for the mass- and momentum-conservation equations. The Euler equations were linearised around the mean value of the independent variables to yield a set of four scalar equations for the fluctuations of π_M and the velocity fluctuations. Note that the mean-velocity field is in this case considered as a transversely sheared, 1-D flow. Non-linear terms were moved to the right-hand side and considered as equivalent acoustic sources. This resulted in the identification of a dilatation-rate source and an applied-force source. The described acoustic analogy, which we refer to as Morris–Farassat analogy, has been used in the RANS-based jet-noise predictions introduced by Morris and Boluriaan[22] and further developed by Raizada and Morris.[23] In developing these acoustic-analogy hybrid techniques, two distinct source-modelling approaches were used. Morris and Boluriaan[22] used a fixed frame time- and space-separation model for the two-point correlation coefficient of both the dilatation-rate and the applied-force sources. They also proposed a frequency/space-separation model, based on the Harper-Bourne[5] model for the space-separation shape of the normalised 2-point CPSD of the turbulent velocity.[g] This model is given as follows:

$$s_M = \frac{q^2 C_\tau \tilde{l}_1}{\bar{u}\left(1+\left(\frac{2\pi f C_\tau \tilde{l}_1}{\bar{u}}\right)^2\right)} \exp\left(-\sqrt{\left(\frac{\eta_1}{\tilde{l}_1}\right)^2+\left(\left(\frac{\eta_2}{\tilde{l}_2}\right)^2+\left(\frac{\eta_3}{\tilde{l}_3}\right)^2\right)^2}\right) \exp\left(\mathrm{j}\ 2\pi f \frac{\eta_1}{\bar{u}}\right) \quad (2.8)$$

Here the mean-square value of the equivalent acoustic sources is indicated by q^2; in Ref. [22] it is appropriately specified for the dilatation-rate and the applied-force sources. In expression (2.8), the quantities $\tilde{l}_i$ (i=1, 2, 3) represent the $1/e$-decay scales of the normalised two-point CPSD,

[f] Only noise spectra where the "fine-scale" source is dominant.

[g] With normalised two-point CPSD function we refer to the two-point CPSD divided by the zero-separation CPSD. The latter function is also referred to as autospectrum.

which is the second factor in expression (2.8); these length scales are frequency-dependent, as measured by Harper-Bourne.[4] The analytical expression used in Ref. [22] to represent the frequency dependence of the length scales $\tilde{l}_i$ is

$$\frac{1-\exp\left(-\tau_\sigma f\right)}{\tau_\sigma f}$$

Note that this function tends to 1 at low frequency and decays as $1/f$ at high frequency. The time scale τ_σ regulates the transition between low- and high-frequency trends. It is expressed as a function of the local turbulent-velocity length scale ($l = C_l k^{3/2}/\epsilon$) by means of a further calibration parameter and the nozzle-exit velocity u_J:

$$\tau_\sigma = \frac{C_s l}{u_J}$$

The calibration parameter C_s is constant for the jet and, together with the parameters C_l, C_τ and A,[h] is part of the set of connection-relation calibration parameters. The second factor in expression (2.8) is the shape of the source autospectrum; this would be corresponding to an exponential-decay autocorrelation coefficient if the pseudo time scale $C_\tau \tilde{l}_1/\bar{u}$ was not frequency dependent.[i] Morris and Boluriaan[22] verified that, at 90-degree polar angle, the CPSD model (2.8) yields predicted-noise spectral shapes in closer agreement with corresponding jet-noise measurements, compared to the CPSD model based on the alternative time-domain formulation also presented in Ref. [22]. As a consequence, the frequency-domain model (2.8) was later used in the development of the RANS-based model, presented by Raizada and Morris.[23] The radiation model used by Morris and Boluriaan[22] was obtained by using low- and high-frequency asymptotic approximations of the Lilley-type operator associated with the Morris–Farassat analogy.[j] Raizada and Morris[23] further developed the radiation model by adding the numerical adjoint Green function of the LEE to the asymptotic solutions[k] used in Ref. [22]. The final jet-noise model, described by Raizada and Morris,[23] contains the following principal components.

i RANS equations with k-ϵ closure, closure parameters as in Thies and Tam[20]

ii Applied-force and dilatation-rate sources of the Morris–Farassat acoustic analogy

[h]The parameters C_l and A are respectively part of traditional connection relation for the length scales, see (2.4), and part of the scaling factor between the source and the turbulent kinetic energy k. Less clear is the origin of the parameter C_τ which is possibly associated with a connection relation of traditional type, see (2.4), for the time scales.

[i]Morris and Boluriaan stated that in their analysis the autocorrelation was modelled with an exponential form; this statement is contradicted by the form chosen for the autospectrum.

[j]The LEE system proposed by Morris and Farassat[21] can be rearranged into a third-order equation for the Lilley analogy. The equation differs from the classical equation, having a different linear operator. The high-frequency solution was obtained by applying to the problem-specific Lilley-type operator the procedure indicated by Balsa.[16] The low-frequency solution was determined by following the steps indicated by Goldstein.[24, 25, 26]

[k]Note that in Ref. [23] the procedures adopted by Balsa[16] and Goldstein[24] were applied to derive high-frequency asymptotic solutions. The procedure used by Dowling Ffowcs-Williams and Goldstein[27] was used to derive the low-frequency solution. The use of new or alternative forms of asymptotic approximations is a further development of the propagation model in Ref. [22].

Common normalised CPSD model for dilatation-rate and components of applied-force sources; different source components assumed as uncorrelated
Source modelling in the fixed frame and in the frequency/space-separation domain
Source CPSD factorised into autospectrum (zero space separation) and normalised CPSD, following the approach indicated by Harper-Bourne[5]
Original source autospectrum, frequency-domain modification of exponential-decay autocorrelation
Analytical model suggested by Harper-Bourne[4] for the normalised CPSD factor

iii Numerical derivation of the adjoint Green function associated with the Morris–Farassat analogy with 1-D, transversely-sheared and axisymmetric base flow
Also asymptotic approximations of the Lilley-analogy (derived from the Morris–Farassat analogy) Green function

A prediction scheme based on the Lilley acoustic analogy was introduced and is under development at the NASA Glenn research centre. The prediction scheme, named JeNo, was derived from a development of the MGBK method.[l] The version 1.0 of the JeNo prediction scheme, described by Khavaran, Bridges and Georgiadis,[28] upgraded the improved MGBK scheme by using a rigorous Lilley-analogy Green function,[m] where the MGBK method used the high-frequency asymptotic approximation proposed by Balsa.[31] JeNo 1.0 implemented the Lilley analogy with the source terms introduced by Goldstein[13] and only retained the applied-stress contribution; Khavaran, Bridges and Georgiadis[28] showed the similarity between the source terms and the sources in the Lilley–Goldstein analogy (Ref. [3]). A more recent implementation of the prediction scheme, referred to as JeNo,v1 by Bridges, Khavaran and Hunter,[33] was described by Khavaran and Kenzakowski;[34] here the principal upgrade is the introduction of the enthalpy-fluctuation source term.[n] The added enthalpy noise source together with an upgraded turbulence modelling in the RANS-solution procedure were used to

[l]The MGBK scheme was subject to a number of improvement steps, starting from the early version by Khavaran, Krejsa and Kim[14] which is described at the beginning of the present chapter. The principal modifications regard the source modelling, where a separable-variable model such as (2.2) was used, but the original Gaussian trends of f(ξ) and g(τ), see expressions (2.3), were substituted by the exponential-decay trends

$$\mathrm{f}(\xi) = \exp\left(-\frac{\xi}{l_m(\mathbf{y})}\right) \qquad \mathrm{g}(\tau) = \exp\left(-\frac{|\tau|}{\tau_m(\mathbf{y})}\right)$$

The change, justified with an improved matching between model and experimental measurements of the velocity two-point correlation coefficient, led to improved spectral shapes for the jet noise predictions. For further information regarding these developments, the reader is addressed to the works by Khavaran[29] and by Khavaran, Bridges and Freund.[30]

[m]In JeNo 1.0, the Green function for the Lilley equation is evaluated by following the adjoint Green function procedure indicated by Tam and Auriault.[32] The singularity appearing at supersonic acoustic Mach number, referred to as critical-layer instability, is removed by means of a modified Doppler factor which is used in proximity of the critical-layer region.

[n]Khavaran and Kenzakowski[34] used a source description which is derived from the Goldstein[35] generalised acoustic analogy. Using the parallel-flow assumption and neglecting the divergence of the Favre-averaged Reynolds stress plus the density fluctuations in the applied-stress sources reduce the applied-stress source to the same form as introduced by Goldstein[13] (the same form as in the version described in Ref. [28]). The more recent implementation, Ref. [34], added 5 terms to the equivalent-source term in the earlier implementation; compare eq. (25) on page 9 of Ref. [34] to eq. (4) on page 6 of Ref. [28].

improve noise predictions for hot jets. The spectral characteristics of the equivalent acoustic sources in JeNo,v1 were determined by modelling the two-point order-4 velocity correlation and the two-point enthalpy–velocity correlation. Both these models were related to the moving reference frame and do not include the convection effect. The models are based on the two-point velocity correlations; while turbulence quasi-normality was invoked for the order-4 velocity correlations, the velocity–enthalpy correlations were modelled by separating the velocity terms from the enthalpy terms through the following factorisation

$$\overline{[u_i h_0]_A \; [u_j h_0]_B} = \overline{[u_i]_A [u_j]_B} \;\; \overline{[h_0]_A [h_0]_B} \tag{2.9}$$

where h_0 indicates the stagnation enthalpy. The absence of experimental data regarding the stagnation-enthalpy two-point correlation required a first-approximation closure assumption for the corresponding two-point correlation coefficient. This was assumed to follow a decay trend similar to the velocity correlation coefficient. The velocity and stagnation-enthalpy two-point correlation coefficients are given by (2.2) which, assuming exponential decay trends for both the time- and space-separation trends (see note l on page 11), can be expressed as follows:

$$\hat{c}_{i,j} = \left(\left(1 + \frac{\pi}{2 l_m} \xi \right) \delta_{ij} - \frac{\pi \xi_i \xi_j}{2 l_m \xi} \right) \exp\left(-\frac{\pi \xi}{l_m} - \frac{|\tau|}{\tau_m} \right) \tag{2.10}$$

Additional turbulent modelling was added in the definition of the RANS equations which, together with mean-flow and isotropic-turbulence variables, contain the stagnation-temperature fluctuation among the variables. The stagnation-temperature fluctuations were used in order to scale the enthalpy-noise term.

The principal components of the JeNo,v1 code can be summarised as follows.

i RANS equations with k-ϵ closure
Additional turbulence modelling for direct output of stagnation-temperature fluctuations

ii Applied-stress and enthalpy-fluctuation sources of the Goldstein[35] analogy
Enthalpy-noise source scaled by stagnation-temperature fluctuations
Source modelling as in the improved MGBK method, with exponential trends for both the space- and time-separation shape functions

iii Numerical derivation of the adjoint Green function associated with the Lilley analogy, with axisymmetric base flow
Critical layer instability removed by adopting modified Doppler factors

A further model based on the MGBK approach was introduced by Self and Azarpeyvand.[36,37] The model contains the main components as the early-version MGBK model described by Khavaran, Krejsa and Kim[6] (reviewed at the beginning of the present chapter). Self and Azarpeyvand[36,37] introduced a connection relation for the time scale τ_m, see time-separation

trend f in (2.3). This time-scale connection relation is given as follows:

$$\tau_m = C_1 \left(C_\tau \frac{k}{\epsilon} \left(\frac{l_m}{d_J} \right)^{\frac{2}{3}} \exp \left(\frac{3}{2} C_2 \left(2\pi \frac{l_K}{l_m} \right)^{\frac{4}{3}} \right) - \sqrt{\pi C_2 \frac{\nu}{\epsilon}} \operatorname{erfi} \left(\frac{3}{2} C_2 \left(2\pi l_K l_m \right)^{\frac{2}{3}} \right) \right) \quad (2.11)$$

Compare to the corresponding traditional relation for τ_m in (2.4). In expression (2.11) l_m denotes the moving frame length scale, as in (2.4), ν is the kinematic viscosity and $l_K = (\nu^3/\epsilon)^{1/4}$ is the Kolmogorov length scale. The function erfi is the imaginary error function. Self and Azarpeyvand[36,37] stated that expression (2.11) is related to a wave-number model of the turbulence spectrum, but they did not clearly explain the relation. Note that further empirical parameters C_1 and C_2 are introduced in the connection relation (2.11), compared to the traditional relation (2.4). This increases the empiricism of the model by Self and Azarpeyvand and extends its prediction range in comparison with the original MGBK model. Presumably, as in the MGBK method, the connection-relation empirical parameters were set by matching far-field model predictions to corresponding jet-noise measurements. We note that, where one bases the definition of the model empirical parameters by simply comparing far-field noise predictions and corresponding experimental data, arbitrarily enlarging the prediction range of the model (by adding further degrees of freedom) implies narrowing the error between predictions and measurements. With zero probability, such arbitrary degree of freedom will improve the physical basis of the model. The prediction method would then better fit the parameter-calibration jet-noise measurements, but not necessarily do the same with measurements outside the range associated with this specific set of experimental data. A consequent criticism to the connection relation (2.11) is that Self and Azarpeyvand[36,37] did not support it with jet-flow experimental data.[o]

The principal components of the model proposed by Self and Azarpeyvand[36,37] are the same as in the MGBK model (see page 7), with the following exception:

ii Original connection relation expressing the moving-frame time scale for the acoustic-source two-point correlation

Goldstein and Leib[38] presented a hybrid model based on the generalised acoustic analogy introduced by Goldstein.[35] In Ref. [38], a parallel base flow assumption is made in order to reduce the model to a Lilley-type acoustic analogy and to determine the far-field acoustic radiation by using a Lilley-analogy Green function. For mean flows including regions at supersonic acoustic Mach number, the Lilley-analogy Green function presents a singularity for sources in the so-called critical layer. Goldstein and Leib[38] removed the critical-layer instability by adopting a matched asymptotic expansion in the proximity of the critical layer region.[p]

[o] As it will be introduced below, a development on the time-scale connection relation was also proposed by Goldstein and Leib.[38] In this case the connection relation was supported by experimental data and the hypothesis of turbulence quasi normality.

[p] As explained in Ref. [38] the critical layer instability is due to the parallel-base-flow assumption and a corresponding unphysical amplification. The relaxation of the parallel-flow hypothesis allows for removing the

In Ref. [38], the modelling of the source two-point cross covariance is restricted to the applied-stress source only. The two-point covariance of the applied-stress sources is associated with the Reynolds-stress two-point covariance.[q] The Reynolds-stress two-point correlation coefficient is modelled in the moving reference frame; here it is assumed to follow a trend which is not separable between space and time. The decaying trend is represented as an infinite series of terms; this series is then truncated to the first two terms in order to get the predictions. The truncated moving-frame two-point correlation coefficient is assumed to follow the trend

$$c_{ij,kl} = C_{0,0}\left(1 - C_{1,0}\tilde{\xi}_1^2/X\right)\exp\left(-X + \sqrt{\tilde{\alpha}_g\xi_\perp}\right) \tag{2.12}$$

where $X = \sqrt{\tilde{\tau}^2 + \tilde{\xi}_1^2 + \tilde{\xi}_\perp^2 + \alpha_g\tilde{\xi}_\perp}$. Here, as above, $\boldsymbol{\xi}$ denotes a moving-frame space separation vector; the tilde is used to indicate the following non dimensional quantities: $\tilde{\xi}_1 = \xi_1/m_1$, $\tilde{\xi}_\perp = \xi_\perp/m_\perp$, $\tilde{\tau}_1 = \tau/\tau_m$. The parameters $C_{1,0}$ and α_g are empirical parameters; the length and time scales m_1, $m_\perp$ and τ_m are to be determined through the connection relations. The parameter $C_{0,0}$ is assumed proportional to $(\bar{\rho}k^2)^2$. The source model introduces a set of empirical parameters plus time and length scales. The length scales are expressed through the traditional connection relation, see equation (2.4) for the length scale l_m. A different connection relation is used for the time scales. This is expressed as

$$\tau_m = C_\tau\frac{k}{\epsilon}\mathrm{F}\left(\frac{k|\nabla\bar{\mathbf{u}}|}{\epsilon}\right) \tag{2.13}$$

where F is an empirical function deduced from two-point measurements of the velocity field. The latter was evaluated by expressing the ratio between measured autocorrelation time scales, Ref. [39], and the value $C_\tau k/\epsilon$.[r] The source-model empirical parameters are chosen by matching the Reynolds-stress two-point covariance model to the turbulent-velocity two-point cross covariance measurements performed by Bridges and Podboy;[39] turbulence quasi-normality must be assumed in this case. A notable characteristic of the model proposed by Goldstein and Leib[38] is that the connection-relation parameters associated with different two-point CPSD components can be different.[s]

instability. The evaluation of the Green function was performed by using two sets of linearised flow equation that respectively assume the mean flow as strictly parallel and slowly diverging. In Ref. [38], the parallel-flow solution, i. e. the Lilley solution, is used at subsonic acoustic Mach number and, in general, in the region of non-singularity of the parallel-flow Green function. The Green function for slowly-diverging parallel flow is used near the critical layer. A matching procedure is used between the parallel-flow and the slowly-diverging-flow solutions in order to get a continuous acoustic-radiation operator.

[q]Note the difference with the present thesis, where the applied-stress source is associated with the unit-density Reynolds-stress. According to the generalised acoustic analogy proposed by Goldstein,[35] the applied-stress equivalent source also depends on the local density and can be approximated as:

$$\rho\mathbf{u}'\otimes\mathbf{u}' - \overline{\rho\mathbf{u}'\otimes\mathbf{u}'}$$

[r]Note that the modelled quantity refers to the Reynolds-stress two point correlation, but the measurements refer to the velocity field.

[s]The modelled far-field jet noise is expressed, in Ref. [38], as a combination of six different two-point CPSD components. The 12,12 component dominates the SPL 1/3-octave spectra at low downstream polar angles. The

The principal components of the model introduced by Goldstein and Leib[38] can be summarised as follows.

i RANS with k-ϵ closure

ii Applied-stress source in the Goldstein[35] acoustic analogy
Non-separable cross covariance model in the moving frame
Direct model of Reynolds-stress two-point statistics, based on turbulent-velocity two-point measurements (quasi-normality hypothesis)
Length scales and mean-square value expressed through traditional connection laws
Original connection relation for time scales, based on turbulent-velocity experimental measurements by Bridges and Podboy[39]
Connection-relation empirical parameters set by matching Reynolds-stress two-point covariance model and turbulent-velocity two-point cross covariance measurement by Bridges and Podboy[39] (quasi-normality hypothesis)
Empirical parameters associated with different two-point CPSD components can be different

iii Matched asymptotic expansion for the Linearised Euler Equations with axisymmetric, slowly-diverging (quasi 1-D and transversely sheared) mean flow

2.2 Present model

The list of RANS-based jet-noise models considered in the present chapter is not complete; it gives anyway an overview of the state of the art associated with this type of jet-noise models. The principal objective of the present thesis is to derive a RANS-based jet-noise model that efficiently uses the information from two-point measurements in turbulent-jet flows. Limited to subsonic conditions, the model incorporates the effect of heating on turbulent mixing noise. The principal components of the model can be outlined as follows:

i RANS with Reynolds-stress modelling (RSM) closure (allows for turbulence anisotropy)

ii Applied-stress and applied-force sources in the Lilley–Goldstein[3] acoustic analogy
Source modelling related to the unit-density Reynolds-stress two-point statistics for both sources (closure hypothesis for applied-force source)
Non-separable unit-density Reynolds-stress cross covariance model in the fixed frame of reference
Direct model of unit-density Reynolds-stress two-point statistics, based on corresponding two-point measurements by Harper-Bourne[4,5,42]

source model for the 12,12 component presents different connection-relation parameters, compared to the other components. This choice assigns different spectral characteristics to the downstream and sideline components of the predicted noise.

Zero-space-separation time scale expressed by adapting[a] the traditional connection relation (2.4)

Connection relations for length scales and mean-square values which incorporate the RANS-solution anisotropy

Detailed description of calibration procedure for connection-relation empirical parameters

Time- and length-scale parameters defined by matching model components and corresponding measurements by Harper-Bourne[4]

Applied-stress- and applied-force-source scaling parameters defined by matching modelled 90-degree 1/3-octave spectra and corresponding measurements

iii Asymptotic approximations of the Lilley–Goldstein[3] analogy (high-frequency solution by geometric acoustics, Ref. [41], and low-frequency solution by flow-factor approach, Ref. [40])

A comparison of the present model to the reviewed RANS-based models show that the model includes an original sequence of components. Some of the model components are original, these can be enumerated as follows:

1. Use of a RANS solution including turbulence anisotropy
2. Closure hypothesis to scale the applied-force source on the basis of the static-temperature gradient and the unit-density Reynolds stress
3. Direct modelling of the unit-density Reynolds-stress two-point covariance, based on time-separation and frequency-domain trends of corresponding flow measurements
4. Connection relations including turbulence anisotropy for the unit-density Reynolds-stress mean-square value and length scales
5. Detailed description of the calibration procedure, characterised by matching the model-components to both velocimetry and jet-noise measurements
6. Asymptotic approximations in the high- and low-frequency limits of the Lilley-analogy Green function[b]

[a]The present work uses the traditional connection relation, which is normally associated with moving-frame decay times, to define a fixed-frame time scale.

[b]Both approximations contain elements of originality. The high-frequency solution is a development of the geometric-acoustics approach used by Morfey, Szewczyk and Tester,[41] where the model for the radiation in the neighbourhood of the source region is the original contribution, defined by using a moving-medium solution of a Lighthill-type analogy. The low-frequency solution has not been developed as part of the thesis work; it has been derived by Morfey as low-frequency limit of the Lilley-analogy flow factor, Ref. [40]. Its use in the present thesis and the coupling to the high-frequency model (for the derivation of the zero-flow solution) constitute further elements of originality.

Chapter 3

Theory for aerodynamic-sound generation and radiation

The sound-production mechanisms associated with unbounded turbulent flows have been put on a rational basis by Lighthill.[1] In his ground-breaking work Lighthill rearranged the continuum-mechanics conservation equations in order to obtain a wave equation forced by non-linear terms (the so-called acoustic analogy). A model based on similar reasoning is introduced in this chapter. The model establishes a relation between the statistics of a given unbounded subsonic turbulent flow and the corresponding sound production. The model utilises two complementary acoustic analogies in order to define a field of equivalent acoustic sources associated with the prescribed stationary turbulence-statistics field. The acoustic analogies can be identified as the high-frequency and the low-frequency limits of the Lilley[2] parallel shear-flow analogy for an ideal fluid, as formulated by Goldstein[3] (Lilley–Goldstein analogy).

- The high-frequency approach combines a Lighthill-type analogy and geometric acoustics. The Lighthill-type analogy is expressed in a moving local medium corresponding to a given location in the turbulent flow. The geometric-acoustics relations are used to connect the acoustic-pressure field in the local medium and the acoustic pressure in the quiescent medium surrounding the turbulent region.

- The low-frequency approach uses a very-low-frequency approximation (Morfey) to the low-frequency asymptotic Green function for the Lilley–Goldstein analogy. The latter is given by Morfey, Tester and Powles.[43]

The equivalent-source fields associated with the two acoustic analogies are the nonlinear forcing terms of the Lilley–Goldstein analogy (see Appendix B). A threshold value for the equivalent source field[a] is used to cut out a connected Euclidean-space domain in which the aerodynamic

[a]For practical reasons an indicator of the equivalent source intensity is used for this purpose. The form of the Lilley–Goldstein equivalent sources identifies the turbulent-kinetic-energy time average as a principal scaling factor for the sound source generation. The threshold value is then set for the turbulent kinetic energy.

sound is generated. This domain is called the source region. The acoustic-field statistics are modelled in the quiescent[b] medium surrounding the source region. The far-field acoustic-pressure statistics are derived by dividing the source region into a number of subregions. Each subregion is characterised by a spatial dimension that guarantees small variations of the equivalent-acoustic-source statistics across its interior, plus small variations of the mean flow. The far-field contribution from each subregion is treated separately by filtering out the equivalent-source field outside the given subregion and using an appropriate Green function; it is evaluated as follows:

- A volumetric source strength is defined as a space integral across separation of the equivalent-source two-point cross power spectral density (CPSD) tensor. The volumetric source strength is evaluated by assuming a uniform acoustic medium; the latter is in motion relative to the sources for the high-frequency model and is quiescent for the low-frequency model. The phase of the two-point CPSD is shifted according to the source–observer time-delay difference, depending on the separation between the two sources.
- The subregion-specific high-frequency and low-frequency Green functions are used to evaluate the contribution to the far-field radiation at prescribed observer locations.

The total noise at the observer location is derived in the high-frequency and low-frequency limits by adding the contributions from all the subregions.

3.1 High-frequency sound generation and radiation

The high-frequency approach defines a Lighthill-type analogy corresponding to each source subregion. The analogy is referred to as local-medium Lighthill analogy. It is used to define the sound-production mechanism in the subregion. The equivalent sound sources in the subregion local flow differ from the standard Lighthill-analogy sources in that the mean-flow velocity does not appear in the forcing terms. The equivalent sources are identical to the forcing terms of the Lilley–Goldstein[3] analogy. The acoustic-pressure power spectral density (PSD) is calculated in the subregion by assuming that the equivalent sources radiate into a uniformly moving medium, this being the medium characterised by the local mean velocity and speed of sound. The geometric-acoustics conservation equations introduced by Blokhintzev[44] are finally used to relate the acoustic-variable PSD in the source subregion to the corresponding acoustic-pressure PSD in the far field outside the source-region.

3.1.1 Local-medium Lighthill analogy

Provided the acoustic wavelength and the characteristic dimension of the source-coherence region are small compared to the scales of the mean flow, and assuming that the acoustic

[b]The model only considers the situation associated with zero velocity for the space surrounding the source region. This limitation can be removed to extend the model to the case of a uniform co-flow.

energy radiated by the source is not scattered back, the radiation problem in the vicinity of any acoustic-source subregion can be viewed as a free-field problem in a locally-uniform medium that is moving at the local mean velocity $\bar{\mathbf{u}}$ and is characterised by the local speed of sound $\bar{c}$. The Goldstein[3] conservation equations for mass (B.6) and momentum (B.7) are formulated in a fixed[a] reference frame. A Galilean transformation is used to refer the same equations to the reference frame that is rigidly connected to the local medium. Assuming the fluid is a perfect gas, the local-medium expression of the mass and momentum conservation equations with viscous stresses and heat conduction neglected is given as follows:

$$mass \qquad \frac{\partial p^{\frac{1}{\gamma}}}{\partial t} + \mathrm{div}\left(p^{\frac{1}{\gamma}}\mathbf{u}'\right) = 0 \tag{3.1}$$

$$momentum \qquad \frac{\partial p^{\frac{1}{\gamma}}\mathbf{u}'}{\partial t} + \mathrm{div}\left(p^{\frac{1}{\gamma}}\mathbf{u}'\otimes\mathbf{u}'\right) + c^2\nabla p^{\frac{1}{\gamma}} = 0 \tag{3.2}$$

Here $\mathbf{u}'$ is the fluctuating velocity and $\mathbf{u}'\otimes\mathbf{u}'$ is the unit-density Reynolds-stress tensor; c denotes the speed of sound, p is the thermodynamic pressure and γ indicates the specific-heat ratio of the perfect gas. The Lighthill-analogy operation

$$\frac{\partial}{\partial t}\left(mass\right) - \bar{c}^2\nabla^2 p^{\frac{1}{\gamma}} - \mathrm{div}(momentum) + \bar{c}^2\nabla^2 p^{\frac{1}{\gamma}}$$

results in the inhomogeneous wave equation

$$\frac{\partial^2 p^{\frac{1}{\gamma}}}{\partial t^2} - \bar{c}^2\nabla^2 p^{\frac{1}{\gamma}} = \mathrm{div}\Big(\mathrm{div}\Big(p^{\frac{1}{\gamma}}\mathbf{u}'\otimes\mathbf{u}'\Big) + \left(c^2 - \bar{c}^2\right)\nabla p^{\frac{1}{\gamma}}\Big) \tag{3.3}$$

Here the overbar indicates the time average. Dividing equation (3.3) by $\bar{c}^2 p_\infty^{\frac{1}{\gamma}}$ allows the acoustic-analogy equation to be written in terms of the Goldstein[3] variable, see expression (B.15) on page 95.

$$\pi_G = \frac{p^{\frac{1}{\gamma}} - p_\infty^{\frac{1}{\gamma}}}{p_\infty^{\frac{1}{\gamma}}} \tag{3.4}$$

The resulting local-medium Lighthill analogy is expressed as follows:

$$\frac{1}{\bar{c}^2}\frac{\partial^2\pi_G}{\partial t^2} - \nabla^2\pi_G = -\frac{1}{\bar{c}^2}\mathrm{div}(\mathrm{div}(\mathbf{Q})) - \frac{1}{\bar{c}^2}\mathrm{div}(\mathbf{d}) \tag{3.5}$$

We note that the analogy equation (3.5) is expressed in the same form as (C.34). The terms on the right-hand side of equation (3.5) constitute the equivalent acoustic-source field. The applied-stress term – referred to by Goldstein[3] as a velocity quadrupole, see (B.19) in Appendix

[a]The essential feature of the fixed frame (meaning fixed with respect to the nozzle, in the case of jet flows) is that an observer in this frame sees time-invariant boundary conditions for the flow. The flow variables are statistically stationary in this reference frame; an observer connected to the reference frame records a statistically stationary signal for the flow variable. The jet-noise reference frames are described in section A.1.

B – is a quadrupole-order source that is expressed as follows:

$$\mathbf{Q} = -\left(\pi_G + 1\right)\mathbf{u}' \otimes \mathbf{u}' \tag{3.6}$$

The applied-force term – referred to by Goldstein[3] as a temperature dipole, compare to equation (B.20) in Appendix B – is expressed as follows:

$$\mathbf{d} = -\left(c^2 - \bar{c}^2\right)\nabla\pi_G \tag{3.7}$$

By using the momentum-conservation equation[b] (3.2), equation (3.7) can be expressed as

$$\mathbf{d} = \left(\pi_G + 1\right)\frac{T - \bar{T}}{T}\frac{D\mathbf{u}}{Dt} \tag{3.8}$$

Here the quantity $(T - \bar{T}) = T'$ represents the static-temperature fluctuation relative to the local medium, and the differential operator acting on $\mathbf{u}$ is the convective time derivative.

3.1.2 Acoustic-field statistics for the local-medium acoustic sources

The radiation in the vicinity of the acoustic subregion is calculated by assuming that the equivalent source in this region is given by two overlapping random fields of quadrupole-order sources $\mathbf{Q}$ and dipole-order sources $\mathbf{d}$, as given by expressions (3.6) and (3.8). Since $\mathbf{Q}$ and $\mathbf{d}$ are related to the local flow variables, we can assume that they are statistically stationary in the fixed frame. A connection needs to be established between the source statistics associated with $\mathbf{Q}$ and $\mathbf{d}$ at a given fixed-frame location $\mathcal{S}$, and the statistics of the corresponding acoustic variable π_G at an observer location $\mathcal{R}$ that does not move with respect to the fixed frame. Note that the acoustic medium is in uniform motion with velocity $\bar{\mathbf{u}}$ relative to $\mathcal{S}$ and $\mathcal{R}$. The acoustic-radiation problem can be solved either by considering the moving-medium wave equation or by using the moving-source solution of the standard wave equation. The schematic in Fig. 3.1 represents the analogy between a problem of radiation in a uniformly moving medium and the radiation by a moving source in a quiescent medium. The emission-time coordinates are time invariant, since there is no relative motion between source and observer.[c]

[b] The inviscid momentum-conservation equation (3.2) written in the form

$$p^{\frac{1}{\gamma}}\frac{D\mathbf{u}}{Dt} + c^2\nabla p^{\frac{1}{\gamma}} = 0$$

and divided by $p_\infty^{\frac{1}{\gamma}}$ can be used to express the gradient of π_G in terms of the acceleration and the speed of sound.

$$\nabla\pi_G = -\frac{p^{\frac{1}{\gamma}}}{c^2 p_\infty^{\frac{1}{\gamma}}}\frac{D\mathbf{u}}{Dt} = -\frac{\pi_G + 1}{c^2}\frac{D\mathbf{u}}{Dt}$$

Considering the perfect-gas relation between the speed of sound and the static temperature yields the applied-force expression on the right-hand side of (3.8).

[c] One implication of this fact is that there is no frequency Doppler shift between the signal emitted by the source and the signal recorded by the observer.

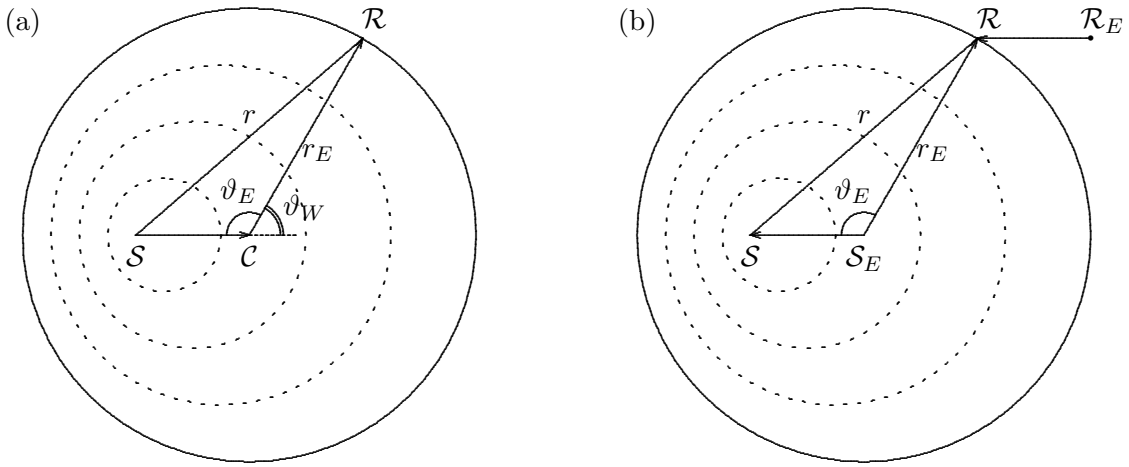

Figure 3.1: Schematic representation of wave propagation with relative motion between medium and acoustic source. The observer is in a position $\mathcal{R}$ that is rigidly connected to the source in $\mathcal{S}$. In (a), the problem is seen from a reference frame connected to the source; here the medium moves, convecting the wavefronts. The point $\mathcal{C}$ indicates the centre of the convected wavefront that is at the observer position. In (b), the reference frame is connected to the medium; the observer and the source move at the same speed $-\bar{u}\hat{\mathbf{e}}_1$. This diagram indicates the current position of source and observer by $\mathcal{S}$ and $\mathcal{R}$. $\mathcal{S}_E$ and $\mathcal{R}_E$ represent the source and observer positions at the time of emission of the wavefront that is at $\mathcal{R}$. The emission-time distance r_E and polar angle ϑ_E are in this case dictated by the speed of sound $\bar{c}$ and by the medium/source velocity $\bar{u}$; thus they are time invariant. The source–observer wavenormal-direction angle ϑ_W is shown in diagram (a).

The general solution for the moving-source acoustic problem, derived in Appendix C for dipole-order and quadrupole-order acoustic sources, is used to solve the fixed-frame radiation problem in the presence of a moving acoustic medium. This is done by specialising the general solution to the local medium

$$\begin{cases} \mathbf{v} \to -\bar{\mathbf{u}} \\ c \to \bar{c} \end{cases}$$

and by introducing the specific expression for the source terms forcing the wave equation. The local-medium acoustic-far-field component associated with a dipole of strength $-\mathbf{d}/\bar{c}^2$ is obtained by specialising expression (C.41). This yields

$$\pi_G^{(1)}(\mathbf{x}|\mathbf{w},t) = \frac{D_{-\bar{u}}^2}{4\pi\bar{c}^3 r_E}\dot{\mathbf{d}}(\mathbf{w}, t - r_E/\bar{c}) \cdot \hat{\mathbf{r}}_E \tag{3.9}$$

Similarly, by specialising expression (C.48), one obtains the following for a quadrupole-order source of strength $-\mathbf{Q}/\bar{c}^2$

$$\pi_G^{(2)}(\mathbf{x}|\mathbf{w},t) = -\frac{D_{-\bar{u}}^3}{4\pi\bar{c}^4 r_E}\ddot{\mathbf{Q}}(\mathbf{w}, t - r_E/\bar{c}) \cdot \hat{\mathbf{R}}_E \tag{3.10}$$

Here the second-order tensor $\hat{\mathbf{R}}_E$ defines the emission-time source–observer direction tensor $\hat{\mathbf{r}}_E \otimes \hat{\mathbf{r}}_E$. In expressions (3.9) and (3.10) the vectors $\mathbf{x}$ and $\mathbf{w}$ respectively indicate the observer

position ($\mathcal{R}$ in Fig. 3.1) and the source position ($\mathcal{S}$ in Fig. 3.1), measured from the origin of a fixed-frame reference system; $\mathbf{r}_E$ denotes the emission-time source–observer separation vector ($\overrightarrow{\mathcal{CR}}$ or $\overrightarrow{\mathcal{S}_E\mathcal{R}}$ in Fig. 3.1) $D_{-\bar{u}}$ indicates the Doppler factor (C.25) specialised to the local medium; it is expressed as follows:

$$D_{-\bar{u}} = \frac{1}{1 + \dfrac{\bar{\mathbf{u}} \cdot \mathbf{r}_E}{\bar{c} r_E}} = \frac{1}{1 + \dfrac{\bar{u}}{\bar{c}} \cos \vartheta_E} = \frac{1}{1 - \dfrac{\bar{u}}{\bar{c}} \cos \vartheta_W}$$

where ϑ_W indicates the moving-medium source–observer wavenormal direction, as indicated in Fig. 3.1.

The volume integral across the local-medium acoustic-source region of expressions (3.9) and (3.10) gives the instantaneous Goldstein variable recorded at the local-medium far-field observer location.

$$\pi_G(\mathbf{x}, t) = \iiint_{\mathbf{w}} \left(\frac{D_{-\bar{u}}^3}{4\pi \bar{c}^4 r_E} \ddot{\mathbf{Q}}(\mathbf{w}, t - r_E/\bar{c}) \cdot \hat{\mathbf{R}}_E - \frac{D_{-\bar{u}}^2}{4\pi \bar{c}^3 r_E} \dot{\mathbf{d}}(\mathbf{w}, t - r_E/\bar{c}) \cdot \hat{\mathbf{r}}_E \right) \mathrm{d}^3\mathbf{w} \tag{3.11}$$

Expression (3.11) can be used to estimate the local-medium power spectral density (PSD) for the acoustic variable. This is done by applying to the acoustic-subregion medium and to the specific source distribution the procedure indicated in Appendix D for a general distribution of dipole-order and quadrupole-order sources embedded in a uniform moving medium. By assuming that the hypotheses enumerated in section D.4 are satisfied, it is possible to express the acoustic-variable power spectral density (PSD) as follows:

$$\begin{aligned} \mathrm{s}_{\pi_G \pi_G}(\mathbf{x}, \mathbf{0}, f) = & \iiint_{\mathbf{y}} \frac{\pi^2 D_{-\bar{u}}^6 f^4}{\bar{c}^8 r_E^2} \iiint_{\boldsymbol{\eta}} \mathrm{s}_{\mathbf{QQ}}(\mathbf{y}, \boldsymbol{\eta}, f) \exp(\mathrm{j}\, 2\pi f \boldsymbol{\eta} \cdot \hat{\mathbf{r}}_E/\bar{c}) \, \mathrm{d}^3\boldsymbol{\eta} \cdot \left(\hat{\mathbf{R}}_E \otimes \hat{\mathbf{R}}_E \right) \mathrm{d}^3\mathbf{y} \\ & + \iiint_{\mathbf{y}} \frac{D_{-\bar{u}}^4 f^2}{4\bar{c}^6 r_E^2} \iiint_{\boldsymbol{\eta}} \mathrm{s}_{\mathbf{dd}}(\mathbf{y}, \boldsymbol{\eta}, f) \exp(\mathrm{j}\, 2\pi f \boldsymbol{\eta} \cdot \hat{\mathbf{r}}_E/\bar{c}) \, \mathrm{d}^3\boldsymbol{\eta} \cdot (\hat{\mathbf{r}}_E \otimes \hat{\mathbf{r}}_E) \, \mathrm{d}^3\mathbf{y} \end{aligned} \tag{3.12}$$

Here $\mathbf{y}$ denotes the reference position associated with the two-point statistics of the source. It is the middle point between the source pair used to estimate the two-point statistics. The separation vector between the source pair is indicated by $\boldsymbol{\eta}$. The source statistics are represented in (3.12) by the two-point cross-power spectral density (CPSD) functions $\mathrm{s}_{\mathbf{QQ}}$ and $\mathrm{s}_{\mathbf{dd}}$, which are fourth-order and second-order tensors respectively. The mixed quadrupole–dipole terms $\mathrm{s}_{\mathbf{Qd}}$ and $\mathrm{s}_{\mathbf{dQ}}$ are assumed not to contribute, due to the symmetry hypothesis (D.16), see Appendix D. A consequence of the symmetry hypothesis (D.16) is that $\mathbf{y}$ can be considered as the centroid of the zero-time-separation source-coherence volumes in the local medium.

3.1.3 Propagation to a far-field observer outside the source region

The propagation of the pressure field out through the non-uniform flow to the ambient medium surrounding the source region is assumed to be such that the pressure-field statistics obey the geometric acoustics conservation laws.[d] This is equivalent to assuming that the acoustic wavelength can be considered as a small parameter if compared to the scales of variation of the mean flow.[e] The ambient fluid far from the source region is assumed to be a quiescent medium with speed of sound c_∞. The propagation starts from the subregion i characterised by medium velocity $\bar{u}^{(i)}$ and speed of sound $\bar{c}^{(i)}$, see Fig. 3.2. The phase-trace matching in the direction parallel to the flow gives a relation between a prescribed quiescent-medium observer position $\mathbf{x}_\infty$ and the corresponding ray-direction image[f] $\mathbf{x}^{(i)}$ in the local medium. The angles defining the wavenormal direction from the mean-flow direction (see Fig. 3.2 where the angles are called ϑ_∞ for the far-field observer and $\vartheta_W^{(i)}$ for the local-medium of subregion i) are related as follows:

$$\bar{u}^{(i)} + \frac{\bar{c}^{(i)}}{\cos\left(\vartheta_W^{(i)}\right)} = \frac{c_\infty}{\cos\left(\vartheta_\infty\right)} \tag{3.13}$$

The local-medium wavenormal-direction polar angle ϑ_W (Fig. 3.1) is related to the local-medium emission-time polar angle as $\vartheta_W = \pi - \vartheta_E$. If we assume axisymmetry for the problem, then as shown by Morfey and Tester[45] it is possible to state the Blokhintzev[44] invariant as follows:

$$\mathrm{s}_{p'p'}^{(i)}\left(\mathbf{x}_\infty, \mathbf{0}, f\right) = \mathrm{s}_{p'p'}^{(i)}\left(\mathbf{x}, \mathbf{0}, f\right) \frac{\rho_\infty}{\left(\bar{\rho} D_{-\bar{u}}^4\right)^{(i)}}$$

Here a common distance $r = r_E^{(i)}$ has been assumed for both the far-field observer and the corresponding wavenormal-direction local-medium image $\mathbf{x}_W^{(i)}$. Note that we assume a spherical-spreading relation between the acoustic intensities in the subregion i and at location $\mathbf{x}^{(i)}$; this implies that we assume small Fresnel corrections inside the subregion, or small source-coherence dimension compared to the acoustic-subregion dimension. The relation (B.16) between the

[d] We follow the same procedure as in Appendix 1 of Morfey, Szewczyk and Tester[41] (section titled Radiation outside the shear layer: acoustic-mean flow interaction effects). Note that here the target is the mean-flow effect on a specific acoustic-source region. The localisation of the procedure indicated in Ref. [41] allows for predictions that are not necessarily limited to the region outside the cone of silence. In the present case there is not a global cone of silence associated with the whole source region, there are instead N cones of silence: one for each source subregion, depending on the local acoustic-medium velocity and speed of sound.

[e] Indicating the acoustic wavelength with λ:

$$\nabla \bar{\mathbf{u}} \cdot \lambda \hat{\mathbf{e}}_i \otimes \hat{\mathbf{e}}_j \ll \bar{u}$$

$$\nabla \bar{c} \cdot \lambda \hat{\mathbf{e}}_i \ll \bar{c}$$

[f] The wavenormal-radiation image $\mathbf{x}_W^{(i)}$ is the virtual image of $\mathbf{x}_\infty$ that is located at distance $|\mathbf{x}_\infty - \mathbf{y}| \simeq r$ and in the wavenormal direction $\vartheta_W^{(i)}$ from the acoustic-source subregion i. The corresponding ray-direction image is indicated from $\mathbf{x}_W^{(i)}$ by the vector connecting the source subregion at reception time to the same subregion at emission time. See Fig. 3.2; compare Fig. 3.1 (a), where point $\mathbf{y}$ is denoted by $\mathcal{S}$ and $\mathbf{x}^{(i)}$ by $\mathcal{R}$.

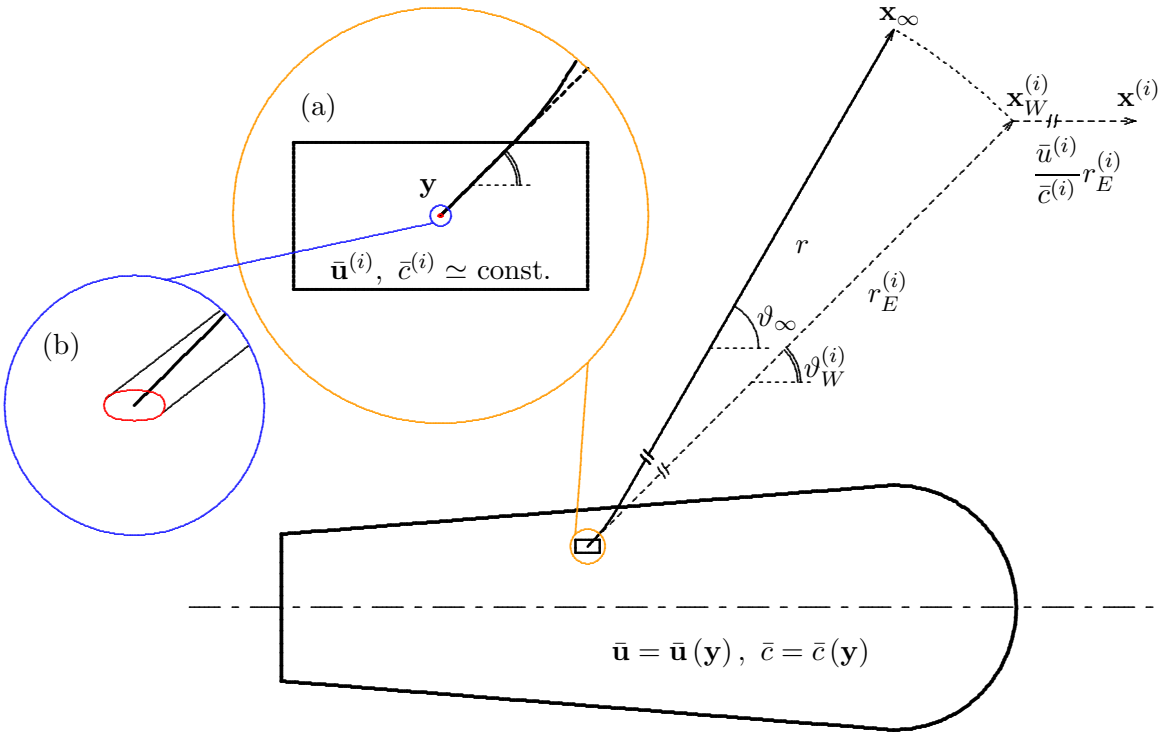

Figure 3.2: High-frequency contribution from the acoustic subregion i to an observer in the quiescent medium outside the source region. The axial section of the acoustic-source region is the area inside the continuous black line, where both the mean velocity $\bar{\mathbf{u}}$ and the mean speed of sound $\bar{c}$ are assumed to vary with position, forming an axisymmetric base flow. The diagram reports observer position $\mathbf{x}_\infty$ in the quiescent medium outside the source region and the corresponding local-medium ray-path image $\mathbf{x}^{(i)}$ as seen from any coherence-volume centroid $\mathbf{y}$ internal to the acoustic subregion i. The solid black line denotes the wavenormal-direction source–observer path. A magnified view of the source region in proximity of the subregion i is shown in (a), where the axial section of subregion i is the area enclosed by the black line. In (b), a further magnification shows sections of the source-coherence volume (area inside the red curve) and of the corresponding source–observer ray tube. Compare with Fig. 3.1 (a) where $\mathbf{y}$ is denoted by $\mathcal{S}$ and $\mathbf{x}^{(i)}$ is $\mathcal{R}$; note that the separation vector $\mathbf{x}^{(i)} - \mathbf{x}_W^{(i)}$ is equivalent to $\overrightarrow{\mathcal{SC}}$ in Fig. 3.1 (a).

variable π_G and the acoustic pressure p' can be introduced to yield

$$\mathrm{s}_{p'p'}^{(i)}(\mathbf{x}_\infty, \mathbf{0}, f) = \gamma^2 p_\infty^2 \mathrm{s}_{\pi_G\pi_G}^{(i)}(\mathbf{x}, \mathbf{0}, f) \frac{\rho_\infty}{\left(\bar{\rho} D_{-\bar{u}}^4\right)^{(i)}} \tag{3.14}$$

The contribution $\mathrm{s}_{\pi_G\pi_G}^{(i)}$ to the acoustic-variable PSD in the local acoustic medium, due to acoustic radiation from the given source subregion i can be evaluated by extending to the whole subregion volume the $\mathbf{y}$ integral of expression (3.12). This can be done by extending the

$\mathbf{y}$ integral in (3.12) to the whole acoustic-source region and by applying spatial windowing:

$$
\begin{aligned}
&\mathrm{s}^{(i)}_{\pi_G\pi_G}\left(\mathbf{x}^{(i)},\mathbf{0},f\right) = \\
&\pi^2 f^4 \left(\frac{D^6_{-\bar{u}}}{\bar{c}^8 r_E^2}\hat{\mathbf{R}}_E \otimes \hat{\mathbf{R}}_E\right)^{(i)} \cdot \iiint_{\mathbf{y}} \mathrm{H}^{(i)}(\mathbf{y}) \iiint_{\boldsymbol{\eta}} \mathrm{s}_{\mathbf{QQ}}\left(\mathbf{y},\boldsymbol{\eta},f\right) \exp\left(\mathrm{j}\ 2\pi f \boldsymbol{\eta}\cdot\hat{\mathbf{r}}_E/\bar{c}\right) \mathrm{d}^3\boldsymbol{\eta}\mathrm{d}^3\mathbf{y} \\
&+\frac{f^2}{4}\left(\frac{D^4_{-\bar{u}}}{\bar{c}^6 r_E^2}\hat{\mathbf{r}}_E \otimes \hat{\mathbf{r}}_E\right)^{(i)} \cdot \iiint_{\mathbf{y}} \mathrm{H}^{(i)}(\mathbf{y}) \iiint_{\boldsymbol{\eta}} \mathrm{s}_{\mathbf{dd}}\left(\mathbf{y},\boldsymbol{\eta},f\right) \exp\left(\mathrm{j}\ 2\pi f \boldsymbol{\eta}\cdot\hat{\mathbf{r}}_E/\bar{c}\right) \mathrm{d}^3\boldsymbol{\eta}\mathrm{d}^3\mathbf{y}
\end{aligned}
\tag{3.15}
$$

The function $\mathrm{H}^{(i)}(\mathbf{y})$ in (3.15) is a distribution that is zero if the coherence-volume centroid $\mathbf{y}$ is outside the given i^{th} acoustic-source subregion. The function $\mathrm{H}^{(i)}(\mathbf{y})$ is equal to one if $\mathbf{y}$ is inside the subregion i.[g] Note that we assume constant Green-function parameters $\mathbf{r}_E$, $D_{-\bar{u}}$ and $\bar{c}$, for the acoustic-source subregion i. Regarding $\mathbf{r}$, we limit attention to observer positions in the geometric far field of the whole source; in this case the subregion value of $\mathbf{r}_E$ and $D_{-\bar{u}}$ is set by the local-medium $\bar{u}$ and $\bar{c}$.[h]

The contribution to the acoustic-variable PSD due to a given acoustic-source subregion is defined by introducing expression (3.15) into (3.14). The sum across the whole acoustic-source field of all the contributions associated with the subregions yields the high-frequency-model contribution to the acoustic field at the observer position $\mathbf{x}_\infty$.

$$
\mathrm{s}^{(HF)}_{p'p'}\left(\mathbf{x}_\infty,\mathbf{0},f\right) = \sum_i \mathrm{s}^{(i)}_{p'p'}\left(\mathbf{x}_\infty,\mathbf{0},f\right) \tag{3.16}
$$

3.2 Low-frequency flow factor for the Lilley–Goldstein analogy

The low-frequency solution assumes, as previously, that the acoustic-source subregion is embedded in an axisymmetric time-invariant flow, but the geometric acoustics approximation is not used. The acoustic radiation is in this case described by the axisymmetric-base-flow Lilley–Goldstein analogy. Solutions of the Lilley–Goldstein equation[3] in the form (B.23) have been developed by Morfey, Tester and Powles.[43] The acoustic variable is in this case given by

$$
\tilde{\pi}_G = \bar{\rho}\bar{c}^2\pi_G = p' + \circ\left(\left(p'\right)^2\right)
$$

The far-field acoustic radiation from a given location in the jet is expressed in terms of a multiplying factor relating the zero-flow solution to the solution including the base flow. The

[g] The function $\mathrm{H}^{(i)}(\mathbf{y})$ can be represented by a Heaviside unit-step function $\mathrm{H}(n)$ as in Ffowcs Williams and Hawkings[46] where n is a local coordinate normal to the surface enclosing the acoustic-source subregion. The coordinate n is negative outside the acoustic-source subregion, is zero on the boundary surface, and is positive inside the acoustic-source subregion.

[h] For receiver locations in the geometric near field of the whole source region, one also needs to determine the acoustic-subregion–observer ray path; assuming a fixed observer, this will depend on the acoustic-subregion centroid position and on the mean-flow distribution.

multiplying factor, called flow factor, is the ratio between the far-field acoustic-pressure PSD derived as solution of equation (B.23) and the acoustic-pressure PSD associated with a zero-flow Lilley–Goldstein analogy. The zero-flow Lilley–Goldstein analogy can be derived by assuming that the base flow (B.8) is given as follows

$$\begin{cases} \bar{\mathbf{u}} = 0 \\ \bar{c} = c_\infty \end{cases} \tag{3.17}$$

Note that we retain the condition $\bar{p} = p_\infty$ that is respected by the generalised Pridmore-Brown base flow (B.8), used in the derivation of the Lilley-Goldstein equation.[a] Introducing the zero-flow hypothesis (3.17) in (B.23) yields the following field equation for the acoustic variable $\tilde{\pi}_G$:

$$\frac{1}{c_\infty^2}\frac{\partial^2 \tilde{\pi}_G}{\partial t^2} - \nabla^2 \tilde{\pi}_G = -\rho_\infty \mathrm{div}(\mathrm{div}(\mathbf{Q}) + \mathbf{d}) \tag{3.18}$$

A division of both sides of equation (3.18) by γp_∞ yields equation (3.5) specialised to the case $\bar{c} = c_\infty$. The solution procedure introduced for the high-frequency solution in section 3.1 can therefore be used to derive the zero-flow contribution associated with the given acoustic-source subregion. The zero-flow PSD corresponding to the variable $\tilde{\pi}_G$ is related to the Goldstein-variable PSD by

$$\mathrm{s}^0_{\tilde{\pi}_G\tilde{\pi}_G} = \left(\rho_\infty c_\infty^2\right)^2 \mathrm{s}^0_{\pi_G\pi_G}$$

and inserting the zero-flow equivalent of (3.15) gives the zero-flow PSD in the far field as

$$\begin{aligned} &\mathrm{s}^{0\ (i)}_{\tilde{\pi}_G\tilde{\pi}_G}(\mathbf{x}, \mathbf{0}, f) = \\ &\frac{\pi^2 \rho_\infty^2 f^4}{c_\infty^4 r^2}\left(\hat{\mathbf{R}} \otimes \hat{\mathbf{R}}\right) \cdot \iiint_{\mathbf{y}} \mathrm{H}^{(i)}(\mathbf{y}) \iiint_{\boldsymbol{\eta}} \mathrm{s}_{\mathbf{QQ}}(\mathbf{y}, \boldsymbol{\eta}, f) \exp\left(\mathrm{j}\ 2\pi f \boldsymbol{\eta} \cdot \hat{\mathbf{r}}/c_\infty\right) \mathrm{d}^3\boldsymbol{\eta}\mathrm{d}^3\mathbf{y} \\ &+\frac{\rho_\infty^2 f^2}{4c_\infty^2 r^2}\left(\hat{\mathbf{r}} \otimes \hat{\mathbf{r}}\right) \cdot \iiint_{\mathbf{y}} \mathrm{H}^{(i)}(\mathbf{y}) \iiint_{\boldsymbol{\eta}} \mathrm{s}_{\mathbf{dd}}(\mathbf{y}, \boldsymbol{\eta}, f) \exp\left(\mathrm{j}\ 2\pi f \boldsymbol{\eta} \cdot \hat{\mathbf{r}}/c_\infty\right) \mathrm{d}^3\boldsymbol{\eta}\mathrm{d}^3\mathbf{y} \end{aligned} \tag{3.19}$$

Provided the typical mean-flow dimension in the cross-stream direction[b] is small compared to the acoustic wavelength, the flow factor corresponding to a given acoustic-source subregion can be expressed as a function of the mean-flow variables in that subregion and their ambient values, and does not depend on the mean-flow profile details outside the subregion.[c] The flow factor will differ for different components of the acoustic-source cross-correlation function. It can be introduced in expression (3.19) as a linear operator that only depends on the position of the subregion; for axisymmetric parallel base flows, the flow factor is a function of $R^{(i)}$ (the subregion radial coordinate) only. The acoustic-subregion contribution including the flow can

[a] Given that the fluid is a perfect gas, the base-flow assumption (3.17) also implies $\bar{\rho} = \rho_\infty$.
[b] For example, the vorticity thickness of the jet shear layer.
[c] In this respect the situation resembles the high-frequency analogy of section 3.1.

therefore be represented in the far field as follows:

$$
\begin{aligned}
&\mathrm{s}^{(i)}_{\tilde{\pi}_G\tilde{\pi}_G}(\mathbf{x},\mathbf{0},f) = \\
&\frac{\pi^2\rho_\infty^2 f^4}{c_\infty^4 r^2}\left(\hat{\mathbf{R}}\otimes\hat{\mathbf{R}}\right)\cdot \mathrm{F}^{(i)}_{\mathbf{QQ}}\cdot\iiint_{\mathbf{y}}\mathrm{H}^{(i)}(\mathbf{y})\iiint_{\boldsymbol{\eta}}\mathrm{s}_{\mathbf{QQ}}(\mathbf{y},\boldsymbol{\eta},f)\exp\left(\mathrm{j}\,2\pi f\boldsymbol{\eta}\cdot\hat{\mathbf{r}}/c_\infty\right)\mathrm{d}^3\boldsymbol{\eta}\mathrm{d}^3\mathbf{y} \\
&+\frac{\rho_\infty^2 f^2}{4{c_\infty}^2 r^2}\left(\hat{\mathbf{r}}\otimes\hat{\mathbf{r}}\right)\cdot \mathrm{F}^{(i)}_{\mathbf{dd}}\cdot\iiint_{\mathbf{y}}\mathrm{H}^{(i)}(\mathbf{y})\iiint_{\boldsymbol{\eta}}\mathrm{s}_{\mathbf{dd}}(\mathbf{y},\boldsymbol{\eta},f)\exp\left(\mathrm{j}\,2\pi f\boldsymbol{\eta}\cdot\hat{\mathbf{r}}/c_\infty\right)\mathrm{d}^3\boldsymbol{\eta}\mathrm{d}^3\mathbf{y}
\end{aligned}
\tag{3.20}
$$

For the applied-stress-source PSD the low-frequency flow factor is an eighth-order tensor field

$$
\mathrm{F}_{\mathbf{QQ}} = \bar{F}_{ijkl}\delta_i^m\delta_j^n\delta_k^o\delta_l^p\hat{\boldsymbol{\gamma}}_i\otimes\hat{\boldsymbol{\gamma}}_j\otimes\hat{\boldsymbol{\gamma}}_k\otimes\hat{\boldsymbol{\gamma}}_l\otimes\hat{\boldsymbol{\gamma}}_m\otimes\hat{\boldsymbol{\gamma}}_n\otimes\hat{\boldsymbol{\gamma}}_o\otimes\hat{\boldsymbol{\gamma}}_p \tag{3.21}
$$

For the applied-force-source PSD contribution it is a fourth-order tensor field

$$
\mathrm{F}_{\mathbf{dd}} = \bar{F}_{ij}\delta_i^k\delta_j^l\hat{\boldsymbol{\gamma}}_i\otimes\hat{\boldsymbol{\gamma}}_j\otimes\hat{\boldsymbol{\gamma}}_k\otimes\hat{\boldsymbol{\gamma}}_l \tag{3.22}
$$

The symbol δ_i^j in expressions (3.21) and (3.22) indicates the Kronecker delta that implies a contraction between directions i and j. Components of the flow-factor tensors have been developed by Morfey Tester and Powles[43] according to the jet-noise cylindrical-coordinate basis, starting from the low-frequency approximate solution in Ref. [40]. The result has been further developed by Morfey to yield simplified flow-factor expressions valid at low Helmholtz number ($d_J << \lambda$), as reported in Appendix E. The sum of the contributions (3.20) across the whole source-region volume yields the low-frequency component of the acoustic-pressure field at a given observer location in the quiescent medium surrounding the source:

$$
\mathrm{s}^{(LF)}_{p'p'}(\mathbf{x}_\infty,\mathbf{0},f) = \sum_i \mathrm{s}^{(i)}_{\tilde{\pi}_G\tilde{\pi}_G}(\mathbf{x}_\infty,\mathbf{0},f) \tag{3.23}
$$

3.3 Conclusions

Two expressions for the power spectrum of the far-field aerodynamic-sound radiation associated with a free turbulent shear flow have been derived, one from a high-frequency acoustic analogy and one from a low-frequency approximation of the Lilley–Goldstein analogy.[3] In both expressions the acoustic-source region is divided into a number of finite-volume acoustic subregions, each subregion guaranteeing quasi-uniform equivalent-source and flow statistics. The far-field acoustic-pressure autocorrelation is then expressed as sum of contributions from all the subregions.

The contribution of each subregion to the acoustic-pressure autocorrelation is approximated (according to frequency) by one of the two expressions mentioned above: a high-frequency term (3.14) and a low-frequency term (3.20). The low-frequency and the high-frequency con-

tributions correspond to the Lilley–Goldstein[3] acoustic analogy contributions in the limit of very small and very large flow-length-scale/wavelength ratio and with the assumption of axisymmetric base flow. One important feature of these Lilley-analogy approximations is that they can be evaluated locally depending on the subregion value of the base-flow variables and their local gradients; this greatly simplifies the solution for the Green function compared to the full Lilley-analogy solution procedure.[a]

In the high-frequency case, a local-medium Lighthill-type analogy has been introduced in order to define an equivalent-acoustic-source distribution based on the fluctuating part of the flow variables. This analogy defines equivalent acoustic sources that are identical to the velocity quadrupole and the temperature dipole, as defined by Goldstein,[3] by removing the effect of a uniform motion of the medium from the standard-Lighthill-analogy forcing terms.

The use of a Lilley-type source field simplifies the determination of the acoustic-source two-point statistics, as mean-velocity terms are not included in the instantaneous quadrupole-source expression (3.6). Note that the two-point CPSD terms between applied-stress and applied-force sources are omitted in the PSD expressions (3.15) and (3.20), due to a symmetry hypothesis (D.16) on the source-field correlation function.

An integral across the source region of the acoustic-subregion contributions in the low-frequency (3.23) and the high-frequency (3.16) limits yields the corresponding components of the acoustic-pressure PSD. Note that the components need in principle to be frequency filtered in order to satisfy the respective hypotheses regarding the wavelength/flow-scale ratio.

[a]The determination of the general Green function for the Lilley analogy includes the integration of an ordinary differential equation in the radial variable. The base-flow radial distribution in the source–observer path is required as input for the determination of this solution.

Chapter 4

Modelling the statistics of the aerodynamic-sound sources

A theory defining the acoustic emission associated with a statistically-stationary turbulent shear flow has been described in Chapter 3. The acoustic-pressure PSD at a given far-field location in the quiescent medium surrounding the turbulent region is given in the high-frequency and the low-frequency limits respectively by expressions (3.16) and (3.23). The acoustic-pressure PSD is derived by defining a volumetric source strength and by performing spatial integration across the turbulent region. The volumetric source strength, defined as the inner integral over separation in expressions (3.15) and (3.20), is a local tensor quantity whose integral over the source region determines the power spectrum of the far-field radiation. The complete expression for the PSD is represented as a dot product between tensors.

The volumetric source strength tensor on the right-hand side of (3.15) and (3.20) is the volume integral across space separation of the phase-shifted two-point CPSD of the equivalent source field. Provided the acoustic-radiation parameters (speed of sound c and source–observer direction $\hat{\mathbf{r}}$) are properly evaluated for the different frequency limits, the volumetric source strength tensor in the high-frequency limit has the same expression as in the low-frequency limit. It is expressed as

$$\iiint_{\boldsymbol{\eta}} \mathrm{s}_{\mathbf{QQ}}\left(\mathbf{y}, \boldsymbol{\eta}, f\right) \exp\left(\mathrm{j}\ 2\pi f \boldsymbol{\eta} \cdot \hat{\mathbf{r}}/c\right) \mathrm{d}^3\boldsymbol{\eta} \tag{4.1}$$

for the applied-stress equivalent source field. It is given by

$$\iiint_{\boldsymbol{\eta}} \mathrm{s}_{\mathbf{dd}}\left(\mathbf{y}, \boldsymbol{\eta}, f\right) \exp\left(\mathrm{j}\ 2\pi f \boldsymbol{\eta} \cdot \hat{\mathbf{r}}/c\right) \mathrm{d}^3\boldsymbol{\eta} \tag{4.2}$$

for the applied-force source field that arises in non-isothermal flows. The functions $\mathrm{s}_{\mathbf{QQ}}$ and $\mathrm{s}_{\mathbf{dd}}$

in (4.1) and (4.2) respectively indicate the two-point CPSD for the applied-stress equivalent sources $\mathbf{Q}$ (3.6) and for the applied-force equivalent sources $\mathbf{d}$ (3.8). These are defined as the Fourier transform with respect to τ of the two-point covariance functions

$$\mathrm{c}_{\mathbf{Q}'\mathbf{Q}'}(\mathbf{y},\boldsymbol{\eta},\tau)=\overline{\left(\mathbf{Q}(\mathbf{y}-\boldsymbol{\eta}/2,t)-\overline{\mathbf{Q}}(\mathbf{y}-\boldsymbol{\eta}/2)\right)\otimes\left(\mathbf{Q}(\mathbf{y}+\boldsymbol{\eta}/2,t+\tau)-\overline{\mathbf{Q}}(\mathbf{y}+\boldsymbol{\eta}/2)\right)} \quad (4.3)$$

and

$$\mathrm{c}_{\mathbf{d}'\mathbf{d}'}(\mathbf{y},\boldsymbol{\eta},\tau)=\overline{\left(\mathbf{d}(\mathbf{y}-\boldsymbol{\eta}/2,t)-\overline{\mathbf{d}}(\mathbf{y}-\boldsymbol{\eta}/2)\right)\otimes\left(\mathbf{d}(\mathbf{y}+\boldsymbol{\eta}/2,t+\tau)-\overline{\mathbf{d}}(\mathbf{y}+\boldsymbol{\eta}/2)\right)} \quad (4.4)$$

where the overbar indicates the time average.

The evaluation of the volume integrals (4.1) and (4.2) is the principal objective in this chapter. This evaluation implies the generation of models for $\mathrm{c}_{\mathbf{QQ}}$ and $\mathrm{c}_{\mathbf{dd}}$. Experimental data in which the two-point statistics of the acoustic-source terms (3.6) and (3.8) are measured directly are not available to the author. Models for $\mathrm{c}_{\mathbf{QQ}}$ and $\mathrm{c}_{\mathbf{dd}}$ can however be based on the available experimental data for the two-point statistics of the fluctuating-velocity field; in particular, the statistics of $\mathbf{u}'\otimes\mathbf{u}'-\overline{\mathbf{u}'\otimes\mathbf{u}'}$ (referred to below as the fluctuating Reynolds stress tensor). While a relation between the applied-stress source and the Reynolds-stress tensor appears clear in expression (3.6), a source-scaling hypothesis needs to be formulated to find a relation between the applied-force source and the fluctuating velocity. The relations between the equivalent-source correlation functions and the fluctuating-Reynolds-stress correlation functions are discussed in section 4.1, where the acoustic-source correlation function is related to the fluctuating-Reynolds-stress two-point statistics for both equivalent source terms.

The fluctuating-Reynolds-stress two-point statistics need to be modelled to close the problem. Parallel to some previous jet-noise source-correlation models, an analytical model for the fluctuating-Reynolds-stress two-point cross-correlation coefficient is introduced.[a] The model, described in section 4.2, is based on the hot-wire measurements of Harper-Bourne[4,5] on a low-Reynolds-number single-stream jet. A review of the Harper-Bourne data is given in section 4.2.1. The analytical model to match the two-point correlation coefficient is introduced in section 4.2.2. A qualitative description of the phenomena involved in a turbulent flow is presented in section 4.2.3, where the extent to which our analytical model covers the various characteristics generally seen in turbulence measurements is investigated.

The final simplified model for the Reynolds-stress two-point correlation function to be used in the characterisation of the acoustic-source is defined in section 4.3. This model is adapted from the Reynolds-stress two-point correlation function that best fits the Harper-Bourne data. In section 4.4 the model for the equivalent-source two-point correlation is then integrated across

[a] Analytical models for the two-point correlation coefficient have been widely used in the past. The most popular two-point-correlation-coefficient model is a separable-variable Gaussian-decay model that we have dated back to Ribner.[47] Recent developments include a separable-variable exponential-Gaussian model introduced by Morris and Boluriaan.[22] The model adopted in this thesis is compared, together with the Gaussian and exponential-Gaussian models, in Ref. [42] with the measurements of Harper-Bourne.[4,5,42]

the separation space to yield an explicit model for the tensors (4.1) and (4.2).

4.1 Relating the equivalent acoustic sources to available measurements

As was shown in Chapter 3, the aeroacoustic sources associated with the theory of noise generation are given by applied-stress and applied-force equivalent sources. At high frequency these correspond to a local-medium Lighthill analogy (section 3.1.1); more generally they correspond to a Lilley–Goldstein[3] analogy (Appendix B). The applied-stress forcing term is given by expression (3.6) and the applied-force source is given by expression (3.8). For a subsonic turbulent flow in the form of a free shear layer, the factor $(\pi_G + 1)$ appearing in both the applied-stress and the applied-force source expressions is close to unity.[a] Neglecting the contribution of $(\pi_G + 1)$ allows for expressing the equivalent-acoustic-source two-point correlation as follows.

- The fluctuating-Reynolds-stress two-point statistics can be used to define the applied-stress two-point statistics

$$\mathrm{c}_{\mathbf{Q}'\mathbf{Q}'}\left(\mathbf{y}, \boldsymbol{\eta}, \tau\right) \simeq \mathrm{c}_{\mathbf{S}'\mathbf{S}'}\left(\mathbf{y}, \boldsymbol{\eta}, \tau\right) \tag{4.5}$$

  where $\mathbf{S}'$ is the fluctuating Reynolds stress $\mathbf{S}' = \mathbf{u}' \otimes \mathbf{u}' - \overline{\mathbf{u}' \otimes \mathbf{u}'}$.

- The applied-force term requires a model for the two-point correlation function of the product between the ratio T'/T and the velocity-field Lagrangian derivative,

$$\mathbf{d} \simeq \frac{T'}{T} \frac{D\mathbf{u}}{Dt} \tag{4.6}$$

  Here T is the static absolute temperature of the gas, and T' is its fluctuating component.

While a model for the fluctuating-Reynolds-stress two-point correlation function can rely on existing published data, no experimental data are available to the author to base a model for the two-point correlation function associated with $\mathbf{d}$. This problem is addressed in section 4.1.1.

[a] As shown by expression (B.16), the Goldstein variable π_G is closely related to the pressure fluctuations. The term $(\pi_G + 1)$ is therefore close to unity for those flows for which

$$p' \ll p$$

The type of flows we are studying are shock-wave free and unbounded. The thermodynamic pressure p_∞ is of the same order of magnitude as the sea-level atmospheric pressure. In these cases the property $p' \ll p$ holds.

4.1.1 Scaling hypotheses for the applied-force equivalent source

In order to represent the applied-force two-point correlation function in terms of published or readily available measured quantities, we need to make assumptions regarding the nature of the temperature fluctuations and regarding the two-point correlation function associated with (4.6). If we assume that the temperature fluctuations are controlled by convection, we can state that the static-temperature convective time derivative is negligible.

$$\frac{DT}{Dt} \simeq \frac{DT'}{Dt} + \nabla\bar{T} \cdot \mathbf{u}' \simeq 0 \tag{4.7}$$

Note that here we are assuming that $\nabla\bar{T}$ is orthogonal to the local mean velocity. The hypothesis (4.7) states a relation between the material derivative of the temperature fluctuations and the velocity fluctuations:

$$\frac{DT'}{Dt} \simeq -\nabla\bar{T} \cdot \mathbf{u}' \tag{4.8}$$

If we also assume that T' is a small fraction of the absolute temperature T, expression (4.6) for the applied-force source term may be written as follows:

$$\begin{aligned} \mathbf{d} &\simeq \frac{1}{\bar{T}} T' \frac{D\mathbf{u}}{Dt} \\ &= \frac{1}{\bar{T}} \left(\mathbf{d}^{(1)} + \mathbf{d}^{(2)} \right), \end{aligned} \tag{4.9}$$

where

$$\mathbf{d}^{(1)} = \left(\frac{D}{Dt} + \nabla\bar{\mathbf{u}}\cdot \right) \left(T'\mathbf{u}' \right) \tag{4.10}$$

and

$$\begin{aligned} \mathbf{d}^{(2)} &= -\mathbf{u}' \frac{DT'}{Dt} \\ &\simeq \left(\mathbf{u}' \otimes \mathbf{u}' \right) \cdot \nabla\bar{T}, \end{aligned} \tag{4.11}$$

using the convective hypothesis (4.8) and assuming the mean-velocity gradient to be orthogonal to the mean-velocity direction. Equation (4.9) identifies the applied-force source as consisting of two components:

1. A term $\mathbf{d}^{(1)}$ given by the convective derivative plus the mean-velocity gradient operating on the product between temperature fluctuations and velocity fluctuations.

2. A term $\mathbf{d}^{(2)}$ given by the scaled projection of the unit-density Reynolds-stress tensor along the direction of the time-averaged static-temperature gradient. Here the scaling factor is given by the modulus of the time-averaged static-temperature gradient.

Based on equation (4.9), the two-point correlation function for the applied-force source is approximated as follows:

$$\mathrm{c}_{\mathbf{dd}} \simeq \frac{1}{\bar{T}^2}\mathrm{c}_{\mathbf{d}^{(1)}\mathbf{d}^{(1)}} + \frac{1}{\bar{T}^2}\mathrm{c}_{\mathbf{d}^{(1)}\mathbf{d}^{(2)}} + \frac{1}{\bar{T}^2}\mathrm{c}_{\mathbf{d}^{(2)}\mathbf{d}^{(1)}} + \frac{1}{\bar{T}^2}\mathrm{c}_{\mathbf{d}^{(2)}\mathbf{d}^{(2)}}$$

Although the first three terms in the correlation function are unknown to the author in terms of published/available experimental data, the fourth term can be derived from the Reynolds-stress correlation function. We also note that the fourth term has a non-zero time average for the component along the mean-temperature-gradient direction. The main closure hypothesis we need to make is that the behaviour of all the τ-dependent[b] terms involved in the applied-force-source correlation function is similar. In other words it is possible to define a constant $\kappa_{\mathbf{d}}$ such that

$$\mathrm{c}_{\mathbf{d}'\mathbf{d}'} \simeq \frac{\kappa_{\mathbf{d}}}{\bar{T}^2}\mathrm{c}_{\left(\mathbf{d}^{(2)}\right)'\left(\mathbf{d}^{(2)}\right)'} \simeq \kappa_{\mathbf{d}}\left(\frac{|\nabla\bar{T}|}{\bar{T}}\right)^2 \overline{\left[\mathbf{S}'\cdot\hat{\boldsymbol{\theta}}\right]_{\mathbf{y}-\boldsymbol{\eta}/2,t} \otimes \left[\mathbf{S}'\cdot\hat{\boldsymbol{\theta}}\right]_{\mathbf{y}+\boldsymbol{\eta}/2,t+\tau}} \tag{4.12}$$

Here $\hat{\boldsymbol{\theta}}$ indicates the direction of the mean-static-temperature gradient

$$\hat{\boldsymbol{\theta}} = \frac{\nabla\bar{T}}{|\nabla\bar{T}|}$$

Recall that $\mathbf{S}'$ denotes the Reynolds-stress fluctuation $\mathbf{S}' = \mathbf{u}'\otimes\mathbf{u}' - \overline{\mathbf{u}'\otimes\mathbf{u}'}$. We note that the scaling law (4.12) for the applied-force two-point correlation function has been obtained by showing a link between the instantaneous values of the Reynolds stress and $\mathbf{d}$. We underline that the link holds provided the static-temperature fluctuations are of purely-convective nature and the mean-flow gradients are orthogonal to the mean velocity. We also note that expression (4.12) yields the same whole-jet behaviour[c] as the scaling law (A31) for the dipole source in Morfey, Szewczyk and Tester.[41]

4.2 A modified-distance model for the Reynolds-stress two-point correlation

As seen in section 4.1, the fluctuating-Reynolds-stress correlation function is the basis for the aerodynamic-noise theory in this work. We express the fluctuating-Reynolds-stress two-point

[b] We only need the correlation function associated with the fluctuating part of the equivalent acoustic field. This is explained in more detail in Appendix D.

[c] Expression (4.12) is local in the sense that it is associated with a specific small region within the turbulent flow. The use of global scaling parameters for the flow, like characteristic dimension and velocity can be used to define a global scaling law that is valid in an average sense for the whole flow.

correlation function in cylindrical-coordinate components at the location[a] $\mathbf{y}$:

$$\mathrm{c}_{\mathbf{S}'\mathbf{S}'}(\mathbf{y},\boldsymbol{\eta},\tau) = c_{ij,kl}\hat{\boldsymbol{\gamma}}_i \otimes \hat{\boldsymbol{\gamma}}_j \otimes \hat{\boldsymbol{\gamma}}_k \otimes \hat{\boldsymbol{\gamma}}_l \tag{4.13}$$

Here $\hat{\boldsymbol{\gamma}}_i$ (i=1,2,3) are the unit basis vectors for the jet-noise cylindrical coordinate system (see section A.3 of Appendix A). The components $c_{ij,kl}$ associated with the two-point correlation function can be modelled by introducing the corresponding two-point correlation coefficient function

$$\hat{c}_{ij,kl}(\mathbf{y},\boldsymbol{\eta},\tau) = \frac{c_{ij,kl}(\mathbf{y},\boldsymbol{\eta},\tau)}{c_{ij,kl}(\mathbf{y},\mathbf{0},0)}$$

and by identifying a model representing $\hat{c}_{ij,kl}$. The model for $\hat{c}_{ij,kl}$ is constructed by introducing an analytical function that fits the main features of available experimental data on turbulent jets. The available experimental data for the Reynolds-stress two-point correlation are described in section 4.2.1. The analytical model to fit the data is introduced in section 4.2.2.

4.2.1 The Harper-Bourne experimental data

Very few experimental data are available for the Reynolds-stress two-point correlation in turbulent jets. Harper-Bourne[4,5] has published a limited set of measurements corresponding to an isothermal axisymmetric-nozzle single-stream air jet. The nozzle-exit diameter was 50.8 mm, and the nozzle-exit velocity was 60 m s^{-1}. The data were acquired by using hot-wire anemometers. The published measurements refer[b] to a single location in the jet turbulent field; the measurement point is indicated from the nozzle-exit-section centre by the vector

$$\mathbf{y}^{(m)} = 4d_J\hat{\boldsymbol{\gamma}}_1 + 0.5d_J\hat{\boldsymbol{\gamma}}_2$$

where d_J indicates the nozzle-exit diameter. The location $\mathbf{y}^{(m)}$ corresponds to a point on the nozzle lip line 4 diameters downstream the nozzle exit. Harper-Bourne measured the two-point

[a] As explained in Appendix A (section A.3), we define a cylindrical-coordinate basis which is function of the given location around the symmetry axis. Note that, given the middle-point convention for the two-point correlation around a generic reference point $\mathbf{y}$, the basis for the correlation tensor is a function of $\mathbf{y}$ only. This means that the azimuthal separations are orthogonal to the plane defined by the symmetry axis and the reference point $\mathbf{y}$.

[b] We note that the correlation function measured by Harper-Bourne does not adopt the same convention that is adopted in this work for the reference point. While the convention used in the present work is

$$\mathrm{c}_{\mathbf{S}'\mathbf{S}'}(\mathbf{y},\boldsymbol{\eta},\tau) = \overline{\mathbf{S}'(\mathbf{y}-\boldsymbol{\eta}/2,t)\,\mathbf{S}'(\mathbf{y}+\boldsymbol{\eta}/2,t+\tau)}$$

the experimental data are measured by using the fixed position of a hot wire as reference position as follows:

$$\mathrm{c}_{\mathbf{S}'\mathbf{S}'}(\mathbf{y},\boldsymbol{\eta},\tau) = \overline{\mathbf{S}'(\mathbf{y},t)\,\mathbf{S}'(\mathbf{y}+\boldsymbol{\eta},t+\tau)}$$

The approximation we are accepting is that the two conventions above coincide. In effect this is equivalent to assuming small variations for $\mathrm{c}_{\mathbf{S}'\mathbf{S}'}(\mathbf{y},\boldsymbol{\eta},\tau)$ for displacements of the reference position $\mathbf{y}$ within the correlation volume.

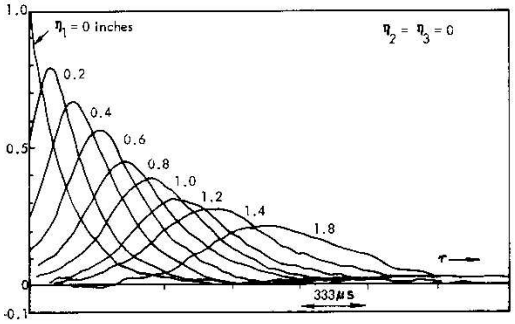

(a) The axial separation η_1 varies between 0 and 46 mm according to labels (labels are in inches). The transverse separation is zero.

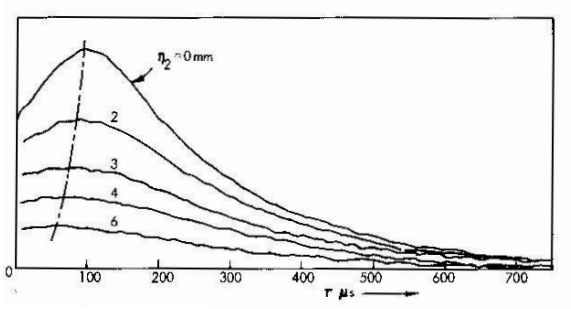

(b) The radial separation η_2 varies between 0 and 6 mm according to labels. The azimuthal separation is zero. The axial separation is held constant at $\eta_1 = 5.08$ mm.

Figure 4.1: Measured two-point correlation coefficient $\hat{c}_{11,11}$ as function of time separation τ at the reference location $\mathbf{y}^{(m)}$. Each curve in the diagrams corresponds to a distinct spatial separation between the hot-wire anemometers. The diagrams have been provided by Harper-Bourne; (a) and (b) respectively correspond to Fig. (7) and (8) (space–time correlations for u_1^2 fluctuations) in Ref. [5]. Note that the axial separation associated with the two-point correlations in (b) has been deduced from the correspondence between the peak time delays for the curve at $\eta_1 = 5.08$ mm in (a) and the curve at zero radial separation in (b); according to that, the vertical scale given in (a) can be extended to (b).

correlation coefficient[c] associated with the Reynolds-stress fluctuation $S'_{11} = u'_1 u'_1 - \overline{u'_1 u'_1}$:

$$\hat{c}_{11,11}\left(\mathbf{y}^{(m)}, \boldsymbol{\eta}, \tau\right) = \frac{c_{11,11}\left(\mathbf{y}^{(m)}, \boldsymbol{\eta}, \tau\right)}{c_{11,11}\left(\mathbf{y}^{(m)}, \mathbf{0}, 0\right)} \tag{4.14}$$

The measured two-point correlation coefficient is shown in Fig. 4.1, where diagrams showing the $\hat{c}_{11,11}$ dependence on the time delay τ are given at different spatial separations $\boldsymbol{\eta}$. The measurements show a pronounced convection effect for the diagrams in Fig. 4.1 (a) where the separation $\boldsymbol{\eta}$ varies along the mean-flow direction. The convection effect implies that the maximum of the correlation coefficient moves towards greater time delays as the space separation increases. For space separations in transverse directions (e. g. Fig. 4.1 (b) for radial separations and Harper-Bourne[5] for azimuthal separations) the correlation-maximum time delay does not sensibly change for increasing space separations.[d] A further characteristic that emerges from the observation of the two-point-correlation-coefficient diagrams is a maximum-broadening effect that is seen as the space-separation modulus η increases.[e] We note that the maximum-

[c]The normalised cross-correlation function defined by (4.14) is not the standard two-point correlation coefficient. See the table on p. 139, note (b). The difference is due to the spatial inhomogeneity of the jet-flow statistics.

[d]Harper-Bourne[4] noted a small convection effect in the two-point correlation time-delay functions for increasing radial separation, and no convection effect in the corresponding functions at increasing azimuthal separations. We observe that in both cases, although the convection effect is present, it is much smaller than the convection effect observed in the flow direction.

[e]We indicate with ζ_{max} the peak-region curvature of the time-delay function representing the two-point correlation coefficient at constant spatial separation. The term maximum-broadening is used to indicate the reduction of ζ_{max} and the corresponding broadening of the peak region.

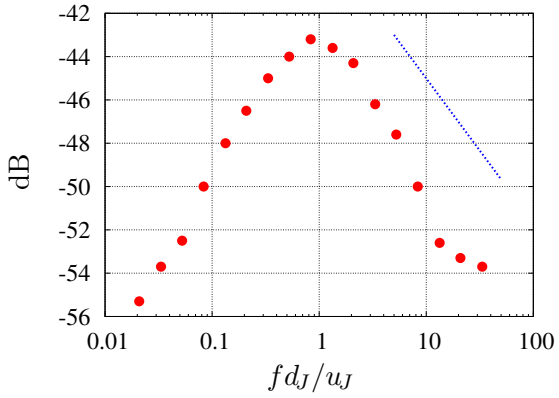

(a) 1/3-octave power spectrum corresponding to $c_{11,11}\left(\mathbf{y}^{(m)}, \mathbf{0}, f\right)/u_J^4$. The dotted line indicates the decay slope corresponding to $f^{-2/3}$.

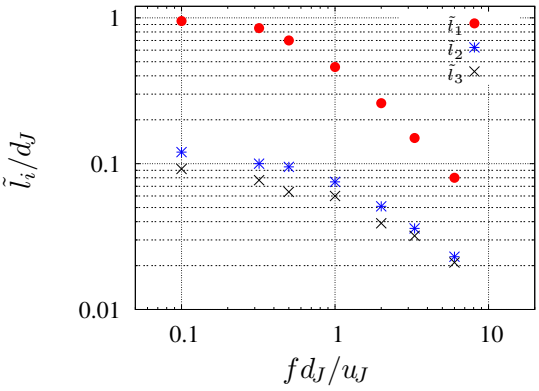

(b) $1/e$-decay length scales for $\sigma_{11,11}$ in axial, radial and azimuthal directions.

Figure 4.2: Frequency-domain Harper-Bourne measurements of the 11 fluctuating-Reynolds-stress component, as function of the nozzle-exit jet Strouhal number.

broadening is a universal effect in the two-point-correlation measurements associated with the fluctuating velocity[f] in turbulent jets. Harper-Bourne measured the frequency-domain characteristics of the fluctuating-Reynolds-stress two-point-correlation-function component $c_{11,11}$ by applying analogue frequency filtering to the hot-wire signals. The 1/3-octave auto spectrum[g] is presented in Fig. 4.2 (a). The autospectrum measurement corresponds to the normalised autocorrelation-function Fourier transform

$$s_{11,11}\left(\mathbf{y}^{(m)}, \mathbf{0}, f\right)/u_J^4$$

integrated across 1/3-octave frequency bands. Note that the high-frequency end of Fig. 4.2 (a) is not well defined by the data; a viscous cut-off is to be expected, at a Strouhal number dependent on Reynolds number.

The Fourier transform of the two-point correlation coefficient, normalised by its value at zero space separation, is indicated as follows:

$$\sigma_{11,11}\left(\mathbf{y}^{(m)}, \boldsymbol{\eta}, f\right) = \frac{\hat{s}_{11,11}\left(\mathbf{y}^{(m)}, \boldsymbol{\eta}, f\right)}{\hat{s}_{11,11}\left(\mathbf{y}^{(m)}, \mathbf{0}, f\right)} \tag{4.15}$$

See page 139 for a table of relevant notation. Note that $\sigma_{11,11}$ is equivalent to the $11,11$ component of the fluctuating-Reynolds-stress two-point CPSD tensor, normalised by its zero-separation value (the $11,11$ component of the single-point CPSD tensor). Fig. 4.2 (b) shows the measured $1/e$-decay length scales of $\sigma_{11,11}\left(\mathbf{y}^{(m)}, \boldsymbol{\eta}, f\right)$, normalised by the nozzle-exit diameter

[f]The effect is observed in the two-point cross-correlation coefficient for both the Reynolds-stress fluctuations ($\hat{c}_{ij,kl}$) and the velocity fluctuations ($\hat{c}_{i,j}$).

[g]The data have been provided by Harper-Bourne. The measured spectrum has been published in Bassetti, Morfey and Harper-Bourne.[42]

(Harper-Bourne,[4] data taken from the top diagrams in Fig. 9). Symbols $\tilde{l}_1$, $\tilde{l}_2$, $\tilde{l}_3$ denote the $1/e$-decay length scales of $\sigma_{11,11}\left(\mathbf{y}^{(m)}, \boldsymbol{\eta}, f\right)$. This definition implies that at the spatial separations

$$\tilde{l}_1\hat{\boldsymbol{\gamma}}_1, \quad \tilde{l}_2\hat{\boldsymbol{\gamma}}_2, \quad \tilde{l}_3\hat{\boldsymbol{\gamma}}_3$$

the amplitude $|\sigma_{11,11}|$ has fallen to the value $1/e = \exp(-1)$.

4.2.2 An analytical function to fit the two-point correlation coefficient

The two-point correlation coefficient $\hat{c}_{11,11}$ defined in section 4.2.1, corresponding to the 11 component of the fluctuating Reynolds stress, is modelled by adopting the following function:

$$\hat{\mathrm{c}}\left(\mathbf{y}, \boldsymbol{\eta}, \tau\right) = \exp\left(-\delta^c\right) \tag{4.16}$$

Here δ is a modified space-time distance defined as

$$\delta = \sqrt{\left(\frac{\tau - \dfrac{\eta_1}{U_c}}{\tau_d}\right)^2 + \left(\frac{|\eta_1|}{l_1}\right)^a + \left(\frac{\eta_\perp}{l_\perp}\right)^b} \tag{4.17}$$

The model is isotropic in the transverse plane as radial and azimuthal separations are expressed by a transverse separation

$$\eta_\perp = \sqrt{\eta_2^2 + \eta_3^2}$$

The reference-position dependence of (4.17) is implicit in the $1/e$-decay parameters τ_d, l_1, $l_\perp$, which are functions of the spatial position $\mathbf{y}$ in the flow. Also the phase-shift parameter U_c depends on $\mathbf{y}$. Function (4.16) has been derived in three steps of progressive refinement trying to follow the characteristics of the Harper-Bourne measurements.

1. The convection effect and the maximum-broadening associated with the Harper-Bourne measurements (Fig. 4.1) can be approximately matched by adopting an exponential-decay function whose argument is given by a simple space–time non-dimensional distance, corresponding to a=b=2 and c=1 in (4.16):

$$\exp\left(-\sqrt{\left(\frac{\tau - \dfrac{\eta_1}{U_c}}{\tau_d}\right)^2 + \left(\frac{\eta_1}{l_1}\right)^2 + \left(\frac{\eta_\perp}{l_\perp}\right)^2}\right) \tag{4.18}$$

   The function (4.18) incorporates the convection effect as a time-delay shift that is proportional to the space separation in the flow direction. We note that this is equivalent to adding a phase shift to the frequency-domain model of the correlation-coefficient Fourier

transform,[h] as in Harper-Bourne.[4] The quasi isotropy of the Harper-Bourne measurements for space separations varying transversely to the flow direction is present in the space-time distance model (4.18). The Fourier transform of expression (4.18) shows similar trends as the corresponding frequency-domain measurements.

2. The more general decay function (4.16) contains additional parameters a and b. These have been added to improve the matching between the frequency-domain measurements in Fig. 4.2 (b), and the corresponding result obtained by applying a digital Fourier transform to the modified-distance model (4.16). This first generalisation of the space–time distance model allows for anisotropy between the decay behaviours associated with time separations and space separations. Provided a and b assume different values, decay-shape anisotropy is also introduced between axial and transverse separations.[i]

3. A further degree of generalisation has been added with the parameter c that allows for adjusting the high-frequency roll-off slope associated with the time-delay Fourier transform of the model.[j]

The degree to which the function (4.16) follows the Harper-Bourne measurements is shown in the time-separation domain in Fig. 4.3 (to be compared against the corresponding measurements in Fig. 4.1) and in the frequency domain in Fig. 4.4, where we indicate with $\hat{\text{s}}$ the Fourier transform of model (4.16). The values $a = 1.8$, $b = 2.8$, and $c = 1$ are used for the model. The parameter U_c is fixed to the value 38.5 m/s ($0.64u_J$). The $1/e$-decay parameters are set as follows: $\tau_d = 0.2\ 10^{-3}$ s, $l_1 = 0.0269$ m ($0.53d_J$), $l_\perp = 0.0035$ m ($0.07d_J$).

4.2.3 Phenomena controlling the turbulent-energy spectrum

In this section we give a qualitative description of a turbulent flow. We argue that model (4.16) is limited to the phenomena where viscous dissipation can be considered as a small parameter. We also argue that, if it was to be used for modelling the fluctuating-velocity correlation, the parameter c in model (4.16) should be set to a value near to 0.8 in order to confirm the theoretical/experimental slope associated with the intermediate range of frequencies in the turbulent-velocity PSD.

[h] For a given space separation and at varying time delay, the function (4.18) reaches a maximum for

$$\tau_{max} = \frac{\eta_1}{U_c}$$

The Fourier transform in τ is complex, as can be seen by operating the time shift $\tau \rightarrow \tau' = \tau - \tau_{max}$. Noting that the function (4.18) is an even function of τ', the Fourier transform is given by a complex solution whose phase is given by $-2\pi f \tau_{max}$.

[i] The term decay shape indicates the normalised decay function that is followed by the correlation as the given separation increases. Decay-shape anisotropy here means that a further degree of directional dependence can be added to model (4.18). The model in (4.18) already allows for decay-length anisotropy as the values l_1, $l_\perp$ are arbitrary and potentially different.

[j] This parameter enlarges the family of functions included by (4.16) to the point that for the choice $(a, b, c) = (2, 2, 2)$ we get a separable-variable function. The choice $(a, b, c) = (2, 2, 2)$ yields a Gaussian shape for the zero-space-separation $\hat{c}_{11,11}$; this is in evident contrast with Fig. 4.1 (a), zero-space-separation curve. The value of c must be close to 1 to achieve a behaviour for (4.16) that is close to the Harper-Bourne measurements.

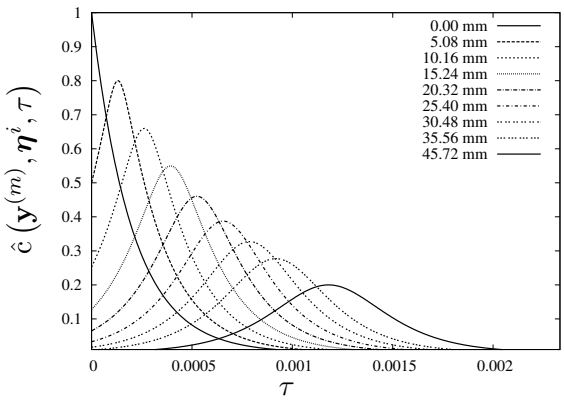

(a) The axial separation η_1 varies between 0 and 46 mm according to labels. The transverse separation is zero.

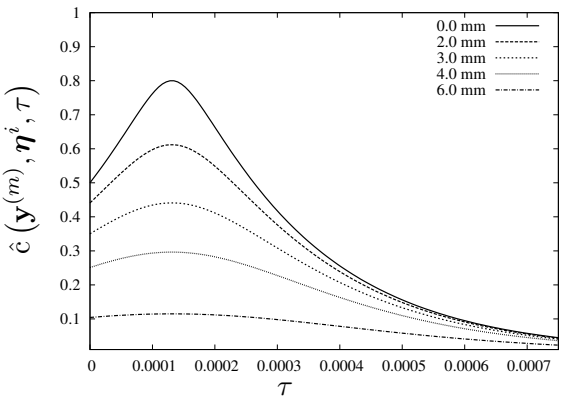

(b) The transverse separation $\eta_\perp$ varies between 0 and 6 mm according to labels. The axial separation is held constant at $\eta_1 = 5.08$ mm.

Figure 4.3: Modelled two-point correlation coefficient $\hat{c}_{11,11} = \hat{\mathrm{c}}\left(\mathbf{y}^{(m)},\boldsymbol{\eta},\tau\right)$ at constant space separations and varying time separation. The parameters in model (4.16) are set to the following values: $\tau_d = 0.24 d_J/u_J$, $U_c = 0.64 u_J$, $l_1 = 0.53 d_J$, $l_\perp = 0.07 d_J$. Also, $a = 1.8$, $b = 2.8$ and $c = 1$.

We can think of a developed turbulence flow as a chaotic ensemble of 3-D vortical structures that are generated at random instants at locations where the instantaneous velocity field is unstable. The vortical structures will grow up to the dimension of the local 3-D sheared flow and dissipate. The dissipation of a given structure is supposed not to happen as a direct consequence of viscosity; an energy transfer to smaller flow structures is assumed to happen through the energy cascade process.[k] The energy cascade operates an erosion of the flow structures offering at a given instant a view of the flow with the presence of a wide range of flow-structure sizes. Structures in the energy cascade process define a size range going from the largest flow dimension, defined by the typical geometries of the flow boundaries, down to a smallest-size limit. The smallest sizes in the flow are controlled by the viscous effect. At this size the work of the viscous forces becomes effective and the fluctuating kinetic energy is converted into heat. The range of eddy scales intermediate between the largest scales (comparable with the shear-layer thickness) and the viscous-dissipation scales is called the inertial subrange. The viscous-effect size range is called the viscous range. This picture of the phenomena involved in the turbulent-energy spectrum falls within the generic description given by Richardson and used by Kolmogorov[49] to derive the theoretical basis supporting the constant-slope decay corresponding to the inertial subrange of flow structures. We note that model (4.16) can be used to partially represent the picture of the turbulent-energy power spectrum. Model (4.16) covers the energy-production and the inertial-subrange frequency

[k]The given vortical structure interacts with similar structures to form a flow pattern that is unstable. The instability results in the formation of further vortical structures at a smaller scale than the initial ones. A smaller-scale flow pattern is in this way generated, from which further instabilities leading to even smaller scales and so on. This break-down process transfers the fluctuating kinetic energy from large structures to progressively smaller structures. A more detailed qualitative description of the process is given in Ref. [48].

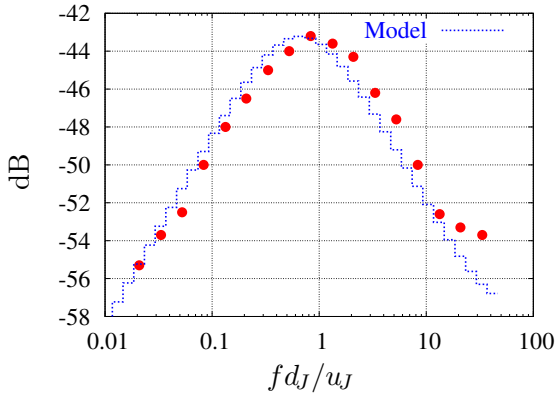

(a) 1/3-octave power spectrum associated with $(0.19)^4\,\hat{\mathrm{s}}\left(\mathbf{y}^{(m)},\mathbf{0},f\right)$ and the corresponding Harper-Bourne data as in Fig. 4.2 (a).

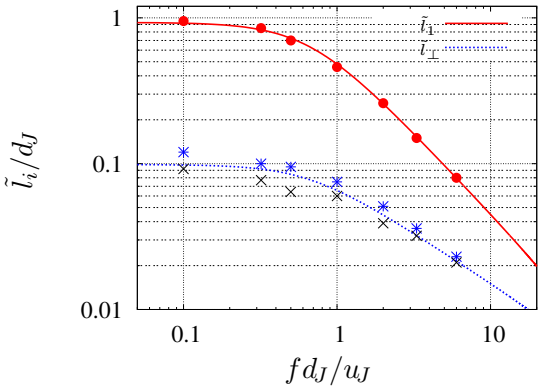

(b) $1/e$-decay length scales for $\sigma\left(\mathbf{y}^{(m)},\boldsymbol{\eta},f\right)$ in axial, and transversal direction against the corresponding Harper-Bourne measurements as in Fig. 4.2 (b).

Figure 4.4: Frequency-domain behaviour of model (4.16) compared to the corresponding Harper-Bourne measurements. The model parameters are as in Fig. 4.3.

regions only.[l] Including the dissipation range is not justified by the measurements available in Ref. [4, 5], and would imply a Reynolds-number dependence of the model. Setting the exponent c to the value 4/5 yields a high-frequency roll-off slope that is equal to the roll-off slope corresponding to the turbulent-kinetic-energy inertial subrange spectrum.[m]

4.3 A simplified model for the acoustic-source correlation function

As was argued in section 4.1, the acoustic-source statistics can with a few assumptions be related to the fluctuating Reynolds-stress correlation function. An initial description of the acoustic source can be made by assuming that the acoustic-source two-point correlation is simply proportional to the Reynolds-stress two-point correlation. The implication of this approach is that a good model of the Reynolds-stress two-point correlation at a given spatial location also represents the source model for the acoustic radiation from the same point. This approach has been followed in Ref. [42] where a model of type (4.16) was adopted with values for a, b and c that ensured a good fit to the Harper-Bourne measurements. However, the resulting frequency-proportional band width (FPBW) acoustic-source spectrum at the Harper-Bourne

[l] The model (4.16) does not represent a dissipation-range frequency region, as a constant high-frequency roll off characterises the function $\hat{\mathrm{s}}\,(\mathbf{y},\mathbf{0},f)$. The high-frequency slope variation typical of the turbulent-kinetic-energy spectral measurements, and explained as effect of viscosity, is not present.

[m] This inertial-range slope has been evaluated numerically by applying DFT to model (4.16). The estimated value is typical in the PSD measurements of turbulent energy. The measurements refer to the second-order statistical moments of the fluctuating velocity and not the fourth-order moments as in the Harper-Bourne measurements. Kolmogorov[49] provided the theoretical foundations to base statistical theories that lead to the same result for the inertial-range slope.

measurement location showed a growing high-frequency trend. This is in contrast with the high-frequency decay observed in jet-noise acoustic measurements. A modification of model (4.16), obtained by changing the values (a, b, c) from those that optimise the fit to the Harper-Bourne measurements, yields a decaying high-frequency slope. We note that access to a more extensive set of Reynolds-stress measurements represents the only way to properly resolve the choice of the best set of coefficients a, b and c. Specifically we need measurements of the two-point Reynolds-stress statistics at a number of different space locations in a given jet and we need to repeat the measurements for different jets, in order to establish if the two-point correlation coefficient can be modelled by adopting a simple modified-distance model as in (4.16). A further interesting point to define is the existence of a time-separation interval where the fluctuating-Reynolds-stress autocorrelation coefficient is negative;[a] once this is defined, an oscillating function can be added to model (4.16). As in Ref. [50],[b] we assume a simplified model for the two-point correlation coefficient in order to easily evaluate the effect of changing the decay shape of the two-point CPSD modulus with increasing space separations. The simplified model is derived from model (4.16) by fixing the value of the exponents a and b to a common value a_l, and by assuming that the exponent c is 1.

$$\hat{\mathrm{c}}_0(\mathbf{y}, \boldsymbol{\eta}, \tau) = \exp\left(- \sqrt{\left(\frac{\tau - \dfrac{\eta_1}{U_c}}{\tau_d} \right)^2 + \frac{\eta_1^{a_l}}{l_1^{a_l}} + \frac{\eta_2^{a_l}}{l_2^{a_l}} + \frac{\eta_3^{a_l}}{l_3^{a_l}}} \right) \tag{4.19}$$

We note that this model allows for a straightforward addition of a possible anisotropy in the transverse plane. For this reason the radial and azimuthal separations appear separately in (4.19), each with their corresponding $1/e$-decay length.[c] A frequency-domain comparison between model (4.19) and the corresponding Harper-Bourne measurement is shown in Fig. 4.5 as function of the reduced frequency $Sr_\tau = f\tau_d$.[d] Note that changing the parameter a_l does

[a] Note that the Harper-Bourne[4,5] measurements do not clearly identify a negative-coefficient time-delay interval; this might be due to the level of noise-to-signal ratio associated with the measurements and a small value for the negative parts of the correlation coefficient; in other words, the correlation has already decayed below the noise level before the first zero of the autocorrelation.

[b] The work in Bassetti and Morfey[50] suggests a solution by assuming that the true frequency dependence of the $\tilde{l}_1$ scale deviates from the measurements in Refs. [4, 5]. The frequency dependence measured for $\tilde{l}_\perp$ is extended to $\tilde{l}_1$ by adopting the values (a, b, c)=$(2.7, 2.7, 1)$ in model (4.16). This yields a physical high-frequency decay for the FPBW acoustic-source power spectrum in the high-frequency solution (3.16) of the modelled 1/3-octave spectra. Note that the low-frequency component (3.23) in Ref. [50] is affected by a mistaken choice of the Reynolds-stress autospectrum; the mistaken spectrum is characterised by a high-frequency decay that is greater than the one associated with model (4.16) and c=1.

[c] This complication of the model is not numerically challenging, within the present framework, as long as the decay-shape function is the same for each type of spatial separation. In this case all the space variables behave isotropically in the stretched-separation space

$$\hat{\eta}_i = \frac{\eta_i}{l_i} \quad \text{(no summation)}$$

[d] Note that assuming that the Reynolds-stress two-point correlation coefficient follows model (4.19) is equivalent to saying that the autospectrum and the $1/e$-decay lengths $\tilde{l}_i$ collapse on corresponding characteristic curves, if expressed as functions of $f\tau_d$ and appropriately scaled. A note regarding the Strouhal scaling of model (4.19) is given in Appendix G.

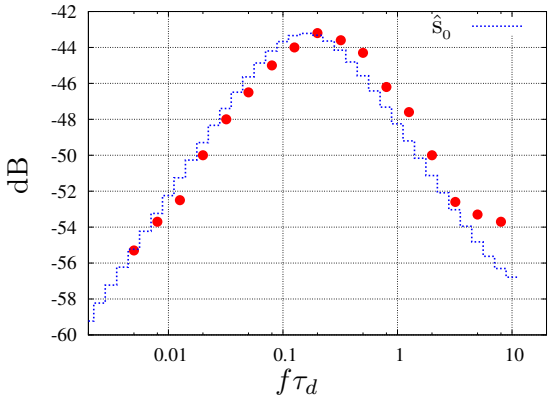

(a) 1/3-octave power spectrum associated with $(0.19)^4\,\hat{s}_0\left(\mathbf{y}^{(m)},\mathbf{0},f\right)$ and the corresponding Harper-Bourne data as in Fig. 4.2 (a).

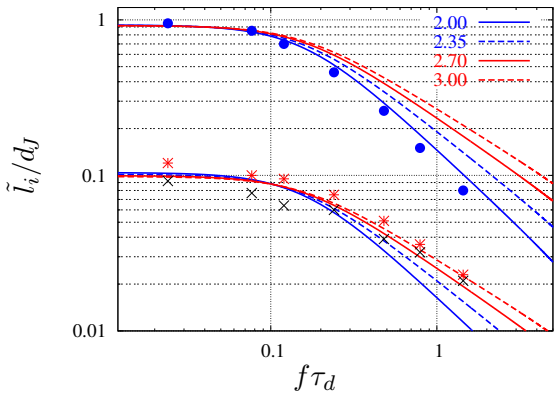

(b) $1/e$-decay length scales for $\sigma_0\left(\mathbf{y}^{(m)},\boldsymbol{\eta},f\right)$ in axial and transversal directions against the corresponding Harper-Bourne measurements as in Fig. 4.2 (b). The labels denote the value of a_l

Figure 4.5: Frequency-domain behaviour of model (4.19) compared to the corresponding Harper-Bourne measurements. The Strouhal number based on the local value of the $1/e$-decay time τ_d is used on the horizontal axis.

not alter the normalised autospectrum $\hat{s}_0(\mathbf{y},\mathbf{0},f)$ derived by Fourier transforming model (4.19). The value assigned to a_l affects the high-frequency trends of the $1/e$-decay lengths $\tilde{l}_i$ associated with the normalised two-point CPSD $\sigma_0(\mathbf{y},\boldsymbol{\eta},f)$, as derived by Fourier transforming model (4.19) and normalising by its zero-separation value $\hat{s}_0(\mathbf{y},\mathbf{0},f)$. For $a_l = 2.0$, the high-frequency roll-off of the modelled $\tilde{l}_i$ is close to the axial-separation Harper-Bourne measurements, points • in Fig. 4.5 (b); it is close to the transverse-separation Harper-Bourne measurements (points ✳ and × in Fig. 4.5) for $a_l = 2.7$.

We assume that the whole set of components of the fluctuating-Reynolds-stress correlation function can be related to the same two-point correlation coefficient. This yields the following assumption for the fluctuating-applied-stress two-point correlation tensor:

$$\mathrm{c}_{\mathbf{Q}'\mathbf{Q}'} \simeq \mathrm{c}_{\mathbf{S}'\mathbf{S}'} \simeq \bar{q}_{ij,kl}\left(\mathbf{y}\right)\hat{\mathrm{c}}_0(\mathbf{y},\boldsymbol{\eta},\tau)\,\hat{\boldsymbol{\gamma}}_i\otimes\hat{\boldsymbol{\gamma}}_j\otimes\hat{\boldsymbol{\gamma}}_k\otimes\hat{\boldsymbol{\gamma}}_l \tag{4.20}$$

Here $\bar{q}_{ij,kl}\left(\mathbf{y}\right) = c_{ij,kl}\left(\mathbf{y},\mathbf{0},0\right)$ denotes the component of the fluctuating-Reynolds-stress mean-product tensor; it is given as follows:

$$\bar{q}_{ij,kl}\left(\mathbf{y}\right) = \overline{\left(u_i'u_j' - \overline{u_i'u_j'}\right)\left(u_k'u_l' - \overline{u_k'u_l'}\right)} \tag{4.21}$$

Similarly, the applied-force two-point covariance tensor is defined as follows:

$$\mathrm{c}_{\mathbf{d}'\mathbf{d}'} \simeq \kappa_{\mathbf{d}}\left(\frac{|\nabla\bar{T}(\mathbf{y})|}{\bar{T}(\mathbf{y})}\right)^2\Delta_{i,j}\left(\mathbf{y}\right)\hat{\mathrm{c}}_0(\mathbf{y},\boldsymbol{\eta},\tau)\,\hat{\boldsymbol{\gamma}}_i\otimes\hat{\boldsymbol{\gamma}}_j \tag{4.22}$$

(compare (4.12)). Here the components $\Delta_{i,j}\left(\mathbf{y}\right)$ are given by the following combination be-

tween the components $\bar{q}_{ij,kl}$ and the components of the static-temperature-gradient unit vector $\hat{\boldsymbol{\theta}}$:

$$\begin{aligned}\Delta_{i,j} = \quad & \hat{\theta}_1^2 \bar{q}_{1i,1j} + \hat{\theta}_1\hat{\theta}_2 \left(\bar{q}_{1i,2j} + \bar{q}_{2i,1j}\right) + \\ & \hat{\theta}_2^2 \bar{q}_{2i,2j} + \hat{\theta}_1\hat{\theta}_3 \left(\bar{q}_{1i,3j} + \bar{q}_{3i,1j}\right) + \\ & \hat{\theta}_3^2 \bar{q}_{3i,3j} + \hat{\theta}_2\hat{\theta}_3 \left(\bar{q}_{2i,3j} + \bar{q}_{3i,2j}\right)\end{aligned} \tag{4.23}$$

For a parallel flow, the orthogonality between $\hat{\boldsymbol{\theta}}$ and the mean velocity implies $\hat{\theta}_1 = 0$;[e] in this case we have

$$\Delta_{i,j} = \hat{\theta}_2^2 \bar{q}_{2i,2j} + \hat{\theta}_3^2 \bar{q}_{3i,3j} + \hat{\theta}_2\hat{\theta}_3 \left(\bar{q}_{2i,3j} + \bar{q}_{3i,2j}\right) \tag{4.24}$$

We note that in the case of axisymmetric parallel flow the mean static-temperature gradient is in the radial direction; in this case expression (4.23) reduces to

$$\Delta_{i,j} = \bar{q}_{2i,2j} \tag{4.25}$$

4.4 The volume integral across space separation

In this section we evaluate the volumetric source strength in the frequency domain, using the simplified source models (4.20) and (4.22) and with the cross-correlation coefficient for each ij, kl fluctuating-Reynolds-stress combination approximated by (4.19). It is therefore necessary to calculate the volume integral of the acoustic-source phase-shifted two-point CPSD as in expressions (4.1) and (4.2). Noting that the cylindrical-coordinate unit vectors do not change orientation under varying separation,[a] the expressions for the applied-stress source and for the applied-force source are

$$\bar{q}_{ij,kl}\left(\mathbf{y}, \mathbf{0}, 0\right) \hat{\boldsymbol{\gamma}}_i \otimes \hat{\boldsymbol{\gamma}}_j \otimes \hat{\boldsymbol{\gamma}}_k \otimes \hat{\boldsymbol{\gamma}}_l \iiint_{\boldsymbol{\eta}} \hat{\mathrm{s}}_0(\mathbf{y}, \boldsymbol{\eta}, f) \exp\left(\mathrm{j}\ 2\pi f \boldsymbol{\eta} \cdot \hat{\mathbf{r}}/c\right) \mathrm{d}^3\boldsymbol{\eta} \tag{4.26}$$

and

$$\kappa_{\mathbf{d}} \left(\frac{|\nabla \bar{T}(\mathbf{y})|}{\bar{T}(\mathbf{y})} \right)^2 \Delta_{i,j}\left(\mathbf{y}\right) \hat{\boldsymbol{\gamma}}_i \otimes \hat{\boldsymbol{\gamma}}_j \iiint_{\boldsymbol{\eta}} \hat{\mathrm{s}}_0(\mathbf{y}, \boldsymbol{\eta}, f) \exp\left(\mathrm{j}\ 2\pi f \boldsymbol{\eta} \cdot \hat{\mathbf{r}}/c\right) \mathrm{d}^3\boldsymbol{\eta} \tag{4.27}$$

Expressions (4.26) and (4.27) both contain the spatial integral

$$\iiint_{\boldsymbol{\eta}} \hat{\mathrm{s}}_0(\mathbf{y}, \boldsymbol{\eta}, f) \exp\left(\mathrm{j}\ 2\pi \boldsymbol{\alpha} \cdot \boldsymbol{\eta}\right) \mathrm{d}^3\boldsymbol{\eta} \tag{4.28}$$

[e] Recall that equation (4.7) has been derived under the hypothesis of orthogonality between the mean-temperature gradient and the mean velocity.

[a] The middle-point definition for the two-point correlation function means that the azimuthal separations are given by moving in the direction orthogonal to the plane defined by the reference point $\mathbf{y}$ and the symmetry axis. The azimuthal extent of the coherent source region is assumed small.

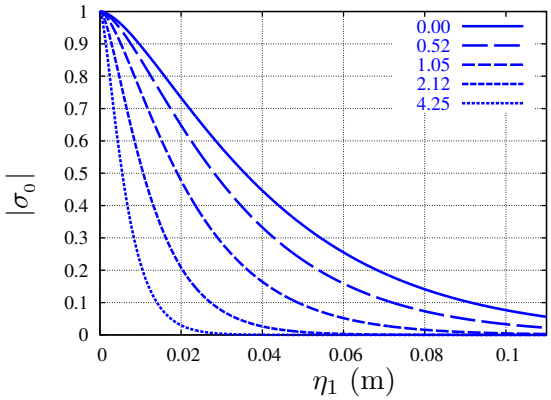

(a) Modulus of the normalised two-point CPSD $\sigma_0(\mathbf{y}, \boldsymbol{\eta}, f)$ as function of spatial separation in the flow direction. The parameter a_l is set to 2. Labels denote the value of the Strouhal number $f d_J / u_J$.

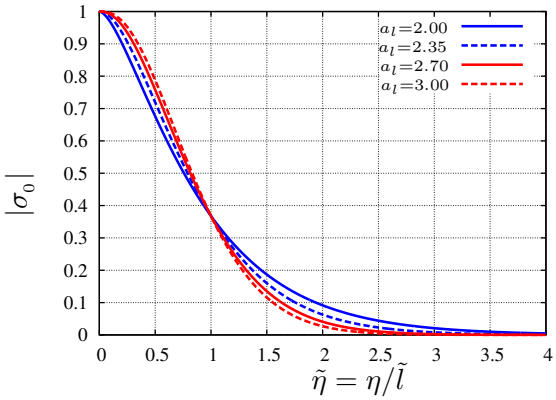

(b) Characteristic curves for the normalised two-point CPSD as function of spatial separation normalised by the corresponding $1/e$-decay length.

Figure 4.6: Modulus of the normalised two-point CPSD $\sigma_0(\mathbf{y}, \boldsymbol{\eta}, f)$ for model (4.19). Normalisation of the spatial separation η by the appropriate frequency-dependent length scale yields a collapse on a characteristic curve. The characteristic curves are shown in (b) for different values of a_l.

where $\boldsymbol{\alpha}$ is the repetency vector

$$\boldsymbol{\alpha} = \frac{f \hat{\mathbf{r}}}{c}$$

The integral can be reduced to a 1-D integral by decomposing the Fourier transform of (4.19) as follows:

$$\hat{\mathrm{s}}_0(\mathbf{y}, \boldsymbol{\eta}, f) = \hat{\mathrm{s}}_0(\mathbf{y}, \mathbf{0}, f)\, \sigma_0(\mathbf{y}, \boldsymbol{\eta}, f) \tag{4.29}$$

Here the first factor represents the normalised spectrum of the fluctuating Reynolds-stress components at point $\mathbf{y}$, and function $\sigma_0(\mathbf{y}, \boldsymbol{\eta}, f)$ represents the separation dependence of the two-point CPSD. The $1/e$-decay length scales $\tilde{l}_i$ associated with the modulus of σ_0 are shown in Fig. 4.5 (b), where the corresponding Reynolds-stress quantities as measured by Harper-Bourne are also shown. Note that the parameter a_l in model (4.19) affects the frequency dependence of $\tilde{l}_i$: a steeper high-frequency decay corresponds to decreasing values of a_l. The numerical evaluation[b] of $|\sigma_0(\mathbf{y}, \boldsymbol{\eta}, f)|$ is reported in Fig. 4.6 (a) at different frequencies and for varying spatial separation. An important characteristic of $|\sigma_0(\mathbf{y}, \boldsymbol{\eta}, f)|$ is reported in Fig. 4.6 (b) where the diagrams representing the modulus decay are shown as a function of the normalised separation: the decay shape does not change with change of frequency. The σ_0 function also exhibits spatial isotropy[c] for the modulus decay shape with respect to the separation direction,

[b]The numerical evaluation has been performed by applying a DFT to sequences given by the sampling of (4.19) at different time separations and space separations. For a given spatial separation a sequence of samples is taken at time separations that resolve the range of variability of (4.19). The sequence is then processed by adopting standard Fast Fourier Transform routines. The processed data are considered up to a maximum frequency guaranteeing a negligible aliasing effect. The accuracy of the routines has been tested against analytical solutions in Ref. [42].

[c]The exponents a and b in (4.16) have a common value a_l in (4.19). This implies isotropy when considering

if the separation coordinates are suitably scaled at each frequency by introducing the new variable

$$\boldsymbol{\eta} \rightarrow \tilde{\boldsymbol{\eta}}(f) = \frac{\eta_i}{\tilde{l}_1}\hat{\boldsymbol{\gamma}}_1 + \frac{\eta_2}{\tilde{l}_2}\hat{\boldsymbol{\gamma}}_2 + \frac{\eta_3}{\tilde{l}_3}\hat{\boldsymbol{\gamma}}_3$$

This property allows for representing σ_0 as an implicit function of frequency. Here $\tilde{l}_i(f)$ (i= 1, 2, 3) denote the amplitudes of the separations η_i at which $|\sigma_0(\mathbf{x}, \boldsymbol{\eta}, f)|$ has decayed to the value $1/e$. Note that $\tilde{l}_i(f)$ is not the same as l_i in (4.19). The expression for the fluctuating-Reynolds-stress normalised two-point CPSD reads:

$$\sigma_0(\mathbf{x}, \boldsymbol{\eta}, f) = |\sigma_0(\mathbf{x}, \tilde{\eta}(f))| \exp(-\mathrm{j}\ 2\pi f \eta_1/U_c) \tag{4.30}$$

Introducing the change of variable $\boldsymbol{\eta} \rightarrow \tilde{\boldsymbol{\eta}}$ into the space-separation integral (4.28) yields

$$\hat{\mathrm{s}}_0(\mathbf{y}, \mathbf{0}, f)\, \tilde{l}_1\tilde{l}_2\tilde{l}_3 \iiint_{\tilde{\boldsymbol{\eta}}} |\sigma_0(\mathbf{x}, \tilde{\eta})| \exp(\mathrm{j}\ 2\pi\tilde{\boldsymbol{\alpha}} \cdot \tilde{\boldsymbol{\eta}})\, \mathrm{d}^3\tilde{\boldsymbol{\eta}} \tag{4.31}$$

Here $\tilde{\boldsymbol{\alpha}}$ is a modified-repetency vector depending on the initial phase shift (dictated by the acoustic-radiation parameters c and $\hat{\mathbf{r}}$), the phase of σ_0 and the $1/e$-decay lengths of $|\sigma_0|$:

$$\tilde{\boldsymbol{\alpha}} = \left(\frac{f\tilde{l}_i}{c}\hat{r}_i\hat{\boldsymbol{\gamma}}_i - \frac{f\tilde{l}_1}{U_c}\hat{\boldsymbol{\gamma}}_1\right) \tag{4.32}$$

The integral (4.31) can be reduced to a 1-D integral by carrying out the space integration in a polar spherical-coordinate system having the polar axis directed along $\tilde{\boldsymbol{\alpha}}$. After solving the integral across azimuth and polar angle, the resulting 1-D integral is given as

$$\hat{\mathrm{s}}_0(\mathbf{y}, \mathbf{0}, f)\, \tilde{l}_1\tilde{l}_2\tilde{l}_3 \frac{2}{\tilde{\alpha}} \int_0^\infty |\sigma_0(\mathbf{x}, \tilde{\eta})|\, \tilde{\eta} \sin(2\pi\tilde{\alpha}\tilde{\eta})\ \mathrm{d}\tilde{\eta} \tag{4.33}$$

Here $\tilde{\alpha}$ is the modulus of the non-dimensional modified-repetency vector $\tilde{\boldsymbol{\alpha}}$,

$$\tilde{\alpha} = \frac{f}{c}\sqrt{\left(\frac{\tilde{l}_1}{U_c/c} + \tilde{l}_1\hat{r}_1\right)^2 + \left(\tilde{l}_2\hat{r}_2\right)^2 + \left(\tilde{l}_3\hat{r}_3\right)^2} \tag{4.34}$$

The integral in (4.33) converges, for the values of parameter a_l considered in model (4.19). This allows one to define a positive-valued real function $\mathrm{C_f}$ of a generic non-negative real variable ξ as follows.

$$\mathrm{C_f}(\xi) = \frac{2}{\xi} \int_0^\infty |\sigma_0(\mathbf{x}, \tilde{\eta})|\, \tilde{\eta} \sin(2\pi\xi\tilde{\eta})\ \mathrm{d}\tilde{\eta} \tag{4.35}$$

model (4.19) in the stretched space η_i/l_i. The isotropy of σ_0 is a consequence of the direct proportionality between $\tilde{l}_i(f)$ and l_i; see Appendix G.

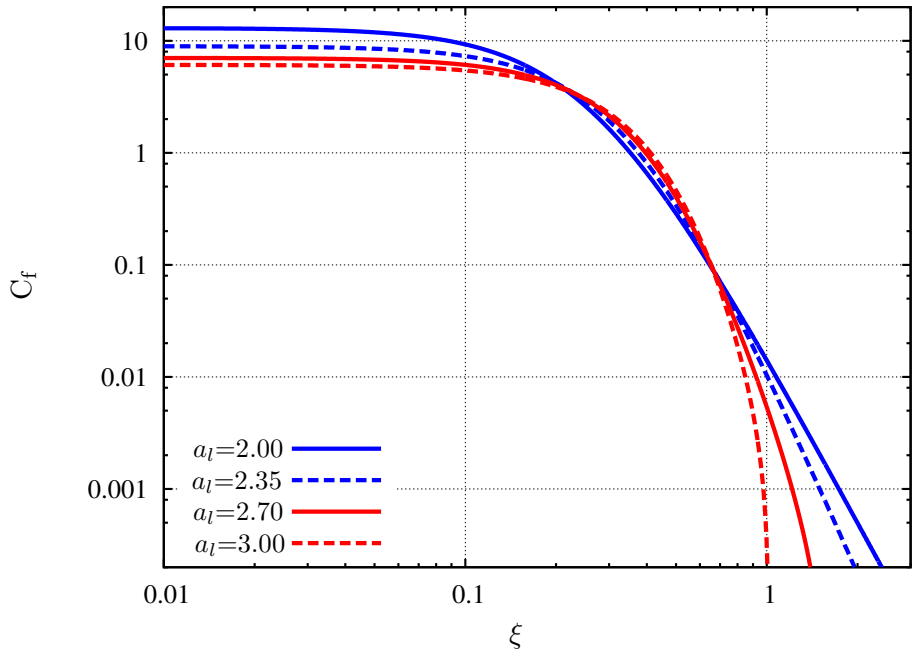

Figure 4.7: Cancellation-factor function (4.35) as function of a general scalar ξ, for a number of values of the parameter a_l in (4.19).

The function $\mathrm{C_f}\,(\xi)$ is shown in Fig.4.7. The integral term (4.33) can be expressed in terms of $\mathrm{C_f}\,(\tilde{\alpha})$ as follows:

$$\hat{\mathrm{s}}_0(\mathbf{y},\mathbf{0},f)\,\tilde{l}_1\,(\mathbf{y},f)\,\tilde{l}_2\,(\mathbf{y},f)\,\tilde{l}_3\,(\mathbf{y},f)\,\mathrm{C_f}\,(\tilde{\alpha}) \tag{4.36}$$

Expression (4.36) allows us to break down the space-separation integral in the volumetric source-strength expressions (4.26) and (4.27) into 5 scalar factors. Each of the 5 scalar factors can be modelled separately on the basis of the time-invariant parameters τ_d, U_c, l_i in (4.19).

The result (4.36) can be input into (4.26) and (4.27) to yield tensor expressions for the acoustic-source volumetric strength. The tensor is given as

$$\bar{q}_{ij,kl}\,(\mathbf{y},\mathbf{0},0)\,\hat{\mathrm{s}}_0(\mathbf{y},\mathbf{0},f)\,\tilde{l}_1\,(\mathbf{y},f)\,\tilde{l}_2\,(\mathbf{y},f)\,\tilde{l}_3\,(\mathbf{y},f)\,\mathrm{C_f}\,(\tilde{\alpha})\,\hat{\boldsymbol{\gamma}}_{\mathrm{i}}\otimes\hat{\boldsymbol{\gamma}}_{\mathrm{j}}\otimes\hat{\boldsymbol{\gamma}}_{\mathrm{k}}\otimes\hat{\boldsymbol{\gamma}}_{\mathrm{l}} \tag{4.37}$$

for the applied-stress sources and

$$\kappa_{\mathbf{d}}\left(\frac{|\nabla\bar{T}(\mathbf{y})|}{\bar{T}(\mathbf{y})}\right)^2\Delta_{i,j}\,(\mathbf{y})\,\hat{\mathrm{s}}_0(\mathbf{y},\mathbf{0},f)\,\tilde{l}_1\,(\mathbf{y},f)\,\tilde{l}_2\,(\mathbf{y},f)\,\tilde{l}_3\,(\mathbf{y},f)\,\mathrm{C_f}\,(\tilde{\alpha})\,\hat{\boldsymbol{\gamma}}_{\mathrm{i}}\otimes\hat{\boldsymbol{\gamma}}_{\mathrm{j}} \tag{4.38}$$

for the applied-force source. Expressions (4.37) and (4.38) need to be input to the high-frequency and low-frequency expressions (3.15) and (3.20). The appropriate sound speed c and unit radiation vector $\hat{\mathbf{r}}$ are to be specified differently for the different frequency limits. These radiation parameters are confined to the argument $\tilde{\alpha}$, expression (4.34), of the cancellation-factor function $\mathrm{C_f}$, defined by (4.35).

4.5 Concluding remarks

On the way to expressions (4.37) and (4.38), which represent the main closure ingredient for the aerodynamic noise model, a number of useful results have been found in the present chapter.

1. The instantaneous local strength of the equivalent acoustic sources has been related to the local value of the unit-density Reynolds stress. Provided the local pressure fluctuations are much smaller than the mean pressure, the instantaneous value of the applied-stress equivalent acoustic source equals the unit-density Reynolds stress. Under the hypothesis of purely convective static-temperature fluctuations and assuming small static-temperature fluctuations compared to the time-averaged absolute static temperature, a relation between the instantaneous value of one of the terms of the applied-force source and the scaled projection of the unit-density Reynolds stress has been identified in expression (4.11). The instantaneous applied-force source also involves a further fluctuating term (4.10) given by the Lagrangian time derivative plus the mean-velocity gradient operating on the product of fluctuating static temperature times fluctuating-velocity vector. In the absence of data from simulations or measurements, this second term is assumed to scale in the same way as the first.

2. It follows that the two-point correlation function associated with the fluctuating part of the applied-stress and the applied-force equivalent acoustic sources is directly related to the two-point correlation function of the fluctuating Reynolds stress. For the applied-force source this requires a further scaling hypothesis implying the full characterisation of its two-point correlation function by means of the source-strength instantaneous component (4.11) given by the scaled projection of the unit-density Reynolds stress.

3. An analytical model (4.16) for the fluctuating Reynolds-stress two-point correlation coefficient has been introduced. The model is based on a modified space–time distance (4.17) in a stretched separation space. It includes a convection effect in the axial direction, given by a time-separation shift that varies linearly with the space-separation axial component. The model closely follows the corresponding Harper-Bourne[4,5,42] measurements both in the time-separation domain and in the frequency domain. This model shows that the frequency-domain behaviour of the Harper-Bourne data can be reproduced by a simple constant-parameter model. The modified-distance model departs from the traditional way of modelling the acoustic-source correlation function via a Gaussian-decay model of the two-point correlation coefficient, which can be dated back to Ribner.[47] This model also constitutes an alternative interpretation for velocity-covariance measurements; in this area the Ribner[47] model was adopted by Chu[51] and is used in the work by Kerhervé, Fitzpatrick and Jordan.[52]

4. A model (4.19) for the acoustic-source two-point correlation coefficient is derived as a simplification of model (4.16). Model (4.19) retains the time-separation dependence of

model (4.16), but spatial-decay shape isotropy is assumed. Note that model (4.19) is used to represent the correlation coefficient for all ij, kl combinations of the fluctuating Reynolds-stress components. The shape isotropy for the space-separation decay of model (4.19) is used in order to reduce the integral across separation space to a 1-D integral that can be evaluated numerically. A cancellation function (4.35) can in this way be tabulated and directly accessed; this greatly reduces the numerical effort for the local evaluation of the acoustic-source volumetric strength.

Further experimental/DNS data on turbulent flows would greatly improve the modelling in this chapter. A DNS analysis of the term (4.10) in the applied-force expression could be used to test the applied-force scaling hypothesis in section 4.1.1 and in point 2 above. Specifically an evaluation of the two-point correlation function associated with the fluctuating part of term (4.10) is required in order to properly characterise the fluctuating-applied-force two-point correlation for flows involving moderate[a] temperature fluctuations where one needs the two-point correlation associated with the fluctuations of the term:

$$\frac{T'}{T}\frac{D\mathbf{u}}{Dt} \simeq \frac{1}{\bar{T}}\left(\left(\frac{D}{Dt} + \nabla\bar{\mathbf{u}}\cdot\right)\left(T'\mathbf{u}'\right) + \left(\mathbf{u}'\otimes\mathbf{u}'\right)\cdot\nabla\bar{T}\right)$$

An important source of additional information would here be given by the two-point statistics of the term $T'\mathbf{u}'$; a similar approach as in Appendix D could be used to scale the terms involving time derivatives of $T'\mathbf{u}'$. Not considering the cross-term covariance functions, this would leave a single statistical function to be modelled by means of a closure hypothesis: the two-point covariance of $\nabla\left(T'\mathbf{u}'\right)\cdot\mathbf{u}$.

Note that the model is based entirely on turbulent-jet experimental data taken at a single location (the end of the potential core, on the nozzle-lip line) in one isothermal single-stream round jet. The source modelling for the aerodynamic sound theory developed in this work is to date very approximate, but the methodology can be used to derive a better model once more data become available. The availability of a solid experimental data base to use as a basis for modelling the two-point correlation of the fluctuating Reynolds-stress field in turbulent jets would greatly improve the source model. The generality and universality of two-point correlation-coefficient models such as (4.16) need to be experimentally assessed for different turbulent jets and at various spatial locations.

[a]For flows including temperature fluctuations of the same order as the local time-averaged static temperature, one requires the evaluation of the two-point correlation associated with the fluctuations of the term:

$$\frac{T'}{T}\frac{D\mathbf{u}}{Dt} \simeq \frac{1}{T}\left(\left(\frac{D}{Dt} + \nabla\bar{\mathbf{u}}\cdot\right)\left(T'\mathbf{u}'\right) + \left(\mathbf{u}'\otimes\mathbf{u}'\right)\cdot\nabla\bar{T}\right)$$

Here we only assumed convective static-temperature fluctuations.

Chapter 5

Application to jet-noise prediction

The aerodynamic-noise theory developed in Chapters 3 and 4 is applied in this chapter to the prediction of jet noise. A solver for the compressible Reynolds-averaged Navier–Stokes equations (RANS) is used to generate fields for the Favre-averaged flow variables, including components of the unit-density Reynolds stress. A description of the RANS solution and the corresponding output variables is given in section 5.1. The RANS solution is used to model the two-point Reynolds-stress statistics. The relations connecting the RANS solution at a given space location to the statistical quantities required by the acoustic model are described in section 5.2. These connection relations involve a set of adjustable parameters. The set of parameters is constant for a given RANS-solution strategy; it needs to be determined via a calibration procedure which is described in section 5.3. The 90-degree 1/3-octave spectral predictions associated with the low-frequency (3.23) and the high-frequency (3.16) solutions are broken down into the corresponding applied-stress (quadrupole) and applied-force (dipole) contributions. The four spectral contributions are compared to model-scale noise measurements on heated and unheated jets in section 5.4.

5.1 Estimation of the flow statistics for a turbulent jet

The solution of the Reynolds-averaged Navier–Stokes (RANS) equations offers an easy-access estimation of the turbulent-jet flow statistics. In this work a commercial solver[a] has been used to provide a Reynolds-transport-closure compressible-flow RANS solution. The RANS-solution strategy is detailed in Appendix F where the RANS solution for a coaxial jet is described as an example. We restrict attention to jet flows with axisymmetric boundary conditions; axisymmetry of Favre averages has therefore been imposed on the RANS solution. The Reynolds-stress closure model (RSM) allows for representing anisotropies in the turbulence

[a]Fluent (version 6.2) has been used by adopting a Reynolds-stress model for the closure of the RANS equations. The meshes have been designed by using the commercial software MSC/PATRAN and specifically implemented computer routines (FORTRAN 77) for designing the mesh pattern in the near-wall region and in those regions where the mesh size changes rapidly.

field. The Favre averages of the unit-density Reynolds-stress components[b] appear among the variables of the compressible RSM RANS equation system; they are therefore output as part of the solver solution. The set of Favre-averaged flow variables that are output by the solver and used by the acoustic model is listed as follows:

- Velocity vector $\langle \mathbf{u} \rangle_\rho$
- Static temperature $\langle T \rangle_\rho$
- Unit-density Reynolds stress $\langle \mathbf{u}' \otimes \mathbf{u}' \rangle_\rho$
- Turbulence-dissipation rate $\langle \epsilon \rangle_\rho$

Here the Favre average is denoted by $\langle\ \rangle_\rho$. As explained in Appendix F, these flow variables are evaluated along radial profiles starting from the symmetry axis in the RANS-solution computational domain.[c]

5.2 Connection between the RANS solution and the acoustic model

The determination of the acoustic-model input (space distribution of flow statistics) needs to be performed on the basis of the RANS-solver output; the base-flow quantities and the volumetric source strength need therefore to be expressed as a function of the Favre-averaged RANS variables defined in section 5.1. Determining the volumetric source strength (4.37) and (4.38) requires the spatial distributions associated with $\bar{q}_{ij,kl}(\mathbf{y})$, $\tilde{l}_i(\mathbf{y}, f)$, $\tilde{\alpha}(\mathbf{x}, \mathbf{y}, f)$, $\hat{\mathrm{s}}_0(\mathbf{y}, \mathbf{0}, f)$, $\nabla \bar{T}(\mathbf{y})$. Note that $\tilde{\alpha}$, see equation (4.34), requires the definition of the source-convection parameter U_c and the appropriate speed of sound and source–observer radiation direction. The latter are given by c_∞ and $\hat{\mathbf{r}}$ for the high-frequency solution (3.23); they are $\bar{c}$ and $\hat{\mathbf{r}}_E$ for the high-frequency solution (3.16). The Green-function parameters are expressed in terms of the mean-velocity field $\bar{\mathbf{u}}(\mathbf{y})$ and the speed of sound $\bar{c}(\mathbf{y})$. The parameters are the Doppler factor $D_{-\bar{u}}$ and emission-time source–observer vector $\mathbf{r}_E$ for solution (3.16); they are the flow-factor components for solution (3.23). We identify the time-averaged velocity and speed of sound with the corresponding Favre averages output by the RANS solver:

$$\bar{\mathbf{u}} = \langle \mathbf{u} \rangle_\rho \qquad \bar{c} = \sqrt{\gamma R \langle T \rangle_\rho} \tag{5.1}$$

[b] In the axisymmetric case the non-zero Favre-averaged components of the unit-density Reynolds stress are $\langle u_1' u_1' \rangle_\rho$, $\langle u_2' u_2' \rangle_\rho$, $\langle u_3' u_3' \rangle_\rho$ and $\langle u_1' u_2' \rangle_\rho$.

[c] This spatial distribution of acoustic-processor sampling points has been chosen in order to simplify the numerical space integration of the acoustic-source volumetric strength. Note that this fact has the drawback of imposing an intermediate step between the RANS solution and the acoustic processing: the RANS solution needs to be interpolated to gather the solution on the acoustic-processor sampling points. The sampling points are chosen in a way that allows for spatially resolving the high-Reynolds-stress region in the flow; the part of the computational domain outside the jet flow is not considered in the acoustic computation.

As explained in Appendix G, assuming that the two-point correlation coefficient is expressed by model (4.19) implies that the frequency-dependent terms $\hat{\mathrm{s}}_0(\mathbf{y},\mathbf{0},f)$ and $\tilde{l}_i(\mathbf{y},f)$ collapse on corresponding characteristic spectra, if expressed as function of the Strouhal number $Sr_\tau = f\tau_d$ and scaled as in equations (G.4) and (G.6). The time scale τ_d is therefore a key parameter to be expressed in terms of the RANS solution; we assume that the time scale is proportional to the ratio between the Favre-averaged turbulent kinetic energy k and turbulent dissipation rate ϵ.

$$\tau_d(\mathbf{y}) = c_\tau \left\langle k \right\rangle_\rho / \left\langle \epsilon \right\rangle_\rho \tag{5.2}$$

Expression (5.2) corresponds to similar expressions introduced in previous hybrid RANS–acoustics models, e. g. Ref. [21], to model the acoustic-source time scale; the different physical meanings of the time scales are to be noted.[a] The connection relation (5.2) defines a spatial variation for the Strouhal number $Sr_\tau = Sr_\tau(\mathbf{y})$ at a fixed frequency; we refer to Sr_τ as the local Strouhal number.

The characteristic spectra $\mathrm{f}_A(Sr_\tau)$ and $\mathrm{f}_L(Sr_\tau)$ associated with $\hat{\mathrm{s}}_0(\mathbf{y},\mathbf{0},f)$ and $\tilde{l}_i(\mathbf{y},f)$ are found as follows:

1. The acoustic-source two-point correlation coefficient at the Harper-Bourne[4] measurement location is estimated from (4.19), based on the values $\tau_d^{(m)}$ and $l_i^{(m)}$ that best fit the Harper-Bourne[4] measurements.

2. A numerical Fourier transform is applied and the result is scaled according to equations (G.4) and (G.6).

The evaluation of the length-scale function $\mathrm{f}_L(Sr_\tau)$ is performed at different values of the parameter a_l; this allows for setting different high-frequency decay trends to the frequency-dependent length scales $\tilde{l}_i(\mathbf{y},f)$.[b] The zero-separation scaled two-point CPSD (see table on p. 139) is expressed at an arbitrary position in the jet by using the local value of τ_d (5.2) as follows:

$$\hat{\mathrm{s}}_0(\mathbf{y},\mathbf{0},f) = \frac{\tau_d(\mathbf{y})}{\tau_d^{(m)}} \hat{\mathrm{s}}_0\Big(\mathbf{y}^{(m)},\mathbf{0},f\tau_d^{(m)}\Big) \tag{5.3}$$

Here we indicate with $\hat{\mathrm{s}}_0(\mathbf{y},\mathbf{0},f)$ and $\hat{\mathrm{s}}_0(\mathbf{y},\mathbf{0},Sr_\tau)$ spectral densities with respect the frequency f and the local Strouhal number Sr_τ, respectively. Note that $\hat{\mathrm{s}}_0\Big(\mathbf{y}^{(m)},\mathbf{0},f\tau_d^{(m)}\Big)/\tau_d^{(m)}$ is the characteristic spectrum function f_A introduced in (G.4). A similar procedure is followed to estimate the local value of the $1/e$-decay lengths of the normalised two-point CPSD $\sigma_0(\mathbf{y},\boldsymbol{\eta},f)$.

[a] In the cited example, Morris and Farassat[21] use a connection relation like (5.2) to define a time-scale in a "moving-axis" correlation-coefficient model. In the present thesis a similar relation is used to define the fixed-frame autocorrelation-coefficient time scale.

[b] Recall that the Harper-Bourne experimental data are insufficient to establish a high-frequency decay which is valid for both the axial and the tranverse separations. The model we use here adopts an isotropic-decay model, where the high-frequency trend for the characteristic function $\tilde{l}_i\left(\mathbf{y}^{(m)},Sr_\tau\right)$ is determined by the parameter a_l. Pending the availability of a more complete set of measurements, we study the effect on the acoustic predictions of the high-frequency roll-off in the modelled $1/e$-decay lengths.

The corresponding connection relation is given as follows:

$$\tilde{l}_i\left(\mathbf{y}, f\right) = \frac{l_i\left(\mathbf{y}\right)}{l_i^{(m)}} \tilde{l}_i\left(\mathbf{y}^{(m)}, f\tau_d^{(m)}\right) \qquad \text{(no summation)} \tag{5.4}$$

The length scale $l_i\left(\mathbf{y}\right)$ needs to be defined in equation (5.4); it is assumed to depend on the local value of the RANS output as

$$l_i\left(\mathbf{y}\right) = c_{L_g}\left(\sqrt{\left\langle k\right\rangle_\rho^3} / \left\langle \epsilon\right\rangle_\rho\right)\left(3\left\langle (u_i')^2\right\rangle_\rho / 2\left\langle k\right\rangle_\rho\right)^{c_{L_e}} \tag{5.5}$$

where the usual k-ϵ length scale $\left(\sqrt{\left\langle k\right\rangle_\rho^3} / \left\langle \epsilon\right\rangle_\rho\right)$, as defined in previous RANS–acoustic-analogy papers (e. g. Ref. [21]), is modified by adopting an anisotropy factor. If the turbulence were isotropic, the averaged Reynolds-stress component $\left\langle (u_i')^2\right\rangle_\rho$ would equal $2\left\langle k\right\rangle_\rho/3$. The ratio of these quantities, raised to the power c_{L_e}, is used as an anisotropy factor in (5.5).[c] This assumption associates a larger length scale with a given direction if the mean square of the fluctuating velocity in that direction is larger than those in the other directions. Note that the ratio $\tilde{l}_i\left(\mathbf{y}^{(m)}, f\tau_d^{(m)}\right)/l_i^{(m)}$, in equation (5.4), is the local-Strouhal characteristic spectrum function f_L, as defined in equation (G.6).

A further frequency-dependent parameter to be defined is $\tilde{\alpha}$. Expression (4.34) gives an explicit frequency dependence for $\tilde{\alpha}$ once the frequency-independent flow parameters U_c and c are determined. The parameter U_c represents the average convection velocity to be associated with the acoustic-source two-point correlation at a given location; we assume that this quantity is proportional to the modulus of the Favre-averaged velocity.

$$U_c\left(\mathbf{y}\right) = c_U\left\langle u\right\rangle_\rho\left(\mathbf{y}\right) \tag{5.6}$$

Note that the U_c convection-velocity parameter is in principle different from the mean velocity, and the radial profiles of U_c can be expected not to be similar to the mean-velocity profiles.[d] However, pending the availability of experimental data across the shear layer for the unit-density Reynolds stress correlation, we propose expression (5.6) as a closure relation.

The value of the speed of sound is set according to equation (5.1) for the high-frequency

[c] Note that this ratio is known, since we are using an RMS-closure RANS solver that provides estimates for individual components of the Reynolds-stress tensor. If two-equation RANS systems are used to provide the input, this ratio will not be locally available. In that case a further parameter needs to be included in order to account for directionality.

[d] Although no measurements are available across the shear layer for the unit-density-Reynolds-stress two-point covariance, in the case of the fluctuating velocity, the phase speed (convection velocity) associated with the two-point correlation measurements presents radial profiles that are different from the time-averaged-velocity profiles. The fluctuating-velocity two-point correlation measurements performed by Lau[53] (also in Fig. 27 of Lau and Fisher,[54] profile corresponding to the velocity fluctuations) showed a convection-velocity radial distribution having a shape across the shear layer that is like a sin function between 0 and 2π. The convection velocity is constant in the potential core and outside the jet, having a value that is close to the nozzle-lip-line value. This picture is consistent with the overlapping of a perturbation field moving at a speed which is close to the lip-line speed and a perturbation field that moves at the local mean velocity.

solution; it is set as the ambient speed of sound $c = c_\infty$ for the low-frequency model.[e] Note that the spectral characteristics associated with the volumetric acoustic-source strength are now assigned in terms of the empirical parameters c_τ, c_{L_g}, c_{L_e}, and c_U. These parameters, for a given two-point correlation coefficient model (4.19), determine the local time scale τ_d together with the $1/e$-decay length scales and phase-shift parameter of the normalised CPSD $\sigma_0(\mathbf{y}, \boldsymbol{\eta}, f)$. The parameter a_l in model (4.19) will influence the source-strength spectrum by varying the decay of the frequency-dependent length scales $\tilde{l}_i$ and, consequently, of $\tilde{\alpha}$ and $\mathrm{C_f}(\tilde{\alpha})$.

The remaining source-strength factors in expressions (4.37) and (4.38) are frequency independent. The Favre-averaged static-temperature field is used to define the static-temperature terms $\nabla\bar{T}$ and $\bar{T}$ in the applied-force source-strength expression (4.12). The time averaged product of two unit-density Reynolds-stress fluctuating components is assumed to be proportional to the product of corresponding Favre-averaged Reynolds-stress components. Zero correlation is assumed between different components of the Reynolds stress to give

$$\bar{q}_{ij,kl}(\mathbf{y}) = \overline{\left(u_i'u_j' - \overline{u_i'u_j'}\right)\left(u_k'u_l' - \overline{u_k'u_l'}\right)} = c_Q \left\langle u_i'u_k' \right\rangle_\rho \left\langle u_j'u_l' \right\rangle_\rho \delta_{ik}\delta_{jl} \quad \text{(no summation)} \quad (5.7)$$

Note that here we use all possible cross products of the principal Reynolds-stress components $\left\langle (u_i')^2 \right\rangle_\rho$ to scale the 6 non-null different components of the fluctuating-Reynolds-stress mean product tensor. Expression (5.7) implies a constant ratio between the mean squared Reynolds-stress fluctuations $\bar{q}_{ij,ij} = \left(S_{ij}'\right)^2$ and the product of the mean Reynolds-stress components $\bar{S}_{ii}\bar{S}_{jj}$.[f]

Expression (5.7) is used with the static-temperature gradient $\nabla\bar{T}$ in expression (4.23) to determine the factor $\Delta_{i,j}$ in the applied-force volumetric source strength. The radial component of the temperature gradient is assumed to dominate the gradient direction to give

$$\Delta_{i,j}(\mathbf{y}) = c_Q \left\langle (u_2')^2 \right\rangle_\rho \left\langle u_i'u_j' \right\rangle_\rho \delta_{ij} \quad \text{(no summation)} \quad (5.8)$$

It is important to note that the connection relations described in this section need to be tested against experimental/DNS data and possibly redefined. A set of empirical relations linking the Reynolds-stress two-point covariance with the local time-stationary statistics such as mean velocity, turbulence intensity, turbulence-dissipation rate, etc. is a key element of the present model. Here we are providing an initial guess, following the lead of previous hybrid jet-noise predictions such as Ref. [21], but using the Harper-Bourne[4] measurements as a constraint, and

[e] We stress that the radiation parameters $\hat{\mathbf{r}}$ and c must be chosen depending on the asymptotic radiation model in use. The source–observer direction $\hat{\mathbf{r}}$ and the ambient speed of sound c_∞ are to be used for the low-frequency model whilst the source–observer emission-time direction $\hat{\mathbf{r}}_E$ and the local speed of sound $\bar{c}$ need to be used for the high-frequency model.

[f] As an example, we give in explicit form the terms $\bar{q}_{11,11}$ and $\bar{q}_{13,13}$:

$$\bar{q}_{11,11} = c_Q \left\langle u_1'u_1' \right\rangle_\rho^2 \qquad \bar{q}_{13,13} = c_Q \left\langle u_1'u_1' \right\rangle_\rho \left\langle u_3'u_3' \right\rangle_\rho$$

including the applied-force equivalent source needed for hot jets.

5.3 Calibration of the jet-noise model

As pointed out in section 5.2, the jet-noise model is connected to the RANS solution by means of a number of dimensionless scaling parameters. The scaling parameters are listed as follows:

$$c_Q,\ \kappa_{\mathbf{d}},\ c_\tau,\ c_{L_g},\ c_{L_e},\ c_U$$

The parameters are respectively introduced in equations (5.7), (4.12), (5.2), (5.5), and (5.6). This section details the method adopted to define the values of these scaling parameters.

The philosophy behind the use of the RANS solution for the jet is to assume a one-to-one correspondence between RANS-solution and experimental quantities at corresponding spatial locations in the axial section of a single-stream jet. The corresponding spatial locations are defined in terms of potential-core lengths in the axial direction and in jet diameters in the radial direction. This establishes a similarity between the RANS-solution field and a corresponding ideal experimental field.

The parameters associated with the model of the Reynolds-stress two-point correlation (c_τ, c_{L_g}, c_{L_e} and c_U) are chosen by matching the model prediction to available Reynolds-stress measurements, Ref [4], as described in chapter 4, and taking into account the jet-stretching associated with the present RANS solution. The remaining parameters ($c_Q,\ \kappa_{\mathbf{d}}$) are set by matching the 1/3-octave spectra associated with the jet-noise-model low-frequency (3.23) and high-frequency (3.16) components to existing far-field measurements. In choosing c_Q and $\kappa_{\mathbf{d}}$ we also evaluate the effect on the noise-model components of varying the correlation-coefficient parameter a_l.

5.3.1 Matching the model prediction to available velocimetry data

A RANS solution has been generated for a round jet whose nozzle-exit velocity and diameter are the same as in the Harper-Bourne[4,5] measurements. The RANS-solution velocity-magnitude (a) and turbulence-intensity (b) radial profiles are shown in Fig. 5.1 for the Harper-Bourne jet.[a] The RANS variables at the measurement location (nozzle lip line, 4 diameters downstream of the nozzle) have been used to generate the turbulence-statistics quantities $\hat{\mathrm{s}}_0(\mathbf{y},\mathbf{0},f)$, $\tilde{l}_i\,(\mathbf{y},\mathbf{0},f)$ and $U_c\,(\mathbf{y})$ as described in section 5.2. A matching of these quantities to the corresponding measurements fixes $c_\tau,\ c_{L_g},\ c_{L_e}$ and c_U. While c_{L_e} has been set to main-

[a]The RANS-solution nozzle is a conical nozzle and a radial component of the velocity is still present at the nozzle-exit section (near-wall region). The jet is under-expanded at the nozzle exit; this implies that the expansion and acceleration continue outside the nozzle. The assigned target conditions for the axial velocity (isentropic 1-D laminar flow) are met downstream of the nozzle exit, where smallness of the radial-velocity component means that the velocity magnitude and the axial velocity are nearly coincident.

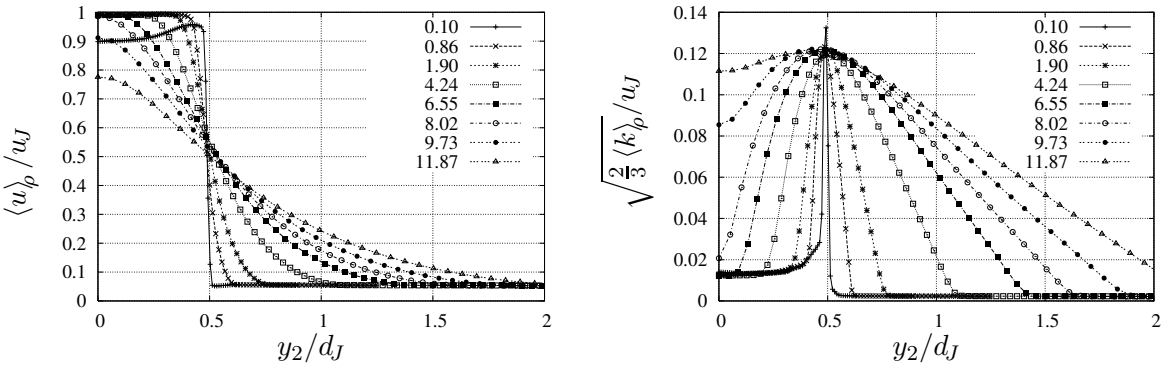

(a) Velocity modulus

(b) Turbulence intensity

Figure 5.1: RANS solution for a single-stream air jet with the same nozzle-exit diameter and centre-line velocity as in the Harper-Bourne measurements ($M_J \simeq 0.18$, $T_J/T_\infty \simeq 1$). Radial profiles are shown for the Favre-averaged velocity and turbulence intensity. The radial position is normalised by the jet nozzle-exit diameter $d_J = 50.8$ mm. The normalisation velocity is the target (isentropic, laminar and perfectly-expanded flow) nozzle-exit jet velocity $u_J = 61$ m/s. The labels indicate the axial coordinate y_1 in jet diameters d_J.

tain the ratio between $\tilde{l}_1$ and $\tilde{l}_\perp$ as in the Harper-Bourne low-frequency measurements,[b] the choice of the parameters c_τ, c_{L_g} and c_U has been made accounting for the jet axial stretching associated with the RANS solution. This is explained in more detail in the next paragraph.

As can be seen in Fig. 5.1 and Fig. 5.2 (a), the potential-core length associated with the RANS solution is close to 8 d_J. Experimental data for low-Mach number turbulent jets with density equal to ambient indicate a potential-core length in the range going from 4 d_J (as reported in Ref. [24]) to 5 d_J (as indicated in Ref. [55]); we assume that the Harper-Bourne[4] measurement location $\mathbf{y}^{(m)} = 4d_J\hat{\boldsymbol{\gamma}}_1 + 0.5d_J\hat{\boldsymbol{\gamma}}_2$ is at the end of the potential core. The axial stretching of the RANS solution,[c] yields a predicted shear-layer thickness which is smaller than the corresponding experimental measurement at the same axial coordinate. The axial variation along the nozzle lip line associated with the variables τ_d and l_i, given by the respective connection relations (5.2) and (5.5), is reported in Fig. 5.2. The trends in Fig. 5.2 suggest a linear growth of these time and length scales in the axial region between the nozzle exit and the end of the potential core. Assuming a similarity with the shear-layer width, we expect the values for the RANS-solution τ_d and l_i to be lower than the corresponding experimental data

[b] The $\tilde{l}_1/\tilde{l}_\perp$ ratio is not frequency independent for the Harper-Bourne measurements. The ratio varies between a value of about 10 at the lowest frequency to a value around 4 at the highest frequencies. Here a value of 10 has been set in order to maintain the ratio shown by the Harper-Bourne data at the lowest frequencies. Note that a more extensive set of measurements (preferably made by adopting less invasive probing, such as laser anemometry) is needed to properly assess the frequency dependence and the range of values of this ratio. We underline that the present jet-noise model assumes a frequency-independent value for the ratio.

[c] Reconsidering the set of empirical parameters associated with the RANS-closure equations could give a RANS solution characterised by an axial evolution that is more rapid and closer to the experimental evidence. In order to simplify the RANS-solution strategy and to have consistency between the various cases reported in this thesis, the default values, assigned to the RANS-closure parameters by the commercial solver, are used in this thesis.

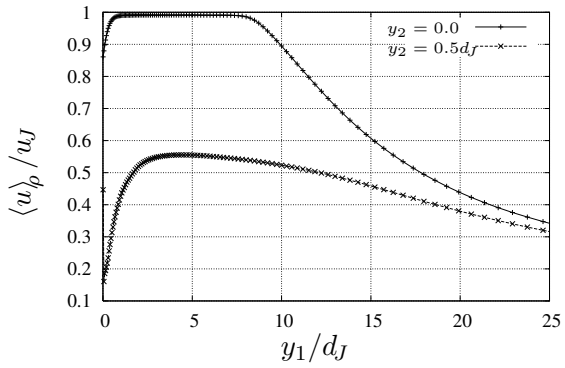

(a) Favre-averaged velocity on the jet axis and on the nozzle-lip line.

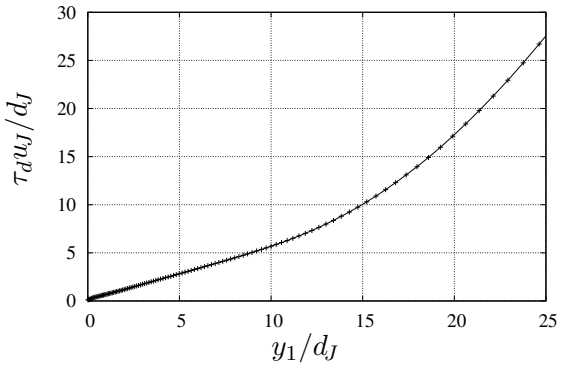

(b) Normalised time scale τ_d, equation (5.2) with $c_\tau = 1$, on the nozzle-lip line.

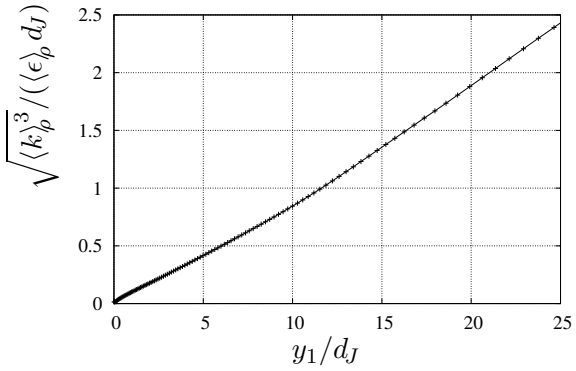

(c) Isotropic k-ϵ length scale on the nozzle-lip line.

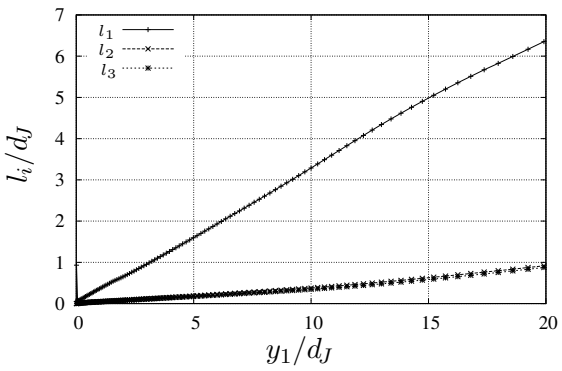

(d) Normalised length scales l_i, equation (5.5) with $c_{L_g} = 1$ and $c_{L_e} = 5$, on the nozzle-lip line.

Figure 5.2: RANS solution for single-stream jet at the Harper-Bourne conditions, as in Fig. 5.1. Variation of $\bar{u}$, τ_d, k-ϵ length scale and l_i along lines parallel to the jet axis. The lengths are normalised by the jet nozzle-exit diameter $d_J = 50.8$ mm. The normalisation velocity is the target (isentropic laminar perfectly-expanded flow) nozzle-exit jet velocity $u_J = 61$ m/s.

at the same lip-line location y_1/d_J. Given the factor two between the experimental and the RANS-solution potential-core lengths we assume that the values of τ_d and l_i, to be associated with the RANS solution at the Harper-Bourne measurement location, are approximately half those in the corresponding Harper-Bourne measurements.

$$\tau_d \left(\mathbf{y}^{(m)} \right) \simeq 0.5 \tau_d^{(m)} \qquad l_i \left(\mathbf{y}^{(m)} \right) \simeq 0.5 l_i^{(m)} \tag{5.9}$$

Note that relations (5.9) and the linear growth of the RANS-solution lip-line $\tau_d(\mathbf{y})$ and $l_i(\mathbf{y})$ in the initial region the jet (Fig. 5.2) imply that the RANS solution is anchored to the Harper-Bourne measurements at the end of the respective potential cores.

For the ratio c_U between U_c and $\bar{u}$ we assume the same value as in the Harper-Bourne

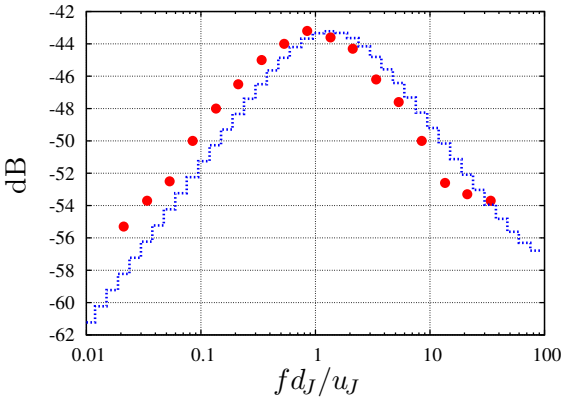

(a) The dotted line shows the normalised 1/3-octave autospectrum associated with model (4.19) at the location $\mathbf{y}^{(m)}$ in the RANS-solution domain. Points, •, show the corresponding Harper-Bourne measurement at the same location $\mathbf{y}^{(m)}$. Note that varying a_l does not change the modelled autospectrum.

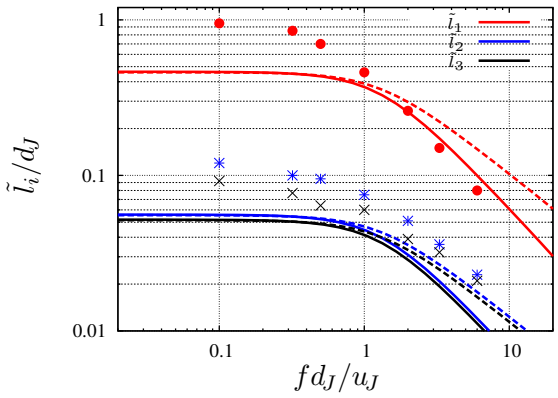

(b) The lines show the modelled $1/e$-decay length scales at the location $\mathbf{y}^{(m)}$ in the RANS-solution domain. Continuous and dashed lines respectively denote model (4.19) with $a_l = 2.0$ and $a_l = 2.7$. Points •, ✳ and × show the corresponding Harper-Bourne measurements at the same location $\mathbf{y}^{(m)}$.

Figure 5.3: Assignment of spectrum and length-scale parameters to the isothermal-jet RANS simulation of Figs. 5.1 and 5.2. The location $\mathbf{y}^{(m)}$ is the same as in the measurements of Harper-Bourne.[4] The figure shows the frequency-domain behaviour of model (4.19) assuming $\tau_d(\mathbf{y}^{(m)}) = 0.5\tau_d^{(m)}$ and $l_i(\mathbf{y}^{(m)}) = 0.5l_i^{(m)}$, where $\tau_d^{(m)}$ and $l_i^{(m)}$ are the best-match values used in model (4.19) as in Fig. 4.5. The Harper-Bourne measurements and the corresponding modelled quantities are shown as a function of the jet Strouhal number.

measurement, to give $c_U = 1.23$; this choice is justified by the nearly constant value of the RANS-solution lip-line velocity between the axial position $4d_J$ and the end of the potential core, as shown in Fig. 5.2 (a). The model prediction for the autospectrum at the location $\mathbf{y}^{(m)}$ is indicated in Fig. 5.3 (a). This corresponds to the fluctuating-Reynolds-stress spectrum obtained by applying a Fourier transform to the correlation coefficient (4.19), with $\eta = 0$, and by scaling (see Fig. 4.5). The modelled $1/e$-decay length scales $\tilde{l}_i$ are reported in Fig. 5.3 (b). Note that reducing τ_d and l_i from the value that gives the best fit to the Harper-Bourne measurements (the best-fit values are used for the model prediction in Fig. 4.5) causes a displacement of the normalised autospectrum and the length scales $\tilde{l}_i$ from the corresponding measurements. As shown in Fig. 5.3 (a), we assign higher frequencies to the modelled 1/3-octave spectrum (the reference model is shown in Fig. 4.5). The $1/e$-decay length scales associated with the modulus of the normalised two-point PSD are modelled as being scaled down and moved to higher frequencies from the corresponding measurement, as shown in Fig. 5.3 (b).

Note that, by reducing the time and length scales associated with the RANS solution at the measurement location $\mathbf{y}^{(m)}$, we are trying to impose similarity between the RANS solution and an idealised physical statistical field that is consistent with experimental observations, Ref. [55, 24], regarding the potential-core length. We are also assuming that the Harper-Bourne[4,5] measurements are part of this idealised physical statistical field. As mentioned in section

5.2, an experimental jet-flow data base, including an accurate description of the boundary conditions and Reynolds-stress single-point and two-point statistics at various locations in a turbulent jet, is needed to accurately define the spatial evolution of quantities such as τ_d and l_i. The availability of such data base is seen as a necessary step in order to

- Better set the RANS-solver closure parameters in order to achieve RANS solutions in closer agreement with the turbulence single-point statistics.

- Validate the modelled spatial evolution of the Reynolds-stress two-point statistics.

The parameters fixed in this section determine the characteristic spectrum of the fluctuating Reynolds stresses as defined in (4.29). They also determine how the two-point CPSD varies with separation, with some uncertainty associated with the value of a_l. It is important to note that this spectral characterisation it is arrived at without using acoustic data, but just by trying to match two-point-correlation flow measurements.

5.3.2 Matching the model prediction to available acoustic data

The scaling parameters c_Q (quadrupole sources) and $\kappa_{\mathbf{d}}$ (dipole sources for non-isothermal jets) will be set in this section by matching the model prediction to available acoustic data. The parameter a_l of model (4.19) is varied across a set of prescribed values in order to assess the effect on the noise prediction. The acoustic data used in this step are single-stream 1/3-octave jet-noise spectra, Ref. [10], for which the nozzle profile and the nozzle-exit flow data are known.

The value c_Q is found by running a RANS solution for an isothermal[d] jet whose far-field 90-degree acoustic spectrum is known. The acoustic data, Ref. [10], have been provided by QinetiQ.[e] The nozzle-exit Mach number is 0.75 and the nozzle diameter is 86 mm. The model prediction is in this case dominated by the applied-stress component, since the mean-static-temperature gradient is very small in the high-turbulence region. The 1/3-octave spectra in

[d]Isothermal here means that the nozzle-exit mean static temperature is the same as the ambient (computational domain) temperature. This condition is an ideal condition that is not exactly satisfied by the RANS solution. Small static-temperature discrepancies due to the non-uniformity of the nozzle-exit velocity profile, the presence of a turbulent boundary layer, viscosity effects etc. are present in the RANS flow.

[e]The data are part of a set of single-stream jet-noise measurements provided by QinetiQ to the European-Community Jet-Noise consortium JEAN (Jet-Exhaust Aerodynamics and Noise). The data have been acquired in December 1983 at the QinetiQ Noise Test Facility (NTF) in Pyestock, Farnborough, United Kingdom. The data have been corrected for atmospheric attenuation; therefore the data ideally represent the free-field jet noise in a loss-less atmosphere. The data include far-field 1/3-octave spectra measured at a set of 10 locations spanning, in an evenly spaced array, the downstream-axis polar angles between 30 and 120 degrees. The measurement locations are at a distance greater than 10 m from the nozzle exit. The spectra are normalised to a constant distance of 6 m. Each data record includes the jet-aerodynamics and anechoic-chamber data (jet-exit velocity, diameter and temperature; stagnation pressure and temperature; ambient pressure and temperature) that are associated with the specific jet-noise measurement. The acoustic data have been used by Harper-Bourne;[56] they were published by Bryce.[57] The data and the related documentation, Ref. [10], are available for public free download at the web address
http://www.qinetiq.com/home/defence/defence_solutions/aerospace/acoustic_solutionsforstructures/ntf.html,
directing to the QinetiQ Internet pages.

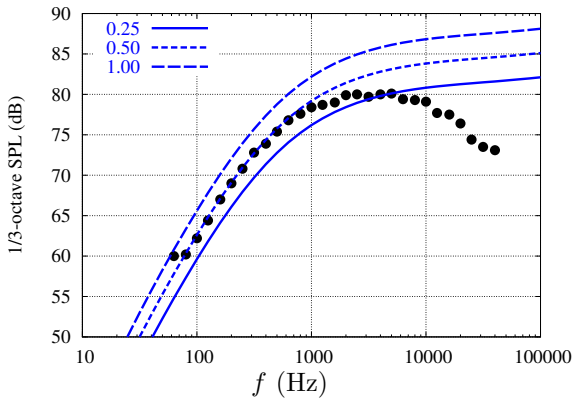

(a) Effect of varying c_Q (values as in the labels). The value of a_l is held fixed at $a_l = 2$

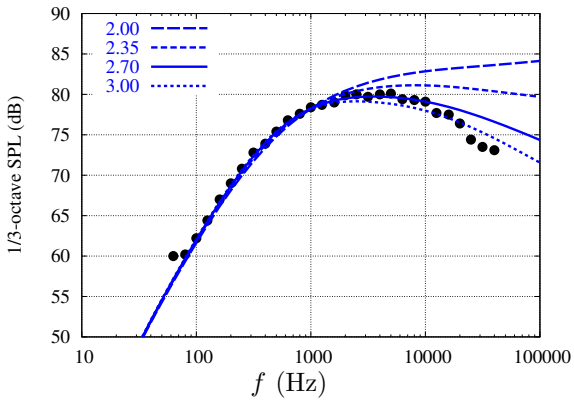

(b) Effect of varying a_l (values as in the labels) in model (4.19). The value of c_Q is held fixed at $c_Q = 0.4$

Figure 5.4: Modelled jet-noise 1/3-octave spectrum at 90-degree polar angle and corresponding measured data. The jet is isothermal; the nozzle-exit parameters are as follows: M_J=0.75, d_J=0.086 m, u_J=256 m/s. The curves denote the applied-stress component of the high-frequency solution (3.16) at varying model parameters. The solid circles indicate the corresponding jet-noise measurement, Ref [10].

Fig. 5.4 (a) show a comparison between the high-frequency model (3.16) and experimental data, for various values of the c_Q parameter.[f] The effect of the parameter a_l, associated with the space-separation decay in the two-point correlation coefficient (4.19), is shown in Fig. 5.4 (b). The value of the parameter a_l greatly affects the high-frequency trends of the modelled spectrum and has little effect on the power assigned by the model to the low-frequency 1/3-octave bands. The parameter c_Q is then defined by matching the low-frequency spectral contribution of the model prediction to the corresponding measurement. This yields the result $c_Q = 0.4$.

The parameter $\kappa_{\mathbf{d}}$ contributes as a scaling factor to the applied-force contributions associated with the high-frequency (3.16) and the low-frequency (3.23) models. The optimal value of $\kappa_{\mathbf{d}}$ is found by running a RANS solution for a heated low-Mach-number jet whose far-field 90-degree acoustic spectrum is known. As indicated by Morfey[58] and confirmed in Morfey, Szewczyk and Tester,[41] in this case, at sufficiently high nozzle-exit static temperatures, the applied-force noise contribution will dominate the 90-degree spectrum. A jet issuing from the QinetiQ single-stream nozzle at acoustic Mach number[g] 0.5 and at a jet–ambient static-temperature ratio 2.5 has been used in this case. The comparison between measured data, Ref. [10], and model prediction with varying $\kappa_{\mathbf{d}}$ is given in Fig. 5.5 (a) and (b), where the applied-stress and applied-force components are reported for the low-frequency (3.23) and the high-frequency (3.16) model components, respectively. Note that the low-frequency asymptotic

[f]The low-frequency solution (3.23) and the high-frequency solution (3.16) generate the same 90-degree 1/3-octave spectrum in this case. At 90-degree polar angle in perfectly isothermal conditions the low-frequency solution and the high-frequency solution coincide. More generally at 90 degrees, for isothermal jets, there is a coincidence of solution for the Lilley analogy and the Lighthill analogy.[1]

[g]The Mach number based on the nozzle-exit velocity and the ambient speed of sound.

solution (3.23) dominates the prediction, Fig. 5.5 (c). As expected, the value of $\kappa_{\mathbf{d}}$ only affects the applied-force contribution where it acts as a scaling factor. The effect of the parameter a_l on the applied-force contribution is shown in Fig. 5.5 (d), where the dipole contributions associated with the low-frequency (3.23) and the high-frequency (3.16) solutions are calculated by adopting different values for a_l in the acoustic-source two-point correlation coefficient (4.19). Varying a_l does not have the marked effect on the applied-force-contribution spectral shape that is seen for the applied-stress contribution in Fig. 5.4 (b). Fig. 5.5 (b) shows that changing a_l from 2.0 to 3.0 has the effect of increasing the spectral peak value by about 1 dB and reducing the power in the low-frequency and high-frequency bands. We set the parameter $\kappa_{\mathbf{d}}$ to the value $\kappa_{\mathbf{d}} = 50$ ($\kappa_{\mathbf{d}} c_Q = 20$)[h] which, as shown in Fig. 5.5 (c), gives a reasonable match between model and measured data.

As shown in Fig. 5.4 (b) the parameter a_l has a significant effect on the applied-stress contributions to the 1/3-octave noise spectrum. The uncertainty regarding this parameter is related to the uncertain high-frequency roll-off associated with the $1/e$-decay length scales $\tilde{l}$ of the fluctuating-Reynolds-stress normalised two-point CPSD, as measured by Harper-Bourne.[4,5] As shown in Fig. 5.4 (b), changing the value of a_l from 2 to 3 reduces the applied-stress noise contribution and significantly changes its spectral shape by varying the high-frequency trend. Recall that, as shown in Fig. 5.3 (b), setting $a_l = 2$ yields a modelled high-frequency trend for $\tilde{l}$ which is close to the Harper-Bourne measurements for $\tilde{l}_1$, while setting $a_l = 2.7$ corresponds to a trend for $\tilde{l}$ close to the Harper-Bourne measurements for $\tilde{l}_\perp$. Pending the availability of a wide set of Reynolds-stress two-point measurements in turbulent jet flows, a convenient choice for the parameter is $a_l = 2.7$. This choice is convenient as, together with having the high-frequency roll off as in the measured $\tilde{l}_\perp$, it allows one to match important characteristics of the measured isothermal jet-noise spectrum:

- It correctly identifies the noise peak and the corresponding frequency.
- It minimises the error between the model components (3.23) and (3.16) and the acoustic measurements in the isothermal-jet case, at frequencies below 10 kHz.[i]

Having fixed a value for a_l, we stress that this is for the moment just a pragmatic choice: the best-match value for a_l is to come from two-point measurements of the Reynolds-stress covariance, once a high-frequency trend for the frequency-dependent length scales is identified for a large set of measurement conditions and locations. Only with this best-match value, possibly joined by a best-match value of parameter c in model (4.16), we will be able to correctly evaluate the high-frequency extrapolation of the modelled spectra for isothermal jets.

[h] The scaling factor for the applied-force component is given by $c_Q \kappa_{\mathbf{d}}$ as obtained by inserting (5.8) into (4.22).

[i] The atmospheric-absorption correction on the acoustic measurement, Ref. [10], is confined below 2 dB for the 1/3-octave bands below 10 kHz; it increases from 1.91 dB for the 1/3-octave band at 10 kHz to 10 dB for the band at 40 kHz. We consider this correction as a possible source of error in the measured 1/3-octave data.

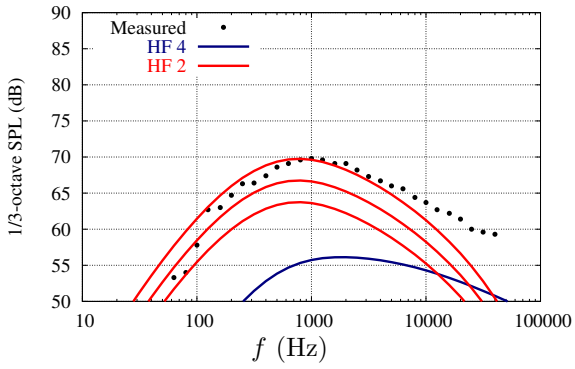

(a) Applied-stress (HF4) and applied-force (LF2) components for the high-frequency solution (3.16), at varying $\kappa_{\mathbf{d}}$ and constant a_l ($\kappa_{\mathbf{d}}$= 25, 50 and 100; a_l=2.7).

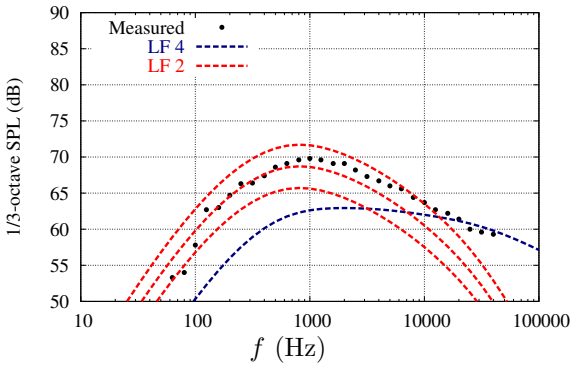

(b) Applied-stress (LF4) and applied-force (LF2) components for the low-frequency solution (3.16), at varying $\kappa_{\mathbf{d}}$ and constant a_l ($\kappa_{\mathbf{d}}$= 25, 50 and 100; a_l=2.7).

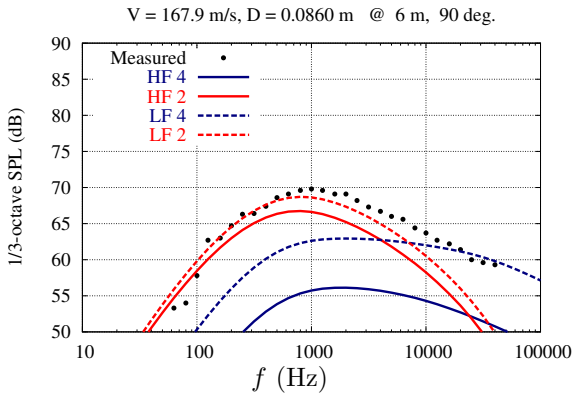

(c) Model components for $\kappa_{\mathbf{d}}$=50 and a_l=2.7. The labels are as in plots (a) and (b).

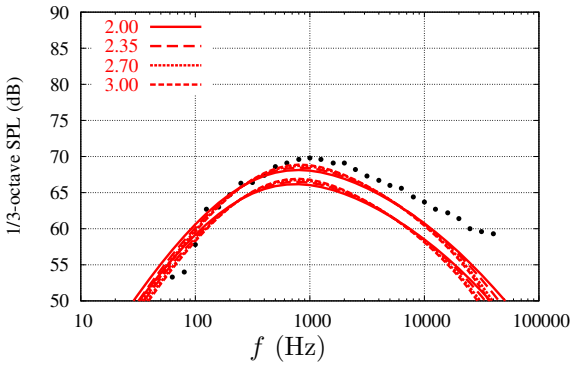

(d) Applied-force model components for the high-frequency (3.16) and low-frequency (3.16) solutions. The parameter $\kappa_{\mathbf{d}}$ is held constant ($\kappa_{\mathbf{d}}$=50), while a_l assumes different values (values as in the labels).

Figure 5.5: Effect of the parameters $\kappa_{\mathbf{d}}$ and a_l on modelled heated-jet 1/3-octave noise spectra. The nozzle-exit acoustic Mach number is 0.5, the jet/ambient temperature ratio T_J/T_∞ is 2.5. The measured data, Ref [10], are shown by the solid circles.

The large value of the scaling parameter $\kappa_{\mathbf{d}}$ indicates that the fluctuating applied-force two-point correlation function is weakly driven by the Reynolds-stress term $\mathbf{u}' \otimes \mathbf{u}' \cdot \nabla \bar{T}$; this fact adds emphasis on studying the correlations of the remaining terms forming the instantaneous applied-force strength (see section 4.1.1), in order to validate or better define expression (4.12) that assumes the two-point covariance function of the applied-force source as being proportional to the two-point covariance of $\mathbf{u}' \otimes \mathbf{u}' \cdot \nabla \bar{T}$.

5.4 Comparison between model components and acoustic measurements

The output of the jet-noise model is systematically compared in this section to corresponding far-field acoustic measurements. The model predictions are broken down to show the separate 1/3-octave spectral contributions due to the high-frequency (3.16) and to the low-frequency (3.23) approximations. Each spectral contribution is in turn broken down to show the dipole or quadrupole nature of the noise emission: the applied-stress (3.6) and the applied-force (3.8) source terms of the Lilley-Goldstein[3] equation are shown separately for each modelled spectrum. According to the flow-factor results in Tester and Morfey,[40] a good approximation of the Lilley-equation Green function can be obtained by simply adding the high-frequency and the low-frequency solutions. This possibility depends on the jet conditions and the observer polar angle.[a] It is important to underline the fact that an appropriate low-pass filter should eventually be applied to the low-frequency solution (3.23) and the opposite frequency filter should be used on the high-frequency solution. The filter should be used to ensure that the low-frequency approximation (3.23) is only used when the acoustic wavelength is much larger than the typical mean-flow spatial dimension in the radiation direction. Note that the implementation of this filter is not part of the present work. For jets with moderate variations of the Favre-averaged density field and at 90-degree polar angles, the far-field noise contributions (3.23) and (3.16) can each be considered as a jet-noise prediction. At the mentioned conditions there are no mean-flow effects on the radiation or on the modelled source strength; the predicted contributions (3.23) and (3.16) both agree with a Lighthill-analogy solution.

5.4.1 Isothermal single-stream jet noise

The 1/3-octave spectra at 90-degree polar angle are shown in Figures 5.6, 5.7 and 5.8 (a) for isothermal jets issuing from two different single-stream nozzles. The nozzles are the conical noz-

[a] An obvious contradiction to this rule is given by the 90-degree contributions for isothermal jets. In this case the high-frequency solution and the low-frequency solution both coincide with the Lilley-analogy solution. Simple addition of the asymptotic approximations would therefore mean a 3-dB overestimation of the Lilley-analogy 1/3-octave spectrum. Morfey, Tester and Powles[43] show other cases for which the addition between the low-frequency solution and the high-frequency solution does not produce a good fit for the numerically evaluated Lilley–Goldstein Green function.

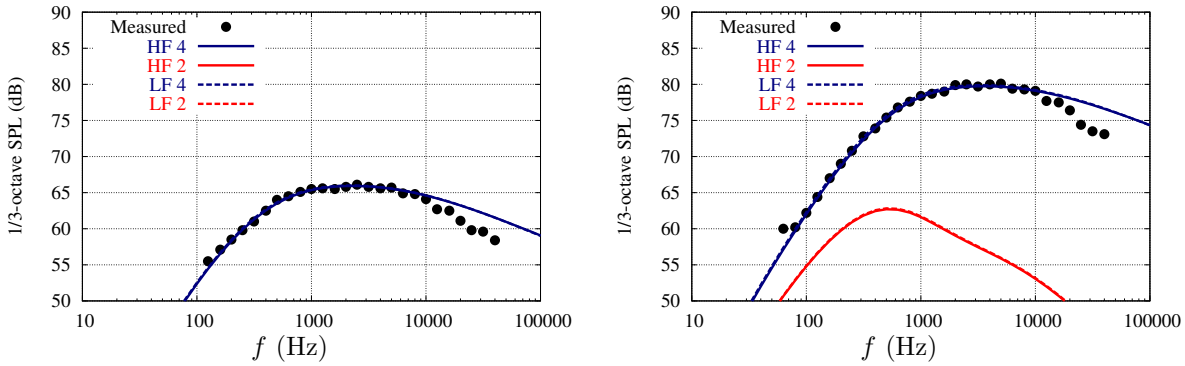

(a) $u_J = 166$ m/s, M_J=0.5

(b) $u_J = 253$ m/s, M_J=0.75

Figure 5.6: Isothermal jet-noise 1/3-octave spectra for jets issuing from the QinetiQ conical nozzle; nozzle-exit diameter $d_J = 0.086$ m. The measured data (QinetiQ, NTF Pyestock, United Kingdom), Ref. [10], were acquired at a distance grater than 10 m, corrected at high frequency for the atmospheric attenuation and normalised assuming a distance of 6 m; the model prediction is related to the normalisation distance. The high-frequency-solution (3.16) applied-stress and applied-force components are respectively labelled HF4 and HF2. The low-frequency-solution (3.23) components are correspondingly indicated by LF4 and LF2. The level associated with the applied-force source in (a) is below 50 dB.

zle already introduced in section 5.3 and the contoured nozzle[b] used in gathering the jet-noise acoustic data published by Tanna Dean and Burrin.[9] The conical-nozzle jet-noise 1/3-octave spectra are reported in Fig. 5.6 at two different nozzle-exit velocities. The measurements have been provided by QinetiQ, Ref. [10]. Note that the acoustic spectrum in Fig. 5.6 (b) has been used in the model calibration. As mentioned in section 5.3, the high-frequency approximation (3.16) and the low-frequency approximation (3.23) yield the same spectral contributions. The predicted quadrupole-contribution spectral shapes are similar to the measured ones in the low-frequency range; the model over-predicts the corresponding measurement for the frequency bands above 10 kHz. The peak frequency and the SPL variation due to the change in velocity from M_J=0.5 (a) to M_J=0.75 (b) are correctly predicted by the model quadrupole contributions. The isothermal jet-noise data from the set of measurements published by Tanna Dean and Burrin[9] are shown with the corresponding model prediction in Fig. 5.7 and in Fig. 5.8 (a). Also in this case, for varying nozzle-exit Mach number, the model-component quadrupole spectra show the same frequency and SPL scaling as the measurements. As shown in Fig. H.1 (b) in Appendix H, where the Tanna[9] measurements are shown normalised by applying Lighthill–Strouhal scaling (H.1), the data in Ref. [9] do not exactly scale according to the Lighthill[1] law. The data show a peak-level scattering of 2.5 dB; this indicates possible contamination due to noise sources different from turbulent mixing. This fact is also in agreement with the difference between model and measurements which, as shown in Fig. 5.7,

[b]The geometry of the nozzle is not specified in Ref. [9]. Technical drawings of the nozzle geometry have been kindly provided by Professor K. K. Ahuja. These drawings have been used to define the RANS-solution boundary conditions.

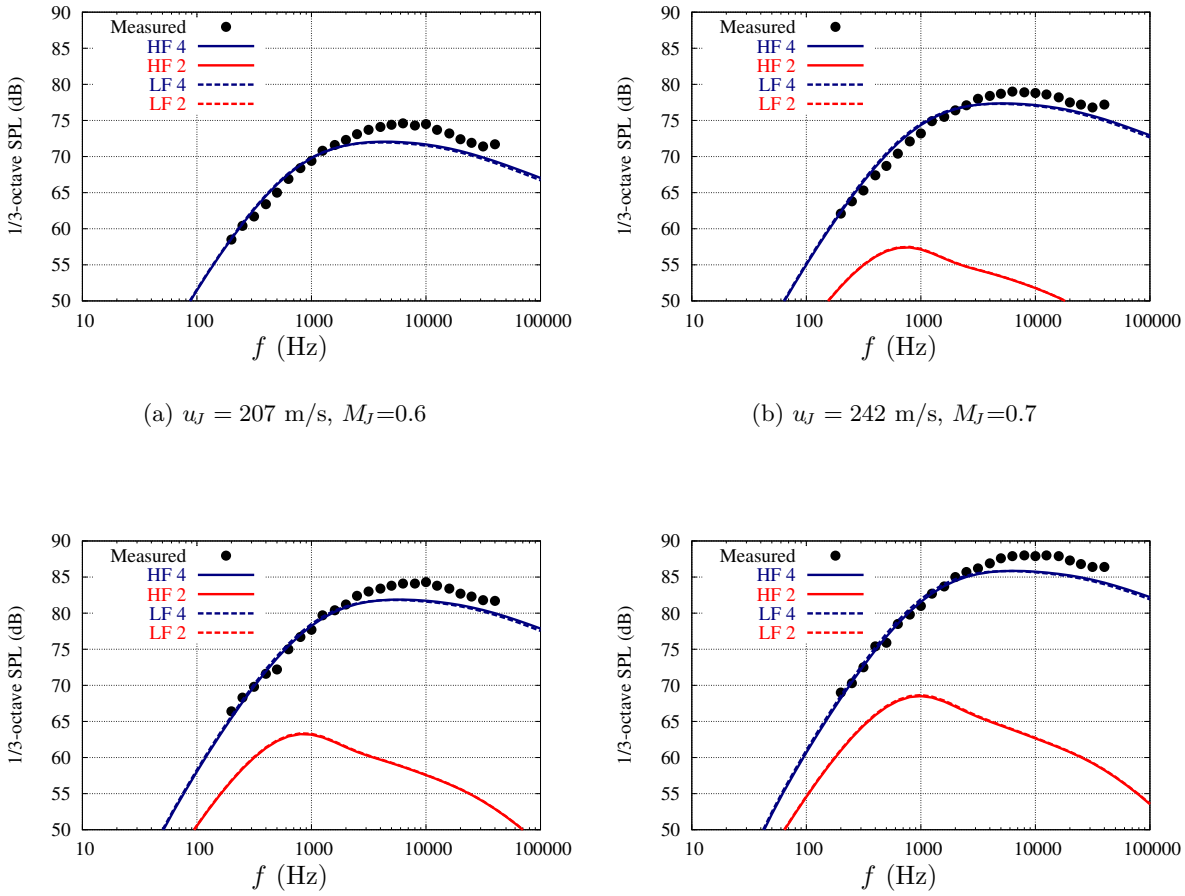

(a) $u_J = 207$ m/s, M_J=0.6

(b) $u_J = 242$ m/s, M_J=0.7

(c) $u_J = 276$ m/s, M_J=0.8

(d) $u_J = 310$ m/s, M_J=0.9

Figure 5.7: Isothermal jet-noise 1/3-octave spectra for jets issuing from the Tanna convergent nozzle; nozzle-exit diameter $d_J = 0.051$ m. The data (Tanna, Dean and Burrin[9]) were measured at 3.60 m (72 d_J) from the nozzle-exit centre and corrected for atmospheric attenuation. The far-field model prediction corresponds to the measurement position. The labels are as in Fig. 5.6.

is maximum in the noise-peak frequency region, with the model predicting lower noise peak (2 to 3 dB) and lower noise-peak frequency (1 octave) compared to the measurements.

Note that a small applied-force contribution is predicted by the jet-noise model in isothermal conditions. This results from the small temperature variations in the RANS solution, due to the presence of vorticity; the corresponding static-temperature gradients drive the dipole-term contribution in the model.

5.4.2 Hot single-stream jet noise

Heating the jet causes a reduction of the density in the jet core and consequent density gradients in the jet shear layer. The applied-stress and the applied-force contributions to the modelled far-field noise respond to heating with opposite changes in intensity:

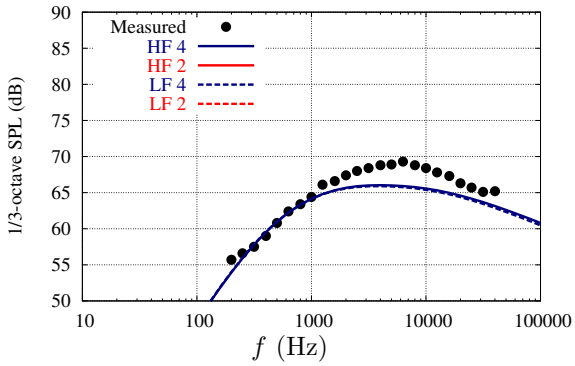

(a) u_J = 172 m/s, M_J=0.5, isothermal. The applied-force model contributions are below the minimum SPL of 50 dB.

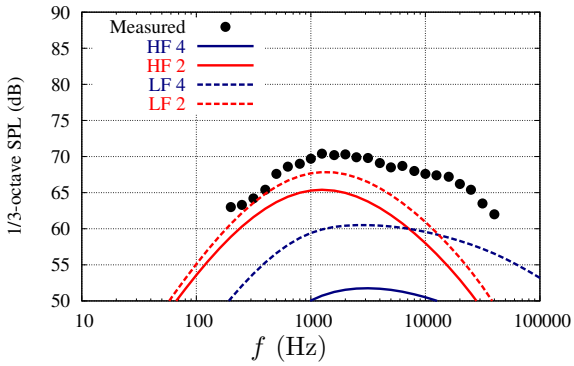

(b) $u_J = 174$ m/s, heated, $T_J/T_\infty = 3.3$

Figure 5.8: Effect of heating on a single-stream jet at nozzle-exit acoustic Mach number $M_J = 0.5$. Jet-noise 1/3-octave spectra for jets issuing from the Tanna convergent nozzle ($d_J = 0.051$ m) in isothermal and heated conditions. The labels are as in Fig. 5.6.

- The applied-stress contribution is reduced due to the density-dependent scaling factor associated with the corresponding acoustic-pressure PSD per unit volume.

- The applied-force volumetric source strength results from fluctuations of the term $\mathbf{u}' \otimes \mathbf{u}' \cdot \nabla \bar{T}$ and is therefore driven by the static-temperature gradient $\nabla \bar{T}$. A higher dipole-order contribution is then expected as a result of heating the jet.

This effect is most evident at low nozzle-exit acoustic Mach number as, by reducing the jet speed, we scale-down the applied-stress contribution, proportional to M_J^8, more rapidly than the applied-force contribution, proportional to M_J^6. Evaluations of the model components in heated conditions have been performed for the QinetiQ[10] conical nozzle and for the Tanna[9] nozzle; in both cases the jet conditions are at the same nozzle-exit acoustic Mach number, $M_J = 0.5$. Fig. 5.8 shows the effect of heating on the model components, as the model is tested in producing 1/3-octave spectra for an isothermal jet (a) and for a heated jet (b); the jets were both considered in the Tanna[9] measurements. Increasing the jet temperature ratio from 1 to 3.3 reduces the peak SPL of the high-frequency model (3.16) applied-stress contribution by 14 dB; it reduces the low-frequency (3.23) applied-stress-contribution maximum level by 6 dB. In the heated case Fig. 5.8 (b), the applied-force contributions dominate the low frequency part of the modelled 1/3-octave spectra for both solutions (3.23) and (3.16), with the low-frequency dipole contribution being greater than the high-frequency dipole contribution (peak-level difference of 2.5 to 3 dB).

As shown in section 5.3, in flows with large density inhomogeneities the low-frequency (3.23) and the high-frequency (3.16) solutions contribute differently to the modelled 1/3-octave spectrum. In these cases it is then important to consider the model contributions (3.23) and (3.16) as raw jet-noise components that need to be opportunely frequency filtered. The comparison

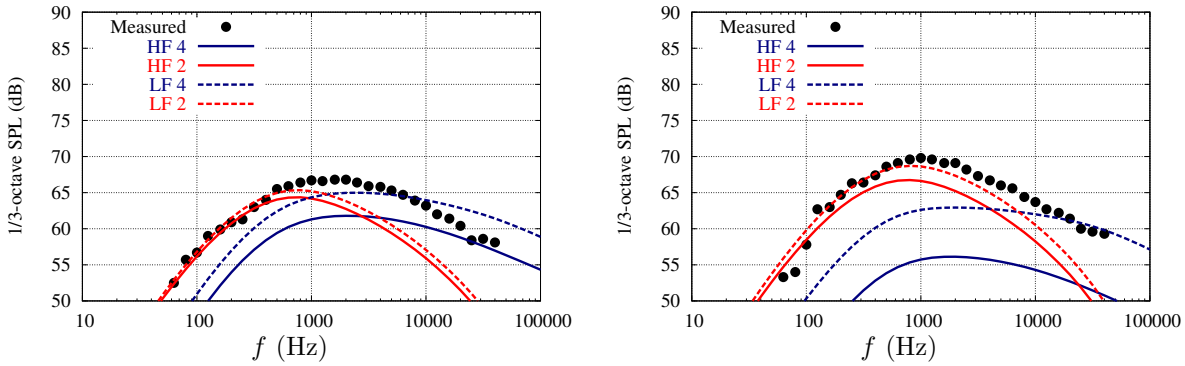

(a) $u_J = 168$ m/s, heated, $T_J/T_\infty = 1.5$

(b) $u_J = 168$ m/s, heated, $T_J/T_\infty = 2.5$

Figure 5.9: Effect of heating on a low-speed single-stream jet. Jet-noise 1/3-octave spectra for jets issuing from the QinetiQ convergent nozzle (see Fig. 5.6) in heated conditions. The labels are as in Fig. 5.6.

between the QinetiQ[10] 90-degree 1/3-octave spectra and the corresponding model contributions is shown in Fig. 5.9, where two cases at different nozzle-exit/ambient static-temperature ratios are reported. Note that the measured data in Fig. 5.9 (b) have been used to define the value of the parameter $\kappa_{\mathbf{d}}$. The applied-force components dominate the low frequency spectrum in both cases.

We note that the high-frequency solution (3.16) behaves similarly to the predictions made by applying the geometric-acoustics scaling laws identified in Ref. [41]. In this case we use a dipole characteristic spectrum that is derived from the Harper-Bourne[4] fluctuating-Reynolds-stress two-point measurements, the volumetric-source-strength spectrum is defined, depending on the position in the jet, as a function of the Strouhal number Sr_τ (based on the fluctuating-Reynolds-stress autocorrelation $1/e$-decay time) and of a non-dimensional repetency $\tilde{\alpha}$, defined in equation (4.34).[c] The low-frequency solution (3.23) shows a different behaviour from the high-frequency solution (3.16), with a higher quadrupole/dipole SPL ratio.

[c]This spectrum is not the same as the dipole master spectrum deduced in Ref. [41] or, more recently, in Ref. [56] from jet-noise acoustic measurements. The dipole master spectrum is defined in the (fd_J/u_J) Strouhal domain. The identification of this dipole master spectrum uses whole-jet scaling laws for the quadrupole (i.e. as in Lighthill[1]) and dipole sources (i.e. as in Morfey[58]). The quadrupole master spectrum is defined by scaling isothermal-jet acoustic data and gathering a collapse in the Strouhal (fd_J/u_J) domain, as in Appendix H. The quadrupole 1/3-octave master spectrum is then used to remove the quadrupole contribution from heated-jet measurements. Given the nozzle-exit characteristics of the jet the 1/3-octave spectrum contribution is derived from the quadrupole master spectrum scaled according to a Lighthill–Strouhal law (see Appendix H); this contribution is then subtracted from the heated-jet 1/3-octave spectra. The resulting dipole-driven 1/3-octave spectra are scaled according to the Morfey[58] dipole-scaling law and then collapsed on a characteristic curve in the Strouhal (fd_J/u_J) domain; this curve is referred to as dipole master spectrum. The identified master spectra can then be used for reproducing jet-noise measurements. The method, recently applied by Harper-Bourne,[56] allows for reproducing 90-degree jet-noise acoustic data at various jet velocities and heating conditions.

5.4.3 Unheated coaxial jet noise

The results in this section compare the model prediction to jet-noise data for unheated coaxial jets. The jet flows issue from two different coaxial nozzles. Both nozzles are axisymmetric and have coplanar exit sections without a bullet. The same inner-flow nozzle-exit area is maintained for both nozzles; two different outer-flow nozzle-exit areas are considered in order to realise outer/inner area ratios of 2 and 4 for the different nozzles. A schematic showing the geometry of the area-ratio 4 nozzle is given in Fig. F.1. The acoustic measurements were performed at the QinetiQ NTF facility.[d] The measured data were corrected in order to simulate loss-free propagation. The data were measured at a distance greater than 10 m and normalised to a distance of 6 m from the nozzle centre. A comparison between measured data and model components is given in Fig. 5.10 and Fig. 5.11 where the 90-degree acoustic spectra are shown respectively for jets issuing from the area-ratio-4 and the area-ratio-2 nozzles. The discrepancies between modelled noise components and measured data are contained within 3 dB for 1/3-octave bands below 10 kHz. At greater frequencies, for secondary/primary velocity ratio 0.6, Fig. 5.10 (a) and Fig. 5.11 (a), the model prediction shows a different high-frequency trend from the measurement. A similar difference in high-frequency trend is not clearly observed at secondary/primary velocity ratio 0.8, Fig. 5.10 (b) and Fig. 5.11 (b). For all cases examined, the model prediction fails to well reproduce the spectral shape associated with the measurement, with the SPL-peak frequency predicted at lower frequency compared to the measurement. Improvements in predicting the spectral shapes are expected with more realistic RANS predictions, without the axial stretching of the flow field.

[d]The measurements were made in 2001 before the recent refurbishment, Ref. [59], of the facility; Ref. [10] can be used as a description of the facility, the jet rig and the measurement set-up. The measurements were performed by QinetiQ for the ISVR as part of a jet-noise programme for the determination of the jet-noise loads on the aircraft structures. The research programme was funded by the Engineering and Physical Science Research Council (EPSRC, United Kingdom); funding for the jet-noise measurements was provided by Airbus UK.

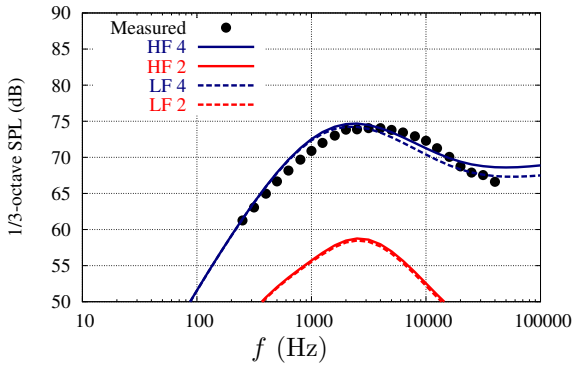

(a) Inner-flow velocity 280 m/s, outer-flow velocity 168 m/s, velocity ratio 0.6

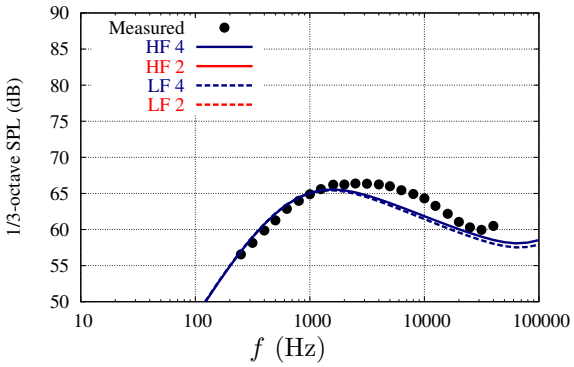

(b) Inner-flow velocity 211 m/s, outer-flow velocity 168 m/s, velocity ratio 0.8

Figure 5.10: 1/3-octave noise spectra for a coaxial coplanar jet in unheated conditions at 90-degree polar angle. The jet issues from a coplanar bullet-free area-ratio-2 nozzle. The nozzle-exit jet diameter is 0.058 m. The labels are as in Fig. 5.6.

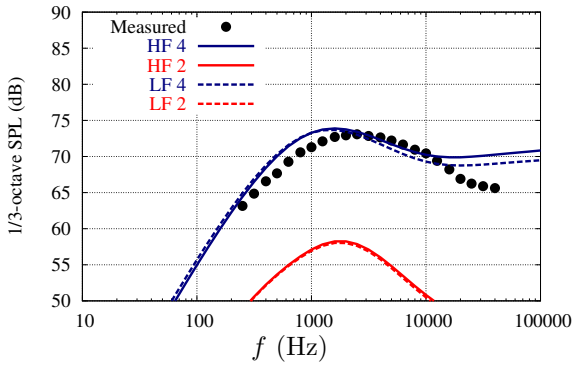

(a) Inner-flow velocity 281 m/s, outer-flow velocity 169 m/s, velocity ratio 0.6

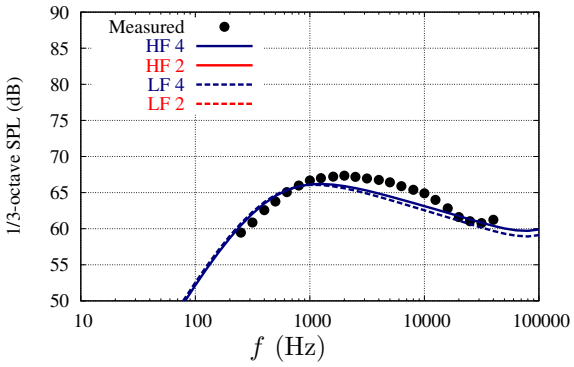

(b) Inner-flow velocity 210 m/s, outer-flow velocity 168 m/s, velocity ratio 0.8

Figure 5.11: 1/3-octave noise spectra for a coaxial coplanar jet in unheated conditions at 90-degree polar angle. The jet issues from a coplanar bullet-free area-ratio-4 nozzle. The nozzle-exit jet diameter is 0.075 m. The labels are as in Fig. 5.6.

5.5 Conclusions

The aerodynamic-noise model developed in chapters 3 and 4 has been applied to jet-noise prediction. We have developed a RANS-based jet-noise prediction scheme, in which a commercial RANS solver is used to provide turbulence statistics as well as the mean-flow field. The principal conclusions are outlined below.

1. The RANS solver uses a Reynolds Stress Model closure; this implies that the RANS solution includes estimates for the mean values of the unit-density Reynolds stress. The mean-flow RANS solution shows axial stretching compared to jet-flow measurements described by Abramovich[55] and Goldstein;[24] the RANS potential-core length is approximately double the experimental value.

2. The empirical scaling relations (connection relations) between the local value of the RANS-solver flow variables and the jet-noise source statistics have been defined by introducing a set of acoustic-model scaling parameters. Note that the local-Strouhal scaling that is a feature of model (4.19) is incorporated into the connection relations; this was not implemented in earlier work by Bassetti and Morfey,[50] where an extra scaling parameter was adopted. It is important to note that the developed connection relations constitute an initial guess inspired by previous papers on jet noise, e. g. [21]. They need to be validated against corresponding experimental/DNS data. This step is a fundamental requirement in order to properly asses the extent to which the proposed empirical relations capture the physics of jet turbulence.

3. The acoustic-model scaling parameters are defined by matching the jet-noise model components to corresponding measured data. In order to do that, RANS solutions are derived for three single-stream jets corresponding to available experimental data. Both two-point measurements of the Reynolds-stress statistics and far-field noise spectra are used in this stage.

   - A first RANS solution is evaluated for the same jet as in the Harper-Bourne[4,5,42] measurements. The parameters defining the model of the Reynolds-stress two-point correlation[a] are chosen in order to match the corresponding measurements at a single location on the jet lip line (i.e. the same location where the Harper-Bourne measurements were performed). The unphysical axial stretching of the RANS solution has been taken into account by assuming correspondence between RANS-solution and measurement positions, mapped in terms of potential-core lengths in the axial direction and in terms of nozzle-exit diameters in the radial direction.
   - Two more RANS solutions are evaluated for jets associated with existing far-field acoustic measurements. As done by previous RANS-based jet-noise models,

[a] Recall that the Reynolds stress two-point correlation function is here used as model for the acoustic-source two-point correlation function both for the Reynolds stress source and the applied-force source.

e. g. [21, 60], the remaining model parameters are chosen by fitting model predictions to corresponding 90-degree far-field jet-noise spectra. This procedure uses measurements acquired for jets issuing from a single-stream axisymmetric conical nozzle: an isothermal jet with $M_J = 0.75$, and a hot jet at nozzle-exit acoustic Mach number 0.5 and temperature ratio T_J/T_∞=2.5. The isothermal-jet data are used to set the scaling factor associated with the applied-stress component. The hot-jet spectrum is used to determine the scaling factor for the applied-force component.

The high-frequency roll-off of the modelled applied-stress spectrum is highly sensitive to variations of the parameter a_l, that controls the spatial-separation decay associated with the two-point correlation coefficient (4.19). Pending the availability of a greater number of two-point measurements for the Reynolds-stress statistics, we fixed the value of $a_l = 2.7$. This value allows for matching the transverse-separation high-frequency roll-off associated with the Harper-Bourne[4,5] measured frequency-dependent length scales (see Fig 4.5). This value also allows for matching, below 10 kHz, the modelled isothermal single-stream far-field jet-noise predictions (3.23) and (3.16) to the corresponding 90-degree 1/3-octave spectra measured by QinetiQ.[10] We note anyway that the jet-noise model predictions (3.23) and (3.16), at frequencies higher than 10 kHz, do not decay with increasing frequency as fast as the corresponding measurements.

4. A comparison between model components and isothermal-jet 90-degree 1/3-octave spectra has been performed for 7 jets issuing from 2 different single-stream nozzles. In this case the low-frequency solution (3.23) and the high-frequency solution (3.16) yield the same result for the modelled 1/3-octave spectrum. The applied-stress components strongly dominate the modelled noise, although a small applied-force contribution is present, due to the moderate temperature gradients in the jet shear layers. The comparison of the applied stress-components of model (3.23) and (3.16) against the QinetiQ[10] measurements shows a difference in the range of 1 dB for frequencies from 100 Hz to 10 kHz. At higher frequencies the model does not follow the same high-frequency trend as the measurement, and over-predicts the measured SPL. The same comparison against the Tanna measurements shows discrepancies within 3 dB between the applied-stress model predictions and the measured spectra, for 1/3-octave bands ranging from 200 Hz to 20 kHz centre-band frequency. In this case the model prediction consistently underestimate the SPL in proximity of the peak value and does not correctly evaluate the SPL-peak frequency. In all cases examined, the dominant applied-stress components reproduce the variations of the measured spectra due to variations in jet-exit Mach number. In the comparison against the Tanna[9] measurements, the difference between model prediction and corresponding measurement is maximum in the same frequency region where the measured data do not scale according to the Lighthill[1] scaling law (peak-level scattering of 2.5 dB, see Appendix H). The difference between model and measurements confirms the hypothesis of extraneous noise contamination present in the measurements, due to noise sources different from turbulent-mixing noise.

5. A study of the model-component behaviour has been offered by jet-noise comparisons for hot jets. The effect of heating has been studied by considering 3 single-stream jets issuing from the axisymmetric nozzles used in acquiring the Tanna[9] and the QinetiQ[10] measurements; all jets are characterised by the same nozzle-exit acoustic Mach number 0.5. Also in this case we compared measurements and corresponding model components at 90 degrees and at different 1/3-octave bands. The applied-force contribution dominates the modelled jet-noise at the highest temperature ratios, confirming the dipole scaling of low-velocity high-static-temperature jets. We note that the model behaviour agrees with the explanation given by Morfey[58] regarding the extra low-frequency noise associated with heating the jet. Contrary to the isothermal case, in the hot-jet case the low-frequency (3.23) and the high-frequency (3.16) solutions yield distinct jet-noise contributions. Provided the different contributions can be accepted as jet-noise predictions,[b] the low-frequency solution is the main contribution for low-density jets.

6. A comparison between model components and unheated-jet 90-degree 1/3-octave spectra has been performed for 4 jets issuing from 2 different coaxial coplanar nozzles. The applied-stress component dominates the model predictions. The low-frequency (3.23) and the high-frequency (3.16) solutions nearly yield the same spectral result with differences near to 1 dB at high frequencies, above 10 kHz. Compared to the isothermal single-stream case, we observe a reduced agreement between modelled and measured 1/3-octave spectra, especially in terms of the spectral shape. In the cases at higher primary velocity, the model components diverge in trend from the measured data at high frequency, above 10 kHz. For all cases examined, in the frequency range from 250 Hz to 10 kHz, the difference in level between model and measurement is contained within 3 dB.

[b]Recall that the high-frequency (3.23) and the low-frequency (3.16) solutions need to be frequency filtered in order to respect the corresponding hypotheses on the flow-scale/wavelength ratio. A low-pass filter on the low-frequency solution, not implemented in the present work, is likely to remove part of the applied-stress low-frequency-model contribution.

Chapter 6

Conclusions

A hybrid jet-noise model has been developed, based on a time-stationary spatial field of the jet-flow statistics. An acoustic-analogy approach has been used to define spatial distributions of equivalent acoustic sources and corresponding Green functions. The far-field jet-noise PSD is determined by modelling a PSD contribution per unit volume in the turbulent region of the flow; this PSD contribution is then integrated across the jet volume. The unit-volume PSD contribution is modelled by combining a Green-function term and a volumetric source strength; the latter is determined on the basis of the two-point statistics of the equivalent acoustic sources. The two-point statistics of the equivalent acoustic sources have been modelled by using available measurements of the Reynolds-stress two-point covariance. The model has been tested to reproduce jet-noise acoustic measurements; here a RANS solution has been adopted as a basis for describing the time-stationary jet-flow statistics. The principal conclusions are outlined in the following sections.

6.1 Acoustic model

The perfect-gas Goldstein[3] equation for the Lilley[2] analogy (the Lilley–Goldstein analogy) has been used to relate the turbulent jet to corresponding volume distributions of applied-force and applied-stress equivalent acoustic sources. The acoustic-source volume has been parted in a number of finite-volume source subregions; each subregion is such that small variations for the acoustic-source and the flow statistics can be assumed in its interior. The far-field acoustic-pressure PSD in the quiescent ambience surrounding the turbulent jet has been expressed as sum of contributions from all the subregions. Each subregion contributes to the acoustic-pressure PSD with a high-frequency term and a low-frequency term. These terms are both expressed as a function of the acoustic-source two-point CPSD and of the source–observer Green function. They share the same acoustic-source statistics, but are characterised by different Green functions. The high-frequency and the low-frequency Green functions result from acoustic analogies corresponding to the Lilley–Goldstein[3] analogy in the limits of very

large and very small flow-dimension/wavelength ratio, respectively.

- The high-frequency approximation has been realised by specifying to the given acoustic subregion the geometric-acoustic jet-noise-scaling approach used by Morfey Szewczyk and Tester.[41] Through the geometric-acoustics laws, the acoustic field at a location in the quiescent-medium is connected to the acoustic field at a ray-direction virtual location in a uniform medium characterised by the same velocity and speed of sound as the subregion mean flow. While the geometric-acoustics scaling has been adapted from previous work, Ref. [41], the virtual-location acoustic-field PSD has been derived in the present work, by adopting the following procedure.

  1. A local-medium Lighthill-type analogy has been formulated by considering a uniformly moving medium whose characteristics are assigned by the subregion mean flow. The analogy, expressed in a frame moving with the medium, removes the mean medium-motion effect from the instantaneous source terms of the standard Lighthill analogy; it yields applied-stress (quadrupole) and applied-force (dipole) terms that are identical to the corresponding forcing terms of the Lilley–Goldstein[3] equation.
  2. Rather than using a convective-wave-equation Green function, the solution for the acoustic field has been determined by adopting a moving-source solution for the standard wave equation. As explained in Appendix C, a Lorentz-transformation technique has been used to gather a solution for a moving monopole. The moving-monopole solution has been expressed in emission-time polar coordinates and extended to dipole-order and quadrupole-order moving sources. Although we only use the acoustic-far-field approximations, the multipole solutions have been expressed including the near-field terms; these are in agreement with corresponding solutions published by Lowson[61] (dipole) and Brentner[62] (quadrupole).
  3. The far-field acoustic-variable autocorrelation in the local medium has been expressed in terms of the two-point correlation function associated with the fluctuating part of the quadrupole-order and dipole-order acoustic-source terms (far-field approximations). The two-point cross correlation terms between applied-stress and applied-force sources are omitted due to a symmetry hypothesis, expression (D.16) on page 116, on the source-field correlation function. Applying Fourier transform with respect to the time delay yields the acoustic-field PSD at the virtual location.

  Note that, in order to realise a spherical-spreading correspondence between the virtual-location and the acoustic-subregion PSD, we require small Fresnel corrections inside the given acoustic subregion, based on the typical dimension of the source-coherence volume. This implies that the model is limited to small-scale coherence regions, compared to the flow-variation scales.

  The acoustic variable PSD is expressed as a sum of applied-stress and applied-force contributions; each of these contributions is given as a dot product between tensors. A

first Green-function tensor depends on the source–virtual-observer emission-time separation, Doppler factor and speed of sound associated with the local acoustic medium. A second tensor, referred to as volumetric source strength, depends on the acoustic-source two-point CPSD. The two-point CPSD is phase-shifted according to the time delay between acoustic emission from the source-coherence centroid and reception at the virtual-observer position. The volumetric source strength is expressed as volume integral across the source-coherence volume of the phase-shifted two-point CPSD of the applied-stress and the applied-force sources.

- For the low-frequency approximation, the far-field solution for the acoustic radiation from an acoustic-source subregion is expressed in terms of a multiplying factor relating a corresponding zero-flow solution to the solution including an axisymmetric base flow. The multiplying factor, called flow factor, is the ratio between the far-field acoustic-pressure PSD derived as solution of the axisymmetric-base-flow Lilley–Goldstein[3] equation and the acoustic-pressure PSD associated with a zero-flow Lilley–Goldstein[3] equation.
  The flow-factor components associated with combinations of the acoustic-source components were developed by Morfey Tester and Powles[43] starting from the low-frequency approximate solution in Ref. [40]. The result has been further developed by Morfey to yield simplified flow-factor expressions valid at low Helmholtz number; see Appendix E. The zero-flow Lilley–Goldstein solution is obtained by specifying the high-frequency solution to the same quiescent-medium conditions as in the ambience surrounding the source region.
  Likewise for the high-frequency solution, the acoustic-variable PSD is expressed as a sum of applied-stress and applied-force components; each component is given by forming a dot product between tensors. In this case the zero-flow Green-function tensor and the zero-flow volumetric source strength are operated by a flow-factor tensor in order to get the components of the far-field acoustic-pressure PSD.

The integration across the source region of the acoustic-subregion contributions yields two separate solutions for the acoustic-pressure PSD, corresponding to the low-frequency and the high-frequency analogies. Note that these solutions need in principle to be frequency filtered, in order to satisfy the respective hypotheses regarding the wavelength/flow-scale ratio; they need then to be combined in order to achieve a jet-noise prediction. Both solutions converge to the standard Lighthill-analogy solution for far-field observation point at 90-degree polar angle and for jet-flows with zero temperature gradient.

Both the high- and the low-frequency solutions need expressions for the frequency-dependent volumetric source strength; this is given by the space integral across the source-correlation volume of the phase-shifted two-point CPSD for both the applied-stress and the applied-force sources. While the phase shift needs to be specified differently for the low- and the high-frequency cases, the same term for the source two-point CPSD is included in both solutions. For jet-noise models based on space–time resolved CFD solutions, the acoustic-source two-

point CPSD can in principle be directly evaluated for each acoustic subregion. In the present work the jet-noise model is based on an incomplete time-stationary space distribution of the jet-flow one-point statistics, as a consequence the acoustic-source two-point CPSD requires modelling.

6.2 Acoustic-source two-point covariance

The model for the acoustic-source two-point covariance has been based on available experimental measurements of the Reynolds-stress two-point covariance. The model has been derived by fitting a suitable analytical model for the two-point correlation coefficient. The acoustic-source two-point CPSD has then been derived by applying Fourier transform with respect to the time-separation variable. The integral across space separation of the appropriately phase-shifted two-point CPSD yields the acoustic-source volumetric source strength tensor. In order to achieve the volumetric source strength we have performed the following.

1. The acoustic-source covariance function has been associated with the correlation function of the fluctuating Reynolds stress.

   - Assuming that the pressure-fluctuations are much smaller than the mean pressure, the instantaneous value of the Lilley–Goldstein[3] applied-stress equivalent acoustic source equals the unit-density Reynolds stress $\mathbf{u}' \otimes \mathbf{u}'$. A direct consequence of this is the identification of the applied-stress-source two-point covariance function with the unit-density Reynolds-stress two-point covariance function.
   - A relation between the instantaneous value of the applied-force source and the scaled projection of the unit-density Reynolds stress has been identified by assuming moderate and purely convective static-temperature fluctuations. Under the same hypotheses, the instantaneous applied-force source involves a second component; this is given by the Lagrangian derivative plus the mean-flow gradient operating on the fluctuating velocity scaled by the fluctuating static temperature. By assuming a closure hypothesis (full characterisation of the two-point covariance function by means of the unit-density Reynolds-stress component), the applied-force two-point covariance function has been related to the unit-density Reynolds-stress two-point covariance function. This closure hypothesis introduces an empirical scaling parameter, that we refer to as the applied-force scaling parameter.

2. Following the analysis of the Harper-Bourne[4,5] estimates for the Reynolds-stress two-point covariance (derived from axial-velocity measurements and therefore related to component $c_{11,11}$ only), an analytical model (4.16) for the fluctuating-Reynolds-stress two-point correlation-coefficient function has been introduced. The model is based on a space–time distance in a normalised-separation space. It includes a convection effect in the axial direction given by a time-separation shift that varies linearly with the

space-separation axial component. The model follows the trends of the Harper-Bourne measurements both in the time-separation domain and in the frequency domain. This model shows that the frequency-domain behaviour of the Harper-Bourne data can be reproduced by a constant-parameter model. The modified-distance model departs from the Gaussian-decay separable-variable model that, introduced by Ribner,[47] has been widely used in jet-noise literature (e.g. Refs. [63,21,60]) to represent the acoustic-source two-point correlation coefficient. Although we renounce to analytical advantages associated with the Ribner[47] model, we propose a model that ensures a closer agreement with available measurements.

3. All components $c_{ij,kl}$ of the two-point Reynolds-stress covariance tensor have been factorised as the product between mean value and correlation-coefficient function (see table on page 139). This allows for confining the dependence on space and time separations in the correlation-coefficient functions. The correlation-coefficient-function model (4.19), a simplification (isotropic shape for the space-separation decay) of the model introduced in point 2 above, has been extended from the $c_{11,11}$ component to all components $c_{ij,kl}$. The acoustic-source two-point CPSD has then been derived by applying Fourier Transform with respect to time separations. By further factorising the correlation-coefficient Fourier transform (or scaled CPSD, table on page 139), the space-separation dependence has been confined in a normalised two-point CPSD function.

4. A frequency–wavenumber expression for the volumetric source strength tensor has been derived by integrating across the space-separation variable the acoustic-source two-point CPSD. The spatial-decay isotropy of the CPSD model has been used to reduce this volume integral to a 1-D integral that has been numerically evaluated at varying wavenumber modulus. A one-variable cancellation function has been tabulated for the numerical integral, to be directly accessed for the evaluation of the acoustic-source volumetric strength.

5. The acoustic-source volumetric strength has been derived by specifying to the given radiation condition the frequency–wavenumber expression. The radiation condition is different for the low-frequency and the high-frequency solution; it is set by imposing the appropriate uniform-medium velocity and speed of sound, together with the source–observer emission-time direction.

The volumetric source strength components, see expressions (4.37) and (4.38), are given by the product of scalar factors: mean value, scaling parameter (only for the applied-force contribution), scaled autospectrum, normalised-CPSD length scales and Cancellation function. While the mean value – $\bar{q}_{ij,kl}$ for the applied stress and $\left(\nabla\bar{T}/\bar{T}\right)\Delta_{i,j}$ for the applied force – varies for different source-strength components, the other factors are the same for all components. The component-invariant factors – scaled-autospectrum model $\hat{\mathrm{s}}_0(\mathbf{y},\mathbf{0},f)$, $1/e$-decay length scales $\tilde{l}_i\,(\mathbf{y},f)$ of the normalised CPSD and Cancellation function $\mathrm{C_f}\,(\tilde{\alpha})$ – are frequency dependent.

Due to the characteristics of the simplified two-point correlation model all these factors can be expressed by means of one-variable functions: the cancellation function $\mathrm{C_f}$ only depends on a modified-wavenumber modulus, while the scaled autospectrum and the length scales can both be related to characteristic functions f_A and f_L of a Strouhal number $Sr_\tau = f\tau_d$, where τ_d represents the autocorrelation-coefficient time scale. The functions $\mathrm{C_f}$, f_A and f_L are numerically evaluated, based on the simplified correlation-coefficient model (4.19); they have been tabulated in order to rapidly evaluate the volumetric source strength at varying $\mathbf{y}$, f and $\tilde{\alpha}$. The parameter a_l controls the spatial-separation decay of the correlation-coefficient model (4.19) and, consequently, the frequency dependence of f_L and the wavenumber-modulus dependence of $\mathrm{C_f}$. A set of different functions f_L and $\mathrm{C_f}$ have been evaluated, depending on different values for the parameter a_l. The different high-frequency trends measured by Harper-Bourne for $\tilde{l}_1\left(\mathbf{y}^{(m)}, f\right)$ or $\tilde{l}_\perp\left(\mathbf{y}^{(m)}, f\right)$ are spanned by the modelled f_L at varying a_l.

6.3 Application to jet-noise prediction

The acoustic model has been applied to predict 90-degree jet noise for single-stream and coaxial jets issuing from axisymmetric nozzles. The acoustic model has been input with a description of the jet-flow time-stationary statistical field, which has been computed as a solution of the compressible steady RANS equations. The RANS solution does not output all the statistical functions required by the acoustic model. In order to get a full description of the volumetric source strength, the missing statistical parameters have then been introduced by means of empirical expressions that supplement the RANS-solution output; we refer to these expressions as the connection relations. The far-field jet-noise components, according to the low-frequency (3.23) and the high-frequency (3.16) solutions, have been systematically compared to corresponding measurements at 90-degree polar angle on unheated, isothermal and hot jets. This part, detailed in Chapter 5, is briefly resumed as follows.

1. The jet-flow steady statistics have been evaluated by using a commercial RANS solver. Solutions of the RANS equations, with Reynolds-stress closure for the turbulent-variable equations, have been determined for a series of turbulent-jet flows. The solutions include spatial distributions for the Favre-averaged[a] velocity, Reynolds-stress components, turbulent-dissipation rate and static temperature. The RANS-solution flow fields, obtained by using the solver-default turbulence-closure empirical parameters, show axial stretching if compared to low-velocity turbulent-jet flow measurements.

2. A set of empirical relations, the connection relations, has been defined to establish a link between the flow variables output by the RANS solver and the jet-noise model (source statistics and Green function). The connection relations have been derived by

[a]Consistently with the adopted acoustic analogy, the jet is considered as an ideal-gas flow. Due to the compressibility, the time averages are changed for the Favre averages. We have assumed that Favre averages can be used in place of the time averages in the expressions associated with the acoustic source strength.

following the lead of previous RANS-based (k-ϵ closure) jet-noise models and by adding further relations that use the extra information arising from the RSM closure (turbulence anisotropies). The connection relations introduce a set of empirical parameters.

3. The values of the acoustic-model parameters (the connection-relation empirical parameters and the applied-force scaling parameter) have been defined by matching the jet-noise model components to corresponding measured data. In order to do that, RANS solutions have been derived for three single-stream jets corresponding to available experimental data.

   - An important aspect of the empirical-parameter definition is given by the use of flow measurements. A first RANS solution has been evaluated for a jet with the same nozzle-exit characteristics as the jet described in the Harper-Bourne[4,5,42] measurements. The Harper-Bourne[4,5,42] estimates for the fluctuating Reynolds-stress scaled autospectrum and the normalised-CPSD $1/e$-decay length scales have been used in matching the corresponding volumetric-source-strength factors. The axial stretching of the RANS-solution mean flow field has been taken in account by putting in correspondence experiment and RANS-solution quantities at locations mapped in potential-core lengths (axial direction) and in nozzle-exit diameters (radial direction). This part of the calibration procedure defines the spectral shape of the 1/3-octave spectra for the modelled applied-stress and applied-force components of the low-frequency (3.23) and the high-frequency (3.16) solutions.
   - As done by previous RANS-based jet-noise models (e. g. in Ref. [21, 60]), the remaining parameters are chosen by adopting 90-degree far-field jet-noise spectra. Note that these parameters act as scaling factors for the applied-stress and for the applied-force contributions to the modelled far-field jet noise.
     - ◇ The applied-stress scaling factor is chosen by performing a RANS solution for an isothermal single-stream jet whose 1/3-octave spectrum is known (QinetiQ[10] measurements). In this case the low-frequency and the high-frequency solutions coincide and both model contributions can be considered as jet-noise predictions. While the high-frequency part of the modelled 1/3-octave spectrum is strongly affected by the frequency trend of the modelled normalised-CPSD $1/e$-decay lengths (parameter a_l in the correlation-coefficient model),[b] the low-frequency part of the modelled 1/3-octave SPL is not affected by changing a_l. Thus the applied-stress scaling factor is assigned by matching the isothermal-jet 90-degree spectral measurements and the low-frequency part of the applied-stress components for both the low-frequency (3.23) and the high-frequency (3.16) solutions.

[b] The modelled normalised-CPSD $1/e$-decay lengths are part of the volumetric source strength both as explicit factors and as argument of the cancellation function C_f. Their frequency trend is controlled by the parameter a_l in the correlation coefficient model (4.19), which we assumed to vary within a set of 4 prescribed values.

◇ The applied-force scaling factor is chosen by performing a RANS solution for a low-Mach-number hot single-stream jet whose 1/3-octave spectrum is known (QinetiQ[10] measurements). In this case the low-frequency and the high-frequency solutions do not coincide and the model contributions can only be considered as raw jet-noise predictions (a high- low-pass filtering procedure needs to be applied on the low-frequency and high-frequency solutions in order to enforce the respective hypotheses concerning the wavelength/flow-scale ratios). The low-frequency solution yields applied-stress and applied-force components for the raw SPL prediction that are greater than the corresponding high-frequency components. The applied-stress raw spectra strongly under-predict the low-frequency part of the measured 1/3-octave spectrum; this part of the spectrum can be successfully modelled by opportunely setting the applied-force scaling parameter $\kappa_{\mathbf{d}}$ which acts as an amplification factor of the applied-force-component 1/3-octave spectra. Note that the applied-force 1/3-octave contributions do not significantly change their spectral shapes, when changing the value of parameter a_l.

As mentioned in the above points, the value of the correlation-coefficient-model spatial-separation-decay parameter a_l strongly affects the high frequency trends of the applied-stress 1/3-octave noise spectrum and has a more limited effect on the applied-force 1/3-octave noise spectrum. Pending the availability of further two-point correlation measurements for the fluctuating Reynolds stress, which are needed in order to properly identify the high-frequency roll-off of the normalised-CPSD length scales, we set the value of a_l in order to best match the isothermal jet-noise measurements at 1/3-octave bands below 10 kHz. This value also allows the modelled trends of $\tilde{l}_i\left(\mathbf{y}^{(m)}, f\right)$ to match the Harper-Bourne measurements for $\tilde{l}_\perp\left(\mathbf{y}^{(m)}, f\right)$.

4. The noise model has been tested on jet flows including moderate temperature gradients (isothermal and unheated jets). At these conditions, being the observer at 90-degree polar angle, no relevant differences appeared between the low-frequency (3.16) and the high-frequency (3.16) solutions. The applied-stress contributions to the modelled spectra can be considered as jet-noise predictions, since they strongly dominate the applied-force contributions.

   - A comparison between modelled isothermal-jet 1/3-octave spectra and corresponding measurements (Refs. [10,9]) has been performed for 7 jets issuing from 2 different single-stream nozzles. The comparison shows discrepancies within 3 dB between the applied-stress model predictions and the measured spectra. The dominant applied-stress components reproduce the variations of the measured spectra due to variations in nozzle-exit Mach number and diameter. The model predictions also show a small applied-force component which is driven by the moderate static-temperature

gradients present in the RANS solutions.

The QinetiQ[10] measurements are closely followed by the model in the frequency range 200 Hz to 10 kHz. For higher frequencies, the model overpredicts the measurements, being the measurements characterised by steeper high-frequency roll-off. The maximum SPL and the SPL-peak frequency are almost coincident between measurement and model prediction.

The agreement between model predictions and measurements reduces when considering the test cases associated with the jet-noise data by Tanna, Dean and Burrin.[9] In this case, the model underestimates the measured SPL in the SPL-peak region for all nozzle-exit velocities considered. The SPL maximum is predicted by the model at a lower frequency compared to the measurements. Note that a similar difference has been identified in Appendix H, comparing the QinetiQ[10] and the Tanna[9] measurements after Lighthill–Strouhal scaling.

- A comparison between modelled components and measured (ISVR data, acquired by QinetiQ) unheated-jet 1/3-octave spectra has been performed for 4 jets issuing from 2 different coaxial coplanar nozzles. The cold-coaxial-jet modelled noise shows a discrepancy contained within 3 dB from the corresponding measurements in the frequency range from 200 Hz to 10 kHz. The difference between modelled and measured spectra increases if compared to the isothermal single-stream jet-noise comparison. For the cases at lower velocity ratio (higher nozzle-exit inner-flow velocity) the modelled-spectrum diverges in trend from the measurement at frequencies above 10 kHz.

5. The effect of density inhomogeneity has been studied by considering 3 hot jets issuing from 2 single-stream nozzles. The observation point has been kept at 90-degree polar angle and a constant nozzle-exit acoustic Mach number has been considered. In this case the low-frequency (3.23) and the high-frequency (3.16) solutions originated different jet-noise contributions, the low-frequency solution being dominant. In this case it is required to apply frequency filtering in order to enforce the hypotheses associated with the different solutions. The problem of appropriately filtering the low-frequency (3.23) and high-frequency (3.16) solutions, and achieve then jet-noise predictions, has not been considered in the present work. Consequently, the different solutions and the corresponding applied-stress and applied-force components need to be viewed as raw contributions. The low-frequency noise amplification observed when heating moderate-velocity turbulent jets is also observed in the modelled raw contributions. Increasing the nozzle-exit temperature causes in the model an amplification of the applied-force source (greater mean-temperature gradient) and a reduction of the applied-stress source. At the considered jet-exit velocities (acoustic Mach number 0.5), the applied-force contributions dominated both the low-frequency (3.23) and the high-frequency (3.16) solutions in the low-frequency range of the modelled 1/3-octave spectra. In this respect, the model behaviour confirms the dipole-source plus quadrupole-source scaling given by Morfey[58]

which was implemented in the scaling laws proposed by Morfey, Szewczyk and Tester.[41]

Preliminary results regarding the model-component evolution at rear-arc polar angles are reported in Appendix I. These results compare the raw model components to the QinetiQ single-stream jet-noise measurements, Ref. [10]. As above, the raw model components are given by the low-frequency (3.23) and the high-frequency (3.16) solutions, each of these solutions is broken down into the applied-stress and the applied-force components. The comparison constitutes a first benchmark for those model components that are silent at 90 degrees, even if we are not able to exactly evaluate the effect on the modelled noise components due to the stretched jet mean flow, computed as RANS solution. The comparison shows that the developed model could be used as a jet-noise prediction tool, provided the low-frequency (3.23) and the high-frequency (3.16) contributions are appropriately frequency filtered and combined. The results also show that the low-frequency solution dominates the predicted noise at the lowest polar angles; here the high-frequency solution decays, due to refraction effects.

6.4 Possible future developments

A refinement of the RANS solution is possibly the first step forward in the future development of the present model. By changing the values of the RANS-closure empirical parameters a RANS-solution which is closer to jet-flow measurements could be achieved. Ideally a study of test cases corresponding to jets with available experimental flow-statistics data can be performed in order to determine best-fit sets of empirical constants for the RANS-system closure.

The jet-noise model needs to be further tested for predictions at polar angles different from 90 degrees. As shown by the results reported in Appendix I, we can expect the noise at low polar angles as being dominated by the low-frequency-solution components. A rear-arc comparison between modelled low-frequency spectral components and corresponding acoustic measurements will possibly clarify aspects of frequency-domain filtering and combining the low-frequency (3.23) and high-frequency (3.16) solutions, once the effect of the RANS-solution stretching is removed from the jet-noise model. An alternative approach for appropriately combining the low-frequency and the high-frequency solutions could use numerically derived Green functions for the Lilley–Goldstein analogy. Comparing the given solutions to a solution obtained by using the exact Green function[a] would give us information about the possibility of constructing the exact Lilley-analogy propagation effect by combining the solutions proposed in the present thesis. These tests will assess the extent to which the present model can be

[a]The method indicated by Tester and Morfey[40] can be applied on the Lilley–Goldstein equation (B.23) for axisymmetric base flow and used to generate numerical solutions for the flow factors between a zero flow solution and the far field pressures. These numerical flow factors will depend on the local mean-flow profile. They can be used to evaluate the exact Lilley-analogy solution for the far-field noise, assuming each source coherence region as being embedded in a stratified, axisymmetric and 1-D base flow which is given by the local mean-velocity/mean-speed-of-sound profiles associated with the jet.

used to achieve a whole-spectrum jet-noise prediction at conditions different from 90-degree polar angle.

The model (4.16) for the two-point correlation coefficient of the fluctuating Reynolds-stress components is central in the present work, this model has been based on available measurements at a single location on a single-stream low-velocity jet, i. e. the Harper-Bourne[4, 5, 42] measurements. The assumption made for this model is that its shape is universal for jets and depends on a number of time-invariant parameters (τ_d, l_i, U_c, a, b, c). A validation of this assumption is required, here we call for a series of two-point velocimetry experiments in jets aimed to an estimate of the Reynolds-stress two-point covariance function on large volumes of the jet flow. Such experiments should be preferably made by adopting the middle point between the probes as fixed reference point, and by minimising the probe-introduction effect on the jet flow. Provided model (4.16) can be used to successfully fit the estimated correlation coefficient at various locations in any turbulent jets and for all Reynolds-stress components, spatial distributions of the time-invariant parameters τ_d, l_i and U_c could be identified; a fine tuning of the covariance-decay exponents a, b, c could also be performed.

Once a reliable model for the Reynolds-stress two-point correlation coefficient is established, the connection relations between the RANS solution and the acoustic model are the area where to concentrate research in order to produce reliable jet-noise predictions, based on time-inexpensive CFD computations. These relations are required in order to complete the RANS-solution description of the single-point statistics and to supply information for the two-point statistics. In addition to the output given by a RANS-solver the model essentially needs a spatial distribution of the following quantities:

- The fluctuating-Reynolds-stress mean-product tensor (components $\bar{q}_{ij,kl}$)
- The fluctuating-Reynolds stress autocorrelation-coefficient time scale τ_d
- The Reynolds-stress two-point covariance length scales l_i (i=1, 2, 3)
- The Reynolds-stress two-point CPSD phase velocity U_c

Velocimetry estimates of these quantities in a large volume of a jet could be used to define empirical relations to replace (or confirm) the proposed connection relations.

As mentioned in Chapter 4, a DNS or experimental analysis of the applied-force term could better frame the closure hypothesis (4.1.1), scaling the applied-force two-point covariance tensor from the fluctuating-Reynolds-stress two-point correlation tensor. We need a measure of the two-point correlation function associated with the fluctuations of

$$\frac{T'}{T}\frac{D\mathbf{u}}{Dt}$$

or, assuming convective temperature fluctuations and a Lilley-type base flow, of the term

$$\frac{1}{T}\left(\frac{D}{Dt}+\nabla\bar{\mathbf{u}}\cdot\right)\left(T'\mathbf{u}'\right)+\frac{1}{T}\left(\mathbf{u}'\otimes\mathbf{u}'\right)\cdot\nabla\bar{T}$$

In the present work we assumed that the applied-force two-point covariance is simply proportional to the two-point covariance of $(\mathbf{u}'\otimes\mathbf{u}')\cdot\left(\nabla\bar{T}/\bar{T}\right)$ and we scaled it, based on the two-point covariance of the unit-density Reynolds-stress $\mathbf{u}'\otimes\mathbf{u}'$. A comparison between a measured applied-force two-point covariance and the corresponding statistical function for the unit-density Reynolds-stress is then needed in order to validate the present model. Note that two-point measurements of the term $T'\mathbf{u}'$ would add important information regarding the two-point covariance function associated with $\left(\frac{D}{Dt}+\nabla\bar{\mathbf{u}}\cdot\right)(T'\mathbf{u}')$, which has not been directly modelled in the present work.

Appendix A

Definitions regarding tensors and reference systems

This appendix briefly describes the notation and the elements of Algebra and Geometry that are used in this work. Some definitions as in Appendix II of Truesdell[64] are adopted with restrictions regarding the vector-space dimensions (the vector spaces used here are of dimension 3) and the definition of the corresponding bases (the bases adopted in this work are always right-handed orthonormal bases; this makes the definition of reciprocal bases and covariant/contravariant coordinates redundant). A further source of information that has been used in this appendix and in general in the whole work is the Dictionary of Acoustics.[65] Section A.1 gives the basic definitions for tensors in the 3-D space and introduces the dot product and the tensor product. Some differentiation rules for tensor fields in the Euclidean space are given in section A.2. Section A.3 defines the jet-noise fixed-frame coordinate systems.

A.1 Definitions and notation for tensors

Scalars are indicated with italic letters. A vector is defined as a geometrical entity carrying the information to define a direction in the 3-D space and having a defined magnitude. Vectors are indicated with lower-case boldfaced letters. The modulus of an arbitrary vector $\mathbf{a}$ is indicated by the scalar a. Unit vectors are indicated by using the symbol $\hat{}$ as follows:

$$\hat{\mathbf{a}} = \mathbf{a}/a$$

A n-order tensor generalises the concept of vector to n directions. A scalar is a zero-order tensor, a vector is a first-order tensor. It is possible to identify tensors of higher order with linear mappings: a linear mapping of vectors into vectors is a second-order tensor, a linear mapping of vectors into second-order tensor is an order-3 tensor, and so on. Given an orthonormal basis

of 3 unit vectors, all vectors can be represented by their components according to this basis. An orthonormal basis will be generally indicated with the three vectors $\hat{\mathbf{e}}_1$, $\hat{\mathbf{e}}_2$, $\hat{\mathbf{e}}_3$. The basis is used to represent a general vector $\mathbf{a}$ as follows:

$$\mathbf{a} = a_1\hat{\mathbf{e}}_1 + a_2\hat{\mathbf{e}}_2 + a_3\hat{\mathbf{e}}_3 = a_i\hat{\mathbf{e}}_i$$

This expression embodies the notation for tensor components (corresponding italic letters with index) and the general use in this work of the Einstein convention for repeated indexes. The component along a given unit vector is extracted by forming the dot product between a vector and the unit vector:

$$\mathbf{a} \cdot \hat{\mathbf{e}}_i = a_i$$

It is easy to demonstrate how the definition above implies that the dot product between two vectors results in the sum of the products between corresponding coordinates.

$$\mathbf{a} \cdot \mathbf{b} = a_i b_i$$

Here $\mathbf{a}$ operates on $\mathbf{b}$ to get a scalar value; viewing $\mathbf{a}$ as linear mapping also identifies the $\cdot$ operator with "operates on" seen above in the general identification of tensors as linear mappings.

A further operation between vectors – the tensor product – allows for extending the concept of basis to tensors of any order greater than one. The tensor product between two vectors is indicated by the symbol $\otimes$. The tensor product between $\mathbf{a}$ and $\mathbf{b}$ is defined as the second-order tensor which operates on the arbitrary vector $\mathbf{c}$ as:

$$(\mathbf{a} \otimes \mathbf{b}) \cdot \mathbf{c} = (\mathbf{b} \cdot \mathbf{c})\,\mathbf{a} \tag{A.1}$$

The use of this operation allows for constructing a basis for second-order tensors by executing the 9 different tensor products between the basis unit vectors $\hat{\mathbf{e}}_1$, $\hat{\mathbf{e}}_2$, $\hat{\mathbf{e}}_3$. A general second-order tensor $\mathbf{S}$ can therefore be expressed in components as follows:

$$\mathbf{S} = S_{ij}\hat{\mathbf{e}}_i \otimes \hat{\mathbf{e}}_j$$

The given component of a tensor is extracted by forming the dot product with the corresponding basis tensor as follows:

$$S_{ij} = \mathbf{S} \cdot (\hat{\mathbf{e}}_i \otimes \hat{\mathbf{e}}_j) = (\mathbf{S} \cdot \hat{\mathbf{e}}_j) \cdot \hat{\mathbf{e}}_i$$

Here the dot-product operation is extended to tensors of order greater than one. The general

rule adopted in this work is expressed by the following examples:

$$\mathbf{S} \cdot \mathbf{a} = S_{ij} a_j \hat{\mathbf{e}}_i$$
$$\mathbf{a} \cdot \mathbf{S} = S_{ij} a_i \hat{\mathbf{e}}_j$$
$$\mathbf{a} \cdot \mathbf{S} \cdot \mathbf{b} = S_{ij} a_i b_j$$
$$\mathbf{S} \cdot \mathbf{T} = S_{ij} T_{ij}$$

It is to be noted that a dot product corresponds to an order contraction. The order contraction involved in the dot-product operation simply depends upon the orders of the two factors involved in the operation; the order of the resulting tensor is given by the difference between the orders of the factors. The components of the tensor product between two arbitrary vectors are given as follows:

$$(\mathbf{a} \otimes \mathbf{b}) \cdot (\hat{\mathbf{e}}_i \otimes \hat{\mathbf{e}}_j) = a_i b_j$$

The concepts of tensor product and dot product can be used to deal with tensors of any order. A basis of 3^3 tensors for order-3 tensors is given by the possible triple tensor products between the basis vectors $\hat{\mathbf{e}}_i$, a basis of 3^4 tensors for order-4 tensors is given by the possible quadruple products between the basis vectors and so on.

A.2 Differentiation rules for tensor fields

Points are locations in the 3-D space and are indicated by using the upper-case letters $\mathcal{A}$, $\mathcal{B}$... $\mathcal{Z}$. The set of all possible points is the Euclidean space. Tensor fields are functions defined over a connected Euclidean-space domain and taking values over any tensor space.[a] Given an arbitrary point $\mathcal{P}$ the functions $\rho(\mathcal{P})$, $\mathbf{v}(\mathcal{P})$, and $\mathbf{S}(\mathcal{P})$ correspondingly indicate the value in $\mathcal{P}$ for arbitrary fields of scalars, vectors and second-order tensors. Let a displacement in the Euclidean space be indicated by a vector $\boldsymbol{\delta}$ and let $\boldsymbol{\delta}$ connect our arbitrary point $\mathcal{P}$ to another point $\mathcal{Q}$ inside the domain of the above tensor fields. The variation of the tensor fields when changing the position from $\mathcal{P}$ to $\mathcal{Q}$ can be described as follows:

$$\rho(\mathcal{Q}) - \rho(\mathcal{P}) = \nabla(\rho) \cdot \boldsymbol{\delta} + \circ(\boldsymbol{\delta} \cdot \boldsymbol{\delta})$$
$$\mathbf{v}(\mathcal{Q}) - \mathbf{v}(\mathcal{P}) = \nabla(\mathbf{v}) \cdot \boldsymbol{\delta} + \circ(\boldsymbol{\delta} \cdot \boldsymbol{\delta})$$
$$\mathbf{S}(\mathcal{Q}) - \mathbf{S}(\mathcal{P}) = \nabla(\mathbf{S}) \cdot \boldsymbol{\delta} + \circ(\boldsymbol{\delta} \cdot \boldsymbol{\delta})$$

The above expressions include the use of the gradient operator ∇. The gradient operator is used to define the part of the tensor-field variation that is linear in the displacement. The gradient operator outputs a tensor field whose order equals $n + 1$ if applied to a continuous and differentiable n-order tensor field. The gradients of general tensors up to second order are

[a] Here tensor space is used as vector space whose elements are tensors of arbitrary order.

expressed as follows:

$$\begin{aligned}
\nabla(\rho) &= \frac{\partial \rho}{\partial x_i}\hat{\mathbf{e}}_i \\
\nabla(\mathbf{v}) &= \frac{\partial v_i}{\partial x_j}\hat{\mathbf{e}}_i \otimes \hat{\mathbf{e}}_j \\
\nabla(\mathbf{S}) &= \frac{\partial S_{ij}}{\partial x_k}\hat{\mathbf{e}}_i \otimes \hat{\mathbf{e}}_j \otimes \hat{\mathbf{e}}_k
\end{aligned} \tag{A.2}$$

The following expressions can be deduced for the gradients of some special tensor fields:

$$\begin{aligned}
\nabla(\mathbf{a}\otimes\mathbf{b}) &= \frac{\partial a_i\ b_j}{\partial x_k}\hat{\mathbf{e}}_i \otimes \hat{\mathbf{e}}_j \otimes \hat{\mathbf{e}}_k \\
&= \left(\frac{\partial a_i}{\partial x_k}\ b_j + a_i\ \frac{\partial b_j}{\partial x_k}\right)\hat{\mathbf{e}}_i \otimes \hat{\mathbf{e}}_j \otimes \hat{\mathbf{e}}_k \\
\nabla(\rho\mathbf{S}) &= \left(\frac{\partial \rho}{\partial x_k}S_{ij} + \rho\frac{\partial S_{ij}}{\partial x_k}\right)\hat{\mathbf{e}}_i \otimes \hat{\mathbf{e}}_j \otimes \hat{\mathbf{e}}_k \\
&= \mathbf{S}\otimes\nabla\rho + \rho\nabla\mathbf{S} \\
\nabla(\mathbf{S}\cdot\mathbf{a}) &= \frac{\partial S_{ij}a_j}{\partial x_k}\hat{\mathbf{e}}_i \otimes \hat{\mathbf{e}}_k \\
&= \nabla^{\mathrm{T}}(\mathbf{S})\cdot\mathbf{a} + \mathbf{S}\nabla(\mathbf{a}) \\
\nabla(\rho\mathbf{a}) &= \frac{\partial \rho a_i}{\partial x_j}\hat{\mathbf{e}}_i \otimes \hat{\mathbf{e}}_j \\
&= \rho\nabla(\mathbf{a}) + \mathbf{a}\otimes\nabla(\rho) \\
\nabla(\mathbf{a}\cdot\mathbf{b}) &= \frac{\partial a_i b_i}{\partial x_j}\hat{\mathbf{e}}_j \\
&= \nabla^T(\mathbf{a})\cdot\mathbf{b} + \nabla^T(\mathbf{b})\cdot\mathbf{a}
\end{aligned} \tag{A.3}$$

Here the superscript $^{\mathrm{T}}$ indicates the transpose operation; the transpose operator swaps the last two directions of a given tensor,

$$a_{i_1 i_2 \ldots i_{n-1} i_n}\left(\hat{\mathbf{e}}_{i_1}\otimes\hat{\mathbf{e}}_{i_2}\otimes\ldots\hat{\mathbf{e}}_{i_{n-1}}\otimes\hat{\mathbf{e}}_{i_n}\right)^{\mathrm{T}} = a_{i_1 i_2 \ldots i_{n-1} i_n}\left(\hat{\mathbf{e}}_{i_1}\otimes\hat{\mathbf{e}}_{i_2}\otimes\ldots\hat{\mathbf{e}}_{i_n}\otimes\hat{\mathbf{e}}_{i_{n-1}}\right)$$

The divergence is defined as the specific flux of a given tensor across a closed surface in the limit of the enclosed volume tending to zero. In contrast to the gradient operator the divergence yields a contraction in the tensor order: the divergence of an order-n tensor is a tensor of order $n-1$. The divergence is here evaluated by forming the trace of the gradient

as follows:

$$\mathrm{div}(\ ) = \nabla(\ ) \cdot \mathbf{I} \tag{A.4}$$

where $\mathbf{I}$ indicates the second-order identity tensor $\mathbf{I} = \delta_{ij}\hat{\mathbf{e}}_i \otimes \hat{\mathbf{e}}_j = \hat{\mathbf{e}}_i \otimes \hat{\mathbf{e}}_i$. Equation (A.4) can be used with the expressions (A.2) and (A.3) to derive the following results for the divergence of some tensor fields.

$$\begin{aligned}
\mathrm{div}(\mathbf{a}) &= \frac{\partial a_i}{\partial x_i} \\
\mathrm{div}(\mathbf{S}) &= \frac{\partial S_{ij}}{\partial x_j}\hat{\mathbf{e}}_i \\
\mathrm{div}(\mathbf{a} \otimes \mathbf{b}) &= \nabla(\mathbf{a}) \cdot \mathbf{b} + \mathbf{a}\ \mathrm{div}(\mathbf{b}) \\
\mathrm{div}(\rho\mathbf{S}) &= \mathbf{S} \cdot \nabla\rho + \rho\mathrm{div}(\mathbf{S}) \\
\mathrm{div}(\mathbf{S} \cdot \mathbf{v}) &= \mathrm{div}\left(\mathbf{S}^{\mathrm{T}}\right) \cdot \mathbf{v} + \mathbf{S}^{\mathrm{T}} \cdot \nabla(\mathbf{v}) \\
\mathrm{div}(\rho\mathbf{v}) &= \rho\mathrm{div}(\mathbf{v}) + \nabla(\rho) \cdot \mathbf{v}
\end{aligned} \tag{A.5}$$

A.3 Jet-noise coordinate systems

This work refers to three reference systems that are fixed to the jet nozzle. The systems describe the space associated with the jet aeroacoustic field by means of Cartesian, cylindrical and polar coordinates. The reference systems are defined by identifying an origin and corresponding fields of vector bases. The systems map the Euclidean space into triplets of scalars that are defined for each different system. The schematic in Fig. A.1 represents the position of the common origin of the three coordinate systems and the orientation of the cylindrical-system and spherical-system bases at an arbitrary location.

The Cartesian-coordinate system $(\mathcal{O}, \hat{\mathbf{e}}_1, \hat{\mathbf{e}}_2, \hat{\mathbf{e}}_3)$ is defined by placing the origin at the jet-exit section on the jet symmetry axis. The unit vector $\hat{\mathbf{e}}_1$ is aligned with the jet centreline and has the same direction as the jet flow. The components in $(\hat{\mathbf{e}}_1, \hat{\mathbf{e}}_2, \hat{\mathbf{e}}_3)$ of the vector $\mathbf{x} = \mathcal{P} - \mathcal{O}$, indicating an arbitrary point $\mathcal{P}$ (see. Fig. A.1) from $\mathcal{O}$, constitute the triplet (x_1, x_2, x_3) of Cartesian coordinates.

The cylindrical-coordinate system $(\mathcal{O}, \hat{\boldsymbol{\gamma}}_1, \hat{\boldsymbol{\gamma}}_2, \hat{\boldsymbol{\gamma}}_3)$ is defined by taking the polar axis coincident with the jet centreline. The azimuth angle φ that is associated with the arbitrary point $\mathcal{P}$ is measured from the plane containing the origin $\mathcal{O}$ and spanned by the unit vectors $\hat{\mathbf{e}}_1$ and $\hat{\mathbf{e}}_2$. Positive φ correspond to positive rotations around $\hat{\mathbf{e}}_1$ from this reference plane to $\mathcal{P}$. The vector bases that are associated with the cylindrical coordinates form a non constant field. Specifically the orientation of $\hat{\boldsymbol{\gamma}}_2$ and $\hat{\boldsymbol{\gamma}}_3$ varies with φ. The field is specified by the following

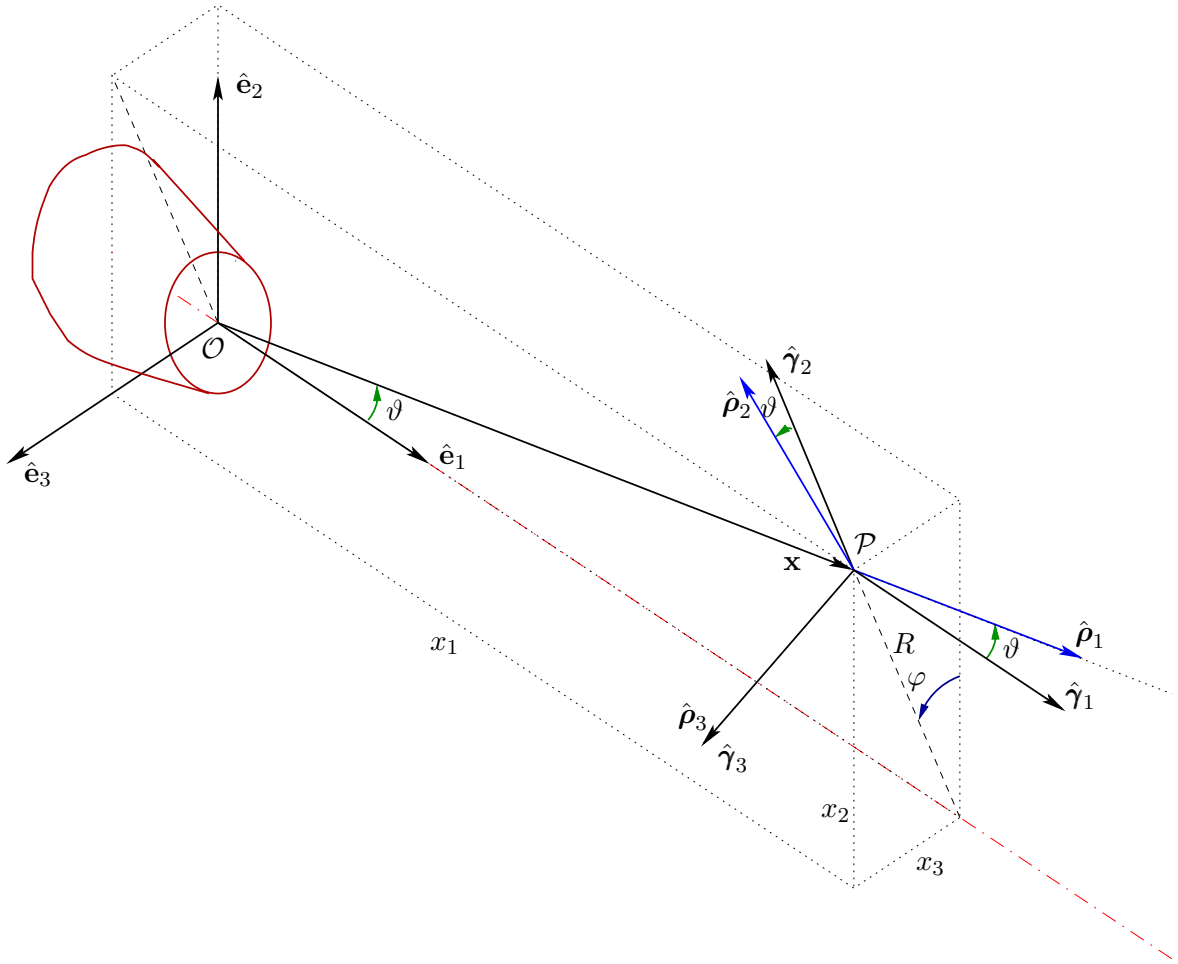

Figure A.1: Jet-noise coordinate systems: the Cartesian-system unit vectors (constant) are drawn at the origin $\mathcal{O}$ of the system. The cylindrical-coordinate and spherical-coordinate unit vectors (function of position) are represented at the generic point $\mathcal{P}$ defined from the origin $\mathcal{O}$ by the vector $\mathbf{x}$.

relations at the arbitrary location $\mathcal{P}$.

$$\begin{aligned}
\hat{\boldsymbol{\gamma}}_1 &= \hat{\mathbf{e}}_1 \\
\hat{\boldsymbol{\gamma}}_2(\varphi) &= (\cos\varphi)\,\hat{\mathbf{e}}_2 + (\sin\varphi)\,\hat{\mathbf{e}}_3 \\
\hat{\boldsymbol{\gamma}}_3(\varphi) &= (-\sin\varphi)\,\hat{\mathbf{e}}_2 + (\cos\varphi)\,\hat{\mathbf{e}}_3
\end{aligned} \tag{A.6}$$

The vector $\mathbf{x}$ can be expressed as:

$$\mathbf{x} = x_1\hat{\boldsymbol{\gamma}}_1 + R\hat{\boldsymbol{\gamma}}_2(0) + R\int_0^{\varphi}\hat{\boldsymbol{\gamma}}_3(\xi)\mathrm{d}\xi$$

or, equivalently,

$$\mathbf{x} = x_1\hat{\boldsymbol{\gamma}}_1 + R\hat{\boldsymbol{\gamma}}_2(\varphi)$$

where R indicates the distance of the point $\mathcal{P}$ from the polar axis. The triplet of cylindrical coordinates indicating the arbitrary point is (x_1, R, φ).

The system of spherical polar coordinates, centred on $\mathcal{O}$ can be indicated as $(\mathcal{O}, \hat{\boldsymbol{\rho}}_1, \hat{\boldsymbol{\rho}}_2, \hat{\boldsymbol{\rho}}_3)$. The field associated with the unit-vector basis can be easily derived for the arbitrary location $\mathbf{x}$ by rotating the corresponding cylindrical-coordinate unit vectors around $\hat{\boldsymbol{\gamma}}_3$ of the polar angle ϑ (angle between $\hat{\mathbf{e}}_1$ and $\mathbf{x}$). The spherical-coordinate unit-vector field is defined as function of ϑ and φ as follows:

$$\begin{aligned}
\hat{\boldsymbol{\rho}}_1(\vartheta,\varphi) &= (\cos\vartheta)\,\hat{\boldsymbol{\gamma}}_1 + (\sin\vartheta)\,\hat{\boldsymbol{\gamma}}_2(\varphi) \\
\hat{\boldsymbol{\rho}}_2(\vartheta,\varphi) &= (-\sin\vartheta)\,\hat{\boldsymbol{\gamma}}_1 + (\cos\vartheta)\,\hat{\boldsymbol{\gamma}}_2(\varphi) \\
\hat{\boldsymbol{\rho}}_3(\varphi) &= \hat{\boldsymbol{\gamma}}_3(\varphi)
\end{aligned} \tag{A.7}$$

As it is seen in Fig. A.1 the unit vector $\hat{\boldsymbol{\rho}}_1$ is aligned with $\mathbf{x}$. The position of the arbitrary point $\mathcal{P}$ can be indicated with respect to the origin as:

$$\mathbf{x} = x\hat{\boldsymbol{\rho}}_1(\vartheta,\varphi)$$

That is equivalent to:

$$\mathbf{x} = x\hat{\boldsymbol{\rho}}_1(0,0) + x\int_0^{\vartheta}\hat{\boldsymbol{\rho}}_2(\zeta,0)\mathrm{d}\zeta + R\int_0^{\varphi}\hat{\boldsymbol{\rho}}_3(\xi)\mathrm{d}\xi$$

The triplet of spherical coordinates associated with the arbitrary position $\mathcal{P}$ is given by (x, ϑ, φ).

Appendix B

Acoustic analogy for radiation through a parallel base flow

A Lilley[2] acoustic analogy has been derived by Goldstein[3] (Lilley–Goldstein analogy) with an exact forcing term given by a velocity quadrupole and a temperature dipole. The Lilley–Goldstein analogy is valid for unbounded inviscid flows of perfect gas. In this appendix, starting from the continuum-thermomechanics balances of mass, momentum, and energy, we derive the Goldstein[3] equation. An intermediate result is the expression of the conservation of mass and momentum in terms of the state variables $p^{\frac{1}{\gamma}}$, $\mathbf{u}$, c. These conservation equations are used for the derivation of the local-medium Lighthill analogy in section (3.1.1). The Goldstein[3] equation is finally rearranged to get the Lilley analogy in the form utilised by Morfey to derive the low-frequency asymptotic solution of the Lilley–Goldstein analogy equation (section 3.2).

For a non-stationary, compressible, isentropic flow that has no external sources of mass, momentum or energy, the conservation of mass, momentum, and energy can be expressed as follows:

$$\frac{D\rho}{Dt} + \rho \mathrm{div}(\mathbf{u}) = 0 \tag{B.1}$$

$$\frac{D\mathbf{u}}{Dt} + \frac{\nabla p}{\rho} = 0 \tag{B.2}$$

$$\frac{Ds}{Dt} = 0 \tag{B.3}$$

Here p is the thermodynamic pressure, ρ is the fluid density, $\mathbf{u}$ is the velocity vector, and s is the specific entropy. Since the fluid is a perfect gas, entropy conservation (B.3) implies for a material volume:

$$\frac{p^{\frac{1}{\gamma}}}{\rho} = \text{const.} \tag{B.4}$$

where γ is the specific-heat ratio c_p/c_ρ of the perfect gas. Taking the logarithm and the material derivative of expression (B.4) yields:

$$\frac{D\rho}{Dt} = \frac{\rho}{p^{\frac{1}{\gamma}}} \frac{Dp^{\frac{1}{\gamma}}}{Dt} \tag{B.5}$$

The entropy-conservation expression (B.5) allows for rewriting the conservation of mass (B.1) and momentum (B.2) as follows:

$$\begin{aligned}
mass \qquad & \frac{Dp^{\frac{1}{\gamma}}}{Dt} + p^{\frac{1}{\gamma}} \mathrm{div}(\mathbf{u}) = 0 \\
& \frac{\partial p^{\frac{1}{\gamma}}}{\partial t} + \mathrm{div}\left(p^{\frac{1}{\gamma}} \mathbf{u}\right) = 0
\end{aligned} \tag{B.6}$$

$$\begin{aligned}
momentum \qquad & \frac{D\mathbf{u}}{Dt} + \frac{\nabla p}{\rho} = 0 \\
& \frac{D\mathbf{u}}{Dt} + \frac{\gamma p}{\rho} \frac{p^{-1}}{\gamma} \nabla p = 0 \\
& p^{\frac{1}{\gamma}} \frac{D\mathbf{u}}{Dt} + c^2 \frac{p^{\frac{1}{\gamma}-1}}{\gamma} \nabla p = 0 \\
& \frac{Dp^{\frac{1}{\gamma}}\mathbf{u}}{Dt} - \frac{Dp^{\frac{1}{\gamma}}}{Dt}\mathbf{u} + c^2 \nabla p^{\frac{1}{\gamma}} = 0 \\
& \frac{\partial p^{\frac{1}{\gamma}}\mathbf{u}}{\partial t} + \nabla\left(p^{\frac{1}{\gamma}}\mathbf{u}\right) \cdot \mathbf{u} + p^{\frac{1}{\gamma}} \mathbf{u} \mathrm{div}(\mathbf{u}) + c^2 \nabla p^{\frac{1}{\gamma}} = 0 \\
& \frac{\partial p^{\frac{1}{\gamma}}\mathbf{u}}{\partial t} + \mathrm{div}\left(p^{\frac{1}{\gamma}} \mathbf{u} \otimes \mathbf{u}\right) + c^2 \nabla p^{\frac{1}{\gamma}} = 0
\end{aligned} \tag{B.7}$$

Here the flow is described by the space–time evolution of the state variables $\mathbf{u}$, $p^{\frac{1}{\gamma}}$, and speed of sound c. The relation $c^2 = \gamma p/\rho$ has been used to obtain (B.7).

A steady flow field is introduced as basis for the flow-variable variations. We we refer to this flow as the base flow; it is defined as follows:

$$\begin{cases}
\bar{\mathbf{u}} = U(x_2, x_3)\hat{\mathbf{e}}_1 \\
\bar{p} = p_\infty \\
\bar{c} = \bar{c}(x_2, x_3)
\end{cases} \tag{B.8}$$

Note that the base flow is invariant to translations in the direction $\hat{\mathbf{e}}_1$; it is a generalised Pridmore-Brown[66] flow admitting general variability in directions orthogonal to $\hat{\mathbf{e}}_1$ for both the velocity and the speed of sound.

The decomposition of the velocity vector into base-flow component and unsteady component

$$\mathbf{u}\left(x_1, x_2, x_3, t\right) = U\left(x_2, x_3\right)\hat{\mathbf{e}}_1 + \mathbf{u}'\left(x_1, x_2, x_3, t\right)$$

and the adoption of the base-flow convective time derivative

$$\frac{\bar{D}}{Dt} = \frac{\partial}{\partial t} + U\frac{\partial}{\partial x_1}$$

are introduced in the mass conservation equation to give: [a]

$$\frac{\bar{D}p^{\frac{1}{\gamma}}}{Dt} + \operatorname{div}\left(p^{\frac{1}{\gamma}}\mathbf{u}'\right) = 0 \tag{B.9}$$

Similarly the momentum balance can be expressed as follows: [b]

$$\frac{\bar{D}p^{\frac{1}{\gamma}}\mathbf{u}'}{Dt} + \left(\mathbf{u}'\cdot\nabla U\right)p^{\frac{1}{\gamma}}\hat{\mathbf{e}}_1 + \operatorname{div}\left(p^{\frac{1}{\gamma}}\mathbf{u}'\otimes\mathbf{u}'\right) + c^2\nabla p^{\frac{1}{\gamma}} = 0 \tag{B.10}$$

[a] Equation (B.9) is obtained by substituting the velocity decomposition in the mass balance, using the linearity of the div operator, and observing that $\operatorname{div}(f\hat{\mathbf{e}}_1) = \partial f/\partial x_1$ and that U does not depend on x_1:

$$\frac{\partial p^{\frac{1}{\gamma}}}{\partial t} + U\frac{\partial p^{\frac{1}{\gamma}}}{\partial x_1} + \operatorname{div}\left(p^{\frac{1}{\gamma}}\mathbf{u}'\right) = 0$$
$$\frac{\bar{D}p^{\frac{1}{\gamma}}}{Dt} + \operatorname{div}\left(p^{\frac{1}{\gamma}}\mathbf{u}'\right) = 0.$$

[b] The procedure to obtain equation (B.10) can be shown in explicit terms as:

$$U\frac{\partial p^{\frac{1}{\gamma}}}{\partial t}\hat{\mathbf{e}}_1 + \frac{\partial p^{\frac{1}{\gamma}}\mathbf{u}'}{\partial t} + \operatorname{div}\left(p^{\frac{1}{\gamma}}\left(U^2\hat{\mathbf{e}}_1\otimes\hat{\mathbf{e}}_1 + U\left(\hat{\mathbf{e}}_1\otimes\mathbf{u}' + \mathbf{u}'\otimes\hat{\mathbf{e}}_1\right) + \mathbf{u}'\otimes\mathbf{u}'\right)\right) + c^2\nabla p^{\frac{1}{\gamma}} = 0$$

$$U\frac{\partial p^{\frac{1}{\gamma}}}{\partial t}\hat{\mathbf{e}}_1 + \frac{\partial p^{\frac{1}{\gamma}}\mathbf{u}'}{\partial t} + \hat{\mathbf{e}}_1\otimes\hat{\mathbf{e}}_1\cdot\nabla\left(p^{\frac{1}{\gamma}}U^2\right) + \left(\hat{\mathbf{e}}_1\otimes\mathbf{u}' + \mathbf{u}'\otimes\hat{\mathbf{e}}_1\right)\cdot\nabla\left(p^{\frac{1}{\gamma}}U\right) +$$
$$+p^{\frac{1}{\gamma}}U\operatorname{div}\left(\hat{\mathbf{e}}_1\otimes\mathbf{u}' + \mathbf{u}'\otimes\hat{\mathbf{e}}_1\right) + \operatorname{div}\left(p^{\frac{1}{\gamma}}\mathbf{u}'\otimes\mathbf{u}'\right) + c^2\nabla p^{\frac{1}{\gamma}} = 0$$

$$U\frac{\partial p^{\frac{1}{\gamma}}}{\partial t}\hat{\mathbf{e}}_1 + \frac{\partial p^{\frac{1}{\gamma}}\mathbf{u}'}{\partial t} + U^2\frac{\partial p^{\frac{1}{\gamma}}}{\partial x_1}\hat{\mathbf{e}}_1 + \mathbf{u}'\cdot\nabla\left(p^{\frac{1}{\gamma}}U\right)\hat{\mathbf{e}}_1 + U\frac{\partial p^{\frac{1}{\gamma}}}{\partial x_1}\mathbf{u}' +$$
$$+p^{\frac{1}{\gamma}}U\left(\operatorname{div}\left(\mathbf{u}'\right)\hat{\mathbf{e}}_1 + \frac{\partial\mathbf{u}'}{\partial x_1}\right) + \operatorname{div}\left(p^{\frac{1}{\gamma}}\mathbf{u}'\otimes\mathbf{u}'\right) + c^2\nabla p^{\frac{1}{\gamma}} = 0$$

$$U\frac{\partial p^{\frac{1}{\gamma}}}{\partial t}\hat{\mathbf{e}}_1 + \frac{\bar{D}p^{\frac{1}{\gamma}}\mathbf{u}'}{Dt} + U^2\frac{\partial p^{\frac{1}{\gamma}}}{\partial x_1}\hat{\mathbf{e}}_1 + \mathbf{u}'\cdot\nabla\left(p^{\frac{1}{\gamma}}U\right)\hat{\mathbf{e}}_1 + p^{\frac{1}{\gamma}}U\operatorname{div}\left(\mathbf{u}'\right)\hat{\mathbf{e}}_1 +$$
$$+\operatorname{div}\left(p^{\frac{1}{\gamma}}\mathbf{u}'\otimes\mathbf{u}'\right) + c^2\nabla p^{\frac{1}{\gamma}} = 0$$

$$\left(\frac{\bar{D}p^{\frac{1}{\gamma}}}{Dt} + \operatorname{div}\left(p^{\frac{1}{\gamma}}\mathbf{u}'\right)\right)U\hat{\mathbf{e}}_1 + \frac{\bar{D}p^{\frac{1}{\gamma}}\mathbf{u}'}{Dt} + \left(\mathbf{u}'\cdot\nabla U\right)p^{\frac{1}{\gamma}}\hat{\mathbf{e}}_1 +$$
$$+\operatorname{div}\left(p^{\frac{1}{\gamma}}\mathbf{u}'\otimes\mathbf{u}'\right) + c^2\nabla p^{\frac{1}{\gamma}} = 0$$

Expression (B.10) is easily deduced by using the mass-conservation equation (B.9).

Some second order terms appearing in the momentum equation can be grouped as follows:

$$\mathbf{f} \coloneqq -\mathrm{div}\left(p^{\frac{1}{\gamma}}\mathbf{u}'\otimes\mathbf{u}'\right) - \left(c^2 - \bar{c}^2\right)\nabla p^{\frac{1}{\gamma}} \tag{B.11}$$

The defined vector $\mathbf{f}$ is equivalent to a scaled force per unit volume.[c] The tensor $p^{\frac{1}{\gamma}}\mathbf{u}'\otimes\mathbf{u}'$ can therefore be regarded as analogous to a scaled applied stress, while the vector $\left(c^2 - \bar{c}^2\right)\nabla p^{\frac{1}{\gamma}}$ is analogous to a scaled volume force. Introducing $\mathbf{f}$ in equation (B.10) gives

$$\frac{\bar{D}p^{\frac{1}{\gamma}}\mathbf{u}'}{Dt} + \left(\mathbf{u}'\cdot\nabla U\right)p^{\frac{1}{\gamma}}\hat{\mathbf{e}}_1 + \bar{c}^2\nabla p^{\frac{1}{\gamma}} = \mathbf{f} \tag{B.12}$$

If the divergence of the momentum equation (B.12) is subtracted from the base-flow convective derivative of the mass equation (B.9), observing that the operators divergence and base convective derivative do not commute,[d] the following scalar equation is obtained:

$$\frac{\bar{D}^2 p^{\frac{1}{\gamma}}}{Dt^2} - \nabla U\cdot\frac{\partial p^{\frac{1}{\gamma}}\mathbf{u}'}{\partial x_1} - \frac{\partial}{\partial x_1}\left(p^{\frac{1}{\gamma}}\mathbf{u}'\cdot\nabla U\right) - \mathrm{div}\left(\bar{c}^2\nabla p^{\frac{1}{\gamma}}\right) = -\mathrm{div}(\mathbf{f})$$

or, developing the x_1 partial derivative in the third term of the above,

$$\frac{\bar{D}^2 p^{\frac{1}{\gamma}}}{Dt^2} - 2\nabla U\cdot\frac{\partial p^{\frac{1}{\gamma}}\mathbf{u}'}{\partial x_1} - \mathrm{div}\left(\bar{c}^2\nabla p^{\frac{1}{\gamma}}\right) = -\mathrm{div}(\mathbf{f}) \tag{B.13}$$

Operating on (B.13) with the base-flow convective time derivative and commuting the operators $\dfrac{\partial}{\partial x_1}$ and $\dfrac{\bar{D}}{Dt}$ equation(B.13) yield the following:

$$\frac{\bar{D}}{Dt}\left(\frac{\bar{D}^2 p^{\frac{1}{\gamma}}}{Dt^2} - \mathrm{div}\left(\bar{c}^2\nabla p^{\frac{1}{\gamma}}\right)\right) - 2\nabla U\cdot\frac{\partial}{\partial x_1}\frac{\bar{D}p^{\frac{1}{\gamma}}\mathbf{u}'}{Dt} = -\frac{\bar{D}}{Dt}\mathrm{div}(\mathbf{f})$$

The momentum equation (B.12) can be used to remove the non-linear term on the left-hand

[c] An applied volume force can be easily introduced as forcing term of the momentum equation (B.2). This forcing term can be generalised as the sum of an applied volume force $\mathbf{f}_a$ and the divergence of an applied stress $\mathbf{S}_a$ (negative trace for compression):

$$\mathbf{f}_m = \mathbf{f}_a + \mathrm{div}(\mathbf{S}_a)$$

This applied load would appear on the right-hand side of equation (B.7) scaled by the factor

$$\frac{c^2}{\gamma\left(p^{\frac{1}{\gamma}}\right)^{\gamma-1}} = \frac{p^{\frac{1}{\gamma}}}{\rho}$$

[d] The divergence of the base convective time derivative of an arbitrary vector field $\mathbf{a}$ is given by:

$$\mathrm{div}\left(\frac{\bar{D}\mathbf{a}}{Dt}\right) = \mathrm{div}\left(\frac{\partial\mathbf{a}}{\partial t} + U\frac{\partial\mathbf{a}}{\partial x_1}\right) = \frac{\partial}{\partial t}\mathrm{div}(\mathbf{a}) + U\frac{\partial}{\partial x_1}\mathrm{div}(\mathbf{a}) + \nabla U\cdot\frac{\partial\mathbf{a}}{\partial x_1} = \frac{\bar{D}}{Dt}\mathrm{div}(\mathbf{a}) + \nabla U\cdot\frac{\partial\mathbf{a}}{\partial x_1}$$

side of the equation to give:

$$\frac{\bar{D}}{Dt}\left(\frac{\bar{D}^2 p^{\frac{1}{\gamma}}}{Dt^2} - \mathrm{div}\left(\bar{c}^2 \nabla p^{\frac{1}{\gamma}}\right)\right) + 2\nabla U \cdot \frac{\partial}{\partial x_1}\left(\left(\mathbf{u}' \cdot \nabla U\right) p^{\frac{1}{\gamma}} \hat{\mathbf{e}}_1 + \bar{c}^2 \nabla p^{\frac{1}{\gamma}} - \mathbf{f}\right) = -\frac{\bar{D}}{Dt}\mathrm{div}(\mathbf{f})$$

or, observing that ∇U is orthogonal to $\hat{\mathbf{e}}_1$ and moving to the right hand side of the equation the nonlinear terms,

$$\frac{\bar{D}}{Dt}\left(\frac{\bar{D}^2 p^{\frac{1}{\gamma}}}{Dt^2} - \mathrm{div}\left(\bar{c}^2 \nabla p^{\frac{1}{\gamma}}\right)\right) + 2\nabla U \cdot \frac{\partial}{\partial x_1}\left(\bar{c}^2 \nabla p^{\frac{1}{\gamma}}\right) = -\frac{\bar{D}}{Dt}\mathrm{div}(\mathbf{f}) + 2\nabla U \cdot \frac{\partial \mathbf{f}}{\partial x_1} \tag{B.14}$$

It is now useful to introduce the Goldstein variable π_G.

$$\pi_G \coloneqq \frac{p^{\frac{1}{\gamma}} - p_\infty^{\frac{1}{\gamma}}}{p_\infty^{\frac{1}{\gamma}}} \tag{B.15}$$

The Taylor expansion of π_G around the ambient pressure p_∞ shows the relation[e] between the Goldstein variable π_G and the acoustic pressure $p' = p - p_\infty$.

$$p - p_\infty + \circ\left(\left(p - p_\infty\right)^2\right) = \gamma p_\infty \pi_G \tag{B.16}$$

Dividing equation (B.14) by $p_\infty^{\frac{1}{\gamma}}$ the Lilley–Goldstein equation is expressed as a function of π_G as follows:

$$\frac{\bar{D}}{Dt}\left(\frac{\bar{D}^2 \pi_G}{Dt^2} - \mathrm{div}\left(\bar{c}^2 \nabla \pi_G\right)\right) + 2\bar{c}^2 \nabla U \cdot \frac{\partial}{\partial x_1}\left(\nabla \pi_G\right) = -\frac{\bar{D}}{Dt}\mathrm{div}(\boldsymbol{\phi}) + 2\nabla U \cdot \frac{\partial \boldsymbol{\phi}}{\partial x_1} \tag{B.17}$$

Here the vector $\boldsymbol{\phi}$ is given by

$$\boldsymbol{\phi} = \mathrm{div}\left(-\left(\pi_G + 1\right)\mathbf{u}' \otimes \mathbf{u}'\right) - \left(c^2 - \bar{c}^2\right)\nabla \pi_G. \tag{B.18}$$

where the applied-stress part $\mathbf{Q}$ is given as

$$\mathbf{Q} = -\left(\pi_G + 1\right)\mathbf{u}' \otimes \mathbf{u}' \tag{B.19}$$

and the applied-force part is

$$\mathbf{d} = -\left(c^2 - \bar{c}^2\right)\nabla \pi_G \tag{B.20}$$

[e]The proportionality between π_G and the acoustic-pressure field in all flow regions characterised by the property $p' << p_\infty$ implies that π_G can be successfully used in problems in which one intends to filter out the acoustic-pressure field from the rest of the flow. An example is given by applications that use Ffowcs Williams Hawkings surfaces for the far-field extrapolation of near-field acoustic fields. Morfey and Wright[67] discuss in detail the advantages of using the Goldstein variable π_G or alternative density-related scalars for acoustic analogies.

Equation (B.17) is the Goldstein[3] equation[f] expressing the Lilley acoustic analogy for a perfect gas in isentropic conditions; including an exact forcing term given by the applied-stress term (B.19), referred to by Goldstein as velocity quadrupole, and by the applied-force (B.20), referred to by Goldstein as temperature dipole.

Further processing of (B.17) is required in order to obtain the equation that is used for the present low-frequency approximation. Restricting (B.14) to axisymmetric base flows and dividing by $\bar{c}^2$ the following is obtained:

$$\frac{\bar{D}}{Dt}\left(\frac{1}{\bar{c}^2}\frac{\bar{D}^2\pi_G}{Dt^2}+\frac{1}{\bar{\rho}}\frac{\mathrm{d}\bar{\rho}}{\mathrm{d}R}\frac{\partial\pi_G}{\partial R}-\nabla^2\pi_G\right)+2\frac{\mathrm{d}U}{\mathrm{d}R}\frac{\partial^2\pi_G}{\partial R\partial x_1}=-\frac{1}{\bar{c}^2}\left(\frac{\bar{D}}{Dt}\mathrm{div}(\boldsymbol{\phi})-2\nabla U\cdot\frac{\partial\boldsymbol{\phi}}{\partial x_1}\right) \quad \text{(B.21)}$$

As explained by Morfey and Wright,[67] Tester and Morfey[40] looked for solutions of an equation having the same linear differential operator as equation (B.21) and forced by the generalised source distribution

$$\bar{\rho}\left(\frac{\bar{D}}{Dt}\right)^m\frac{(-\partial)^n s_{ij\ldots}}{\partial x_i\partial x_j\ldots} \quad \text{(B.22)}$$

If equation (B.21) is scaled by the factor $\bar{\rho}\bar{c}^2$ that – being proportional to $\bar{p}$ – is constant for the base flow, the following is obtained:

$$\frac{\bar{D}}{Dt}\left(\frac{1}{\bar{c}^2}\frac{\bar{D}^2\tilde{\pi}_G}{Dt^2}+\frac{1}{\bar{\rho}}\frac{\mathrm{d}\bar{\rho}}{\mathrm{d}R}\frac{\partial\tilde{\pi}_G}{\partial R}-\nabla^2\tilde{\pi}_G\right)+2\frac{\mathrm{d}U}{\mathrm{d}R}\frac{\partial^2\tilde{\pi}_G}{\partial R\partial x_1}=-\bar{\rho}\left(\frac{\bar{D}}{Dt}\mathrm{div}(\boldsymbol{\phi})-2\nabla U\cdot\frac{\partial\boldsymbol{\phi}}{\partial x_1}\right) \quad \text{(B.23)}$$

where

$$\tilde{\pi}_G=\bar{\rho}\bar{c}^2\pi_G$$

Solutions of equation (B.23) can be found by adopting the same procedure as in Tester and Morfey.[40] Analytical expressions of the solutions are available in the low and high frequency limits. The low-frequency Green function adopted in this work has been derived by Morfey as a solution of (B.23) in the low-frequency limit, by introducing the further small parameter d_J/λ and expanding the low-frequency solution of Ref. [40] to lowest order in this parameter.

[f] Equation (B.17) corresponds to equation (3.11) in Ref. [3]. Note that a sign difference in the forcing terms appears between the present solution and the equation published by Goldstein.[3]

Appendix C

The sound field of moving acoustic sources

The acoustic field associated with a constant-velocity moving monopole source in a stationary unbounded uniform medium is studied in this appendix. The Lorentz-transformation procedure as indicated in Morse and Ingard[68] and generalised by Morfey as in Hu Morfey and Sandham[69] is detailed in section C.1. By means of a Galilean transformation the monopole solution is expressed for an observer that is in general uniform motion relative to the medium. The source–observer emission-time coordinates are introduced in section C.2. In section C.3 the moving-monopole solution is rearranged and expressed in emission-time coordinates. The emission-time solution is then extended to singularities of dipole and quadrupole order. The acoustic fields for the moving singularities are developed retaining the near-field terms.

C.1 The pressure field of a moving monopole by Lorentz transformation

This section details the solution for the acoustic pressures generated by a constant-velocity moving point source. The acoustic medium is assumed to be at rest. A reference frame fixed to the medium is indicated as $(\mathcal{P}, \hat{\mathbf{e}}_1, \hat{\mathbf{e}}_2, \hat{\mathbf{e}}_3)$, where the unit vector $\hat{\mathbf{e}}_1$ is aligned with the source velocity $\mathbf{v}$. The point-source position in $(\mathcal{P}, \hat{\mathbf{e}}_1, \hat{\mathbf{e}}_2, \hat{\mathbf{e}}_3)$ is indicated by the coordinates (y_1, y_2, y_3). A second frame of reference is connected to the moving source and is called $(\mathcal{P}', \hat{\mathbf{e}}_1, \hat{\mathbf{e}}_2, \hat{\mathbf{e}}_3)$. Frames $(\mathcal{P}, \hat{\mathbf{e}}_1, \hat{\mathbf{e}}_2, \hat{\mathbf{e}}_3)$ and $(\mathcal{P}', \hat{\mathbf{e}}_1, \hat{\mathbf{e}}_2, \hat{\mathbf{e}}_3)$ coincide at $t = 0$. The position of the source in $(\mathcal{P}', \hat{\mathbf{e}}_1, \hat{\mathbf{e}}_2, \hat{\mathbf{e}}_3)$ is constant and is indicated by the coordinates (y'_1, y'_2, y'_3). The coordinates indicating the source position in $(\mathcal{P}, \hat{\mathbf{e}}_1, \hat{\mathbf{e}}_2, \hat{\mathbf{e}}_3)$ and $(\mathcal{P}', \hat{\mathbf{e}}_1, \hat{\mathbf{e}}_2, \hat{\mathbf{e}}_3)$ are related by

the Galilean transformation associated with the uniform motion of the source:

$$\begin{cases} y_1 = y_1' + vt \\ y_2 = y_2' \\ y_3 = y_3' \end{cases}$$

The acoustic problem can be formulated in the reference frame $(\mathcal{P}, \hat{\mathbf{e}}_1, \hat{\mathbf{e}}_2, \hat{\mathbf{e}}_3)$ as a wave equation that is forced by a spatial Dirac function of prescribed time-varying intensity a and whose position changes according to the source velocity:

$$\frac{1}{c^2}\frac{\partial^2 p}{\partial t^2} - \nabla^2 p = \mathrm{a}(t)\delta(x_1 - y_1' - vt)\delta(x_2 - y_2')\delta(x_3 - y_3') \tag{C.1}$$

Here p is the acoustic pressure. If the modulus of the source velocity v is smaller than the speed of sound c the following Lorentz transformation can be defined:

$$\begin{cases} x_1'' = \beta^2 (x_1 - vt) \\ x_2'' = \beta x_2 \\ x_3'' = \beta x_3 \\ t'' = \beta^2 \left(t - \dfrac{v}{c^2} x_1\right) \end{cases} \qquad \beta^2 = \frac{1}{1 - v^2/c^2} \qquad \begin{cases} x_1 = x_1'' + vt'' \\ x_2 = x_2''/\beta \\ x_3 = x_3''/\beta \\ t \ = t'' + \dfrac{v}{c^2} x_1'' \end{cases} \tag{C.2}$$

Using the transformations (C.2) the scalar field p can be considered as function of the variables x_1'', x_2'', x_3'' and t''. The problem expressed by equation (C.1) can be moved to the new space-time coordinates to give:

$$\beta^2 \left(\frac{1}{c^2}\frac{\partial^2 p}{\partial t''^2} - \nabla^2 p\right) = \beta^4 \mathrm{a}\left(t'' + \frac{v}{c^2} x_1''\right) \delta\left(x_1'' - \beta^2 y_1'\right) \delta\left(x_2'' - \beta y_2'\right) \delta\left(x_3'' - \beta y_3'\right) \tag{C.3}$$

In order to obtain equation (C.3), the following equivalence has been used for the Dirac distribution

$$\delta\left(\frac{x}{\beta}\right) = \beta\delta\left(x\right)$$

and the partial derivatives have been developed by using the chain rule as follows:

$$\begin{aligned} \frac{\partial^2 p}{\partial t^2} &= \beta^4 \left(\frac{\partial^2 p}{\partial t''^2} - 2v\frac{\partial^2 p}{\partial x_1'' \partial t''} + v^2 \frac{\partial^2 p}{\partial x_1''^2}\right) \\ \frac{\partial^2 p}{\partial {x_1}^2} &= \beta^4 \left(\frac{\partial^2 p}{\partial x_1''^2} - 2\frac{v}{c^2}\frac{\partial^2 p}{\partial x_1'' \partial t''} + \frac{v^2}{c^4}\frac{\partial^2 p}{\partial t''^2}\right) \\ \frac{\partial^2 p}{\partial {x_2}^2} &= \beta^2 \frac{\partial^2 p}{\partial x_2''^2} \\ \frac{\partial^2 p}{\partial {x_3}^2} &= \beta^2 \frac{\partial^2 p}{\partial x_3''^2} \end{aligned}$$

Equation (C.3) can be further developed by dividing with β^2 and using the sifting property of the Dirac function operating on x_1'', to give:

$$\frac{1}{c^2}\frac{\partial^2 p}{\partial t''^2} - \nabla^2 p = \beta^2 \mathrm{a}\left(t'' + \frac{v}{c^2}\beta^2 y_1'\right)\delta\left(x_1'' - \beta^2 y_1'\right)\delta\left(x_2'' - \beta y_2'\right)\delta\left(x_3'' - \beta y_3'\right) \tag{C.4}$$

Equation (C.4) is a wave equation forced by a stationary point source. The solution of equation (C.4) with free-field boundary conditions for an observer located at the position indicated by the coordinates (x_1'', x_2'', x_3'') and at the time t'' is given by:

$$p\left(x_1'', x_2'', x_3'', t''\right) = \frac{\beta^2 \mathrm{a}\left(t'' + \beta^2 \frac{v}{c^2} y_1' - \frac{r''}{c}\right)}{4\pi r''} \tag{C.5}$$

where r'' indicates the source–observer distance in the transformed coordinates:

$$r'' \coloneqq \sqrt{\left(x_1'' - \beta^2 y_1'\right)^2 + \left(x_2'' - \beta y_2'\right)^2 + \left(x_3'' - \beta y_3'\right)^2}$$

Going back to the original coordinates and defining r_M as

$$r_M \coloneqq \frac{r''}{\beta^2} = \sqrt{\left(x_1 - y_1' - vt\right)^2 + \left(1 - \frac{v^2}{c^2}\right)\left(\left(x_2 - y_2'\right)^2 + \left(x_3 - y_3'\right)^2\right)} \tag{C.6}$$

equation (C.5) is transformed to give

$$p\left(x_1, x_2, x_3, t\right) = \frac{\mathrm{a}\left(\beta^2\left(t - \frac{v}{c^2}\left(x_1 - y_1'\right) - \frac{r_M}{c}\right)\right)}{4\pi r_M} \tag{C.7}$$

Expression (C.7) represents the free-field solution for a prescribed point source moving with constant subsonic velocity in a stationary medium. This solution is valid for a generic observer in a position (x_1, x_2, x_3) which is rigidly connected to the medium. It can be rearranged to make explicit the dependence on the source–observer relative position at the time t:

$$p\left(x_1, x_2, x_3, t\right) = \frac{\mathrm{a}\left(t - \beta^2\left(\frac{v}{c^2}\left(x_1 - y_1' - vt\right) - \frac{r_M}{c}\right)\right)}{4\pi r_M} \tag{C.8}$$

The solution for an observer that is in uniform motion relative to the medium is derived by applying to expressions (C.8) and (C.6) the Galilean transformation:

$$\begin{cases} \tilde{x}_1 = x_1 - \tilde{u}_1 t \\ \tilde{x}_2 = x_2 - \tilde{u}_2 t \\ \tilde{x}_3 = x_3 - \tilde{u}_3 t \end{cases}$$

where $\tilde{\mathbf{u}}$ is the time-invariant velocity of the observer. The acoustic-pressure field at the generic position indicated by the vector $\tilde{\mathbf{x}}$ from the origin[a] of a reference frame fixed with the observer (the moving-observer frame) is given as follows:

$$p\left(\tilde{\mathbf{x}},t\right)=\frac{\mathrm{a}\left(t-\beta^2\left(\frac{v}{c^2}\left(\tilde{x}_1-y_1'+\left(\tilde{u}_1-v\right)t\right)-\frac{r_M}{c}\right)\right)}{4\pi r_M} \tag{C.9}$$

where the modified distance is given by

$$r_M=\sqrt{\left(\tilde{x}_1-y_1'+\left(\tilde{u}_1-v\right)t\right)^2+\left(1-\frac{v^2}{c^2}\right)\left(\left(\tilde{x}_2-y_2'+\tilde{u}_2t\right)^2+\left(\tilde{x}_3-y_3'+\tilde{u}_3t\right)^2\right)} \tag{C.10}$$

We now identify with $\tilde{\mathbf{y}}$ the vector that, at the instant t, indicates the source position from the origin of the moving-observer frame.

$$\tilde{\mathbf{y}}=\tilde{y}_1\hat{\mathbf{e}}_1+\tilde{y}_2\hat{\mathbf{e}}_2+\tilde{y}_3\hat{\mathbf{e}}_3=\left(y_1'+vt-\tilde{u}_1t\right)\hat{\mathbf{e}}_1+\left(y_2'-\tilde{u}_2t\right)\hat{\mathbf{e}}_2+\left(y_2'-\tilde{u}_3t\right)\hat{\mathbf{e}}_3 \tag{C.11}$$

Expressions (C.9) and (C.10) are here viewed as function of the source-position coordinates $(\tilde{y}_1,\tilde{y}_2,\tilde{y}_3)$ in the moving-observer frame, corresponding to expressions (C.8) and (C.6) in the medium-fixed frame $(\mathcal{P},\hat{\mathbf{e}}_1,\hat{\mathbf{e}}_2,\hat{\mathbf{e}}_3)$. Indicating with $\mathbf{r}$ the vector that connects the source position to the observer position,

$$\mathbf{r}=\tilde{\mathbf{x}}-\tilde{\mathbf{y}}(t)=\mathbf{x}(t)-\mathbf{y}(t) \tag{C.12}$$

the moving-source acoustic field is related to the instantaneous separation between source and observer as follows:

$$p\left(\mathbf{x},t\right)=\frac{\mathrm{a}\left(t-\beta^2\left(\frac{vr_1}{c^2}-\frac{r_M}{c}\right)\right)}{4\pi r_M} \tag{C.13}$$

where the modified distance is given by

$$r_M=\sqrt{r_1^2+\left(1-\frac{v^2}{c^2}\right)\left(r_2^2+r_3^2\right)} \tag{C.14}$$

Provided the symbols always indicate the same corresponding physical quantities, and the given reference frame is aligned with the velocity of the source relative to the medium, expressions (C.13) and (C.14) are symbolically invariant for Galilean transformations associated with the observer motion.

The solution for the acoustic pressures recorded by an observer which moves at the same speed as the source[b] is of interest in the study of random pressure fields. This solution can be

[a]Note that at $t=0$ the origin of this reference frame coincides with the origin of the reference frame that is fixed to the medium. Corresponding basis vectors of the reference frames are aligned.

[b]In Appendix D, we generalise the notion of source speed. The source velocity $\mathbf{v}$ becomes simply the velocity

obtained by specialising expressions (C.9) and (C.10) to the case

$$\tilde{\mathbf{u}} = v\hat{\mathbf{e}}_1$$

This yields

$$p\left(\mathbf{x}', t\right) = \frac{\mathrm{a}\left(t - \beta^2 \frac{v}{c^2}\left(x_1' - y_1'\right) - \beta^2 \frac{r_M'}{c}\right)}{4\pi r_M} \tag{C.15}$$

$$r_M = \sqrt{\left(x_1' - y_1'\right)^2 + \left(1 - \frac{v^2}{c^2}\right)\left(\left(x_2' - y_2'\right)^2 + \left(x_3' - y_3'\right)^2\right)} \tag{C.16}$$

The acoustic-pressure solution (C.15) corresponds to the problem of a fixed source, fixed observer, and moving medium between source and observer. In this problem the medium moves with constant velocity $-v\hat{\mathbf{e}}_1$. This solution coincides with the solution of the convective wave equation forced by a fixed space-time Dirac function.

C.2 Emission-time coordinates

The use of emission-time coordinates allows a compact expression for the acoustic field associated with moving sources. This section introduces the concepts of emission-time separation, emission-time polar angle and Doppler factor for a source that is moving in a uniform medium at rest. A series of spatial derivatives that need to be computed to obtain the Green functions for multipole moving sources are also derived. As in section C.1, it is assumed that a point source is in motion with velocity $\mathbf{v}$ in a uniform medium at rest (constant speed of sound c). If a wave is emitted by the source at a given instant t_E it will propagate in the medium maintaining a spherical wavefront. The wavefront will hit a given stationary observer (location indicated by $\mathbf{x}$ from the origin $\mathcal{P}$) at the instant t. The schematic in Fig. C.1 presents the situation at the instant t. If the position of the source at the times t_E ($\mathcal{S}_E$) and t ($\mathcal{S}$) is indicated respectively by the vectors $\mathbf{y}_E$ and $\mathbf{y}$ from the origin $\mathcal{P}$, the emission-time separation vector $\mathbf{r}_E$ is defined as follows:

$$\mathbf{r}_E \coloneqq \mathbf{x} - \mathbf{y}_E \tag{C.17}$$

The modulus of $\mathbf{r}_E$ is the emission-time distance between source and observer. The emission-time distance r_E divided by the speed of sound will give the time lag between emission at the source location and reception at the observer position:

$$r_E/c = t - t_E$$

of the reference frame that most conveniently describes the source region. In aeroacoustic applications, this is the reference frame in which the source distribution is statistically stationary.

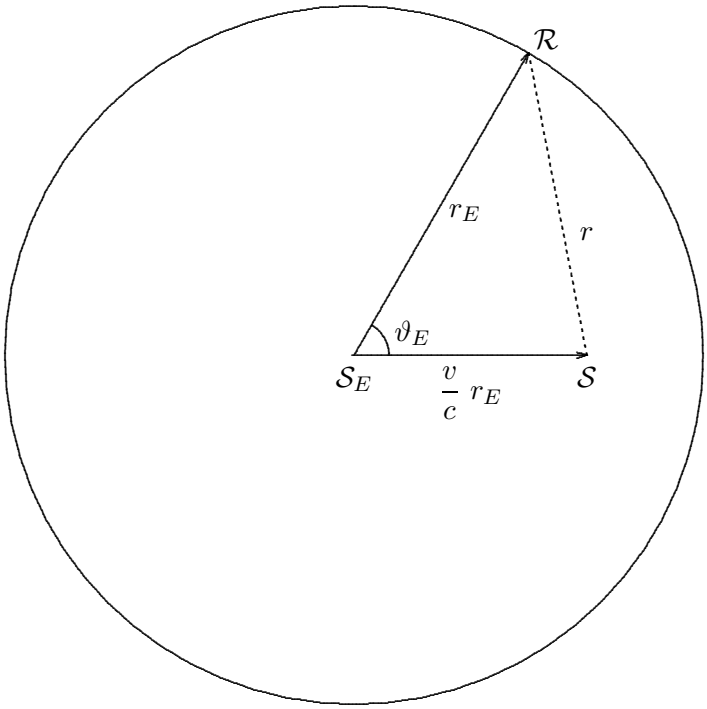

Figure C.1: The circle in the diagram indicates the wavefront at the time t when it reaches the observer at $\mathcal{R}$. The wave is emitted by a moving source of velocity $v\hat{\mathbf{e}}_1$ in a quiescent medium. The location of the source at time of emission is indicated by $\mathcal{S}_E$. The emission-time separation $\mathbf{r}_E = \overrightarrow{\mathcal{S}_E\mathcal{R}} = \mathbf{x} - \mathbf{y}_E$ and the vector $Mr_E\hat{\mathbf{e}}_1 = \overrightarrow{\mathcal{S}\mathcal{S}_E} = \mathbf{y} - \mathbf{y}_E$ are indicated by solid lines. The dashed line indicates the separation vector $\mathbf{r} = \overrightarrow{\mathcal{S}\mathcal{R}} = \mathbf{x} - \mathbf{y}$ giving the observer position from the source location at time t. The emission-time polar angle is indicated by ϑ_E.

The emission-time separation is related to the source–observer separation $\mathbf{r}$ as follows (see Fig. C.1):

$$\mathbf{r}_E = \frac{r_E}{c}\mathbf{v} + \mathbf{r} = \left(r_1 + \frac{r_E v}{c}\right)\hat{\mathbf{e}}_1 + r_2\hat{\mathbf{e}}_2 + r_3\hat{\mathbf{e}}_3$$

where r_i are the components of the separation vector $\mathbf{r}$. If we indicate with M the source-motion Mach number

$$M \coloneqq \frac{v}{c} \tag{C.18}$$

the emission-time separation vector can be expressed as follows:

$$\mathbf{r}_E = (r_1 + Mr_E)\,\hat{\mathbf{e}}_1 + r_2\hat{\mathbf{e}}_2 + r_3\hat{\mathbf{e}}_3 \tag{C.19}$$

The squared emission-time distance is therefore given by

$$r_E^2 = (r_1 + M\ r_E)^2 + r_2^2 + r_3^2. \tag{C.20}$$

The latter allows for expressing the emission-time distance as function of the components r_i and the signed Mach number M. By solving (C.20) for r_E and considering the positive solution

at subsonic source velocity the following is obtained:

$$r_E = \frac{Mr_1 + \sqrt{M^2 r_1^2 + r^2 - M^2 r^2}}{1 - M^2} \tag{C.21}$$

It is noted that the square-root term in equation (C.21) equals the modified distance r_M which has been introduced for the acoustic field of moving sources in expression (C.6). This leads to the simpler expression for the emission-time distance:

$$r_E = \frac{Mr_1 + r_M}{1 - M^2} \tag{C.22}$$

The emission-time polar angle (Fig. C.1) is defined as the angle between the source-velocity vector $\mathbf{v}$ and the emission-time separation vector $\mathbf{r}_E$. The relation linking the r_1 component to the emission-time distance and polar angle is

$$r_1 = r_E \cos\vartheta_E - Mr_E. \tag{C.23}$$

This expression, inserted in (C.22), gives for the emission-time distance:

$$r_E = \frac{r_M}{1 - M\cos\vartheta_E} \tag{C.24}$$

The ratio between the emission-time distance and the modified distance is a scalar. This scalar is generally referred to as a Doppler factor and is defined by the following expression:

$$D_v \coloneqq \frac{1}{1 - \dfrac{\mathbf{v}\cdot\mathbf{r}_E}{cr_E}} = \frac{1}{1 - M\hat{\mathbf{r}}_E\cdot\hat{\mathbf{e}}_1} = \frac{1}{1 - M\cos\vartheta_E} \tag{C.25}$$

The gradient $\nabla_{\mathbf{x}}$ of the emission-time distance, calculated by varying the observer position with t held constant, needs to be evaluated when deriving the acoustic field of moving multipole inhomogeneities. Taking the partial derivatives in expression (C.22) with respect to x_i, t being held constant, gives:

$$\begin{aligned}
\frac{\partial r_E}{\partial x_1} &= \frac{M + \dfrac{\partial r_M}{\partial x_1}}{(1 - M^2)} = \frac{M + \dfrac{r_1}{r_M}}{(1 - M^2)} \\
\frac{\partial r_E}{\partial x_2} &= \frac{\dfrac{\partial r_M}{\partial x_2}}{(1 - M^2)} = \frac{\dfrac{\left(1 - M^2\right) r_2}{r_M}}{(1 - M^2)} \\
\frac{\partial r_E}{\partial x_2} &= \frac{\dfrac{\partial r_M}{\partial x_3}}{(1 - M^2)} = \frac{\dfrac{\left(1 - M^2\right) r_3}{r_M}}{(1 - M^2)}
\end{aligned} \tag{C.26}$$

By using (C.24) and simplifying, (C.26) becomes:

$$\begin{aligned}\frac{\partial r_E}{\partial x_1} &= \frac{M + \dfrac{r_1}{r_E\left(1 - M\cos\vartheta_E\right)}}{\left(1 - M^2\right)} \\ \frac{\partial r_E}{\partial x_2} &= \frac{r_2}{r_E\left(1 - M\cos\vartheta_E\right)} \\ \frac{\partial r_E}{\partial x_2} &= \frac{r_3}{r_E\left(1 - M\cos\vartheta_E\right)}\end{aligned} \tag{C.27}$$

Here we used expression (C.14) and the identity $\partial/\partial x_i = \partial/\partial r_i$. The partial derivative $\partial r_E/\partial x_1$ can be further simplified by introducing equation (C.23) to get:

$$\frac{\partial r_E}{\partial x_1} = \frac{M r_E\left(1 - M\cos\vartheta_E\right) + r_E\cos\vartheta_E - M r_E}{r_E\left(1 - M\cos\vartheta_E\right)\left(1 - M^2\right)} = \frac{r_E\cos\vartheta_E}{r_E\left(1 - M\cos\vartheta_E\right)} \tag{C.28}$$

Finally, by noting that

$$\mathbf{r}_E \cdot \hat{\mathbf{e}}_1 = r_E\cos\vartheta_E \qquad \mathbf{r}_E \cdot \hat{\mathbf{e}}_2 = r_2 \qquad \mathbf{r}_E \cdot \hat{\mathbf{e}}_3 = r_3$$

and by introducing (C.28) into (C.27), the expression for the partial derivatives of the emission-time distance is given as follows:

$$\begin{aligned}\frac{\partial r_E}{\partial x_1} &= \frac{\mathbf{r}_E \cdot \hat{\mathbf{e}}_1}{r_E\left(1 - M\cos\vartheta_E\right)} \\ \frac{\partial r_E}{\partial x_2} &= \frac{\mathbf{r}_E \cdot \hat{\mathbf{e}}_2}{r_E\left(1 - M\cos\vartheta_E\right)} \\ \frac{\partial r_E}{\partial x_2} &= \frac{\mathbf{r}_E \cdot \hat{\mathbf{e}}_3}{r_E\left(1 - M\cos\vartheta_E\right)}\end{aligned} \tag{C.29}$$

This means that the observer-position gradient $\nabla_{\mathbf{x}}$ of the emission-time distance is given by the unit vector which points towards the observer location from $\mathbf{y}_E$ scaled by a Doppler factor:

$$\nabla_{\mathbf{x}}\left(r_E\right) = D_v\frac{\mathbf{r}_E}{r_E} = D_v\hat{\mathbf{r}}_E \tag{C.30}$$

A further expression to be evaluated when deriving the acoustic field of moving multipole inhomogeneities is the gradient $\nabla_{\mathbf{x}}$ of the ratio between Doppler factor and emission-time distance, calculated by varying the observer position with t held constant. In order to derive $\nabla_{\mathbf{x}}\left(D_v/r_E\right)$, the observer-position gradient, with t constant, of the emission-time separation vector is determined first. Expression (C.30) is used to express the gradient of the emission-

time separation vector $\mathbf{r}_E$ as follows:[a]

$$\nabla_{\mathbf{x}}(\mathbf{r}_E) = \mathbf{I} + MD_v\hat{\mathbf{e}}_1 \otimes \hat{\mathbf{r}}_E \tag{C.31}$$

The observer-position gradient of the ratio between the Doppler factor and the emission-time distance is evaluated as follows:

$$\nabla_{\mathbf{x}}\left(\frac{D_v}{r_E}\right) = \nabla_{\mathbf{x}}\left(\frac{1}{r_E + M\mathbf{r}_e \cdot \hat{\mathbf{e}}_1}\right) = \left(\frac{D_v}{r_E}\right)^2 \left(-\nabla_{\mathbf{x}}(r_E) + M\nabla_{\mathbf{x}}^{\mathrm{T}}(\mathbf{r}_e) \cdot \hat{\mathbf{e}}_1\right) \tag{C.32}$$

By using equations (C.30) and (C.31) expression (C.32) can be expressed as follows:

$$\nabla_{\mathbf{x}}\left(\frac{D_v}{r_E}\right) = \left(\frac{D_v}{r_E}\right)^2 \left(-D_v\hat{\mathbf{r}}_E + M\left(\hat{\mathbf{e}}_1 + MD_v\hat{\mathbf{r}}_E\right)\right)$$

Grouping the components along the same direction yields the following

$$\nabla_{\mathbf{x}}\left(\frac{D_v}{r_E}\right) = \left(\frac{D_v}{r_E}\right)^2 \frac{\mathbf{v}}{c} - \left(1 - M^2\right)\left(\frac{D_v}{r_E}\right)^3 \mathbf{r}_E \tag{C.33}$$

C.3 The acoustic field of moving singularities in emission-time coordinates

The result found in section C.1 for the acoustic-pressure field of a moving point source in a uniform medium is used to write the solution for the acoustic monopole in emission-time coordinates. The solution is generalised to any scalar field g that is a solution of the wave equation

$$\frac{1}{c^2}\frac{\partial^2 g}{\partial t^2} - \nabla^2 g = a(t)\delta(\mathbf{x} - \mathbf{y})$$

where $\delta(\mathbf{x} - \mathbf{y}) = \delta(x_1 - y_1)\delta(x_2 - y_2)\delta(x_3 - y_3)$ and $\mathbf{y}$ varies with time as seen in section C.1. Free-field boundary conditions are assumed for the problem. The solution for moving dipoles and quadrupoles is obtained by generalising the problem to multipole sources. This is obtained by assuming that the forcing term is a N-order tensor that is operated N times by a divergence operator.

$$\frac{1}{c^2}\frac{\partial^2 g^{(N)}}{\partial t^2} - \nabla^2 g^{(N)} = \mathrm{div}\big(...\mathrm{div}\big(\mathrm{div}(a_{i_1 i_2 ... i_N}(t)\hat{\mathbf{e}}_{i_1} \otimes \hat{\mathbf{e}}_{i_2} \otimes ... \otimes \hat{\mathbf{e}}_{i_N}\delta(\mathbf{x} - \mathbf{y}))_1\big)_2 ...\big)_N \tag{C.34}$$

[a] The emission-time separation vector is given by expression (C.19). By noting that the gradient $\nabla_{\mathbf{x}}$ of the source-observer separation $\mathbf{r}$ is given by the identity tensor $\mathbf{I}$ and by using (A.3), the observer-position gradient of $\mathbf{r}_E$ is expressed as follows:

$$\nabla_{\mathbf{x}}(\mathbf{r}_E) = \mathbf{I} + M\hat{\mathbf{e}}_1 \otimes \nabla_{\mathbf{x}}(r_e)$$

Expression (C.31) is obtained by introducing equation (C.30).

In general the solution of the N-order problem (C.34) can be obtained by taking the divergence of the vector field that is solution of the $(N-1)$-order problem. This procedure is applied in this section to obtain the dipole solution $g^{(1)}$ and the quadrupole solution $g^{(2)}$ from the monopole solution $g^{(0)}$. For the multipole cases the full free-field solution is derived; the higher-order terms in the emission-time distance are then removed, leaving a solution whose validity is limited to the acoustic far field.

C.3.1 The acoustic field of moving monopoles

As shown in section C.1 the acoustic field of a subsonic moving point source in an undisturbed uniform medium at rest can be conveniently evaluated as a function of the separation vector between source and observer. Assuming that the reference-frame base vector $\hat{\mathbf{e}}_1$ is aligned with the velocity $\mathbf{v}$ of the source relative to the medium, this acoustic field is given by generalising expressions (C.13) and (C.14) to the arbitrary source position $\mathbf{y}$ and the arbitrary acoustic field g:

$$\begin{cases} g^{(0)}\left(\mathbf{x}|\mathbf{y},t\right) = \dfrac{a\left(t-\beta^2\dfrac{vr_1}{c^2}-\beta^2\dfrac{r_M}{c}\right)}{4\pi r_M} \\ \\ r_M = \sqrt{r_1^2+\left(1-M^2\right)\left(r_2^2+r_3^2\right)} \end{cases} \tag{C.35}$$

Here M indicates the non-dimensional velocity of the source (C.18) relative to the medium, β is the Lorentz-transformation contraction factor as in (C.2), and $\mathbf{r}$ indicates the source–observer separation vector at the time t.

Equation (C.35) can be rearranged by introducing the emission-time distance r_E and the emission-time polar angle ϑ_E between source and observer. The modified distance r_M can be expressed as function of the emission-time coordinates by using (C.24) to give:

$$r_M = \frac{r_E}{D_v} \tag{C.36}$$

where the Doppler factor D_v is given by (C.25). If expression (C.36) is introduced into (C.35), the acoustic field associated with the moving point source can be expressed as follows:

$$g^{(0)}\left(\mathbf{x}|\mathbf{y},t\right) = \frac{D_v}{4\pi r_E}\, a\left(t-\frac{r_E}{c}\right) \tag{C.37}$$

It is noted that equation (C.37) is general to the extent of any constant subsonic velocity of the source relative to the medium. Expression (C.37) conveniently separates the effects of the source–medium relative motion and the observer–acoustic-field relative motion. The directional distribution of the acoustic field over a given wavefront is controlled by the source–medium relative motion and confined to the Doppler factor D_v. The observer position with respect to wavefronts in the acoustic field is expressed by the emission-time coordinates ϑ_E

(in the Doppler-factor expression) and r_E.[a]

C.3.2 The acoustic field of moving dipoles

For the moving-dipole case the forcing term in the wave equation is given by the divergence of a moving vector. The possibility of commuting the D'Alembert operator and the divergence operator, combined with the linearity of the D'Alembert operator, gives a solution[b] for the acoustic field of a general dipole:

$$g^{(1)}(\mathbf{x}|\mathbf{y},t) = \mathrm{div}_{\mathbf{x}}\left(\frac{D_v}{4\pi r_E}\,\mathbf{a}\left(t-\frac{r_E}{c}\right)\right) \tag{C.38}$$

where the subscript $_{\mathbf{x}}$ on the divergence operator indicates that the divergence is evaluated by varying the observer position, t being held constant. The Doppler factor D_v is given by (C.25) for a dipole source which moves with constant velocity $\mathbf{v}$. It is useful to give an expression for the observer-position divergence of any tensor function depending upon the variable $t - r_E/c$:

$$\mathrm{div}_{\mathbf{x}}\left(\mathbf{T}\left(t-\frac{r_E}{c}\right)\right) = \frac{\partial \mathbf{T}}{\partial r_E}\cdot\nabla_{\mathbf{x}}(r_E) = -\frac{1}{c}\frac{\partial \mathbf{T}}{\partial t}\cdot\nabla_{\mathbf{x}}(r_E) = -\frac{D_v}{c}\dot{\mathbf{T}}\cdot\hat{\mathbf{r}}_E \tag{C.39}$$

Here the partial time derivative represents the time variation of the source field as observed from a reference frame that is connected to the source;[c] it is indicated with the symbol $\dot{}$ over the argument variable. Note that the gradient $\nabla_{\mathbf{x}}(r_E)$ has been derived by using expression (C.30). The divergence on the right-hand side of equation (C.38) can be expressed by using (A.5) as follows:

$$\frac{1}{4\pi}\left(\frac{D_v}{r_E}\mathrm{div}_{\mathbf{x}}\left(\mathbf{a}\left(t-\frac{r_E}{c}\right)\right) + \mathbf{a}\left(t-\frac{r_E}{c}\right)\cdot\nabla_{\mathbf{x}}\left(\frac{D_v}{r_E}\right)\right)$$

Using expressions (C.39) and (C.33), the above expression develops as

$$\frac{1}{4\pi}\left(-\frac{D_v^2}{cr_E}\dot{\mathbf{a}}\cdot\hat{\mathbf{r}}_E + \mathbf{a}\cdot\left(\left(\frac{D_v}{r_E}\right)^2\frac{\mathbf{v}}{c} - \frac{1}{\beta^2}\left(\frac{D_v}{r_E}\right)^3\mathbf{r}_E\right)\right)$$

Using the above expression, equation (C.38) can finally be written as:

$$g^{(1)}(\mathbf{x}|\mathbf{y},t) = -\frac{D_v^2}{4\pi cr_E}\dot{\mathbf{a}}\cdot\hat{\mathbf{r}}_E + \frac{D_v^2}{4\pi r_E^2}\mathbf{a}\cdot\left(\frac{\mathbf{v}}{c} - \frac{D_v}{\beta^2}\hat{\mathbf{r}}_E\right) \tag{C.40}$$

[a] The emission-time coordinates indicate the current position of the observer from the centre of the wavefront that is being currently recorded by the observer.

[b] Note that the solution given by Garrick an Watkins[8] for a moving dipole is the equivalent of (C.38) expressed by using the source-observer separation r and the modified distance r_M. Equations (4) and (5) in Ref. [8] have been obtained by applying a "procedure which consists of scheduling a succession of fixed sources in a path to act consecutively one after the other so as to represent in effect the desired source moving along its path." The procedure is explained in the appendix of Ref. [8].

[c] The derivative does not include the time dependence of r_E.

Here the characteristic feature associated with multipole acoustic sources emerges: the solution is given by a combination of terms carrying different dependences on the emission-time distance and therefore falling more or less rapidly as the distance r_E increases.

The radiation in the acoustic far field will be dominated by the first term in equation (C.40) to give:

$$g^{(1)}(\mathbf{x}|\mathbf{y},t) = -\frac{D_v^2}{4\pi c r_E}\dot{\mathbf{a}}\cdot\hat{\mathbf{r}}_E \tag{C.41}$$

Expressions (C.40) and (C.41) are equivalent to the moving-dipole solutions identified by Lowson[61] for zero acceleration of the point dipole.[d]

C.3.3 The acoustic field of moving quadrupoles

The solution for quadrupole-order sources is obtained from the monopole solution (C.37) by applying twice the observer-position divergence. The quadrupole source field is in this case given by a symmetric second-order tensor field $\mathbf{A}$. The expression of the acoustic field for a quadrupole which moves with velocity $\mathbf{v}$ is given as follows:

$$g^{(2)}(\mathbf{x}|\mathbf{y},t) = \mathrm{div}_{\mathbf{x}}\left(\mathrm{div}_{\mathbf{x}}\left(\frac{D_v}{4\pi r_E}\,\mathbf{A}\left(t-\frac{r_E}{c}\right)\right)\right) \tag{C.42}$$

The inner divergence operator can be developed applying (A.5) to result in

$$g^{(2)}(\mathbf{x}|\mathbf{y},t) = \frac{1}{4\pi}\mathrm{div}_{\mathbf{x}}\left(\frac{D_v}{r_E}\mathrm{div}_{\mathbf{x}}(\mathbf{A}) + \mathbf{A}\cdot\nabla\left(\frac{D_v}{r_E}\right)\right)$$

Similarly, operating the second divergence results in

$$g^{(2)}(\mathbf{x}|\mathbf{y},t) = \frac{1}{4\pi}\left(\frac{D_v}{r_E}\mathrm{div}_{\mathbf{x}}(\mathrm{div}_{\mathbf{x}}(\mathbf{A})) + 2\mathrm{div}_{\mathbf{x}}(\mathbf{A})\cdot\nabla\left(\frac{D_v}{r_E}\right) + \mathbf{A}\cdot\nabla\left(\nabla\left(\frac{D_v}{r_E}\right)\right)\right) \tag{C.43}$$

Where use has been made of the symmetry property of the quadrupole tensor.[e] The three terms that sum to give the moving-quadrupole pressure field in (C.43) can be taken separately.

[d] Lowson[61] published a solution for the pressure field associated with moving dipole-order sources. The source motion was not uniform and a source-acceleration term appears in the far-field acoustic solution. Equations (17) and (18) in Ref. [61] respectively give the far-field and the near-field terms. Note that, in Ref. [61], the wave equation is in the Lighthill[1] form; the retarded time notation is equivalent to the emission-time coordinates for medium-fixed observer. Provided the retarded-time formulae are applied by considering the current-time for the observer position, as in Garrick and Watkins,[8] the zero-acceleration Lowson[61] solution is fully equivalent to (C.40). The far-field contribution for the acoustic field of uniformly moving dipole-order sources is included in the Bakerian lecture 1961 by Lighthill.[70]

[e] The form for a non symmetric tensor is given by

$$g^{(2)}(\mathbf{x}|\mathbf{y},t) = \frac{1}{4\pi}\left(\frac{D_v}{r_E}\mathrm{div}_{\mathbf{x}}(\mathrm{div}_{\mathbf{x}}(\mathbf{A})) + \nabla\left(\frac{D_v}{r_E}\right)\cdot\mathrm{div}_{\mathbf{x}}(\mathbf{A}) + \mathrm{div}_{\mathbf{x}}\left(\mathbf{A}^{\mathrm{T}}\right)\cdot\nabla\left(\frac{D_v}{r_E}\right) + \mathbf{A}^{\mathrm{T}}\cdot\nabla\left(\nabla\left(\frac{D_v}{r_E}\right)\right)\right).$$

The double divergence term can be developed as:

$$\mathrm{div}_{\mathbf{x}}(\mathrm{div}_{\mathbf{x}}(\mathbf{A})) = \frac{D_v^2}{c^2}\ddot{\mathbf{A}}\cdot\hat{\mathbf{r}}_E\otimes\hat{\mathbf{r}}_E - \frac{D_v}{cr_E}\dot{\mathbf{A}}\cdot\left(\mathbf{I} + 2D_v\mathrm{Sym}\left(\hat{\mathbf{r}}_E\otimes\frac{\mathbf{v}}{c}\right) - \frac{D_v^2}{\beta^2}\hat{\mathbf{r}}_E\otimes\hat{\mathbf{r}}_E\right) \tag{C.44}$$

Here Sym( ) indicates the symmetric part of a tensor.[f] The steps involved in the derivation of (C.44) used expressions (C.39), (A.5), (A.3), (C.31) and (C.33). Similarly, the mixed divergence-gradient term develops as:

$$\mathrm{div}_{\mathbf{x}}(\mathbf{A})\cdot\nabla\left(\frac{D_v}{r_E}\right) = -\frac{D_v^3}{cr_E^2}\dot{\mathbf{A}}\cdot\left(\hat{\mathbf{r}}_E\otimes\frac{\mathbf{v}}{c} - \frac{D_v}{\beta^2}\hat{\mathbf{r}}_E\otimes\hat{\mathbf{r}}_E\right) \tag{C.45}$$

The derivation of (C.45) used expressions (C.39) and (C.33). The double gradient term can be developed as:

$$\nabla\left(\nabla\left(\frac{D_v}{r_E}\right)\right) = \frac{D_v^3}{r_E^3}\left(2\frac{\mathbf{v}}{c}\otimes\frac{\mathbf{v}}{c} - \frac{1}{\beta^2}\mathbf{I}\right) - \frac{6D_v^4}{\beta^2 r_E^3}\mathrm{Sym}\left(\hat{\mathbf{r}}_E\otimes\frac{\mathbf{v}}{c}\right) + \frac{3D_v^5}{\beta^4 r_E^3}\hat{\mathbf{r}}_E\otimes\hat{\mathbf{r}}_E \tag{C.46}$$

Here expressions (A.3), (C.31) and (C.33) have been used. Introducing (C.44), (C.45) and (C.46) into (C.43) results in the following expression for the acoustic field of a moving quadrupole:

$$\begin{aligned} g^{(2)}(\mathbf{x}|\mathbf{y},t) \;=\; & \frac{D_v^3}{4\pi c^2 r_E}\ddot{\mathbf{A}}\cdot\hat{\mathbf{r}}_E\otimes\hat{\mathbf{r}}_E \\ & + \frac{3D_v^2}{4\pi c r_E^2}\dot{\mathbf{A}}\cdot\left(\frac{D_v^2}{\beta^2}\hat{\mathbf{r}}_E\otimes\hat{\mathbf{r}}_E - \frac{1}{3}\mathbf{I} - \frac{4}{3}D_v\mathrm{Sym}\left(\hat{\mathbf{r}}_E\otimes\frac{\mathbf{v}}{c}\right)\right) \\ & + \frac{3D_v^3}{4\pi r_E^3}\mathbf{A}\cdot\left(\frac{D_v^2}{\beta^4}\hat{\mathbf{r}}_E\otimes\hat{\mathbf{r}}_E - \frac{1}{3\beta^2}\mathbf{I} - \frac{2D_v}{\beta^2}\mathrm{Sym}\left(\hat{\mathbf{r}}_E\otimes\frac{\mathbf{v}}{c}\right) + \frac{2}{3}\frac{\mathbf{v}}{c}\otimes\frac{\mathbf{v}}{c}\right) \end{aligned} \tag{C.47}$$

Expression (C.47) contains all the terms of sound propagation from a moving quadrupole-order point source. As for the dipole source, the multipole nature of the source implies a solution that includes terms characterised by different dependences upon the emission-time distance r_E. Note that the solution (C.47) is equivalent to the zero-acceleration terms associated with the moving-quadrupole solution[g] introduced by Brentner.[62]

[f] The symmetric part of a tensor is given as follows:

$$\mathrm{Sym}(\mathbf{A}) = \frac{\mathbf{A}+\mathbf{A}^{\mathrm{T}}}{2}$$

[g] Equation (17) in Ref. [62] includes a free-field Green function for generally-moving quadrupole-order sources. The Green function includes the effect of source acceleration; both the near-field and far-field terms are considered. Note that, provided the retarded-time notation includes the observer position at current time (as in Garrick and Watkins[8] or Farassat[71]), the retarded-time solution is equivalent to the emission-time solution.

The far-field radiation will be dominated by the first term of (C.47):

$$g^{(2)}\left(\mathbf{x}|\mathbf{y},t\right)=\frac{D_v^3}{4\pi c^2 r_E}\ddot{\mathbf{A}}\cdot\left(\hat{\mathbf{r}}_E\otimes\hat{\mathbf{r}}_E\right) \tag{C.48}$$

The specialisation of (C.47) to the case of zero source velocity gives the solution

$$g^{(2)}\left(\mathbf{x}|\mathbf{y},t\right)=\frac{1}{4\pi c^2 r}\ddot{\mathbf{A}}\cdot\hat{\mathbf{r}}\otimes\hat{\mathbf{r}}+\frac{3}{4\pi c r^2}\dot{\mathbf{A}}\cdot\left(\hat{\mathbf{r}}\otimes\hat{\mathbf{r}}-\frac{1}{3}\mathbf{I}\right)+\frac{3}{4\pi r^3}\mathbf{A}\cdot\left(\hat{\mathbf{r}}\otimes\hat{\mathbf{r}}-\frac{1}{3}\mathbf{I}\right) \tag{C.49}$$

Noting the differences between corresponding definitions of the source strength,[h] expression (C.49) is equivalent to the pressure field of non-periodic quadrupole sources given by equation (7.1.13) in Ref. [68]. Equation (C.49) can be rearranged by noting that

$$\mathbf{A}\cdot\mathbf{I}=\left(\mathbf{A}\cdot\mathbf{I}\right)\mathbf{I}\cdot\left(\hat{\mathbf{r}}\otimes\hat{\mathbf{r}}\right)$$

to give

$$g^{(2)}\left(\mathbf{x}|\mathbf{y},t\right)=\frac{1}{4\pi c^2 r}\left(\ddot{\mathbf{A}}+\frac{3c}{r}\mathrm{Dev}\left(\dot{\mathbf{A}}\right)+\frac{3c^2}{r^2}\mathrm{Dev}\left(\mathbf{A}\right)\right)\cdot\left(\hat{\mathbf{r}}\otimes\hat{\mathbf{r}}\right) \tag{C.50}$$

where the operator Dev ( ) extracts the deviatoric part of $\mathbf{A}$.[i] It is observed that (C.50) can be derived directly by considering the radiation problem for the case of stationary medium and stationary quadrupole-order point source. The contributions associated with the spherical[j] and the deviatoric parts are shown separately in (C.50). The spherical part $\mathrm{Sph}\left(\mathbf{A}\right)$ is only included in the far-field radiation. As explained by Morse and Ingard,[68] the acoustic-radiation field generated by $\mathrm{Sph}\left(\mathbf{A}\right)$ is identical to a monopole-source acoustic field; the 5 independent components of $\mathrm{Dev}\left(\mathbf{A}\right)$ generate corresponding acoustic-pressure fields that are characteristic of the quadrupole radiation. This justifies the form of the near-field terms in (C.50), only including the deviatoric part of the quadrupole tensor.

[h] Morse and Ingard[68] derive the quadrupole-source pressure field superposition of monopole-source fields; where the monopole sources are opportunely placed and phase shifted, in order to obtain the various components of the quadrupole tensor. The monopole source strength in Ref. [68] is given by s, being

$$a=\rho\dot{s}$$

The same relation holds between $\mathbf{A}$ and the quadrupole source as in Ref. [68].

[i] The deviatoric part of a tensor is given by

$$\mathrm{Dev}\left(\mathbf{T}\right)=\mathbf{T}-\frac{1}{3}\left(\mathbf{T}\cdot\mathbf{I}\right)\mathbf{I}$$

[j] The spherical part of a tensor is given as follows:

$$\mathrm{Sph}\left(\mathbf{T}\right)=\mathbf{T}-\mathrm{Dev}\left(\mathbf{T}\right)=\frac{1}{3}\left(\mathbf{T}\cdot\mathbf{I}\right)\mathbf{I}$$

Appendix D

The acoustic-field of a source distribution in a moving medium

The expression for the acoustic-variable autocorrelation function in the far field, associated with a spatial distribution of acoustic sources in relative uniform motion with respect to a uniform medium, is derived in this appendix. The acoustic-source distribution is considered as a statistically-stationary random field in a fixed reference frame $(\mathcal{O}, \hat{\mathbf{e}}_1, \hat{\mathbf{e}}_2, \hat{\mathbf{e}}_3)$ that is rigidly connected to the sources.[a] The acoustic sources are characterised by multipole orders 1 and 2. The dipole source distribution is indicated as follows:

$$\mathbf{d}(\mathbf{w}, t)$$

where $\mathbf{w}$ is the vector indicating the source position from $\mathcal{O}$ and t is the time. The quadrupole source distribution is referred to as

$$\mathbf{Q}(\mathbf{w}, t)$$

The acoustic-field statistics are derived for an observer fixed in $(\mathcal{O}, \hat{\mathbf{e}}_1, \hat{\mathbf{e}}_2, \hat{\mathbf{e}}_3)$. The maximum wave length of interest in the problem is assumed small compared to the emission-time distance between any source volume and the observer. The acoustic-variable autocorrelation function[b] at the observer-position $\mathbf{x}$ is indicated as

$$\mathrm{c}_{gg}(\mathbf{x}, \mathbf{0}, \tau) = \overline{g(\mathbf{x}, t)\, g(\mathbf{x}, t+\tau)} \tag{D.1}$$

The autocorrelation $\mathrm{c}_{gg}(\mathbf{x}, \mathbf{0}, \tau)$ can be evaluated by using the far-field expressions (C.48) and (C.41). Assuming that the medium is moving with uniform velocity $\mathbf{v}$ with respect to the fixed

[a] This means that the uniform medium is moving with respect to the frame of reference in which the source statistics are time-stationary; one could also consider the sources as moving with respect to a stationary medium.

[b] Here we use the two-point correlation function with zero separation to indicate the autocorrelation function. The overbar indicates the time average.

reference frame, means that equations (C.48) and (C.41), expressing the far-field radiation for moving sources at velocity $\mathbf{v}$ and fixed medium, must be specialised for source velocity $-\mathbf{v}$. The instantaneous acoustic variable for a far-field observer is given by the source-effect superposition as a volume integral across the source region.

$$g(\mathbf{x},t) = \frac{1}{4\pi c}\iiint_{\mathbf{w}} \left(\frac{D_{-v}^3}{c r_E} \ddot{\mathbf{Q}}(\mathbf{w}, t - r_E/c) \cdot \hat{\mathbf{R}}_E - \frac{D_{-v}^2}{r_E} \dot{\mathbf{d}}(\mathbf{w}, t - r_E/c) \cdot \hat{\mathbf{r}}_E \right) \mathrm{d}^3\mathbf{w} \tag{D.2}$$

Here $\hat{\mathbf{R}}_E$ indicates the emission-time radiation-direction tensor $\hat{\mathbf{r}}_E \otimes \hat{\mathbf{r}}_E$. Indicating with $\mathcal{P}_1$ and $\mathcal{P}_2$ two arbitrary positions within the source region and introducing expression (D.2) into (D.1) one obtains

$$\begin{aligned}
&\mathrm{c}_{gg}(\mathbf{x},\mathbf{0},\tau) = \\
&= \iiint_{\mathbf{z}}\iiint_{\mathbf{w}} \frac{D_{-v}^6}{16\pi^2 c^4 r_E r_E} \overline{\left(\ddot{\mathbf{Q}}(\mathbf{z}, t - r_E(\mathbf{z})/c) \otimes \ddot{\mathbf{Q}}(\mathbf{w}, t + \tau - r_E(\mathbf{w})/c) \right)} \cdot \left(\hat{\mathbf{R}}_E \otimes \hat{\mathbf{R}}_E \right) \mathrm{d}^3\mathbf{w}\mathrm{d}^3\mathbf{z} \\
&+ \iiint_{\mathbf{z}}\iiint_{\mathbf{w}} \frac{D_{-v}^4}{16\pi^2 c^2 r_E r_E} \overline{\left(\dot{\mathbf{d}}(\mathbf{z}, t - r_E(\mathbf{z})/c) \otimes \dot{\mathbf{d}}(\mathbf{w}, t + \tau - r_E(\mathbf{w})/c) \right)} \cdot (\hat{\mathbf{r}}_E \otimes \hat{\mathbf{r}}_E) \, \mathrm{d}^3\mathbf{w}\mathrm{d}^3\mathbf{z} \\
&+ \iiint_{\mathbf{z}}\iiint_{\mathbf{w}} \frac{D_{-v}^5}{16\pi^2 c^3 r_E r_E} \overline{\left(\ddot{\mathbf{Q}}(\mathbf{z}, t - r_E(\mathbf{z})/c) \otimes \dot{\mathbf{d}}(\mathbf{w}, t + \tau - r_E(\mathbf{w})/c) \right)} \cdot \left(\hat{\mathbf{r}}_E \otimes \hat{\mathbf{r}}_E \right) \mathrm{d}^3\mathbf{w}\mathrm{d}^3\mathbf{z} \\
&+ \iiint_{\mathbf{z}}\iiint_{\mathbf{w}} \frac{D_{-v}^5}{16\pi^2 c^3 r_E r_E} \overline{\left(\dot{\mathbf{d}}(\mathbf{z}, t - r_E(\mathbf{z})/c) \otimes \ddot{\mathbf{Q}}(\mathbf{w}, t + \tau - r_E(\mathbf{w})/c) \right)} \cdot \left(\hat{\mathbf{r}}_E \otimes \hat{\mathbf{R}}_E \right) \mathrm{d}^3\mathbf{w}\mathrm{d}^3\mathbf{z}
\end{aligned} \tag{D.3}$$

where $\mathbf{z}$ and $\mathbf{w}$ indicate the positions $\mathcal{P}_1$ and $\mathcal{P}_2$ from the origin $\mathcal{O}$. We now indicate with $\mathcal{P}$ the middle point between $\mathcal{P}_1$ and $\mathcal{P}_2$. The location $\mathcal{P}$ is indicated by $\mathbf{y}$ from $\mathcal{O}$. The separation vector indicating $\mathcal{P}_2$ from $\mathcal{P}_1$ is $\boldsymbol{\eta}$.

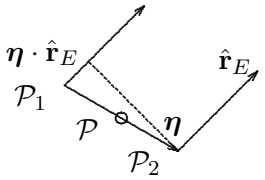

$$\begin{cases} \mathbf{y} = \dfrac{\mathbf{z} + \mathbf{w}}{2} \\ \boldsymbol{\eta} = \mathbf{w} - \mathbf{z} \end{cases} \tag{D.4}$$

Introducing, in expression (D.3), the unit-Jacobian change of integration variables from the coordinates given by the components of $\mathbf{z}$, $\mathbf{w}$ to the coordinates associated with $\mathbf{y}$ and $\boldsymbol{\eta}$ yields

$$\begin{aligned}
&\mathrm{c}_{gg}(\mathbf{x},\mathbf{0},\tau) = \\
&= \iiint_{\mathbf{y}} \frac{D_{-v}^6}{16\pi^2 c^4 r_E^2} \iiint_{\boldsymbol{\eta}} \overline{\left(\ddot{\mathbf{Q}}\left(\mathbf{y} - \frac{\boldsymbol{\eta}}{2}, t \right) \otimes \ddot{\mathbf{Q}}\left(\mathbf{y} + \frac{\boldsymbol{\eta}}{2}, t + \tau + \frac{\boldsymbol{\eta} \cdot \hat{\mathbf{r}}_E}{c} \right) \right)} \mathrm{d}^3\boldsymbol{\eta} \cdot \left(\hat{\mathbf{R}}_E \otimes \hat{\mathbf{R}}_E \right) \mathrm{d}^3\mathbf{y} \\
&+ \iiint_{\mathbf{y}} \frac{D_{-v}^4}{16\pi^2 c^2 r_E^2} \iiint_{\boldsymbol{\eta}} \overline{\left(\dot{\mathbf{d}}\left(\mathbf{y} - \frac{\boldsymbol{\eta}}{2}, t \right) \otimes \dot{\mathbf{d}}\left(\mathbf{y} + \frac{\boldsymbol{\eta}}{2}, t + \tau + \frac{\boldsymbol{\eta} \cdot \hat{\mathbf{r}}_E}{c} \right) \right)} \mathrm{d}^3\boldsymbol{\eta} \cdot \hat{\mathbf{R}}_E \mathrm{d}^3\mathbf{y} \\
&+ \iiint_{\mathbf{y}} \frac{D_{-v}^5}{16\pi^2 c^3 r_E^2} \iiint_{\boldsymbol{\eta}} \overline{\left(\ddot{\mathbf{Q}}\left(\mathbf{y} - \frac{\boldsymbol{\eta}}{2}, t \right) \otimes \dot{\mathbf{d}}\left(\mathbf{y} + \frac{\boldsymbol{\eta}}{2}, t + \tau + \frac{\boldsymbol{\eta} \cdot \hat{\mathbf{r}}_E}{c} \right) \right)} \mathrm{d}^3\boldsymbol{\eta} \cdot \left(\hat{\mathbf{R}}_E \otimes \hat{\mathbf{r}}_E \right) \mathrm{d}^3\mathbf{y} \\
&+ \iiint_{\mathbf{y}} \frac{D_{-v}^5}{16\pi^2 c^3 r_E^2} \iiint_{\boldsymbol{\eta}} \overline{\left(\dot{\mathbf{d}}\left(\mathbf{y} - \frac{\boldsymbol{\eta}}{2}, t \right) \otimes \ddot{\mathbf{Q}}\left(\mathbf{y} + \frac{\boldsymbol{\eta}}{2}, t + \tau + \frac{\boldsymbol{\eta} \cdot \hat{\mathbf{r}}_E}{c} \right) \right)} \mathrm{d}^3\boldsymbol{\eta} \cdot \left(\hat{\mathbf{R}}_E \otimes \hat{\mathbf{r}}_E \right) \mathrm{d}^3\mathbf{y}
\end{aligned} \tag{D.5}$$

We note that the change of integration variables (D.4) corresponds to rearranging the integral sum (D.3), of the correlations between all possible combination of source volumes, by associat-

ing all the source volumes that form a group of source-volume pairs with respect to a common centre $\mathbf{y}$. The source-pair centre $\mathbf{y}$ is then moved in order to span the whole set of possible source-volume combinations. Equation (D.5) includes an offset of the time-average variable $t = t' + r_E(\mathbf{z})/c$. We have also assumed that

$$r_E(\mathbf{y} - \boldsymbol{\eta}/2) - r_E(\mathbf{y} + \boldsymbol{\eta}/2) \simeq \hat{\mathbf{r}}_E(\mathbf{y}) \cdot \boldsymbol{\eta} \tag{D.6}$$

For each source pair, i. e. an element of the $\boldsymbol{\eta}$ volume integral in (D.5), the approximation (D.6) is valid in the Fresnel far field[c]

$$\frac{\eta}{r_E},\ \frac{\eta^3}{r_E^2 \lambda} << 1 \tag{D.7}$$

where λ denotes the acoustic wavelength. Note that the geometric far-field hypothesis $\eta/r_E <<$

[c]We assume correlated harmonic sources placed in $\mathcal{P}_1$ and $\mathcal{P}_2$ at emission time, see equations and schematic (D.4). In order to derive the exact path difference between $\mathcal{P}_1$ and $\mathcal{P}_2$, with the middle point as reference, we consider the triangle having as vertices the positions of sources and observer.

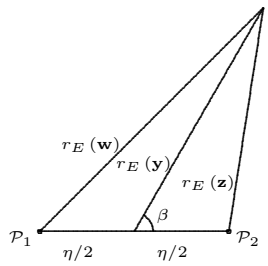

Note that the diagram tends to the diagram in (D.4) for observer positions in the geometric far field, where $r_E >> \eta$. We use the Carnot cosine theorem to derive $r_E(\mathbf{z})$ and $r_E(\mathbf{w})$ in terms of $r_E(\mathbf{y})$ and the separation modulus η as

$$r_E(\mathbf{y} - \boldsymbol{\eta}/2) = r_E(\mathbf{y})\sqrt{1 + \varepsilon\cos\beta + \frac{\varepsilon^2}{4}}$$

$$r_E(\mathbf{y} + \boldsymbol{\eta}/2) = r_E(\mathbf{y})\sqrt{1 - \varepsilon\cos\beta + \frac{\varepsilon^2}{4}}$$

where ε denotes the ratio $\eta/r_E(\mathbf{y})$ and β is the angle between $\boldsymbol{\eta}$ and $\mathbf{r}_E(\mathbf{y})$. By expanding the above expressions around $\varepsilon = 0$ (geometric far field), the path-length difference can be expressed as follows

$$r_E(\mathbf{y} - \boldsymbol{\eta}/2) - r_E(\mathbf{y} + \boldsymbol{\eta}/2) = \boldsymbol{\eta} \cdot \hat{\mathbf{r}}_E(\mathbf{y}) - \frac{1}{8}\eta\varepsilon^2(\sin\beta)^2\cos\beta + \circ\left(\eta\varepsilon^4\right)$$

Here we have used the relation $\boldsymbol{\eta} \cdot \hat{\mathbf{r}}_E(\mathbf{y}) = \eta\cos\beta$. The Fresnel correction to be applied to the path-difference Fraunhofer approximation (D.6) is then given by the following:

$$-\frac{1}{8}\eta\varepsilon^2(\sin\beta)^2\cos\beta + \circ\left(\eta\varepsilon^4\right)$$

The validity of the approximation (D.6) is limited to observer locations that guarantee small Fresnel corrections, compared to the acoustic wavelength λ associated with the harmonic sources

$$-\frac{1}{8}\eta\varepsilon^2(\sin\beta)^2\cos\beta + \circ\left(\eta\varepsilon^4\right) << \lambda$$

or, considering the leading term in the geometric far field ($\varepsilon << 1$),

$$\frac{\eta\varepsilon^2}{\lambda} << 1$$

This relation defines the Fresnel far field for two correlated sources separated by η, when the middle point $\mathbf{y}$ is the Fraunhofer-approximation reference point:

$$r_E >> \sqrt{\frac{\eta^3}{\lambda}}$$

Note that this differs from the definition using one of the sources as reference point for the source-pair Fraunhofer approximation. In this case small Fresnel corrections are associated with observers that are at a distance

$$r_E >> \frac{\eta^2}{\lambda}$$

from the sources.

1 allows for approximating the factor

$$\frac{1}{r_E(\mathbf{y}+\boldsymbol{\eta}/2)r_E(\mathbf{y}-\boldsymbol{\eta}/2)} \simeq \frac{1}{\left(r_E(\mathbf{y})\right)^2} \tag{D.8}$$

which has been taken out from the $\boldsymbol{\eta}$ integral of equation (D.5); the geometric far-field hypothesis also lets us assume constant emission-time radiation direction $\hat{\mathbf{r}}_E$ within the $\boldsymbol{\eta}$ integral.

Assuming that the two-point correlation function of the acoustic-source field decays to 0 for large separations allows for formulating the geometric and Fresnel far-field hypotheses in terms of a correlation length. Given a typical separation η_{max} such that for $\eta > \eta_{max}$ we can assume zero correlation between any source-volume pairs, equation (D.5) is valid for source–observer emission-time distances r_E respecting the hypotheses of

- Geometric far field, or $r_E >> \eta_{max}$
- Fresnel far field, or geometric far field plus $r_E >> \sqrt{\eta_{max}^3/\lambda}$; as derived from equation (D.7) with $\eta = \eta_{max}$

The acoustic-field autocorrelation function is connected by expression (D.3) to the symmetric[d] part of the two-point correlation function corresponding to the source tensor-field time derivatives $\ddot{\mathbf{Q}}$ and $\dot{\mathbf{d}}$. In the following sections the source two-point correlation terms are discussed separately for different tensor orders. The time derivative are changed into time-separation derivatives to give a simplified expression of the frequency-domain acoustic-field autocorrelation function.

D.1 Quadrupole–quadrupole correlation

The quadrupole-acceleration–quadrupole-acceleration two-point correlation function is an order-4 tensor that is defined as follows:

$$\mathrm{c}_{\ddot{\mathbf{Q}}\ddot{\mathbf{Q}}}(\mathbf{y},\boldsymbol{\eta},\tau) = \overline{\ddot{\mathbf{Q}}(\mathbf{y}-\boldsymbol{\eta}/2,t) \otimes \ddot{\mathbf{Q}}(\mathbf{y}+\boldsymbol{\eta}/2,t+\tau)} \tag{D.9}$$

Operating as follows

$$\begin{aligned}
\overline{\ddot{\mathbf{Q}}(\mathbf{y}-\boldsymbol{\eta}/2,t) \otimes \ddot{\mathbf{Q}}(\mathbf{y}+\boldsymbol{\eta}/2,t+\tau)} &= \frac{\partial^2}{\partial\tau^2}\overline{\ddot{\mathbf{Q}}(\mathbf{y}-\boldsymbol{\eta}/2,t) \otimes \mathbf{Q}(\mathbf{y}+\boldsymbol{\eta}/2,t+\tau)} \\
&= \frac{\partial^2}{\partial\tau^2}\overline{\ddot{\mathbf{Q}}(\mathbf{y}-\boldsymbol{\eta}/2,t'-\tau) \otimes \mathbf{Q}(\mathbf{y}+\boldsymbol{\eta}/2,t')} \\
&= \frac{\partial^4}{\partial\tau^4}\overline{\mathbf{Q}(\mathbf{y}-\boldsymbol{\eta}/2,t'-\tau) \otimes \mathbf{Q}(\mathbf{y}+\boldsymbol{\eta}/2,t')}
\end{aligned}$$

[d] The tensors $\hat{\mathbf{R}}_E \otimes \hat{\mathbf{R}}_E$, $\hat{\mathbf{R}}_E \otimes \hat{\mathbf{r}}_E$ and $\hat{\mathbf{R}}_E$ are symmetric. The dot product between a general tensor and an equal-order symmetric tensor extracts the symmetric part of the general tensor.

allows for expressing (D.9) as

$$\mathrm{c}_{\ddot{\mathbf{Q}}\ddot{\mathbf{Q}}}\left(\mathbf{y},\boldsymbol{\eta},\tau\right)=\frac{\partial^4}{\partial\tau^4}\overline{\mathbf{Q}\left(\mathbf{y}-\boldsymbol{\eta}/2,t\right)\otimes\mathbf{Q}\left(\mathbf{y}+\boldsymbol{\eta}/2,t+\tau\right)}=\frac{\partial^4}{\partial\tau^4}\mathrm{c}_{\mathbf{QQ}}\left(\mathbf{y},\boldsymbol{\eta},\tau\right) \tag{D.10}$$

D.2 Dipole–dipole correlation function

The dipole-velocity–dipole-velocity two-point correlation function is a second-order tensor that can be defined as follows

$$\mathrm{c}_{\dot{\mathbf{d}}\dot{\mathbf{d}}}\left(\mathbf{y},\boldsymbol{\eta},\tau\right)=\overline{\dot{\mathbf{d}}\left(\mathbf{y}-\boldsymbol{\eta}/2,t\right)\dot{\mathbf{d}}\left(\mathbf{y}+\boldsymbol{\eta}/2,t+\tau\right)} \tag{D.11}$$

Operating as in section D.1 for the quadrupole–quadrupole term, the change of derivative from time t to time separation τ results in

$$\mathrm{c}_{\dot{\mathbf{d}}\dot{\mathbf{d}}}\left(\mathbf{y},\boldsymbol{\eta},\tau\right)=-\frac{\partial^2}{\partial\tau^2}\overline{\mathbf{d}\left(\mathbf{y}-\boldsymbol{\eta}/2,t\right)\otimes\mathbf{d}\left(\mathbf{y}+\boldsymbol{\eta}/2,t+\tau\right)}=-\frac{\partial^2}{\partial\tau^2}\mathrm{c}_{\mathbf{dd}}\left(\mathbf{y},\boldsymbol{\eta},\tau\right) \tag{D.12}$$

D.3 Quadrupole–dipole correlation function

The mixed dipole-velocity–quadrupole-acceleration term is a third-order tensor given by two correlation-function terms as follows:

$$\begin{aligned}&\mathrm{c}_{\ddot{\mathbf{Q}}\dot{\mathbf{d}}}\left(\mathbf{y},\boldsymbol{\eta},\tau\right)+\mathrm{c}_{\dot{\mathbf{d}}\ddot{\mathbf{Q}}}\left(\mathbf{y},\boldsymbol{\eta},\tau\right)\\&=\overline{\ddot{\mathbf{Q}}\left(\mathbf{y}-\boldsymbol{\eta}/2,t\right)\otimes\dot{\mathbf{d}}\left(\mathbf{y}+\boldsymbol{\eta}/2,t+\tau\right)+\dot{\mathbf{d}}\left(\mathbf{y}-\boldsymbol{\eta}/2,t\right)\otimes\ddot{\mathbf{Q}}\left(\mathbf{y}+\boldsymbol{\eta}/2,t+\tau\right)}\end{aligned} \tag{D.13}$$

Expression (D.13) can be developed as follows:

$$\begin{aligned}&\overline{\ddot{\mathbf{Q}}\left(\mathbf{y}-\boldsymbol{\eta}/2,t\right)\otimes\dot{\mathbf{d}}\left(\mathbf{y}+\boldsymbol{\eta}/2,t+\tau\right)+\dot{\mathbf{d}}\left(\mathbf{y}-\boldsymbol{\eta}/2,t\right)\otimes\ddot{\mathbf{Q}}\left(\mathbf{y}+\boldsymbol{\eta}/2,t+\tau\right)}\\&=\frac{\partial}{\partial\tau}\overline{\ddot{\mathbf{Q}}\left(\mathbf{y}-\boldsymbol{\eta}/2,t\right)\otimes\mathbf{d}\left(\mathbf{y}+\boldsymbol{\eta}/2,t+\tau\right)}+\frac{\partial^2}{\partial\tau^2}\overline{\dot{\mathbf{d}}\left(\mathbf{y}-\boldsymbol{\eta}/2,t\right)\otimes\mathbf{Q}\left(\mathbf{y}+\boldsymbol{\eta}/2,t+\tau\right)}\\&=\frac{\partial}{\partial\tau}\overline{\ddot{\mathbf{Q}}\left(\mathbf{y}-\boldsymbol{\eta}/2,t-\tau\right)\otimes\mathbf{d}\left(\mathbf{y}+\boldsymbol{\eta}/2,t\right)}+\frac{\partial^2}{\partial\tau^2}\overline{\dot{\mathbf{d}}\left(\mathbf{y}-\boldsymbol{\eta}/2,t-\tau\right)\otimes\mathbf{Q}\left(\mathbf{y}+\boldsymbol{\eta}/2,t\right)}\\&=\frac{\partial^3}{\partial\tau^3}\overline{\mathbf{Q}\left(\mathbf{y}-\boldsymbol{\eta}/2,t-\tau\right)\otimes\mathbf{d}\left(\mathbf{y}+\boldsymbol{\eta}/2,t\right)}-\frac{\partial^3}{\partial\tau^3}\overline{\mathbf{d}\left(\mathbf{y}-\boldsymbol{\eta}/2,t-\tau\right)\otimes\mathbf{Q}\left(\mathbf{y}+\boldsymbol{\eta}/2,t\right)}\\&=\frac{\partial^3}{\partial\tau^3}\overline{\mathbf{Q}\left(\mathbf{y}-\boldsymbol{\eta}/2,t-\tau\right)\otimes\mathbf{d}\left(\mathbf{y}+\boldsymbol{\eta}/2,t\right)-\mathbf{d}\left(\mathbf{y}-\boldsymbol{\eta}/2,t\right)\otimes\mathbf{Q}\left(\mathbf{y}+\boldsymbol{\eta}/2,t+\tau\right)}\end{aligned} \tag{D.14}$$

Noting that only the symmetric parts of the tensors contribute to the acoustic-field autocorrelation, the averaged part of (D.14) can be put in the form

$$\overline{\mathbf{d}\left(\mathbf{y}+\boldsymbol{\eta}/2,t\right)\otimes\mathbf{Q}\left(\mathbf{y}-\boldsymbol{\eta}/2,t-\tau\right)-\mathbf{d}\left(\mathbf{y}-\boldsymbol{\eta}/2,t\right)\otimes\mathbf{Q}\left(\mathbf{y}+\boldsymbol{\eta}/2,t+\tau\right)}$$

or equivalently

$$\overline{\mathbf{Q}\left(\mathbf{y}-\boldsymbol{\eta}/2,t\right)\otimes\mathbf{d}\left(\mathbf{y}+\boldsymbol{\eta}/2,t+\tau\right)-\mathbf{Q}\left(\mathbf{y}+\boldsymbol{\eta}/2,t\right)\otimes\mathbf{d}\left(\mathbf{y}-\boldsymbol{\eta}/2,t-\tau\right)}$$

The mixed dipole-velocity–quadrupole-acceleration term can therefore be expressed as

$$\begin{aligned}\mathrm{c}_{\ddot{\mathbf{Q}}\dot{\mathbf{d}}}\left(\mathbf{y},\boldsymbol{\eta},\tau\right)+\mathrm{c}_{\dot{\mathbf{d}}\ddot{\mathbf{Q}}}\left(\mathbf{y},\boldsymbol{\eta},\tau\right) &= \frac{\partial^3}{\partial\tau^3}\left(\mathrm{c}_{\mathbf{dQ}}\left(\mathbf{y},-\boldsymbol{\eta},-\tau\right)-\mathrm{c}_{\mathbf{dQ}}\left(\mathbf{y},\boldsymbol{\eta},\tau\right)\right)\\ &= \frac{\partial^3}{\partial\tau^3}\left(\mathrm{c}_{\mathbf{Qd}}\left(\mathbf{y},\boldsymbol{\eta},\tau\right)-\mathrm{c}_{\mathbf{Qd}}\left(\mathbf{y},-\boldsymbol{\eta},-\tau\right)\right)\end{aligned} \tag{D.15}$$

We observe that, if the quadrupole–dipole two-point correlation function is characterised by the symmetry property

$$\mathrm{c}_{\mathbf{dQ}}\left(\mathbf{y},\boldsymbol{\eta},\tau\right)=\mathrm{c}_{\mathbf{dQ}}\left(\mathbf{y},-\boldsymbol{\eta},-\tau\right) \tag{D.16}$$

the symmetric part of expression (D.13) is zero.

D.4 Acoustic-field autocorrelation and PSD

The acoustic-variable autocorrelation function (D.3) can be expressed as follows:

$$\begin{aligned}\mathrm{c}_{gg}\left(\mathbf{x},\mathbf{0},\tau\right) =& \iiint_{\mathbf{y}}\frac{D_{-v}^6}{16\pi^2c^4r_E^2}\iiint_{\boldsymbol{\eta}}\frac{\partial^4}{\partial\tau^4}\mathrm{c}_{\mathbf{QQ}}\left(\mathbf{y},\boldsymbol{\eta},\tau-\boldsymbol{\eta}\cdot\hat{\mathbf{r}}_E/c\right)\mathrm{d}^3\boldsymbol{\eta}\cdot\left(\hat{\mathbf{R}}_E\otimes\hat{\mathbf{R}}_E\right)\mathrm{d}^3\mathbf{y}\\ &-\iiint_{\mathbf{y}}\frac{D_{-v}^4}{16\pi^2c^2r_E^2}\iiint_{\boldsymbol{\eta}}\frac{\partial^2}{\partial\tau^2}\mathrm{c}_{\mathbf{dd}}\left(\mathbf{y},\boldsymbol{\eta},\tau-\boldsymbol{\eta}\cdot\hat{\mathbf{r}}_E/c\right)\mathrm{d}^3\boldsymbol{\eta}\cdot\left(\hat{\mathbf{r}}_E\otimes\hat{\mathbf{r}}_E\right)\mathrm{d}^3\mathbf{y}\end{aligned} \tag{D.17}$$

Here we are assuming that the symmetry property (D.16) holds for the quadrupole–dipole contribution. It is useful to summarise the hypotheses under which expression (D.17) holds; the conditions are listed as follows:

1. A source distribution of quadrupole-order and dipole-order acoustic sources is embedded in a uniform moving medium. The distribution is statistically time-stationary in a reference frame that is fixed to the sources. The observer position $\mathbf{x}$ is fixed to the sources.

2. The maximum wavelength of interest in the source emission is negligible if compared to the source–observer emission-time distance. This assumption, referred to as acoustic

far field, is used to express the dipole and quadrupole acoustic-field contributions in the form given by expressions (C.41) and (C.48), respectively.

3. The two-point correlation functions associated with the possible combinations of quadrupole and dipole sources are characterised by a spatial dimension η_{max} such that values of the separation with amplitude greater than η_{max} imply a negligible value for the modulus of the two-point correlation function. We have assumed that, respect to the source volume at emission time, the observer position is in the geometric far field and in the Fresnel far field, both far-field conditions being based on η_{max}. Note that using middle-point referenced two-point correlation functions has implications on the Fresnel-correction expression, see note c on page 113.

4. The two-point correlation functions associated with quadrupole–dipole mixed terms are characterised by the symmetry property (D.16). This hypothesis justifies not considering the contributions corresponding to the quadrupole–dipole two point correlation function.

For source distributions with non-zero time average,[a] the two-point correlation function can be decomposed as

$$\mathrm{c}_{\mathbf{QQ}} = \mathrm{c}_{\mathbf{Q'Q'}} + \overline{\mathbf{Q}}\,(\mathbf{y}-\boldsymbol{\eta}/2) \otimes \overline{\mathbf{Q}}\,(\mathbf{y}+\boldsymbol{\eta}/2) \tag{D.18}$$

where we indicate with $\mathbf{Q'}$ the instantaneous fluctuation around the mean value, such that:

$$\mathbf{Q}\,(\mathbf{y},t) = \overline{\mathbf{Q}}\,(\mathbf{y}) + \mathbf{Q'}\,(\mathbf{y},t)$$

We note that the τ partial derivatives in (D.17) remove the effect of the τ-independent part of the source correlation functions $\mathrm{c}_{\mathbf{QQ}}$ and $\mathrm{c}_{\mathbf{dd}}$. The acoustic-variable autocorrelation function can then be expressed as follows:

$$\begin{aligned}\mathrm{c}_{gg}\,(\mathbf{x},\mathbf{0},\tau) =& \iiint_{\mathbf{y}} \frac{D_{-v}^6}{16\pi^2 c^4 r_E^2} \iiint_{\boldsymbol{\eta}} \frac{\partial^4}{\partial\tau^4} \mathrm{c}_{\mathbf{Q'Q'}}\,(\mathbf{y},\boldsymbol{\eta},\tau-\boldsymbol{\eta}\cdot\hat{\mathbf{r}}_E/c)\,\mathrm{d}^3\boldsymbol{\eta}\cdot\left(\hat{\mathbf{R}}_E\otimes\hat{\mathbf{R}}_E\right)\mathrm{d}^3\mathbf{y} \\ &- \iiint_{\mathbf{y}} \frac{D_{-v}^4}{16\pi^2 c^2 r_E^2} \iiint_{\boldsymbol{\eta}} \frac{\partial^2}{\partial\tau^2} \mathrm{c}_{\mathbf{d'd'}}\,(\mathbf{y},\boldsymbol{\eta},\tau-\boldsymbol{\eta}\cdot\hat{\mathbf{r}}_E/c)\,\mathrm{d}^3\boldsymbol{\eta}\cdot(\hat{\mathbf{r}}_E\otimes\hat{\mathbf{r}}_E)\,\mathrm{d}^3\mathbf{y}\end{aligned} \tag{D.19}$$

Applying Fourier transform to expression (D.19) yields the following relation for the acoustic-variable power spectral density (PSD):

$$\begin{aligned}\mathrm{s}_{gg}\,(\mathbf{x},\mathbf{0},f) =& \iiint_{\mathbf{y}} \frac{\pi^2 D_{-v}^6 f^4}{c^4 r_E^2} \iiint_{\boldsymbol{\eta}} \mathrm{s}_{\mathbf{QQ}}\,(\mathbf{y},\boldsymbol{\eta},f)\exp\left(\mathrm{j}\ 2\pi f\boldsymbol{\eta}\cdot\hat{\mathbf{r}}_E/c\right)\mathrm{d}^3\boldsymbol{\eta}\cdot\left(\hat{\mathbf{R}}_E\otimes\hat{\mathbf{R}}_E\right)\mathrm{d}^3\mathbf{y} \\ &+ \iiint_{\mathbf{y}} \frac{D_{-v}^4 f^2}{4c^2 r_E^2} \iiint_{\boldsymbol{\eta}} \mathrm{s}_{\mathbf{dd}}\,(\mathbf{y},\boldsymbol{\eta},f)\exp\left(\mathrm{j}\ 2\pi f\boldsymbol{\eta}\cdot\hat{\mathbf{r}}_E/c\right)\mathrm{d}^3\boldsymbol{\eta}\cdot(\hat{\mathbf{r}}_E\otimes\hat{\mathbf{r}}_E)\,\mathrm{d}^3\mathbf{y}\end{aligned} \tag{D.20}$$

[a] An example is given by the principal components of the unit-density Reynolds-stress tensor. In the present work we use the unit-density Reynolds-stress tensor to represent the applied-stress equivalent acoustic source in the Lilley–Goldstein analogy.

Note here that we define the two-point CPSD of a given random variable as the Fourier transform of the corresponding fluctuating-value correlation function

$$\mathrm{s}_{\mathbf{dd}}\left(\mathbf{y},\boldsymbol{\eta},f\right)=\int_{-\infty}^{\infty}\mathrm{c}_{\mathbf{d}'\mathbf{d}'}\left(\mathbf{y},\boldsymbol{\eta},\tau\right)\exp\left(-\mathrm{j}\ 2\pi f\tau\right)\mathrm{d}\tau \tag{D.21}$$

In equation (D.20) the acoustic-variable PSD is related to the integral across separation of the phase-shifted two-point CPSD associated with the acoustic-source distribution.

Appendix E

Low-frequency flow factors for the Lilley–Goldstein source term

As shown in section 3.2, in the low-frequency limit and for axisymmetric base flow, it is possible to represent the far-field acoustic contribution, that is output from a specific location in the turbulent flow, as a flow-factor linear operator acting on the separation integral of the phase-shifted two-point PSD of the acoustic source field. An important assumption on the two-point PSD of the source field allows for restricting the number of flow factor components needed in the problem. We assume that the two-point correlation function associated with different components of the applied-stress (3.6) and applied-force (3.8) fluctuating source fields is negligible if compared to the two-point correlation function between identical components.

$$\mathrm{c}_{Q'_{ij}Q'_{kl}} \ll \mathrm{c}_{Q'_{ij}Q'_{ij}} \qquad \mathrm{c}_{d'_i d'_k} \ll \mathrm{c}_{d'_i d'_i} \qquad i,j \neq k,l \quad \text{(no summation)} \tag{E.1}$$

Under the hypotheses (E.1), the flow-factor expressions (3.21) and (3.22) can be respectively simplified as

$$\mathrm{F}_{\mathbf{QQ}} = \bar{F}_{ij}\delta_i^m\delta_j^n\delta_k^o\delta_l^p\hat{\boldsymbol{\gamma}}_i\otimes\hat{\boldsymbol{\gamma}}_j\otimes\hat{\boldsymbol{\gamma}}_k\otimes\hat{\boldsymbol{\gamma}}_l\otimes\hat{\boldsymbol{\gamma}}_m\otimes\hat{\boldsymbol{\gamma}}_n\otimes\hat{\boldsymbol{\gamma}}_o\otimes\hat{\boldsymbol{\gamma}}_p$$

and

$$\mathrm{F}_{\mathbf{dd}} = \bar{F}_i\delta_i^k\delta_j^l\hat{\boldsymbol{\gamma}}_i\otimes\hat{\boldsymbol{\gamma}}_j\otimes\hat{\boldsymbol{\gamma}}_k\otimes\hat{\boldsymbol{\gamma}}_l$$

where only the PSD-contributing cylindrical-coordinate[a] components are considered. The components $\bar{F}_{ij}$ and $\bar{F}_i$ have been calculated by Morfey. The procedure in Appendix D of Morfey Tester and Powles[43] has been followed. The low-frequency-limit leading terms associated with the low-frequency flow-factor[b] have then been identified. The results for $\bar{F}_{ij}$ and $\bar{F}_i$ are reported in this appendix.

[a] The unit vectors $\hat{\boldsymbol{\gamma}}_i$ form the jet-noise cylindrical-coordinate basis as described in section A.3.

[b] A small-argument Bessel-function expansion has been applied to equations (A.20), (A.21) and (A.23) in Morfey et al.[43]

The axisymmetric base flow associated with a given acoustic-source sub region can be described as follows:

1. We define as sub-region radial line the perpendicular to the jet axis that goes through a given acoustic-source sub region.[c]

2. The distribution of the mean axial-velocity component along the sub-region radial line defines the sub-region velocity profile. Equally a sub-region speed-of-sound profile is defined as the distribution of speed of sound along the sub-region radial line.

3. A transverse-section flow is generated by rotating the sub-region velocity and speed-of-sound profiles around the jet centreline. The transverse-section flow is then translated along the jet centreline to generate the Pridmore-Brown base flow.

In the low-frequency approximation the axisymmetric Pridmore-Brown flow described above is simplified by assuming a top-hat profile with the source in proximity or inside the transition region. The flow-factor will therefore depend upon the flow variables at three different positions.

- The centreline, where the mean axial velocity and mean density are respectively indicated as $\breve{U}$ and $\breve{\rho}$

- The point at radial cylindrical coordinate R that corresponds to the acoustic-source sub region. Here mean axial velocity and mean density are respectively indicated as $\bar{U}$ and $\bar{\rho}$

- The region of quiescent medium outside the acoustic-source region, where mean speed of sound and mean density are respectively indicated as c_∞ and ρ_∞

Indicating with ϑ_∞ the angle between the source-region–observer unit vector and the downstream jet centreline, a centreline ambient-sound-speed Doppler factor is defined as

$$\breve{D} = \frac{1}{1 - \dfrac{\breve{U}}{c_\infty}\cos\vartheta_\infty}$$

It is useful to define a scalar value $\breve{E}$ related to the centreline Doppler factor and the centreline density $\breve{\rho}$.

$$\breve{E} = \frac{\breve{\rho}}{\rho_\infty \breve{D}^2}$$

Correspondingly, an ambient-sound-speed Doppler factor $\bar{D}$ and a scalar $\bar{E}$ are defined at the

[c]The sub-region radial line contains half of the points associated with the corresponding jet-centreline perpendicular. In other words starts at the jet centreline and goes indefinitely far from it.

space location $\mathbf{y}$ corresponding to the acoustic sub region:

$$\bar{D} = \frac{1}{1 - \dfrac{\bar{U}}{c_\infty}\cos\vartheta_\infty}$$

$$\bar{E} = \frac{\bar{\rho}}{\rho_\infty \bar{D}^2}$$

The components $\bar{F}_{ij}$ associated with the applied-stress flow factor are given as follows:

$$\bar{F}_{11} = \bar{D}^4$$

$$\bar{F}_{12} = 2\left(\frac{\mathrm{d}\bar{U}}{\mathrm{d}R}\frac{\bar{D}^3\cos\theta_\infty}{2\pi f\sin\theta_\infty}\right)^2 + \left(\frac{2\breve{E}\bar{D}^2}{1+\breve{E}}\right)^2$$

$$\bar{F}_{13} = \left(\frac{2\breve{E}\bar{D}^2}{1+\breve{E}}\right)^2$$

$$\begin{aligned}\bar{F}_{22} = {} & \frac{8}{3}\frac{\bar{D}^4}{(\sin\theta_\infty)^4}\left(\frac{1}{2}\left(\breve{E} - (\cos\theta_\infty)^2\right)\left(\frac{\bar{E}}{\breve{E}} - R\frac{\mathrm{d}\bar{E}}{\mathrm{d}R}\right) - \left(\bar{E} - (\cos\theta_\infty)^2\right)\right)^2 \\ & + \frac{1}{3}\left(\frac{4\bar{D}^2}{1+\breve{E}}\right)^2\left(R\frac{\mathrm{d}\bar{E}}{\mathrm{d}R} + \breve{E} - \bar{E}\right)^2\left(\frac{c_\infty}{2\pi f R\sin\theta_\infty}\right)^2 \\ & + \frac{1}{3}\left(\frac{2\bar{D}^2}{1+\breve{E}}\right)^2\left(R\frac{\mathrm{d}\bar{E}}{\mathrm{d}R} + 2\breve{E} - \bar{E}\right)^2\end{aligned} \tag{E.2}$$

$$\bar{F}_{23} = \left(\frac{4\bar{D}^2}{1+\breve{E}}\right)^2\left(\left(\frac{c_\infty}{2\pi f R}\ \frac{\breve{E}-\bar{E}}{\sin\theta_\infty} - \frac{\bar{D}\breve{E}\cos\theta_\infty}{2\pi f\sin\theta_\infty}\ \frac{\mathrm{d}\bar{U}}{\mathrm{d}R}\right)^2 + \left(\bar{E} - \frac{1}{2}\breve{E}\right)^2\right)$$

$$\begin{aligned}\bar{F}_{33} = {} & \frac{2}{3}\left(\frac{\bar{E}\left(\breve{E} - (\cos\theta_\infty)^2\right)\bar{D}^2}{\breve{E}\sin\theta_\infty}\right)^2 + \frac{1}{3}\left(\frac{4c_\infty\left(\breve{E}-\bar{E}\right)\bar{D}^2}{2\pi f R\left(1+\breve{E}\right)\sin\theta_\infty}\right)^2 \\ & + \frac{4}{3}\left(\frac{\left(2\breve{E}-\bar{E}\right)\bar{D}^2}{1+\breve{E}}\right)^2\end{aligned}$$

The remaining components of the applied-stress flow factor can be determined by using the symmetry property $\bar{F}_{ij} = \bar{F}_{ji}$. The components $\bar{F}_i$ associated with the applied-force flow factor

are given as follows:

$$\begin{aligned} \bar{F}_1 &= \bar{D}^4 \\ \bar{F}_2 &= \left(\frac{2\bar{E}}{1+\breve{E}}\right)^2 \bar{D}^4 \\ \bar{F}_3 &= \left(\frac{2\breve{E}}{1+\breve{E}}\right)^2 \bar{D}^4 \end{aligned} \tag{E.3}$$

Appendix F

Solution of the averaged equations for jet flows

In this appendix the solution strategy for the Reynolds Averaged Navier–Stokes equations (RANS) associated with a jet issuing from an axisymmetric nozzle is described. A description of the steps involved in the general solution strategy is given in section F.1. A detailed solution for a two-stream nozzle is presented as an example (section F.2) to show how the RANS solutions in this work are achieved. Possible developments of the solution strategy are listed in section F.3.

F.1 Step-by-step RANS solution

The RANS solution strategy is described by specifying all the steps involved from the input to the output. The methodology described here is general for all solutions included in this work. The input and output data involved in the procedure can be summarised as follows.

- Input: axisymmetric nozzle geometry, nozzle-exit flow variables, ambient pressure and temperature.[a]
- Output: Favre-averaged velocity, temperature, Reynolds stress and turbulence-dissipation rate on a set of prescribed acoustic-model points.

The sequence of steps that are made to achieve the solution is given in the following list.

1. The computational domain is defined as a cylindrical volume having the same symmetry axis as the nozzle. The domain diameter and axial dimension are defined according to

[a]The aim of the RANS solutions described here is to produce the turbulence statistics for a jets that correspond to available noise measurements. In the measurements the nozzle-exit velocity and static temperature are recorded with the acoustic data. The data also include the reservoir pressure and temperature together with the anechoic-chamber pressure and temperature.

the nozzle-exit diameter d_J (both lengths exceed $100d_J$). A constant-velocity ambient co-flow is introduced along the volume/nozzle axis, having the same direction as the jet. The co-flow velocity is determined as 5% of the jet nozzle-exit mean velocity (outer-flow nozzle-exit velocity for coaxial-jet cases).

2. The nozzle-inlet static/dynamic pressure and total temperature are calculated starting from the corresponding nozzle-exit conditions. Laminar and isentropic internal flow is assumed for the nozzle. The domain boundary conditions are set by imposing constant pressure and constant static temperature as the ambient characteristics.

3. The flow-field domain is defined as the simply connected 2-D region delimited by

   - Symmetry axis
   - Domain-outlet section (extending radially from the axis to the domain outer boundary, more than 100 d_J downstream the nozzle exit)
   - Domain outer boundary (constant distance from the symmetry axis)
   - Co-flow inlet section (extending radially from the outer nozzle wall to the domain outer boundary)
   - Nozzle wall
   - Nozzle inlet (extending radially from the symmetry axis to the nozzle wall)

   For coannular nozzles a secondary-flow inlet will extend from the inner-nozzle wall to the outer-nozzle wall. All the inlet sections are located at the same axial coordinate upstream of the nozzle exit.

4. The flow-field domain is designed and discretised by adopting the commercial software MSC/PATRAN. Due to RANS-solver requirements, the symmetry axis has to be located at $y_2 = 0$. In-house FORTRAN77 routines are combined with MSC/PATRAN to generate the near-wall mesh, where the RANS solver requires a particularly fine mesh due to the selected near-wall turbulence model (enhanced wall treatment). The flow-field discretisation is made by dividing it into quadrilateral elements, the set of elements and corresponding nodes defines a CFD mesh. All CFD meshes designed in this work contain a number of nodes included between 10^5 and 4×10^5.

5. The CFD mesh is imported into Fluent 6.2 (2-D, axisymmetric solver, double precision), where the boundary conditions are defined as follows:

   - Slip boundary condition (zero-friction wall) on the domain outer boundary
   - Symmetry-axis condition for the axis line
   - No-slip condition for the nozzle-section wall
   - Pressure-inlet conditions for the nozzle and computational-domain inlets. Constant radial profiles are assigned for total temperature, static and total pressure, as determined from the nozzle-exit and ambient conditions

- Pressure-outlet condition at constant static pressure (ambient pressure) for the domain outflow boundary.

6. The turbulence-closure model (Fluent 6.2, viscous panel) is set to RSM. The enhanced wall treatment is selected for the near-wall turbulence model.

7. The flow is initialised starting from the nozzle-inlet conditions. The iteration-step relaxation parameters are reduced for the pressure and for the momentum, as suggested in Ref. [72] for segregated-solver solution of compressible flows. The solver default target residuals are reduced to avoid a premature automatic stop of the iteration procedure. The iteration procedure is started. Provided the iteration converges towards a solution,[b] the residuals of the RANS equations are reduced at each step in the discretised flow field. The iteration procedure is stopped when a sufficiently small field for the residuals is obtained. A constant number of iterations is used for all the cases from a given nozzle. With exception of cases with convergence problems,[c] the residuals always fall below the value 10^{-5}. The corresponding field of Favre-averaged flow variables is the RANS solution. The field is sampled at the nodes of the CFD mesh.

8. The RANS solution is resampled on a set of acoustic-model points ordered along prescribed radial profiles (acoustic mesh). The resampling is performed by means of interpolation routines relating the CFD-mesh solution to a solution on the acoustic mesh. The interpolation routines use linear polynomial interpolation in the 2-D space domain defined as the smallest triangle having three CFD-mesh nodes as vertices and containing the given acoustic-mesh point.[d]

[b] The convergence of the solver depends on various parameters that have to be carefully evaluated. Parameters affecting the convergence of the iterative process are the zero-iteration conditions of the flow (the convergence is normally easier if the initial conditions are not very far from the final conditions; the test-cases discussed here demonstrate anyway that the solver converges also in cases initialised at conditions relatively far from the final solution, although it seems important to give to the initial flow the same direction as the solution), the choice of the length of each iteration step (parameters to reduce the amplitude of each step can be defined for each PDE), the capability of the mesh to capture the variations in the specific flow.

[c] Jet-flow cases for a specific single-stream nozzle geometry show a strange convergence behaviour. The solver achieves first a low-residuals condition and then proceeds with the iterations marching towards an unphysical solution and increasing the residuals until divergence. Further understanding of this specific problem is highly desirable to assess the limitations involved with the solution to this specific RANS system. The specific convergence problem has been one of the most time-consuming problems among those targeted in this work; we can say that the reasons behind the strange convergence/divergence behaviour might rely on the given flow setup rather than on a problem with the solution strategy. We note that in this case we are changing the experimental-flow setup by adding a co-flow stream that was not present in the experiments.

[d] The acoustic processor uses the RANS-solver output on a prescribed set set of spatial sampling points. The RANS solution is sampled at the nodal points of the CFD-mesh (e. g. Fig. F.2). An interpolation procedure has been implemented to transfer the solution from the CFD nodal points to the acoustic-model sample points. The interpolation procedure performs a loop across the acoustic-model sample points. For each point the two closest CFD nodes are identified. A third node is then found such that it is the closest to the sample point and –with the previously found two nodes– forms a triangle containing the sample point. A linear polynomial interpolation between the three nodal values is finally adopted. This assumes that the solution varies linearly with varying position inside the node triangle,

$$\mathrm{p}(y_1, y_2) = a_0 + a_1 y_1 + a_2 y_2$$

The imposition of the nodal values for the given flow variable f determine a solution for the coefficients a_i. The interpolated value is finally obtained by specifying the coordinates of the sample point in the function p.

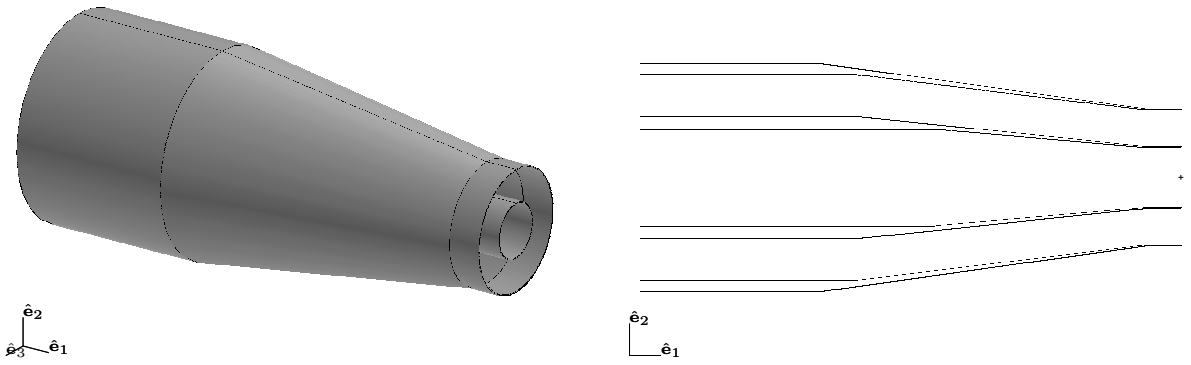

(a) 3-D view

(b) Axial section

Figure F.1: Geometry of the coaxial nozzle. The nozzle-exit diameters based on the internal wall are 0.0333 m for the inner wall and 0.0750 m for the outer wall. The thickness is 0.5 mm for the inner wall at the exit section. The jet is issued from a round exit section (primary flow) and an annular exit section (secondary flow). The area ratio between secondary section and primary section is 4.

F.2 A coaxial-jet solution

A case study for the RANS solution on a two-stream jet is detailed here to show with an example the method that is generally used in this work and described in section F.1 above. The preparation of the discretised flow field associated with the coaxial nozzle is first described. The RANS solution is then shown for a single flow condition.

F.2.1 Boundary conditions and flow-field discretisation

The nozzle is an area-ratio 4 coplanar nozzle. The geometry of the nozzle is shown in Fig. F.1, where both a 3-D view (a) and the axial section of the nozzle (b) are sketched. The geometry of the nozzle is axisymmetric. The jet leaves the nozzle with a nozzle-exit velocity profile determined by two different internal flows. The inner-nozzle flow (primary flow) has a higher nozzle-exit average speed than the flow in the annular-section nozzle (secondary flow), with a primary to secondary velocity ratio of 0.6. As described in section F.1, the jet forms part of the inflow boundary of a computational domain that is cylindrical, having the same symmetry axis as the nozzle. The computational domain is bounded by a slip-condition wall parallel to the axis and it is open transversely to the axis. The domain is characterised by a constant-velocity very-low-Mach-number ambient co-flow in the same direction as the jet. The domain has an annular-section inlet extending from the outer nozzle-rig wall to the slip-condition wall. The whole transverse section of the domain constitutes the flow outlet. The inlet conditions for the flow are set depending on the nozzle-exit conditions and by assigning the ambient co-flow.[a] The inlet conditions are defined as follows:

[a]The ambient co-flow is assigned trying to maintain a constant Mach-number ratio between secondary flow and ambient co-flow for all the flow cases.

1. The inner nozzle-inlet conditions are set as the static and stagnation pressures that guarantee the primary-flow nozzle-exit conditions.

2. The outer nozzle-inlet conditions are set as the static and total pressures that correspond to the prescribed secondary-flow nozzle-exit conditions.

3. The co-flow inlet, whose annular section extends from the nozzle outer wall to the top-domain wall, is set at the computational-domain static pressure and at a total pressure that guarantee a co-flow stream at a Mach number that equals the 5% of the secondary-flow nozzle-exit Mach number.

The nozzle-inlet conditions are determined by assuming an isentropic laminar flow in the interior of the nozzle and solving for the corresponding non-linear relation between the prescribed nozzle-exit flow characteristics and the nozzle-inlet flow characteristics.[b] The inlet boundary conditions are set by imposing a constant distribution of static pressure, total pressure and total temperature across the inlet sections. The outlet boundary conditions are set by imposing the ambient static pressure on the outlet section.[c]

The boundary conditions assumed for the flow imply axisymmetric flow statistics and therefore the RANS solution is taken as axisymmetric. The discretisation of the flow field is performed on half axial section. The half-plane section is bounded in the radial direction by the symmetry axis and by the domain outer boundary; it is limited by the inlet/outlet prescribed-pressure boundaries in the axial direction. The nozzle walls constitute the further boundary of this simply-connected plane domain. The flow-field discretisation is reported in Fig. F.2 (a), where the flow direction is from left to right. The mesh density is increased in those region where a large mean-flow gradient is expected, for this reason the region close to the no-friction wall (nearly uniform flow) is discretised with a mesh that is much coarser than the region in proximity of the symmetry axis (flow distortion due to the presence of the jet). Fig. F.2 (b) shows the mesh in greater detail for the region that is immediately downstream the nozzle exit. As mentioned in section F.1, the nozzle wall is assigned as a zero-flow boundary condition. The boundary layer is treated in the RANS by adopting an enhanced wall function (described in Chapter 11 of Ref. [72]) for the turbulence modelling inside the boundary layer. This type of wall function requires a fine discretisation in the near-wall region to allow for the resolution of the viscous sub layer in the vicinity of the wall. The field discretisation in proximity of the wall is shown in Fig. F.2 (c) and (d).[d] The mesh has been generated by adopting a commercial

[b] The isentropic-flow conservation relations corresponding to the average flow characteristics at two sections of prescribed area are solved iteratively by FORTRAN-77 routines. The prescribed nozzle-exit and computational-domain flow conditions are assigned in input together with the inlet/outlet areas associated with the primary and secondary flows and the computational-domain flow. Note that the calculation assumes the same fluid characteristics as the RANS solver (Table F.1).

[c] Being the computational-domain section constant downstream the jet rig, the mean static pressure is constant for all the flow inside the computational domain. The flow inside the nozzle is an expanding flow inside a subsonic convergent nozzle for both the primary (inner) and the secondary (outer) flows.

[d] Note that a quality assessment of the mesh needs to be performed a posteriori by visualising the y^+ (see Ref. [72]) distribution along the nozzle walls. An analysis for the highest-velocity case on the given mesh is needed to ensure that the solver limits for the y^+ parameter are respected.

Air as perfect gas ($p = \rho\ R\ T$)	
Constant-pressure specific heat	$c_p = 1006.43$ J kg^{-1}K^{-1}
Molar mass	$M = 0.02897$ kg mol^{-1}
Viscosity	$\mu = 1.789\ 10^{-5}$ kg m^{-1}s^{-1}
Thermal conductivity	$k_q = 0.0242$ W m^{-1}K^{-1}
Perfect-gas constant	$R = 287.0$ J kg^{-1}K^{-1}

Table F.1: Characteristics of the fluid used for the RANS solution. The values of $c_p,\ M,\ \mu, k_q$ and R are constant. R has been calculated by taking the value per mole ($\hat{R} = 8.314472$ J mol^{-1} K^{-1}) and by adopting the given molar mass.

software (MSC/PATRAN) combined with specifically implemented FORTRAN77 routines for the near-wall discretisation.

The fluid in the RANS solver is an ideal gas whose characteristics are summarised in Table F.1. Note that the viscosity μ and the thermal conductivity k_q are considered as constant.[e]

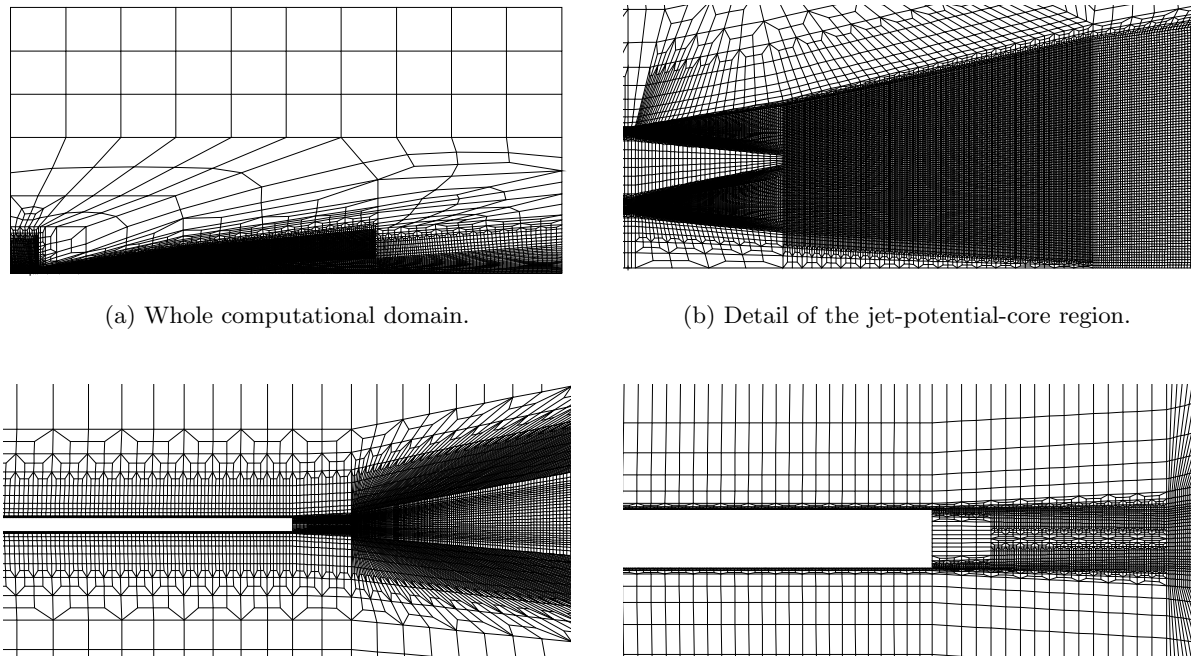

(a) Whole computational domain.

(b) Detail of the jet-potential-core region.

(c) Detail of the primary-secondary nozzle lip.

(d) Zoom-in detail of the primary-secondary nozzle lip.

Figure F.2: Mesh for the solution of the axisymmetric RANS with RSM closure and enhanced wall treatment.

The presence of compressibility implies that the RANS are written in terms of Favre-averaged variables. The energy-balance equation needs to be solved together with the continuity equation and the momentum-conservation equations. The closure of the averaged equations is performed by adopting the Reynolds-transport closure; this adds five equations for the turbulence modelling in the axisymmetric case (the reader is addressed to Ref. [72] for the full set of RANS equations). The turbulent-closure constant parameters appearing in the relations be-

[e]The dependence of μ and k_q on the static temperature has not been implemented in the solution. The solver default options for the ideal-gas have been used.

tween turbulent and standard flow variables (viscous-model panel of Fluent 6.2) have been set at the default value assigned by the solver. Fluent 6.2 allows for different solution strategies: the segregated solver with default discretisation order has been used in the present case. The iterative procedure converges to an approximate RANS solution that ensures residuals below the value 10^{-5} for all the equations.

F.2.2 Results

The solution achieved for a cold jet whose target axial-velocity ratio is 0.6 and whose target primary-flow velocity[f] is 280.7 m/s is reported in Fig. F.3 where contour plots indicate the averaged flow variables in the axial section of the flow domain near to the nozzle. The axial velocity peak value (a) is in good agreement with the target value for the flow. The radial-velocity contour plot (b) shows the entrainment flow due to the presence of the jet. The effect of compressibility are evident in the static-temperature distribution (d) showing static-temperature differences for differently expanded subsonic (c) flows. The level of anisotropy between the principal Reynolds stress components is given in (f), (g) and (h); where a good level of transverse isotropy is shown together with a marked difference between the amplitude of the axial component $\langle u_1' u_1' \rangle_{\rho}$ and the transverse components $\langle u_2' u_2' \rangle_{\rho}$ and $\langle u_3' u_3' \rangle_{\rho}$.

The Fluent solution is sampled at the nodal values of the CFD mesh (Fig. F.2) and interpolated on a different mesh to be used for the acoustic processing (acoustic mesh). The acoustic-mesh normalised axial-velocity and turbulence-intensity radial profiles in Fig. F.4 give a quantitative view of the flow solution. The axial-velocity profiles show the extent to which the target values are met by the calculated velocity field.

F.3 Possible developments

The RANS solution methodology described above can probably be improved in order to reduce the computational time, to further understand stability problems and to gather more accurate solutions. Some possible developments of the explained RANS solution strategy are here listed.

- A change to the adopted near-wall turbulence model could be implemented, to assess the possibility of using a less refined near-wall mesh. This step would reduce the computational time and seems essential if one needs to predict the flow-field statistics for 3-D cases.

- Further understanding of certain flow cases with solution-convergence problems is required. It would be helpful if the solution strategy can be improved in terms of stability.

[f]The velocities are defined at the nozzle exit. They are called target quantities because the inlet boundary conditions have been calculated from the target values by assuming isentropic flow inside the nozzle. A deviation from this target value is expected for the RANS solution; this is due to the combined effect of losses inside the nozzle and absorption of part of the laminar-flow kinetic energy by the fluctuating field.

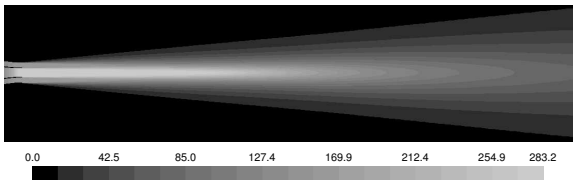

(a) Axial velocity $\langle u_1 \rangle_\rho$ (m/s).

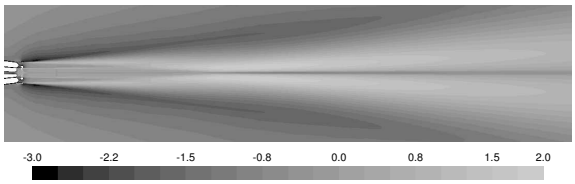

(b) Radial velocity $\langle u_2 \rangle_\rho$ (m/s).

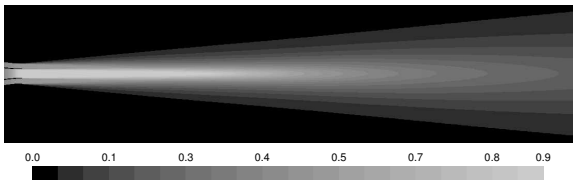

(c) Mach number $\langle u \rangle_\rho / \langle c \rangle_\rho$.

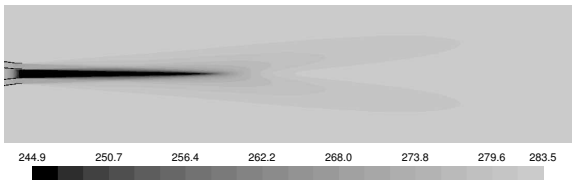

(d) Static temperature $\langle T \rangle_\rho$ (K).

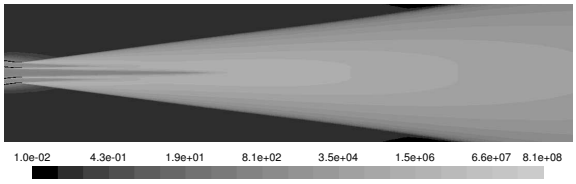

(e) Turbulence dissipation rate $\langle \epsilon \rangle_\rho$ (m^2/s^3).

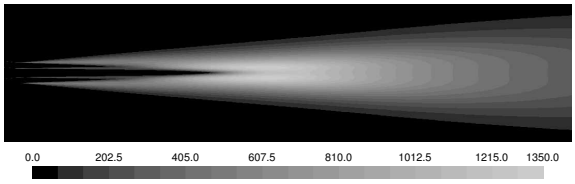

(f) Unit-density Reynolds-stress $\langle u_1' u_1' \rangle_\rho$ (m^2/s^2).

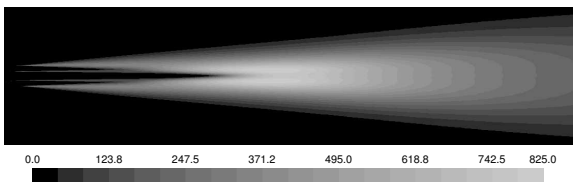

(g) Unit-density Reynolds-stress $\langle u_2' u_2' \rangle_\rho$ (m^2/s^2).

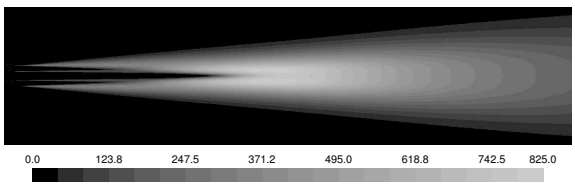

(h) Unit-density Reynolds-stress $\langle u_3' u_3' \rangle_\rho$ (m^2/s^2).

Figure F.3: RANS solution, Favre-averaged flow variables in the axial section of the jet flow. The tensor components are expressed along the cylindrical-basis unit vectors $\hat{\boldsymbol{\gamma}}_1, \hat{\boldsymbol{\gamma}}_2, \hat{\boldsymbol{\gamma}}_3$. All the diagrams represent the same spatial region in the axial section of the jet. The nozzle section is represented in black. The contour plots are symmetric with respect to the jet centreline as they are obtained by reflecting the solution initially obtained on half section. The visible asymmetries are due the graphic sampling of the diagram.

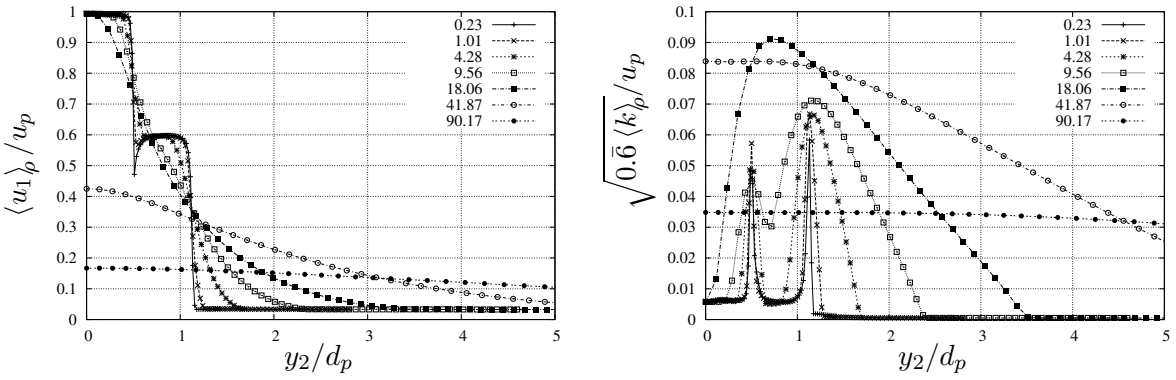

(a) Axial velocity

(b) Turbulence intensity

Figure F.4: Radial profiles for the Favre-averaged axial velocity and turbulence intensity after interpolation on the acoustic mesh. The radial position has been normalised with the inner diameter of the nozzle $d_p = 33.3$ mm. The normalisation velocity is the inner-flow target velocity $u_p = 280.7$ m/s. The labels indicate the axial coordinate y_1 in inner diameters d_p.

- Validation of the RANS-results against corresponding experimental data is desirable. This could open the way to a further investigation aiming to realise an optimal turbulent-jet set of turbulence-model constant parameters.[a] Improvements in terms of solution accuracy are possible if one changes from the solver-default turbulence-model parameters to the optimised set of turbulent-jet parameters.

- RANS systems with two-equation closure could be tested. This would require a supplement to the acoustic model to extrapolate the turbulent-jet anisotropy.

[a] Changing the turbulence-model parameters affects the spatial distribution and the amplitudes of the predicted flow statistics. As shown by Thies and Tam[20] for a two-equation turbulence model, altering the values of some of the closure-equation parameters produces a set of predicted turbulence statistics that is closer to measured turbulent-jet-statistics data. The solver used in this work allows for modifying the value of the closure-equation parameters.

Appendix G

Strouhal scaling of the two-point correlation coefficient model

In this appendix we show that the modulus of the two-point CPSD derived from the two-point correlation coefficient model (4.19) can be collapsed on a characteristic curve, if expressed as a function of the reduced frequency $Sr_\tau = f\tau_d$ and appropriately scaled. An important consequence of this property is that the scaled autospectrum $\hat{\mathrm{s}}_0(\mathbf{y}, \mathbf{0}, f)/\tau_d$ and the normalised $1/e$-decay length scales $\tilde{l}_i(\mathbf{y}, f)/l_i$ of the normalised two-point CPSD σ_0 can be collapsed on corresponding characteristic curves, if expressed as function of Sr_τ.

The Fourier transform of the simplified[a] correlation-coefficient model (4.19) is given as follows

$$\hat{\mathrm{s}}_0(\mathbf{y}, \boldsymbol{\eta}, f) = \int_{-\infty}^{\infty} \exp\left(-\sqrt{\left(\frac{\tau - \eta_1/U_c}{\tau_d}\right)^2 + \left(\frac{\eta_1}{l_1}\right)^{a_l} + \left(\frac{\eta_2}{l_2}\right)^{a_l} + \left(\frac{\eta_3}{l_3}\right)^{a_l}} - \mathrm{j}\ 2\pi f\tau\right) \mathrm{d}\tau \quad \text{(G.1)}$$

By introducing the time shift $\tau' = \tau - \eta_1/U_c$, it is possible to express equation (G.1) as

$$\hat{\mathrm{s}}_0(\mathbf{y}, \boldsymbol{\eta}, f) = \exp\left(-\mathrm{j}\ 2\pi f\eta_1/U_c\right) \int_{-\infty}^{\infty} \exp\left(-\sqrt{\left(\frac{\tau'}{\tau_d}\right)^2 + \eta_i^{a_l}/l_i^{a_l}} - \mathrm{j}\ 2\pi f\tau'\right) \mathrm{d}\tau' \quad \text{(G.2)}$$

The imaginary part of the integrand in (G.2) is an odd function that integrates to zero. The integral in (G.2) converges to a real and positive value. This implies that (G.2) is a modulus–phase description of the complex Fourier transform of model (4.19), where the modulus is given by the value of the integral, the phase angle is given by the value $-2\pi f\eta_1/U_c$. Since the

[a]Note that the results found in this appendix for the simplified model (4.19) are also valid for the more general model (4.16). In the latter case one needs to add the hypothesis of convergence of the Fourier integral with respect to τ; this imposes restrictions on the value of the exponent c.

real part of the integrand in (G.2) is even, the modulus of G.2 can be expressed as

$$|\hat{\mathrm{s}}_0(\mathbf{y},\boldsymbol{\eta},f)| = 2\int_0^\infty \exp\left(-\sqrt{\left(\frac{\tau'}{\tau_d}\right)^2+\eta_i^{a_l}/l_i^{a_l}}\right)\cos\left(2\pi Sr_\tau\frac{\tau'}{\tau_d}\right)\mathrm{d}\tau' = \tau_d\,|\hat{\mathrm{s}}_0(\mathbf{y},\eta,Sr_\tau)| \quad \text{(G.3)}$$

Here $Sr_\tau = f\tau_d$ indicates a non-dimensional frequency. We give it the name local Strouhal number, due to the spatial variability of the parameter τ_d. The normalised-CPSD modulus $|\hat{\mathrm{s}}_0(\mathbf{y},\eta,Sr_\tau)|$ is a density with respect to Sr_τ, rather than f. Note that equation (G.3) states that, given a space separation and the local value of the time constant τ_d, a characteristic function of the local Strouhal number Sr_τ represents the scaled modulus of the normalised two-point CPSD (G.3).

A first implication is that the zero-separation scaled two-point CPSD – the autospectrum divided by the mean squared value – can be scaled from non-dimensional to dimensional frequency as follows:

$$\hat{\mathrm{s}}_0(\mathbf{y},\mathbf{0},f) = \tau_d\hat{\mathrm{s}}_0(\mathbf{y},\mathbf{0},Sr_\tau) = \tau_d\,(\mathbf{y})\,\mathrm{f}_A\,(Sr_\tau\,(\mathbf{y})) \quad \text{(G.4)}$$

A characteristic-spectrum collapse is therefore obtained for $\hat{\mathrm{s}}_0(\mathbf{y},\mathbf{0},f)$ by expressing it as function of Sr_τ and by dividing with τ_d.

A second implication is that the modulus of the normalised two-point CPSD at a given space-separation $\boldsymbol{\eta}$ collapse on a single curve in the Sr_τ domain,

$$|\sigma_0(\mathbf{y},\boldsymbol{\eta},Sr_\tau)| = \frac{|\hat{\mathrm{s}}_0(\mathbf{y},\boldsymbol{\eta},Sr_\tau)|}{\hat{\mathrm{s}}_0(\mathbf{y},\mathbf{0},Sr_\tau)} = \mathrm{f}\,(\eta_1/l_1\,(\mathbf{y})\,,\eta_2/l_2\,(\mathbf{y})\,,\eta_3/l_3\,(\mathbf{y})\,,Sr_\tau\,(\mathbf{y}))$$

The corresponding $1/e$-decay length scales are obtained by solving for

$$\begin{cases} \left|\sigma_0\left(\tilde{l}_1/l_1,0,0,Sr_\tau\right)\right| = \exp(-1) \\ \left|\sigma_0\left(0,\tilde{l}_2/l_2,0,Sr_\tau\right)\right| = \exp(-1) \\ \left|\sigma_0\left(0,0,\tilde{l}_3/l_3,Sr_\tau\right)\right| = \exp(-1) \end{cases} \quad \text{(G.5)}$$

Since σ_0 is a monotonic decaying function of the normalised space-separation coordinates η_i/l_i (no summation), equations (G.5) have single solutions $\tilde{l}_i/l_i$ corresponding to a given local Strouhal number. The length scales $\tilde{l}_i\,(\mathbf{y},f)$ will then collapse to give a characteristic normalised-length-scale spectral dependence in the Sr_τ domain if divided by $l_i\,(\mathbf{y})$; they can be defined as follows:

$$\tilde{l}_i\,(\mathbf{y},f) = l_i\,(\mathbf{y})\,\mathrm{f}_L\,(Sr_\tau\,(\mathbf{y})) \quad \text{(G.6)}$$

Appendix H

Scaling quadrupole-dominated measured spectra for single-stream jets

In order to validate the jet-noise model, the far-field jet-noise predictions made in the present work are compared to corresponding experimental data acquired in anechoic facilities. The calibration procedure associated with the jet-noise model is also based on available measurements for jet-noise 1/3-octave spectra. This means that the noise prediction is dependent on the accuracy of selected noise measurements and that possible errors in the measurements can affect both the noise prediction and the model validation. In this appendix we try to assess the error level that can be associated with jet-noise measurements.

It is generally accepted that, for subsonic exhaust velocities, far-field single-stream jet-noise measurements should scale according to the Lighthill[1] scaling law if the applied-stress equivalent sources dominate the noise production and the noise is measured at a 90-degree polar angle from the jet. In this appendix we consider available far-field jet-noise data which were acquired at 90-degree polar angle for single-stream jets characterised by moderate temperature gradients. We use the isothermal single-stream measurements acquired by QinetiQ[10] and by Tanna, Dean and Burrin;[9] we also consider the measurements performed by Lush[73] on unheated single-stream jets. We restrict attention to the 90-degree 1/3-octave spectra;[a] these were acquired at a distance exceeding $70d_J$ for all considered cases. A comparison between the experimental data is made by normalising the acquired jet-noise 1/3-octave spectra, based on a Lighthill–Strouhal scaling as explained in [56]. We normalise the 90-degree acoustic measurements by using the Lighthill[1] scaling law. The normalised SPL associated with a given

[a] In the present work, regarding jet-noise experimental data, we only consider 1/3-octave spectra representative of far-field jet noise.

measurement is scaled as follows:

$$\mathrm{SPL_N} = \mathrm{SPL} - 20\log_{10}(d_J) + 20\log_{10}(r) - 80\log_{10}(u_J) - 20\log_{10}(p_\infty) + 40\log_{10}(T_\infty) \quad \text{(H.1)}$$

Here we use the international system for the units of velocity, temperature, length and pressure; these are m/s, K, m and Pa, respectively. Here SPL denotes the measured sound pressure level; note that we have assumed $T_J = T_\infty$.[b] We assume a Strouhal-domain collapse for the normalised-SPL 1/3-octave spectra, with non-dimensional frequency given by $Sr = fd_J/u_J$. We refer to the application of the normalisation (H.1) and the presentation of frequency-dependent data in the Sr domain as Lighthill–Strouhal scaling. The result of applying Lighthill–Strouhal scaling to the measurements by QinetiQ,[10] by Tanna et al[9] and by Lush[73] is shown in Fig. H.1. Jet-noise measurements from each facility at varying nozzle-exit velocity u_J are shown in Fig. H.1 (a), (b) and (c). These are compared in Fig. H.1 (d). As shown in Fig. H.1 (a) the Lighthill–Strouhal scaling of the data results in a good collapse for the QinetiQ[10] data, with a scatter of 1 to 2 dB in the Strouhal range from 0.1 to 3; the scatter is 2 to 3 dB at low and high frequencies. A greater SPL scatter is present in the earlier measurements[c] performed by Lush[73] and by Tanna, Dean and Burrin.[9]The combined dependence of the measured jet noise on jet rig/measurement environment can be seen when we place all the Lighthill–Strouhal scaled measurements on the same diagram, Fig. H.1 (d). Here a difference of 3 to 4 dB in level characterises the data at low frequency; the difference grows with increasing frequency to 5 dB at $Sr = 1$, and to 7 dB at $Sr = 10$.

The comparison made in this appendix shows us that, although quadrupole-dominated 90-degree jet-noise 1/3-octave spectra from subsonic single-stream jets approximately collapse on a characteristic spectrum – if normalised according to (H.1) and represented as a function of the Strouhal number fd_J/u_J – an error is associated with this collapse. This error, appearing as a scatter in the collapse of Lighthill–Strouhal normalised isothermal 1/3-octave SPL spectra, is present even for different measurements taken in the same facility (with reduced magnitude for the QinetiQ[10] measurements) and increases when data measured at different facilities are compared. The failure to collapse can be attributed to a series of different phenomena that are not considered by the Lighthill–Strouhal scaling. These include Reynolds-number effects,[d]

[b] While the assumption $T_J = T_\infty$ is coherent with the isothermal-jet data of Refs. [10,9], it is an approximation for the Lush measurements, Ref. [73] (unheated flow). No records of the nozzle-exit/ambient static temperature are available for the Lush measurements, we assumed in this case an ambient/nozzle-exit temperature of 278 K. Note that at temperatures around 273 K, an error of 20 K for the ambient temperature results in a 1.3 dB correction on $\mathrm{SPL_N}$ (H.1).

[c] A major improvement of the quality of the jet-noise measurement, especially in terms of reduced noise pollution from sources that are different from the turbulence-mixing, is expected to be associated with the state-of-the-art jet-noise facility utilised for the QinetiQ[10] measurements. We must anyway note that, in the comparisons presented in this thesis, the M_J range is wider for the measurements in Ref. [9] and Ref. [73] that were performed in the 1970s, respectively in the Lockheed jet-noise facility and in the ISVR large anechoic chamber. Harper-Bourne[56] recently published the Lighthill–Strouhal scaled QinetiQ[10] data, as in Fig. H.1 (a) and including a measurement at $M_J = 1$. The addition of the higher-velocity spectrum does not sensibly change the $\mathrm{SPL_N}$ scatter observed in the collapse of Fig. H.1 (a).

[d] The term Reynolds-number effect refers both to partially-developed turbulence at the upstream region of the jet, and to a different rate of boundary-layer development at constant nozzle geometry. In both cases we can

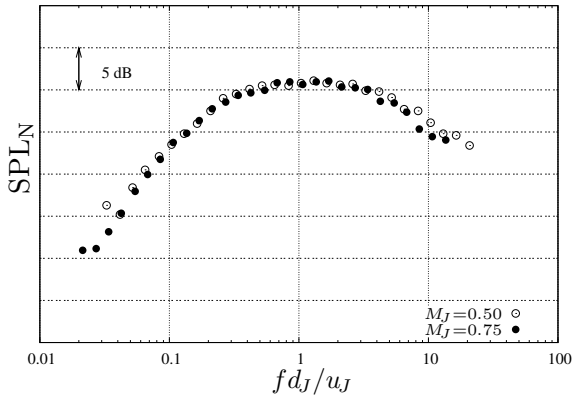

(a) Data from Ref. [10].

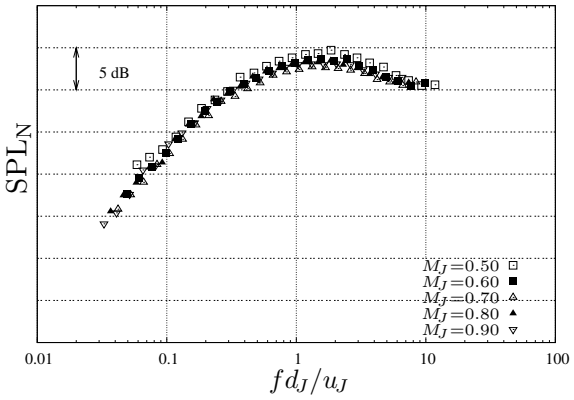

(b) Data from Ref. [9].

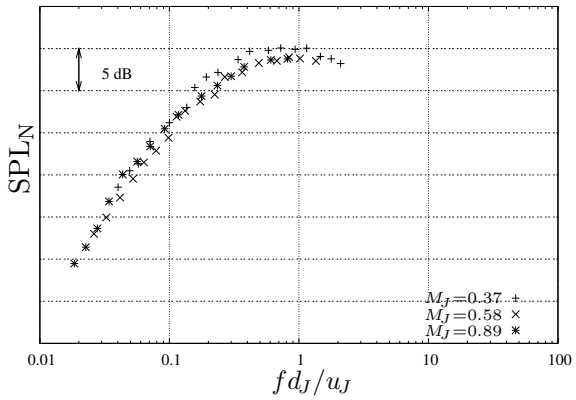

(c) Data from Ref. [73].

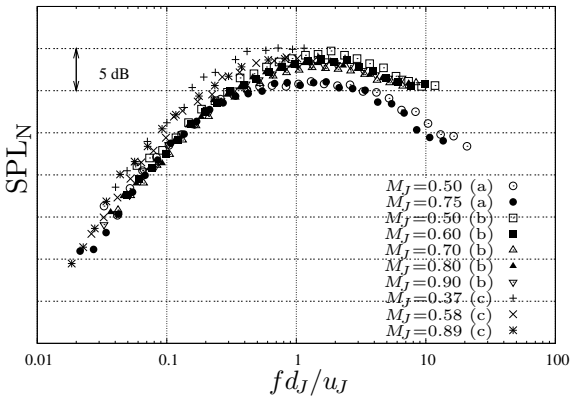

(d) Data from Ref. [10], [9] and [73]

Figure H.1: Lighthill–Strouhal scaling of 90-degree jet noise. Measured SPL 1/3-octave spectra are normalised according to equation (H.1) and plotted as a function of the Strouhal number $Sr = fd_J/u_J$.

effect of the convection speed on the volumetric source strength, contamination of the data from noise sources different from jet noise, different methods of correcting the data,[e] and boundary-condition effects.[f]

expect variations of the turbulence field characteristics in the initial region of the jet. This can have implications both on the peak level and on the spectral shape of the measured noise. Measurements regarding the frequency-dependent axial distribution of jet-noise source strength, e. g. the polar correlation technique Ref. [74], indicate upstream shifting of the acoustic-source centroid at increasing frequencies. This implies that changes of the turbulence characteristics in the upstream region of the jet are expected to affect the high-frequency region of the measured jet-noise spectra.

[e]An atmospheric-absorption correction is present in the QinetiQ[10] and in the Tanna[9] measurements. As reported in Ref. [73], the Lush[73] measurements were not corrected for atmospheric attenuation. Furthermore the latter data are affected by non-linear microphone response at frequencies above 10 kHz. While the whole 1/3-octave spectra from Ref. [10,9] have been used in the present appendix, the 1/3-octave bands above 10 kHz have been removed from the Lush[73] spectra. Note that we can assume an atmospheric absorption ¡ 0.5 dB at frequencies below 10 kHz.

[f]Alteration of the turbulent mixing due to variations in the co-flow stream, potential-core turbulence intensity, small-scale characteristics of the nozzle wall.

Appendix I

Jet-noise model components in the downstream polar arc

In this appendix, the far-field 1/3-octave components associated with the jet-noise model developed in the present thesis are evaluated for observer positions in the rear arc and compared to corresponding jet-noise measurements. As explained in Chapter 5, this comparison is to be considered as a preliminary result, due to the stretching of the RANS-solution flow-statistics field and to the preliminary connection relations used in the thesis. It is anyway of interest, in order to give a first evaluation to the acoustic-propagation model and to assess how the modelled SPL spectral components compare to corresponding jet-noise measurements. The comparison is made for an isothermal single-stream jet at nozzle-exit Mach number $M_J = 0.75$. The result is shown in Fig. I.1, where the QinetiQ[10] jet-noise measurements at a set of polar angles spanning the rear arc from 30° to 80° are compared to corresponding model components. Note that the corresponding sideline-noise comparison, at 90° polar angle, is reported in Fig. 5.6 (b). The model components overpredict the measured 1/3-octave spectra; this is an encouraging result meaning that the model has the potential of being used as a prediction tool once the components are opportunely frequency-filtered and combined. The modelled noise is dominated by the applied-stress source contributions. The preliminary result shows that applied-stress component HF4 of the high-frequency solution (3.16) presents an increasing-SPL trend when the observer polar angle varies from 90° to 60°; the SPL decreases going from 60° to 30° polar angles, with a great reduction moving from 50° to 40°, as the component is subject to a substantial cone-of-silence effect at 40°. The applied-stress component LF2, associated with the low-frequency solution (3.23), shows monotonically increasing SPL as the observer polar angles change from 90° to 30°. The model predicts a dominating low-frequency solution (3.23) in the region closest to the jet axis.

The results in the present appendix suggests that the changes in spectral shape of isothermal jet-noise measurements at varying observer polar angle are the result of a varying propagation factor acting on a constant volumetric-source-strength factor. This view of one source

mechanism with varying propagation factor is in line with previous acoustic-analogy jet-noise theories, e. g. works by Morris and Boluriaan[22] or by Goldstein and Leib.[38]

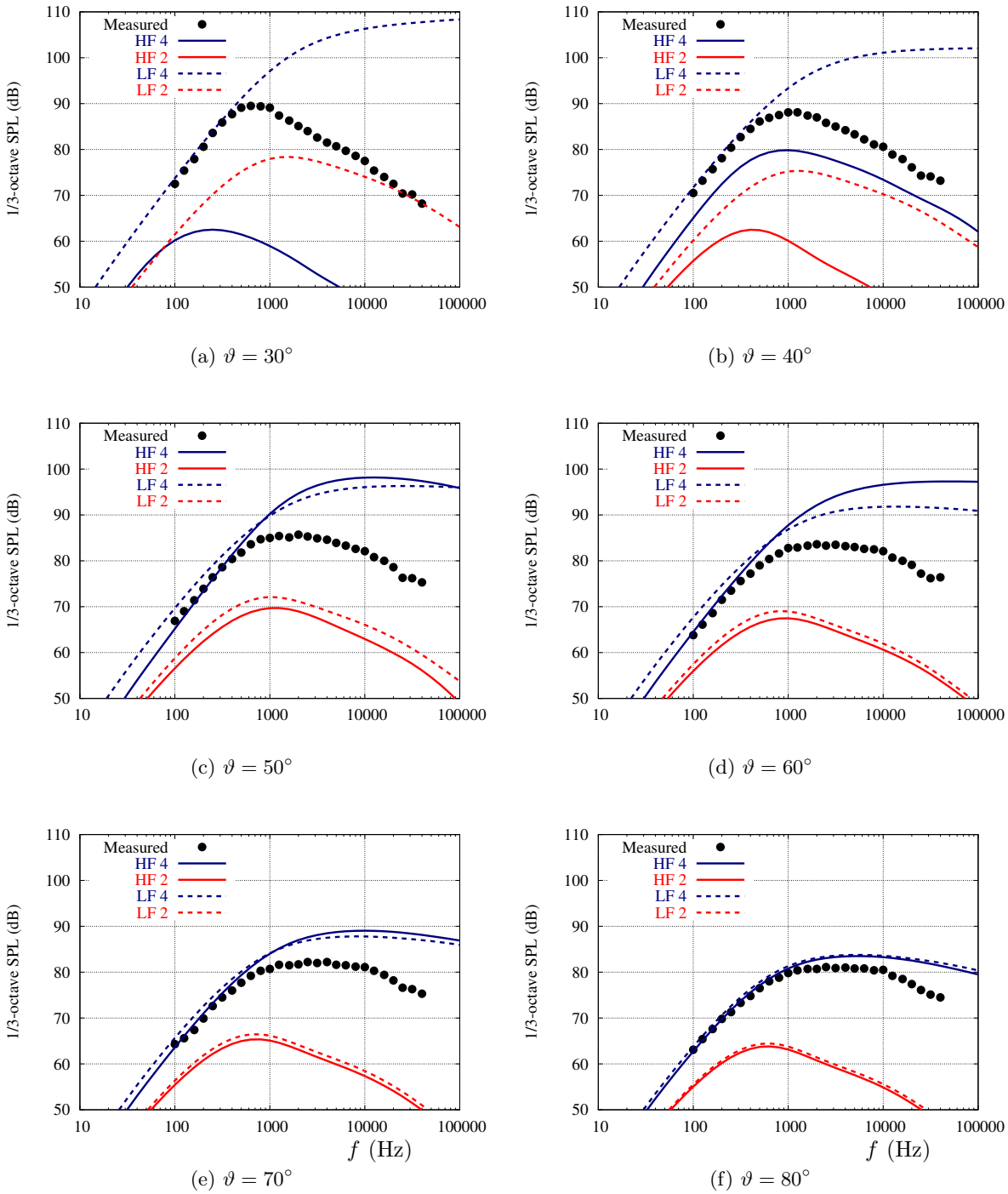

(a) $\vartheta = 30°$ (b) $\vartheta = 40°$

(c) $\vartheta = 50°$ (d) $\vartheta = 60°$

(e) $\vartheta = 70°$ (f) $\vartheta = 80°$

Figure I.1: Jet-noise 1/3-octave spectra at varying downstream polar angle ϑ. Model components and measured data correspond to the isothermal jet issuing from the QinetiQ conical nozzle with nozzle-exit characteristics: $u_J = 253$ m/s, M_J=0.75 and $d_J = 0.086$ m. The measured data (QinetiQ, NTF Pyestock, United Kingdom), Ref. [10], were acquired at a distance greater than 10 m, corrected at high frequency for the atmospheric attenuation and normalised assuming a distance of 6 m; the model components are related to the normalisation distance. The labels are as in Fig. 5.6, compare Fig. 5.6 (b) for sideline noise.

Table of statistical functions

Quantity	Definition	Symbol
2-point correlation function for vectors $\mathbf{a}$ and $\mathbf{b}$	$\langle \mathbf{a}\left(\mathbf{y}-\boldsymbol{\eta}/2,t\right) \otimes \mathbf{b}\left(\mathbf{y}+\boldsymbol{\eta}/2,t+\tau\right)\rangle_t$	$\mathrm{c}_{\mathbf{ab}}\left(\mathbf{y},\boldsymbol{\eta},t\right)$
2-point correlation function for tensors $\mathbf{A}$ and $\mathbf{B}$	$\langle \mathbf{A}\left(\mathbf{y}-\boldsymbol{\eta}/2,t\right) \otimes \mathbf{B}\left(\mathbf{y}+\boldsymbol{\eta}/2,t+\tau\right)\rangle_t$	$\mathrm{c}_{\mathbf{AB}}\left(\mathbf{y},\boldsymbol{\eta},\tau\right)$
2-point correlation function for the fluctuating part of tensors $\mathbf{A}$ and $\mathbf{B}$[a]	$\langle \mathbf{A}'(\mathbf{y}-\boldsymbol{\eta}/2,t) \otimes \mathbf{B}'(\mathbf{y}+\boldsymbol{\eta}/2,t+\tau)\rangle_t$	$\mathrm{c}_{\mathbf{A'B'}}(\mathbf{y},\boldsymbol{\eta},\tau)$
Component of the latter due to A_{ij} and B_{kl}	$\left\langle A'_{ij}(\mathbf{y}-\boldsymbol{\eta}/2,t)\, B'_{kl}(\mathbf{y}+\boldsymbol{\eta}/2,t+\tau)\right\rangle_t$	$c_{ij,kl}\left(\mathbf{y},\boldsymbol{\eta},\tau\right)$
2-point correlation-coefficient function (CCF)[b] for components of $\mathrm{c}_{\mathbf{A'B'}}$	$c_{ij,kl}\left(\mathbf{y},\boldsymbol{\eta},\tau\right)/c_{ij,kl}\left(\mathbf{y},\mathbf{0},0\right)$	$\hat{c}_{ij,kl}\left(\mathbf{y},\boldsymbol{\eta},\tau\right)$
2-point cross power spectral density (CPSD) of tensors $\mathbf{A}$ and $\mathbf{B}$	FT$[\mathrm{c}_{\mathbf{A'B'}}\left(\mathbf{y},\boldsymbol{\eta},\tau\right)]$ with respect to τ	$\mathrm{s}_{\mathbf{AB}}\left(\mathbf{y},\boldsymbol{\eta},f\right)$
Component of the latter due to A_{ij}, B_{kl}; 2-point CPSD of A_{ij}, B_{kl}	FT$[c_{ij,kl}\left(\mathbf{y},\boldsymbol{\eta},\tau\right)]$ with respect to τ	$s_{ij,kl}\left(\mathbf{y},\boldsymbol{\eta},f\right)$
Scaled 2-point CPSD of A_{ij}, B_{kl}	$s_{ij,kl}\left(\mathbf{y},\boldsymbol{\eta},f\right)/c_{ij,kl}\left(\mathbf{y},\mathbf{0},0\right)$, FT$[\hat{c}_{ij,kl}\left(\mathbf{y},\boldsymbol{\eta},\tau\right)]$ with respect to τ	$\hat{s}_{ij,kl}\left(\mathbf{y},\boldsymbol{\eta},f\right)$
Normalised 2-point CPSD of A_{ij}, B_{kl}	$s_{ij,kl}\left(\mathbf{y},\boldsymbol{\eta},f\right)/s_{ij,kl}\left(\mathbf{y},\mathbf{0},f\right)$	$\sigma_{ij,kl}\left(\mathbf{y},\boldsymbol{\eta},f\right)$
Scalar CCF functions used for modelling $\mathrm{c}_{\mathbf{A'B'}}$ when $\mathbf{A}$ and $\mathbf{B}$ are Reynolds stresses	$\hat{c}_{ij,kl}\left(\mathbf{y},\boldsymbol{\eta},\tau\right) \simeq \hat{\mathrm{c}}\left(\mathbf{y},\boldsymbol{\eta},\tau\right)$ or $\hat{\mathrm{c}}_0(\mathbf{y},\boldsymbol{\eta},\tau)$	$\hat{\mathrm{c}}, \hat{\mathrm{c}}_0(\mathbf{y},\boldsymbol{\eta},\tau)$
Fourier transform of CCF model functions	FT$[\hat{\mathrm{c}}, \hat{\mathrm{c}}_0(\mathbf{y},\boldsymbol{\eta},\tau)]$ with respect to τ	$\hat{\mathrm{s}}, \hat{\mathrm{s}}_0(\mathbf{y},\boldsymbol{\eta},f)$
Scalar functions used for modelling the separation dependence of the 2-point CPSD[c]	$\hat{\mathrm{s}}\left(\mathbf{y},\boldsymbol{\eta},f\right)/\hat{\mathrm{s}}\left(\mathbf{y},\mathbf{0},f\right)$ and likewise for $\hat{\mathrm{s}}_0$	$\sigma, \sigma_0(\mathbf{y},\boldsymbol{\eta},f)$

(*a*) This is the two-point covariance function for $\mathbf{A}$ and $\mathbf{B}$, or the τ-dependent part of $\mathrm{c}_{\mathbf{AB}}$:

$$\mathrm{c}_{\mathbf{AB}}\left(\mathbf{y},\boldsymbol{\eta},\tau\right) = \mathrm{c}_{\mathbf{A'B'}}\left(\mathbf{y},\boldsymbol{\eta},\tau\right) + \langle \mathbf{A}\left(\mathbf{y}-\boldsymbol{\eta}/2,t\right)\rangle_t \otimes \langle \mathbf{B}\left(\mathbf{y}+\boldsymbol{\eta}/2,t\right)\rangle_t$$

We assume that $\mathbf{A}' = \mathbf{A} - \langle \mathbf{A}\rangle_t$ and $\mathbf{B}' = \mathbf{B} - \langle \mathbf{B}\rangle_t$ are such that $\mathrm{c}_{\mathbf{A'B'}}$ always decays to 0 for large τ, satisfying the hypotheses for the application of the Fourier transform (FT[ ]).

(*b*) This differs from the standard definition which has denominator (no summation)

$$\left(c_{ij,ij}\left(\mathbf{y}-\boldsymbol{\eta}/2,\mathbf{0},0\right) c_{kl,kl}\left(\mathbf{y}+\boldsymbol{\eta}/2,\mathbf{0},0\right)\right)^{1/2} = \left(\left\langle \left(A'_{ij}\right)^2\left(\mathbf{y}-\boldsymbol{\eta}/2\right)\right\rangle_t \left\langle \left(B'_{kl}\right)^2\left(\mathbf{y}+\boldsymbol{\eta}/2\right)\right\rangle_t\right)^{1/2}$$

However, if A'_{ij} and B'_{ij} are statistically homogeneous with respect to $\mathbf{y}$, the definitions coincide.

(*c*) The functions also model the normalised 2-point CPSD of A_{ij}, B_{kl} when these are Reynolds-stress components.

Nomenclature

a, $\mathbf{a}$, $\mathbf{A}$	Source strength for moving acoustic point sources of monopole, dipole and quadrupole order, see Appendix C.
a_l	Spatial decay parameter of the isotropic-shape Reynolds-stress two-point correlation coefficient model (4.19).
$\mathrm{C_f}(\tilde{\alpha})$	Cancellation-factor function. It is defined as the volume integral across separation of the generally phase-shifted normalised two-point CPSD model σ_0. See equation (4.35).
c, $\bar{c}$	Speed of sound, averaged value.
$\mathrm{c}_{\mathbf{Ss}}(\mathbf{y}, \boldsymbol{\eta}, \tau)$	Tensor function representing the two-point cross correlation between the random tensor variables $\mathbf{S}(\mathbf{y} - \boldsymbol{\eta}/2, t)$ and $\mathbf{s}(\mathbf{y} + \boldsymbol{\eta}/2, t + \tau)$; it is expressed as $\overline{\mathbf{S} \otimes \mathbf{s}}$, where the overbar indicates averaging.
$\mathrm{c}_{\mathbf{S's'}}(\mathbf{y}, \boldsymbol{\eta}, \tau)$	Tensor function representing the two-point cross covariance between the random tensor variables $\mathbf{S}(\mathbf{y} - \boldsymbol{\eta}/2, t)$ and $\mathbf{s}(\mathbf{y} + \boldsymbol{\eta}/2, t + \tau)$; it is expressed as $\overline{\mathbf{S}' \otimes \mathbf{s}'}$, where the overbar indicates averaging; $\mathbf{S}'$ and $\mathbf{s}'$ are the fluctuating parts of $\mathbf{S}$ and $\mathbf{s}$.
$c_{ij,kl}(\mathbf{y}, \boldsymbol{\eta}, \tau)$	Component of the two-point covariance function of the Reynolds-tress; it corresponds to the ij and kl Reynolds-stress components with respect to the cylindrical-coordinate unit-vector basis in $\mathbf{y}$.
$\hat{c}_{ij,kl}(\mathbf{y}, \boldsymbol{\eta}, \tau)$	Two-point correlation-coefficient function of $c_{ij,kl}$.
$\hat{\mathrm{c}}, \hat{\mathrm{c}}_0(\mathbf{y}, \boldsymbol{\eta}, \tau)$	Model and simplified isotropic-decay model for $\hat{c}_{ij,kl}$; see equations (4.16) and (4.19).
D_v	Doppler factor associated with an acoustic problem where an acoustic source moves with velocity $\mathbf{v}$ with respect to a uniform medium; see expression (C.25).
$\mathbf{d}$	Applied-force equivalent acoustic source in the acoustic analogy; see (3.8).
$\mathbf{d}^{(1)}$	Contribution to the applied-force equivalent acoustic source $\mathbf{d}$, associated with the term $T'\mathbf{u}'$; see (4.10).

$\mathbf{d}^{(2)}$	Contribution to the applied-force equivalent acoustic source $\mathbf{d}$, due to the unit-density Reynolds-stress $\mathbf{u}' \otimes \mathbf{u}'$; see (4.11).
d_J	Nozzle-exit diameter of a turbulent jet.
$\bar{F}_{ij},\ \bar{F}_i$	Flow-factor for the ij applied-stress-source component and for the i component of the applied-force source.
$\mathrm{F}_{\mathbf{QQ}},\ \mathrm{F}_{\mathbf{dd}}$	Flow-factor tensors for applied-stress and applied-force sources.
$\mathrm{f}_A\,(Sr_\tau)$	Characteristic spectrum function for the Reynolds-stress autospectrum; see (G.4).
$\mathrm{f}_L\,(Sr_\tau)$	Characteristic spectrum function for the Reynolds-stress frequency-dependent length scales $\tilde{l}_i$; see (G.6).
$\mathrm{H}^{(i)}(\mathbf{y})$	Spatial Heaviside function; its value is 0 or 1 depending on $\mathbf{y}$ being external or internal to the i^{th} acoustic-source subregion.
k	Turbulent kinetic energy.
$l_i\,(\mathbf{y})$	Length scale associated with the Reynolds-stress two-point correlation coefficient model. It is the $1/e$-decay space separation of $\hat{\mathrm{c}}\,(\mathbf{y}, \eta\hat{\boldsymbol{\gamma}}_i, 0)$ or $\hat{\mathrm{c}}_0(\mathbf{y}, \eta\hat{\boldsymbol{\gamma}}_i, 0)$. Introduced in equations (4.16) and (4.19).
$\tilde{l}_i\,(\mathbf{y}, f)$	Length scale associated with the Reynolds-stress normalised two-point CPSD model. It is the 1/e-decay space separation of $\sigma\,(\mathbf{y}, \eta\hat{\boldsymbol{\gamma}}_i, f)$ or $\sigma_0(\mathbf{y}, \eta\hat{\boldsymbol{\gamma}}_i, f)$. See Fig. 4.4 and Appendix G.
M	Mach number; also used to indicate the source-motion acoustic Mach number; see (C.18).
M_J	Mean centreline acoustic Mach number at the nozzle exit of a turbulent jet.
$p,\ p'$	Thermodynamic pressure, acoustic pressure or pressure fluctuation; $p = p_\infty + p'$.
$\mathbf{Q}$	Applied-stress equivalent acoustic source in the acoustic analogy; see (3.6).
$\bar{q}_{ij,kl}$	Time averaged product between fluctuations of the Reynolds stress components $u_i' u_j'$ and $u_k' u_l'$; see equation (4.21).
$\hat{\mathbf{R}}$	Source–observer direction tensor $\hat{\mathbf{r}} \otimes \hat{\mathbf{r}}$.
$\hat{\mathbf{R}}_E$	Source–observer emission-time direction tensor $\hat{\mathbf{r}}_E \otimes \hat{\mathbf{r}}_E$.
$\mathbf{r}, \hat{\mathbf{r}}$	Source–observer separation vector, unit vector indicating its direction. The amplitude r denotes the distance between source and observer.

$\mathbf{r}_E, \hat{\mathbf{r}}_E$ Source–observer emission-time separation vector, unit vector indicating its direction. They are evaluated by considering the reception-time observer position and the acoustic-source position at emission time t_E; see section C.2.

r_E Source–observer emission-time distance, modulus of $\mathbf{r}_E$.

r_M Modified source–observer distance in the moving-source acoustic field; see equation (C.10).

$\mathbf{S}, \mathbf{S}'$ Unit-density Reynolds stress, fluctuating part; they are the tensor quantities $\mathbf{S} = \mathbf{u}' \otimes \mathbf{u}'$ and $\mathbf{S}' = \mathbf{u}' \otimes \mathbf{u}' - \overline{\mathbf{u}' \otimes \mathbf{u}'}$.

$\mathrm{s}_{\mathbf{Ab}}(\mathbf{y}, \boldsymbol{\eta}, f)$ Two-point CPSD tensor between the general random variables $\mathbf{A}(\mathbf{y} - \boldsymbol{\eta}/2, t)$ and $\mathbf{b}(\mathbf{y} + \boldsymbol{\eta}/2, t)$, defined as Fourier transform of the two-point cross correlation function $\mathrm{c}_{\mathbf{A'b'}}$ of the fluctuating parts of $\mathbf{A}$ and $\mathbf{b}$; see equation (D.21).

$s_{ij,kl}(\mathbf{y}, \boldsymbol{\eta}, f)$ Component of the two-point CPSD function of the fluctuating Reynolds-tress; it corresponds to the ij and kl Reynolds-stress components with respect to the cylindrical-coordinate unit-vector basis in $\mathbf{y}$.

$\hat{s}_{ij,kl}(\mathbf{y}, \boldsymbol{\eta}, f)$ Scaled two-point Reynolds-stress CPSD function. It is defined as $s_{ij,kl}(\mathbf{y}, \boldsymbol{\eta}, f)$ divided by the corresponding mean square Reynolds-stress fluctuation $q_{ij,kl}(\mathbf{y})$; it is equivalent to the Fourier transform of $\hat{c}_{ij,kl}(\mathbf{y}, \mathbf{0}, 0)$.

$\hat{\mathrm{s}}, \hat{\mathrm{s}}_0(\mathbf{y}, \boldsymbol{\eta}, f)$ Model and simplified isotropic-decay model for $\hat{s}_{ij,kl}(\mathbf{y}, \boldsymbol{\eta}, f)$.

Sr Nozzle-exit Strouhal number; $Sr = f d_J / u_J$.

Sr_τ Local Strouhal number, defined on the basis of the position-dependent $1/e$-decay time of the Reynolds-stress autocorrelation coefficient $\tau_d(\mathbf{y})$; $Sr_\tau(\mathbf{y}) = f\tau_d$.

T, $\bar{T}$, T' Static temperature, averaged value, fluctuating part; $T = \bar{T} + T'$.

T_J Centreline nozzle-exit mean static temperature for a turbulent jet.

t_E Emission time of an acoustic signal which is emitted in a uniform medium by a moving source and received by an observer at current time t; see section C.2.

$U_c(\mathbf{y})$ Convection parameter associated with the Reynolds-stress two-point correlation coefficient model. Introduced in equations (4.16) and (4.19).

$\mathbf{u}$, $\bar{\mathbf{u}}$, $\mathbf{u}'$ Flow velocity, averaged value, fluctuating part; $\mathbf{u} = \bar{\mathbf{u}} + \mathbf{u}'$.

u_J Nozzle-exit centreline velocity of a turbulent jet.

$\mathbf{v}$ Constant velocity of an acoustic singularity as seen from a reference fixed to the medium.

$\mathbf{x}$ Vector indicating the observer position from the origin of the reference system.

$\mathbf{x}_W$ Vector indicating the wavenormal-direction image of the observer position $\mathbf{x}$ from the origin of the reference system. This is different from $\mathbf{x}$ if the acoustic medium moves with respect to acoustic source and observer (source and observer are fixed). $\mathbf{x}_W$ is indicated by the separation vector $\mathbf{r}_E$ from the source position; $\mathbf{r}_E$ is evaluated depending on the medium characteristics at the source. See Fig. 3.2.

$\mathbf{y}$ Vector indicating the two-point source-coherence reference position from the reference-system origin. It is also used to indicate the point-source position in Appendix C.

$\mathbf{y}_E$ Vector indicating the emission-time source position from the reference-system origin.

$\mathbf{y}^{(m)}$ Vector connecting the nozzle-exit-section centre and the measurement location for the Harper-Bourne[4] data. The measurement location is on the nozzle lip line 4 diameters downstream the nozzle-exit section; see section 4.2.1.

$\boldsymbol{\alpha}$ Acoustic repetency vector, first introduced in equation (4.28).

$\tilde{\boldsymbol{\alpha}}$ Non-dimensional modified acoustic repetency vector, first introduced in equation (4.31).

β Lorentz-transformation transverse-length contraction factor; see (C.2).

$\Delta_{i,j}$ Component of the tensor $\overline{\left(\mathbf{S}' \cdot \hat{\boldsymbol{\theta}}\right) \otimes \left(\mathbf{S}' \cdot \hat{\boldsymbol{\theta}}\right)}$, according to $\hat{\boldsymbol{\gamma}}_i \otimes \hat{\boldsymbol{\gamma}}_j$, first introduced in (4.22).

δ_{ij} Kronecker symbol.

ϵ Turbulence dissipation rate.

$\boldsymbol{\eta}$ Spatial separation in the evaluation of the two-point flow/acoustic source statistics.

π_G Acoustic variable used in the perfect-gas Goldstein equation for the Lilley analogy, see equation (B.15).

$\tilde{\pi}_G$ Acoustic variable for the perfect-gas the Lilley-analogy equation used by Tester and Morfey, first introduced in equation (B.23).

$\sigma_{ij,kl}\left(\mathbf{y}, \boldsymbol{\eta}, f\right)$ Normalised two-point CPSD $s_{ij,kl}\left(\mathbf{y}, \boldsymbol{\eta}, f\right) / s_{ij,kl}\left(\mathbf{y}, \mathbf{0}, f\right)$; see equation (4.15).

$\sigma, \sigma_0(\mathbf{y}, \boldsymbol{\eta}, f)$ Model and simplified isotropic-decay model for $\sigma_{ij,kl}\left(\mathbf{y}, \boldsymbol{\eta}, f\right)$; they are derived from $\hat{\mathrm{c}}$ and $\hat{\mathrm{c}}_0$ respectively. We use σ_0, first introduced in (4.29), in determining the acoustic-source volumetric strength.

τ	Time separation in the evaluation of the correlation functions.
$\tau_d\,(\mathbf{y})$	Time scale in the Reynolds-stress autocorrelation coefficient model. It is the $1/e$-decay time separation of $\hat{\mathrm{c}}\,(\mathbf{y},\mathbf{0},\tau)$ or $\hat{\mathrm{c}}_0(\mathbf{y},\mathbf{0},\tau)$. Introduced in equations (4.16) and (4.19).
ϑ	Angle between the mean-flow (jet-axis) and the source–observer directions.
ϑ_W	Angle between the local-medium wavenormal direction and the mean flow direction; see Fig. 3.1.
$\hat{\boldsymbol{\theta}}$	Unit vector indicating the direction of the spatial gradient of the time-averaged absolute static temperature.
$\boldsymbol{\xi}$	Spatial separation corresponding to $\boldsymbol{\eta}$ after transformation to the moving reference frame; $\boldsymbol{\xi} = \boldsymbol{\eta} - \tau\mathbf{u}_{MF}$. Here $\mathbf{u}_{MF}$ indicates the velocity of the moving frame.
Subscripts	
∞	Value of a given variable in the ambient region outside the jet.
Supersripts	
(i)	Mean value of a given variable in the spatial region associated with the i-th acoustic-source subregion.
(m)	Quantity associated with the Harper-Bourne[4] measurements of the Reynolds-stress two-point statistics.

References

[1] Lighthill, M. J., "On sound generated aerodynamically. I. General theory," *Proceedings of the Royal Society of London. Series A, Mathematical and Physical Sciences*, Vol. 211, No. 1107, 1952, pp. 564–587.

[2] Lilley, G. M., "Generation of sound in a mixing region," *The Generation and Radiation of Supersonic Jet Noise — Volume IV — Theory of Turbulence Generated Jet Noise, Noise Radiation from Upstream Sources, and Combustion Noise*, Vol. 4, Air Force Aero Propulsion Laboratory, 1972, pp. 1–84.

[3] Goldstein, M. E., "An exact form of Lilley's equation with a velocity quadrupole/temperature dipole source term," *Journal of Fluid Mechanics*, Vol. 443, 2001, pp. 231–236.

[4] Harper-Bourne, M., "Jet near-field noise prediction," Aiaa paper 99–3068, Aug. 1999.

[5] Harper-Bourne, M., "Jet-noise turbulence measurements," Aiaa paper 2003–3214, May 2003.

[6] Khavaran, A., Krejsa, E. A., and Kim, C. M., "Computation of supersonic jet mixing noise for an axisymmetric CD nozzle using k–ϵ turbulence model," Aiaa paper 92–0500, Jan 1992.

[7] Bailly, C., Lafon, P., and Candel, S., "Subsonic and supersonic jet noise predictions from statistical source models," *AIAA Journal*, Vol. 35, No. 11, Nov. 1997, pp. 1688–1696.

[8] Garrick, I. E. and Watkins, C. E., "A theoretical study of the effect of forward speed on the free-space sound-pressure field around propellers," Naca tn 3018, National Advisory Committee for Aeronautics, Langley Aeronautical Laboratory, Langley Field, VA, USA, Oct. 1953.

[9] Tanna, H. K., Dean, P. D., and Burrin, R. H., "The generation and radiation of supersonic jet noise. Volume III, turbulent mixing noise data," Afapl–tr–76–65, Air Force Aero-propulsion Laboratory, Lockheed Georgia Company, Marietta, Georgia 30063, USA, Sept. 1976.

[10] "Results from an experimental programme on static single-stream jet noise," Internal report fst/tn026455, QinetiQ Ltd, 2003.

[11] Colonius, T. and Lele, S. K., "Computational aeroacoustics: progress on nonlinear problems of sound generation," *Progress in Aerospace Sciences*, Vol. 40, 2004, pp. 345–416.

[12] Balsa, T. F. and Gliebe, P. R., "Aerodynamics and noise of coaxial jets," *AIAA Journal*, Vol. 15, No. 11, 1977, pp. 1550–1558.

[13] Goldstein, M. E., "Aeroacoustics of turbulent shear flows," *Annual Reviews of Fluid Mechanics*, Vol. 16, 1984, pp. 263–295.

[14] Khavaran, A., Krejsa, E. A., and Kim, C. M., "Computation of supersonic jet mixing noise for an axisymmetric convergent-divergent nozzle," *Journal of Aircraft*, Vol. 31, No. 3, 1994, pp. 603–609.

[15] Batchelor, G. K., *The theory of homogeneous turbulence*, Cambridge University Press, 1953.

[16] Balsa, T. F., "The far field of high frequency convected singularities in sheared flows, with an application to jet-noise prediction," *Journal of Fluid Mechanics*, Vol. 74, No. 2, 1976, pp. 193–208.

[17] Tam, C. K. W. and Auriault, L., "Jet-mixing noise from fine-scale turbulence," *AIAA Journal*, Vol. 37, No. 2, 1999, pp. 145–153.

[18] Tam, C. K. W., Golebiowski, M., and Seiner, J. M., "On the two components of turbulent mixing noise from supersonic jets," Aiaa paper 96–1716, May 1996.

[19] Davies, P. O. A. L., Fisher, M. J., and Barratt, M. J., "The characteristics of the turbulence in the mixing region of a round jet," *Journal of Fluid Mechanics*, Vol. 15, No. 3, 1963, pp. 337–367.

[20] Thies, A. T. and Tam, C. K. W., "Computation of turbulent axisymmetric and non-axisymmetric jet flows using the k-ϵ model," *AIAA Journal*, Vol. 34, No. 2, 1996, pp. 309–316.

[21] Morris, P. J. and Farassat, F., "Acoustic analogy and alternative theories for jet noise prediction," *AIAA Journal*, Vol. 40, No. 4, 2002, pp. 671–680.

[22] Morris, P. J. and Boluriaan, S., "The prediction of jet noise from CFD data," Aiaa paper 2004–2977, May 2004.

[23] Raizada, N. and Morris, P. J., "Prediction of noise from high speed subsonic jets using an acoustic analogy," Aiaa paper 2006–2596, May 2006.

[24] Goldstein, M. E., *Aeroacoustics*, McGraw-Hill, 1976.

[25] Goldstein, M. E., "The low frequency sound from multipole sources in axisymmetric shear flow, with applications to jet noise," *Journal of Fluid Mechanics*, Vol. 70, No. 3, 1975, pp. 595–604.

[26] Goldstein, M. E., "The low frequency sound from multipole sources in axisymmetric shear flow. Part 2," *Journal of Fluid Mechanics*, Vol. 75, No. 1, 1976, pp. 17–28.

[27] Dowling, A. P., Ffowcs-Williams, J. E., and Goldstein, M. E., "Sound production in a moving stream," *Philosophical transactions of the Royal Society of London. Series A, Mathematical and Physical Sciences*, Vol. 288, No. 1353, 1978, pp. 321–349.

[28] Khavaran, A., Bridges, J., and Georgiadis, N., "Prediction of turbulence-generated noise in unheated jets," Nasa/tm–2005-213827, NASA Glenn Research Center, Cleveland, OH, USA, July 2005.

[29] Khavaran, A., "Role of anisotropy in turbulent mixing noise," *AIAA Journal*, Vol. 37, No. 7, 1999, pp. 832–841.

[30] Khavaran, A., Bridges, J., and Freund, J. B., "A parametric study of fine-scale turbulence mixing noise," Nasa/tm–2002-211696, NASA Glenn Research Center, Cleveland, OH, USA, July 2002.

[31] Balsa, T. F., "The acoustic field of sources in shear flow with application to jet-noise: convective amplification," *Journal of Fluid Mechanics*, Vol. 79, No. 1, 1977, pp. 33–47.

[32] Tam, C. K. W. and Auriault, L., "Mean flow refraction effects on sound radiated from localised source in jets," *Journal of Fluid Mechanics*, Vol. 370, No. 2, 1998, pp. 149–174.

[33] Khavaran, A., Bridges, J., and Hunter, C. A., "Assesment of current jet-noise prediction capabilities," Aiaa paper–2008-2933, May 2008.

[34] Khavaran, A. and Kenzakowski, D. C., "Noise Generation in hot jets," Nasa/cr–2007-214924 (aiaa paper 2007–3640), NASA Glenn Research Center, Cleveland, OH, USA, July 2007.

[35] Goldstein, M. E., "A generalized acoustic analogy," *Journal of Fluid Mechanics*, Vol. 488, 2003, pp. 315–333.

[36] Self, R. H. and Azarpeyvand, M., "Utilization of turbulent energy transfer rate time-scale in aeroacoustics with application to heated jets," *International Journal of Aeroacoustics*, Vol. 7, No. 2, 2008, pp. 83–102.

[37] Self, R. H. and Azarpeyvand, M., "Noise prediction of a coaxial jet using energy transfer rate time-scale," Aiaa paper 2007–3639, May 2007.

[38] Goldstein, M. E. and Leib, S. J., "The aeroacoustics of slowly diverging supersonic jets," *Journal of Fluid Mechanics*, Vol. 600, 2008, pp. 291–337.

[39] Bridges, J. and Podboy, G. G., "Measurements of two point velocity correlations in a round jet with application to jet noise," Aiaa paper 99–1966, 1999.

[40] Tester, B. J. and Morfey, C. L., "Developments in jet noise modelling—Theoretical predictions and comparison with measured data," *Journal of Sound and Vibration*, Vol. 46, No. 1, 1976, pp. 79–103.

[41] Morfey, C. L., Szewczyk, V. M., and Tester, B. J., "New scaling laws for hot and cold jet mixing noise based on a geometric acoustic model," *Journal of Sound and Vibration*, Vol. 61, No. 2, 1978, pp. 255–292.

[42] Bassetti, A., Morfey, C. L., and Harper-Bourne, M., "Impact of the source-correlation model in jet-noise prediction by acoustic analogy," Aiaa paper 2007–3604, May 2007.

[43] Morfey, C. L., Tester, B. J., and Powles, C. J., "Numerical and asymptotic Lilley-equation solutions for the Goldstein jet-noise source model," Aiaa paper 2007–3592, May 2007.

[44] Blokhintzev, D., "The propagation of sound in an inhomogeneous and moving medium I," *The Journal of the Acoustical Society of America*, Vol. 18, No. 2, 1946, pp. 322–334.

[45] Morfey, C. L. and Tester, B. J., "Noise measurements in a free-jet flight-simulation facility: shear-layer refraction and facility-to-flight corrections," *Journal of Sound and Vibration*, Vol. 54, No. 1, 1977, pp. 83–106.

[46] Ffowcs-Williams, J. E. and Hawkings, D. L., "Sound generation by turbulence and surfaces in arbitrary motion," *Philosophical transactions of the Royal Society of London. Series A, Mathematical and Physical Sciences*, Vol. 264, No. 1151, 1969, pp. 321–342.

[47] Ribner, H. S., "New theory of jet-noise generation, directionality, and spectra," *Journal of the Acoustical Society of America*, Vol. 31, No. 2, 1959, pp. 245–246.

[48] Frisch, U., *Turbulence: The Legacy of A. N. Kolmogorov*, Cambridge University Press, 1995.

[49] Kolmogorov, A. N., "Dissipation of energy in the locally isotropic turbulence (first published in Russian in *Dokl. Akad. Nauk SSSR* 1941 **32**1)," *Proceedings of the Royal Society of London. Series A, Mathematical and Physical Sciences*, Vol. 434, No. 1890, 1991, pp. 15–17.

[50] Bassetti, A. and Morfey, C. L., "An acoustic-analogy model for jet noise prediction," Aiaa paper 2007–3642, May 2007.

[51] Chu, W. T., "Turbulence measurements relevant to jet noise," UTIAS Technical Report 119, Institute for Aerospace Studies, University of Toronto, Toronto 5, Ont., Canada, Nov. 1966.

[52] Kerhervé, F., Fitzpatrick, J., and Jordan, P., "The frequency dependence of jet turbulence for noise source modelling," *Journal of Sound and Vibration*, Vol. 296, 2006, pp. 209–225.

[53] Lau, J. C., *The coherent structure of jets*, Ph.D. thesis, Institute of Sound and Vibration Research, University of Southampton, 1971.

[54] Lau, J. C. and Fisher, M. J., "The vortex-street structure of 'turbulent' jets. I," *Journal of Fluid Mechanics*, Vol. 67, No. 2, 1975, pp. 299–337.

[55] Abramovich, G. N., *The Theory of Turbulent Jets*, The Massachusetts Institute of Technology Press, 1963.

[56] Harper-Bourne, M., "Some observations on the noise of heated jets," Internal report 07/01953; aiaa/ceas presentation 2007–3632, QinetiQ Ltd, July 2007.

[57] Bryce, W. D., "The prediction of static-to-flight changes in jet noise," Aiaa paper 84–2358, Oct. 1984.

[58] Morfey, C. L., "Amplification of aerodynamic noise by convected flow inhomogeneities," *Journal of Sound and Vibration*, Vol. 31, No. 4, 1973, pp. 391–397.

[59] Pinker, R. A., "The enhancement of the QinetiQ Noise Test Facility for larger-scale exhaust system," Aiaa paper 2004–3019, May 2004.

[60] Page, G. J., McGuirk, J. J., Hossain, M., Self, R., and Bassetti, A., "A CFD coupled acoustics approach for coaxial jet noise," Aiaa paper 2003–3286, May 2003.

[61] Lowson, M. V., "The sound field for singularities in motion," *Proceedings of the Royal Society of London. Series A, Mathematical and Physical Sciences*, Vol. 286, No. 1407, 1965, pp. 559–572.

[62] Brentner, K. S., "An efficient and robust method for predicting helicopter high-speed impulsive noise," *Journal of Sound and Vibration*, Vol. 203, No. 1, 1997, pp. 87–100.

[63] Ffowcs-Williams, J. E., "The noise from turbulence convected at high speed," *Philosophical transactions of the Royal Society of London. Series A, Mathematical and Physical Sciences*, Vol. 255, No. 1061, 1963, pp. 469–503.

[64] Truesdell, C. A., *A First Course in Rational Continuum Mechanics*, Academic Press, 1991.

[65] Morfey, C. L., *Dictionary of Acoustics*, Academic Press, 2001.

[66] Pridmore-Brown, D. C., "Sound propagation in a fluid flowing through an attenuating duct," *Journal of Fluid Mechanics*, Vol. 4, No. 4, 1958, pp. 393–406.

[67] Morfey, C. L. and Wright, M. C. M., "Extensions of Lighthill's acoustic analogy with application to computational aeroacoustics," *Proceedings of the Royal Society of London. Series A*, Vol. 463, 2007, pp. 2101–2127.

[68] Morse, P. M. and Ingard, K. U., *Theoretical Acoustics*, Princeton University Press, 1986.

[69] Hu, Z. W., Morfey, C. L., and Sandham, N. D., "Two-dimensional Green function for moving line source with spanwise variation," Technical report afm-02/03, University of Southampton, School of Engineering, Aeronautics and Astronautics Department, 2002.

[70] Lighthill, M. J., "The bakerian lecture, 1961. Sound generated aerodynamically," *Proceedings of the Royal Society of London. Series A, Mathematical and Physical Sciences*, Vol. 267, No. 1329, 1962, pp. 147–182.

[71] Farassat, F., "Derivation of Formulations 1 and 1A of Farassat," Nasa/tm-2007-214853, NASA Langley Research Center, Hampton, VA, USA, March 2007.

[72] "FLUENT 6.2 User's Guide," Tech. rep., Fluent Inc, Lebanon (NH), 2005.

[73] Lush, P. A., "Measurements of subsonic jet noise and comparison with theory," *Journal of Fluid Mechanics*, Vol. 46, No. 3, 1971, pp. 477–500.

[74] Fisher, M. J., Harper-Bourne, M., and Glegg, S. A. L., "Jet engine noise source location: the polar correlation technique," *Journal of Sound and Vibration*, Vol. 51, No. 1, 1977, pp. 23–54.